The effects of curing- and service-conditions on durability of reinforced concrete structures.

by

Colin Bradley Van Niejenhuis

A thesis
presented to the University of Waterloo
in fulfilment of the
thesis requirement for the degree of
Doctor of Philosophy
in
Civil Engineering

Waterloo, Ontario, Canada, 2020

Examining Committee Membership

The following served on the Examining Committee for this thesis. The decision of the Examining Committee is by majority vote.

External Examiner	Samir Chidiac, PhD Professor, Civil Engineering McMaster University
Supervisor(s)	Carolyn Hansson, PhD Professor, Mechanical and Mechatronics Engineering University of Waterloo
	Maria Anna Polak, PhD Professor, Civil and Environmental Engineering University of Waterloo
Internal Member	Giovanni Cascante, PhD Professor, Civil and Environmental Engineering University of Waterloo
	Scott Walbridge, PhD Professor, Civil and Environmental Engineering University of Waterloo
Internal-external Member	Duane Cronin, PhD Professor, Mechanical and Mechatronics Engineering University of Waterloo

Author’s Declaration

This thesis consists of material all of which I authored or co-authored: see Statement of Contributions included in the thesis. This is a true copy of the thesis, including any required final revisions, as accepted by my examiners.

I understand that my thesis may be made electronically available to the public.

Statement of Contributions

Professor Carolyn Hansson and Professor Maria Anna Polak supervised all work completed in this thesis as well as provided valuable data, feedback, and constructive criticism to the authors work.

Dr Ibrahim Ogunsanya performed equal work in preparation of the work in section entitled “Pore solution composition of cement pastes with admixed chlorides”. The experimental work, which included cement paste casting, and pore solution expression, was done in collaboration with Dr Ogunsanya. We also co-wrote a paper entitled “Analysis of pore solution of different cements with and without admixed chlorides” which was accepted for publication in ACI Structural and Materials Journal on January 20, 2020.

Abstract

Reinforced structural concrete is a critical building block of our civil infrastructure, especially our roads and bridges. As the transportation network grows, and our current infrastructure continues to age, the social cost of rehabilitation and maintenance must be considered. Recently, the onus has been placed on the designer to consider how new methods and materials can create structures which will last longer in the harsh Canadian climate.

Thus, with the goal of improving long term design considerations for reinforced concrete structures, an experimental and analytical research project was undertaken to determine how the environmental conditions in which the concrete is cast as well as subjected to over its useful service life affects the properties of the composite structure. This was divided into to unique components. First, the effect of concrete curing conditions and in-service temperature on the structural properties of reinforced concrete structures, especially those containing glass fibre reinforced polymer (GFRP) reinforcement was investigated. Secondly, the effect of salt use on the structure of concrete and its potential effect on reinforcing steel was examined.

To explore the impact of curing and service conditions, four experimental programs were conducted. Two of these programs investigated the effect of thermal fatigue on GFRP reinforced structures in both a lab and field setting. The laboratory tests varied the temperature of concrete prisms containing GFRP between 20°C and -20°C for over 300 freeze-thaw cycles. Over the duration of the test, the dynamic modulus was monitored to assess for any internal microcracking. For the field program, concrete prisms reinforced with GFRP were placed outdoors and exposed to the Ontario climate for approximately four years. The internal strains were recorded and compared to those without GFRP. From both of these procedures it was concluded that the differential coefficient of thermal expansion between GFRP and concrete posed no direct risk to the concrete surrounding the GFRP due to cyclic effects alone. The third program evaluated the impact of curing- and testing-temperatures on the bond between the GFRP and concrete. This was investigated by casting GFRP from two different suppliers, and in two different bar sizes, into concrete cured at 60°C, 70°C, 80°C and ambient lab conditions. After 28-days, the bond strength of the specimens was tested, at either ambient lab conditions or -30°C, and the variance compared. Contrary to the hypothesis, the bond increased at -30°C, which was directly correlated to the increase in compressive strength that the frozen specimens experienced. The fourth program examined why frozen concrete experienced strength increases of up to 46% compared to identical concrete tested at ambient conditions. This was correlated to the amount of pore water which, when frozen, provides crushing resistance to the concrete. The results of these experiments, alongside code and literature analysis, have suggested that the code development length of GFRP in high strength concrete is currently highly conservative.

In order to examine the effects of salt use on the structure of concrete, two experimental programs were conducted. First, a 5-year study was conducted to compare the compressive strength of concrete submerged in: $MgCl_2$, $CaCl_2$, NaCl, or a multi-chloride brine and compared

to specimens placed in a humidity chamber. The results indicated compressive strength reductions of up 25% in concretes exposed to $MgCl_2$ or $CaCl_2$, caused by chemical reactions between the chloride and the cement paste. Statistical analysis of the reduction indicated that these chemical reactions lead to changes in failure mechanisms between what the designer assumed and the structure experiences. The second program was designed to understand the influence of supplementary cementitious materials (SCM's) and the water to binder ratio on the pore solution composition of cement pastes. Sodium chloride was admixed into cement pastes containing ordinary Portland cement as well as ground granulated blast furnace slag, fly ash, and silica fume with water to binder ratios ranging between 0.40 and 0.55. The pore solution of the cured cement paste was then extracted and chemically analyzed using ion chromatography (IC) for the anions and inductively coupled plasma (ICP) for the cations. The results indicate that the concentration of chloride in the pore solution rises with increasing amounts of admixed chloride in the cement paste. Unexpectedly, the increase in admixed chloride also led to an increase in the sulphates in the pore solution, leading to higher chloride concentrations required to initiate corrosion.

Acknowledgements

I would like to sincerely thank Dr. Marianna Polak, and Dr. Carolyn Hansson, for fostering my passion for learning. The advice given, and the questions asked have profoundly changed my view on how engineers should assess both materials and design.

I would like to thank my colleagues who helped with the unending lab work required to complete my graduate school work: Dr Ibrahim Ogunsanya, Leah Kristufek, Peter Loudfoot, Adam Felinczak, Marc Johnson, and Graeme Milligan. I would also like to thank the lab technicians who provided input, support, and freedom in the lab: Douglas Hirst, Peter Volcic, Mark Griffet, and most of all Richard Morrison.

Without the financial support of the Ministry of Transportation of Ontario and materials supplied by: Holcim Canada, Pultrall, Schöck – Combar, this project would not have been possible.

Table of Contents

List of Figures

List of Tables

List of Variables

Variable	Units	Definition
A	$\frac{m^2}{m^2}$	Total area of sound concrete per metre squared of deck area
a	mm	Depth of equivalent rectangular stress block
a_g	mm	Specified nominal maximum soze of course aggregate
A_{frp}	mm^2	Area of non-prestressed tension FRP reinforcement
A_s	mm^2	Area of non-prestressed tension steel reinforcement
C(x,T)	(kg/m^3)	Free chloride concentration at depth x at time T
C	mm	Depth to neutral axis
C_s	(kg/m^3)	Surface chloride content
C_r	kN	Compression resistance provided by concrete above neutral axis
C-S-H		Calcium Silicate Hydrate
D	(m^2/s)	Apparent diffusion coefficient
d	mm	Distance from extreme compression fibre to centroid of longitudinal tensile reinforcement
d_b	mm	Diameter of bar
d_{cs}		Cover and spacing factor
E_c	MPa	Modulus of Elasticity for concrete
E_{frp}	MPa	Modulus of Elasticity for non-prestressed reinforcing FRP bars
E_s	MPa	Modulus of Elasticity for non-prestressed reinforcing steel bars
f_{cr}	MPa	Cracking stress
f'_c	MPa	Specified concrete strength
f'_{field}	MPa	Field In-situ concrete strength
f_{fe}	MPa	Allowable bar stress based on FRP embedment length
f_F	MPa	The design stress in tension at ultimate limit state
f_n	Hz	Natural frequency
f_y	MPa	Yield strength of reinforcing bars
k_{cp}		Compaction coefficient
k_{cr}		Curing coefficient
K_r	MPa	Moment resistance factor
k_{tr}		Transverse reinforcement index
l_d	mm	Development length
M_r	kN·m	Factored moment resistance
n		Fundamental transverse frequency at 0 cycles of freeze thawing
n_1		Fundamenta/ transverse frequency after c cycles of freeze thawing
P_c	%	Relative dynamic modulus
s_{min}	mm	Minimum spacing between bars to ensure proper concrete consolidation
T_n	Hz	Natural Period

$\mathbf{T}_r$	kN	Tensile resistance provided by longitudinal reinforcement
$\boldsymbol{w_n}$	Hz	Undamped natural frequency
$\mathbf{W_D}$	g	Weight of the dry sample
$\mathbf{W}_e$	%	Evaporable water content
$\mathbf{W}_w$	g	Weight of the wet sample
w/cm	%	Water to cementitious material
$\boldsymbol{\alpha_1}$		Ratio of average stress in rectangular compression block to the specified concrete strength
$\boldsymbol{\beta_1}$		Ratio of depth of rectangular compression block to depth to the neutral axis
$\boldsymbol{\varepsilon_{cr}}$	$\frac{mm}{mm}$	Cracking strain
$\boldsymbol{\varepsilon_{cu}}$		Maximum strain at the extreme concrete compression fibre at ultimate
ρ		Reinforcement ratio
$\boldsymbol{\rho_b}$		Balanced Reinforcement ratio where tensile reinforcement fails when concrete crushes
$\boldsymbol{\tau_m}$	MPa	Bond Stress
$\boldsymbol{\phi_c}$		Resistance factor for concrete
$\boldsymbol{\phi_s}$		Resistance factor for non-prestressed reinforcing steel bars
$\boldsymbol{\phi_{frp}}$		Resistance factor for non-prestressed reinforcing FRP bars
ACAC		ambient curing + ambient conditioning
ACMC		ambient curing + moist conditioning
ECAC		elevated curing + ambient conditioning
ECMC		elevated curing + moist conditioning

Chapter 1 Introduction

1.1. Background

Although Joseph Aspdin patented the process for creating modern day Portland cement in 1824 [1], it was not until 30 years later (1854) that Wilkinson filed a patent to include iron bars to reinforce the concrete in areas where tensile stress is highest [2]. Initially, this approach appeared to have been successful in addressing the tensile weakness of concrete, but also introduced the threat of corroding reinforcement. Reinforcement corrosion has been documented as far back as the early 1900's where Mahgnusson and Smith [3] noted that, under regular conditions, the iron is protected. However, in 1911, Brown [4] reported a phenomena called "stray current corrosion" whereby corrosion occurs due to an electrical short created through a positive potential between internal concrete and a nearby power supply.

Although stray current corrosion is still an ongoing threat to the integrity of reinforcements, the most common type of reinforcement corrosion is caused by the diffusion of chlorides from the surface of the structure to the level of the reinforcing bars, typically observed in marine environments or highway structures exposed to de-icing salts [5]. Carbon steel (black steel) is usually chosen for its low cost and passive nature in high pH environments. This is usually between 12.5 and 13.5 for concrete but reported as high as 13.75 [6]. Once surface chloride concentrations surpass the material specific threshold level, active corrosion is likely to initiate. As this occurs, corrosion products form on the surface of the rebar. These compounds have a greater volume than that of the original steel, and induce a tensile stress within the concrete, ultimately leading to cracking and spalling. For traditional black steel, the corrosion products are typically Fe_2O_3 and Fe_3O_4 which Marcotte [7, 8] noted have specific volumes between two and three times that of the original steel, Figure 1-1.

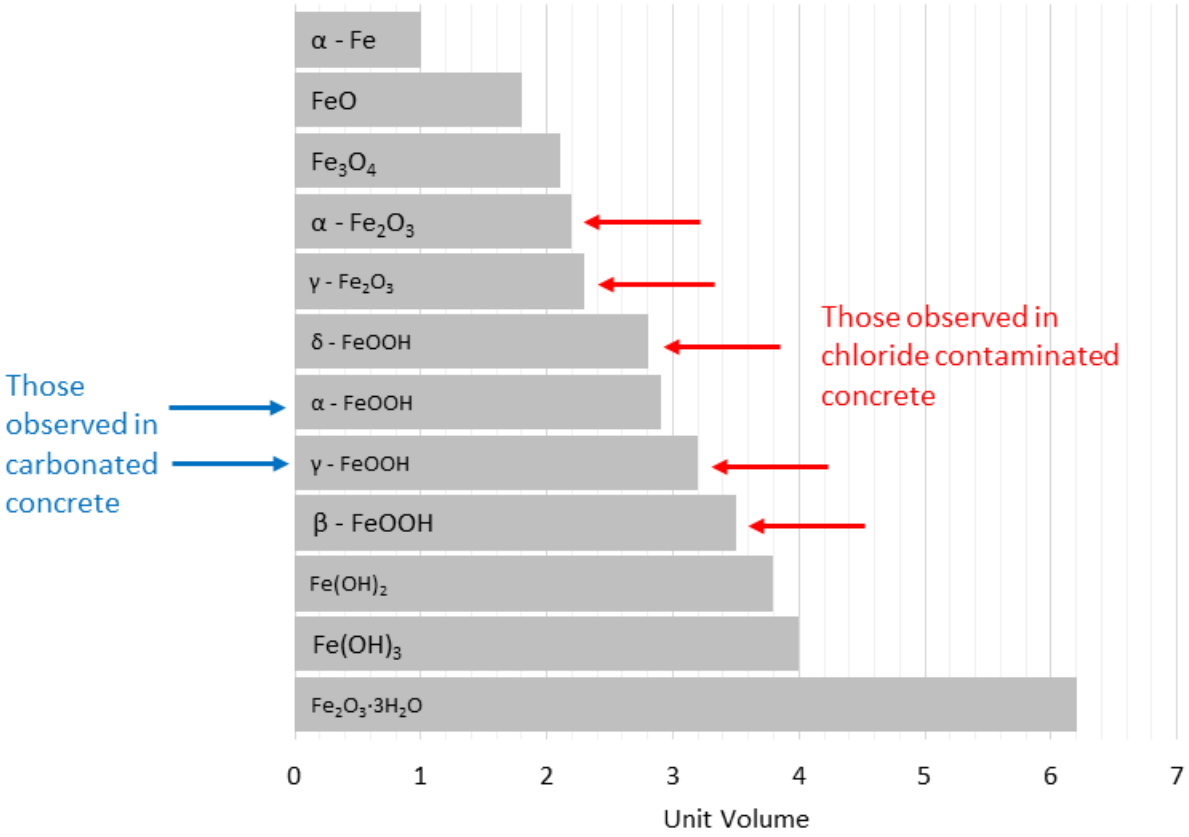

Figure 1-1: Relative volumes of iron corrosion products as compared to carbon steel

In order to mitigate the risk of corrosion, corrosion resistant or immune reinforcement materials have been developed which include: epoxy-coated carbon steel, galvanized carbon steel, basalt fibre reinforced polymers (BFRP), glass fibre reinforced polymers (GFRP), carbon fibre reinforced polymers (CFRP), and several different grades of stainless steel (including UNS: S30403, S31653, S32101, S32304, S32205, S24100). The drawback of utilizing these products is the increased cost relative to that of traditional carbon steel.

Consequently, Knudsen et al. [9] recommends using stainless steel (or corrosion resistant reinforcement) exclusively in the extremely susceptible regions of highway structures such as: the base of columns in chloride splash zones, expansion joints, and the top layer of rebar in the deck of a bridge.

In 2002, the United States Department of Transportation Federal Highway Administration [10] estimated that corrosion of infrastructure directly cost the American people $20.1 billion per year, with approximately 37 percent of that ($8.3 billion) spent on highway bridges. In order to reduce those costs, commercially available life cycle analysis software (e.g. Life 365), as well as research modelling (eg. Kikpatrick et al. [11], Benz [12], Hartt [13]) has been developed. This software allows designers predict the behaviour and lifespan of several different materials based

on environmental variables and make a site-specific selection accordingly. However, this software is limited in that it is unable to compare GFRP to traditional steels, lacks a set corrosion propagation time for stainless steels, fails to consider the effect of cracks on time to corrosion initiation, and cannot analyze the life cycle costs of the different options based on the desired service life.

At the request of the Ministry of Transportation of Ontario (MTO), the author was commissioned to collect and analyze "real" data that can be used in design considerations for durability of structures in the future. The focus was to provide experimental and analytical analysis of structural concerns over differences in the coefficient of thermal expansion of GFRP and concrete, as well as the effects of chloride on the properties of concrete. The primary tasks are marked in orange on Figure 1-2.

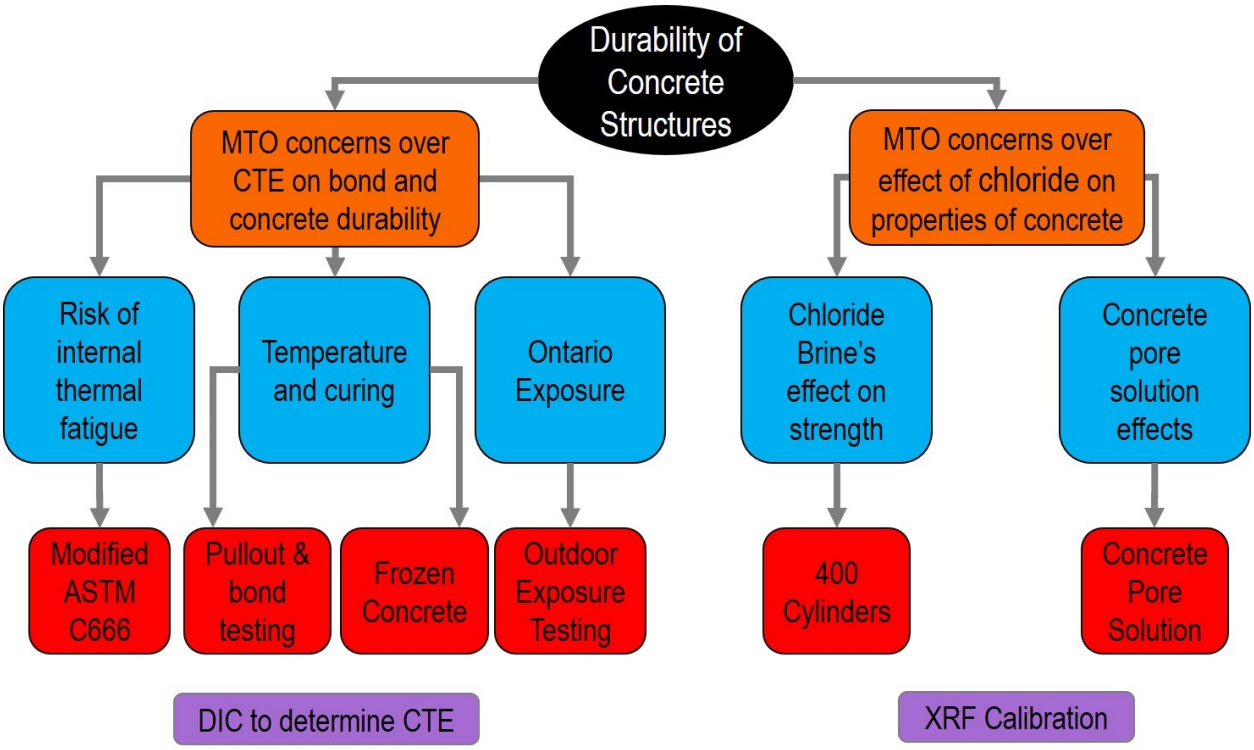

Figure 1-2: Experimental program designed to directly address Ministry of Transportation of Ontario structural issues

The MTO raised specific issues, indicated in blue, experienced in the field which raised concerns over design practices across the province. The red boxes show the tests designed to directly investigate these concerns, while the purple boxes indicate supplementary tests conducted to aid in the analysis of results of the preliminary test, each corresponding to the research objectives. These eight experimental procedures, encompassing hundreds of tests, are the backbone of the investigative research.

1.2. Research objectives

In order to aid the Ministry of Transportation of Ontario (MTO) in the selection of materials for use in highway infrastructure, with desired service lives of 75 – 100 years, as well as determine factors affecting design considerations for reinforced concrete structures the research objectives have been separated into two parts. The first was to investigate the effect of concrete curing conditions and in-service temperature on the structural properties of reinforced concrete structures, especially those containing GFRP. The second was to examine the effect of salt use on the structure of concrete and its potential effect on reinforcing steel.

To investigate the effect of curing and service temperature on the structural properties of concrete structures reinforced with GFRP, the following experiments and analyses were completed:

1a. Determination of the effect of thermal fatigue on the bond between GFRP and concrete using a modified ASTM C666 Test [14];

1b. Examination of the practicality/feasibility of using GFRP reinforcing bars in reduced concrete cover structures exposed to the southern Ontario climate;

1c. Investigation of the effect of curing- and testing-temperatures on the bond of GFRP and concrete using a modified ASTM D7913 Test [15];

1d. Evaluation of the effects that test temperature has on the compressive strength of concrete;

To examine the effect of salt on the structure and properties of concrete and its potential effect on reinforcing steel following experiments and analyses were completed:

2a. Determination of the effect of exposure to sodium, magnesium, calcium or multi chloride brine on the compressive strength of the concrete cylinders;

2b. Analysis of the pore solution composition of cement pastes with admixed chlorides to (a) understand the influence of supplementary cementitious materials and water/cementiteous ratio and (b) aid in investigations of the corrosion resistance of steel in synthetic pore solution

To garner supplementary data to aid in the analysis of the results from the six test methodologies described above two additional experiments were run.

3a. Exploration of the use of digital image correlation to determine the coefficient of thermal expansion of GFRP reinforcing bars;

3b. Calibration of X-ray fluorescent scanning for determining the concentration of chlorides in concrete;

1.3. Thesis organization

Chapter 2: Describes the knowledge available in the literature at the time of writing the thesis. It explains how the coefficient of thermal expansion of GFRP has been shown to affect the

interaction between concrete and GFRP in the past, as well as the gaps in the literature. It also reviews the detrimental effects of chloride on the structure of the concrete and on the corrosion of traditional carbon steel and stainless steel reinforcement. Last, it relates the gaps in the literature to the research objectives of the thesis.

Chapter 3: Describes the sample preparation and the experimental test program used to conduct the research. This includes material properties, specimen design and geometry, equipment calibration, test procedures, and test matrices

Chapter 4: Presents the experimental results, examines the statistical significance of the work, and discusses the causes and implications of the findings.

Chapter 5: Describes the analytical program that was utilized to supplement the experimental findings. Specifically, it analyzes the effects of the changes in compressive strength to the long-term design of concrete structures, and on potential failure mechanisms. Additionally, the experimental bond results are compared to those of the Canadian and American design codes and recommendations based on that analysis are given.

Chapter 6: Presents the conclusions of the experimental and analytical research. It also provides recommendations for interpretation of the data and proposals for further research needed to further the understanding of the use of GFRP in concrete structures.

Chapter 2 Literature Review

2.1. The effect of curing- and service-temperature on reinforced concrete structures

Both the temperature and environment that a concrete structure is exposed to greatly affect its long-term performance. These conditions need to be effectively controlled, especially when the concrete is still plastic and during the week following the cast.

2.1.1. The effect of curing temperature on the properties of concrete

The Canadian climate is one of the harshest exposure environments for reinforced concrete. Exposure to stressors such as ice and snow, de-icing and anti-icing brines, as well as extreme temperature fluctuations (as low as -63°C in Snag Yukon in 1947 to as high as 45°C in Yellow Grass Saskatchewan in July of 1937), can all compromise the integrity of concrete through direct freezing and thawing impact as well as exacerbating the corrosion of steel reinforcements.

Concrete structures are not only exposed to these extreme temperatures in the field. Precast components are often subject to extreme temperature fluctuations due to steam curing which causes the concrete temperature to rise and fall, often in less than 24 hours. This allows the compression strength to reach levels similar to high strength early setting cements, which Hooton et al. [16] show can achieve greater than 40MPa at 18 hours (up 89% strength increase versus ambient curing), often with long term durability repercussions.

The Ontario Provincial Standard Specification (OPSS) 1350 restricts the placement of cast-in-place concrete when the ambient air temperature is above 30°C. It also requires the internal temperature of the concrete to be between 20°C and 28°C [17], to ensure that the concrete has not begun to set before placement. If the concrete is placed in cold weather, for example when the temperature is expected to fall below zero °C, heating must be provided to ensure the concrete does not freeze before it sets [18] If steam curing is used, the internal temperature, which increases with the exothermal chemical hydration process (Figure 2-1), must stay below the limit of 70°C which CSA 23.4, OPSS 904 and 909 specify [18-20].

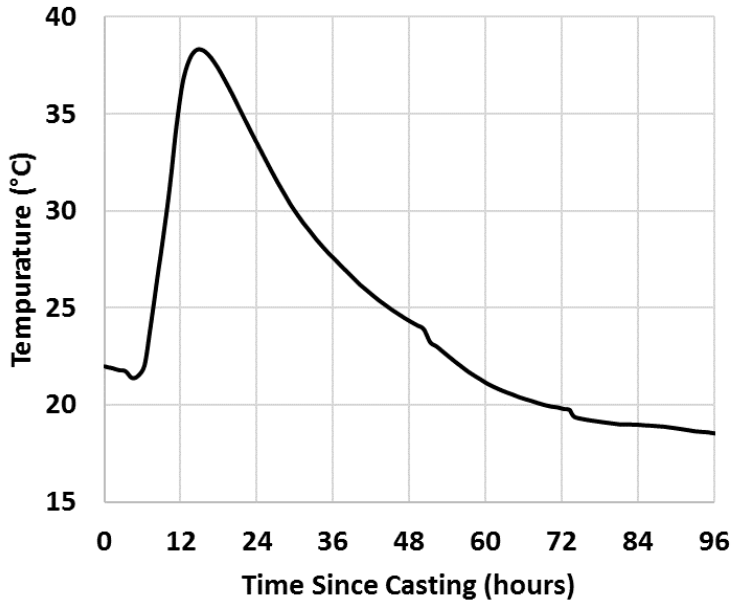

Figure 2-1: Internal concrete temperature during first three days of curing

Internal temperature limitations are necessary due to the negative correlation between curing temperature and compressive strength at a prolonged elevated temperature. Verbeck and Helmuth [21] demonstrate this by comparing compressive strength of concretes held at varying curing temperatures for 1 and 28 days. They noted that as the curing temperatures increased from 55°F to 120°C for 1-day curing, the corresponding compressive strength also increase. Contrastingly, the same concrete tested at 28 days had the opposite trend, with higher curing temperatures leading to lower compressive strength. They equated this to an increased initial hydration of the cement with temperature, raising the 1-day compression strength, which led to a non-homogenous distribution of hydration products later, reducing the 28-day strength.

Limiting the internal temperature is also necessary to prevent the risk of delayed ettringite formation (DEF). Taylor et al. [22] define DEF as:

> *"the formation of ettringite in a cementitious material by a process that begins after hardening is substantially complete and in which none of the sulphate come from outside the cement paste".*

Heinz and Ludwig [23] show that for DEF to take place, the internal temperature must exceed 70°C for an appropriate amount of time, and the concrete must be sufficiently wet once returned to ambient conditions. The formation of ettringite leads to complications, as it doubles the volume of the solids if it forms in an already hardened mix [24] . This ultimately compromises the structural integrity of the concrete structure by causing tensile stresses, leading to swelling and cracking.

2.1.2. Glass Fibre-Reinforced Polymers (GFRP)

To mitigate the structural issues caused by the corrosion of reinforcing steel in concrete, researchers and designers alike have been experimenting with alternative, corrosion resistant materials, such as glass fibre reinforced polymers.

Glass fibre reinforced polymers (GFRP) have been developed over the past 100 years, becoming commercially available by the Owens Corning Company in the 1930s. GFRP production was later refined to use extruded glass, and first used in Russia in 1975 as pre-stressing strands for a timber bridge [25]. There are six major types of glass fibres, Table 2-1, with E-glass being the most common and used for 90% of fibre glass applications, whereas the others are limited to specialty application, [26], due to their increased manufacturing costs. The physical properties of 4 of the fibre types are summarized in Table 2-2.

Table 2-1: Six different types of glass fibers [26]

Letter Designation	Property or Characteristic
E, Electrical	Low electrical conductivity
S, Strength	High Strength
C, Chemical	High chemical durability
M, Modulus	High stiffness
A, Alkali	High alkali or soda lime glass
D, Dielectric	Low dielectric constant

Table 2-2: Typical physical and mechanical properties of commercial glass fibre at room temperature [27]

Parameter	E-glass	S-glass	C-glass	A-glass
Tensile Strength (GPa)	3.45	4.30	3.03	2.50
Tensile Modulus (GPa)	72.40	86.90	69.00	70.00
Ultimate Strain (%)	4.80	5.00	4.80	3.60
Poisson's ratio	0.20	0.22	-	-
Density (g/cm^3)	2.54	2.49	2.49	2.78
Diameter (µm)	10.00	10.00	4.50	-
Longitudinal CTE (10^{-6}/°C)	5.00	2.90	7.20	-
Dielectric constant	6.30	5.10	-	-

GFRP rebar is a composite product that relies on both the strength of the fibre being used as well as the bond between the resin matrix and the fibre. It is typically manufactured by either immersing the fibres in the resin before orienting, heating, molding, and wrapping, Figure 2-2, or

by injecting the resin between the oriented fibre strands, Figure 2-3.The composite is then heated to crosslink the resin chains and provide the required properties.

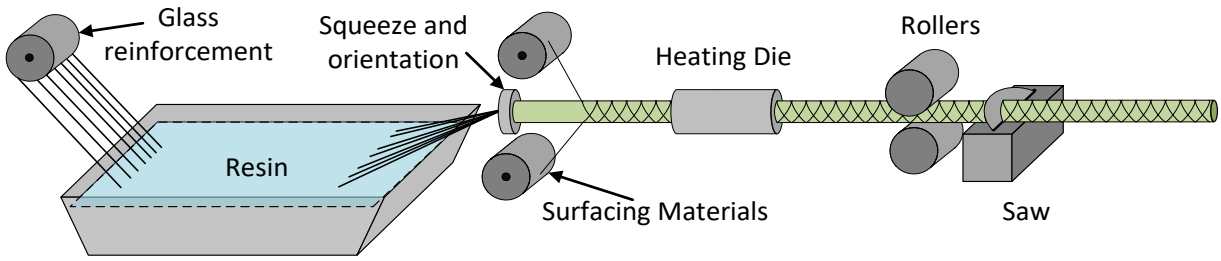

Figure 2-2: GFRP reinforcing bar production using fibre submersion [27]

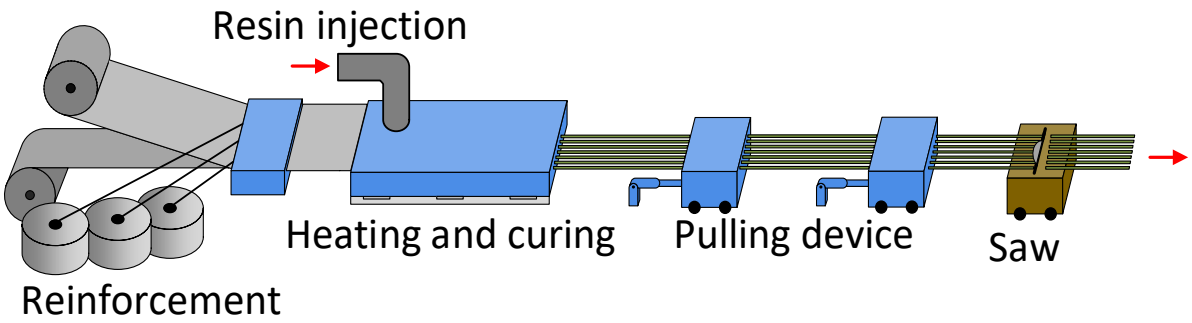

Figure 2-3: FRP production using resin [28]

The three main types of resin used as the binding matrix for FRP are: polyester, epoxy, and vinyl ester, with vinyl ester currently the most common. A summary of their physical and mechanical properties is given in Table 2-3.

Table 2-3: Typical physical and mechanical properties of commercial matrix materials [27]

Parameter	Polyester	Epoxy	Vinyl Ester
Tensile Strength (MPa)	20-100	55-130	70-80
Tensile Modulus (GPa)	2.1-4.1	2.5-4.1	3.0-3.5
Ultimate Strain (%)	1-6	1-9	3.5-5.5
Poisson's ratio	-	0.2-0.33	-
Density (g/cm^3)	1.0-1.45	1.1-1.3	1.1-1.3
Tg (°C)	10-140	50-260	90-140
CTE (10^{-6}/°C)	55-100	45-90	21-73
Cure Shrinkage (%)	5-12	1-5	5.4-10.3

When comparing the process of designing reinforced concrete with GFRP or with steel there are two key mechanical properties that must be considered. First, brittle failure occurs when the GFRP fibres exceed their tensile capacity whereas steel yields prior to failure. This is important because it means that GFRP reinforced concrete structures must be designed to be over

reinforced, thereby allowing the concrete will crush before the rebar fails. In contrast, steel reinforced concrete structures are designed as under reinforced, allowing the steel to yield before the concrete crushes. This is typically observed with large deflections in the structural members, allowing users to unload the structure or evacuate the area before their safety is at risk. The second consideration is the coefficient of thermal expansion (CTE), specifically in the transverse direction. The CTE of the GFRP in the transverse direction is controlled by the type of resin, Table 2-3, and can be 3 to 10 times higher than that of concrete, Table 2-4. As a composite, the GFRP's transverse CTE typically ranges between 2 to 3 times higher than that of concrete due to the high content of fibre compared to resin.

Table 2-4: Typical coefficient of thermal expansion for reinforcing bars [29]

	CTE, x 10^{-6}/°C (x 10^{-6}/°F)			
Direction	Concrete	Steel	GFRP	Stainless
Longitudinal, α_L	7.2 - 10.8 (4 - 6)	11.7 (6.5)	6.0 - 10.0 (3.3 - 5.6)	10.3 - 14.0 (5.7 - 7.8)
Transverse, α_T	7.2 - 10.8 (4 - 6)	11.7 (6.5)	21.0 - 23.0 (11.7 - 12.8)	10.3 - 14.0 (5.7 - 7.8)

The ACI 440 [29] Committee summarizes the advantages and disadvantages of FRP reinforcement using the following table, Table 2-5.

Table 2-5: Advantages and disadvantages of GFRP reinforcement [29]

Advantages of FRP Reinforcement	**Disadvantages of FRP Reinforcement**
-Nonmagnetic	-No yielding before brittle rupture
-Corrosion Resistance (not dependent on a coating)	-Low transverse strength (varies with sign and direction of loading relative to fibres)
-High longitudinal tensile strength (varies with sign and direction of loading relative to fibres)	-Low modulus of elasticity (varies with type of reinforcing fibre)
-High fatigue endurance (varies with type of reinforcing fibres)	-Susceptibility of damage to polymeric resins and fibres under ultraviolet radiation exposure
-Lightweight (about 1/5 to 1/4 the density of steel)	-Low durability of glass fibres in a moist environment
-Low thermal and electric conductivity (for glass and aramid fibres)	-Low durability of some glass and aramid fibres in an alkaline environment
	-High coefficient of thermal expansion perpendicular to the fibres, relative to concrete
	-May be susceptible to fire depending on matrix type and concrete cover thickness

2.1.2.1. Durability of glass fibre reinforced polymer reinforcing bars (GFRP Rebar) exposed to temperature variations

Although short-term elevated curing temperatures can be beneficial to early age concrete strength, there may be a deleterious effect on the bond between GFRP rebar and the concrete due to differential coefficients of thermal expansion, shown in Table 2-4.

While test programs have been conducted to determine the effect of elevated test temperature on the bond, shear, and flexural strength of GFRP in hardened concrete [30, 31], with temperatures ranging between -100°C and 325°C, no information on the effect of elevated curing temperatures was observed. In the elevated temperature test, Robert and Benmokrane [31] noted that the flexural and shear properties of GFRP reinforcement varied very little between -40°C and 50°C, which they described as the "standard environmental conditions of Canada and north U.S.A". Once the temperature exceeded 120°C, the glass transition temperature, there was a steep decline in both the shear and flexural capacity, which at 320°C were approximately 23 and 8 percent of the original values. When Katz et al. [30] compared the bond strength of five GFRP bars between 20°C and 250°C, they reported an average bond loss of 76 percent ranging between 38.4 and 91.7 percent. Although these temperatures are not typically experienced by highway infrastructure, they are significantly lower than those experienced in extreme cases. The two following cases demonstrate temperatures that, in rare cases, a structure could potentially experience. In 1989 there was a building material fire under the I-78 viaduct over Frelinghuysen Avenue in New Jersey, which burned for approximately 24 hours and reached estimated temperatures of 620°C (1150°F), causing the girder to sag approximately 230 mm (9 inches) [32]. Similarly, in 1998, a fuel truck explosion on the Chester Creek overpass on I-95 south of Philadelphia, Pennsylvania, caused severe sagging when 32,930 litres (8700 gallons) of gasoline caught fire reaching temperatures greater than 1,093°C (2,000°F) [33].

Although specific instances of extreme temperatures definitely pose a significant risk to structures reinforced with GFRP, these situations are rare. Exposed concrete structures in Canada experience ongoing, annual thermal cycling which can lead to thermal fatigue. This thermal fatigue has been reported to cause resin matrix hardening and a debonding between the fibre and the matrix [34, 35]. When Alves et al. [36] compared the bond strength of specimens exposed to freeze thaw cycles with temperatures cycling between -25°C and 15°C, for 250 cycles, they determined that the bond actually increased, up to 40%. They explained this phenomenon by stating that the GFRP bar absorbs moisture, making the bar swell and increasing the cross-sectional area. This then enhances the mechanical bond of the GFRP rebar and concrete by friction and mechanical interlock.

2.2. The effect of salt use on reinforced concrete structures

Concrete is a composite material composed of: aggregate (coarse and fine), a binder (typically Portland cement) and water (used to hydrate the cement). The aggregates, once bound by the hydrated cement, or cement paste, are usually inert. Thus, when examining the environmental deterioration mechanisms of reinforced concrete structures, researchers often focus on how these environments affect the chemical and physical properties of the cement paste.

Although the use of rock salt is the traditional material for melting ice on roadways, anti-icing brines have been used recently. These anti-icing brines are much more effective than rock which is often blown away by passing traffic, reducing its efficiency which in turn contaminates the adjacent property. The brines not only have a negative effect on the structures on which they are applied, but salt water runoff also damage roadside vegetation and contaminate nearby water bodies with concentrated chloride runoff, altering the structure of the biodiversity [37].

Depending on local availability, Ontario municipalities use magnesium chloride ($MgCl_{2)}$, calcium chloride ($CaCl_2$) sodium chloride (NaCl) or a natural, multi-chloride solution. Aside from the availability, municipalities must consider the local temperature as the viable, eutectic temperature (the lowest temperature at which the brine solution remains 100% liquid), varies drastically, Table 2-6. Although these brines effectively keep our roads safe, the damage to both the concrete [38, 39] as well as the reinforcing steel is well documented [40-42].

Table 2-6: Eutectic temperature and practical application range for common anti-icing brines

SOLUTION	EUTECTIC TEMPERATURE
NaCl	-21°C
$MgCl_2$	-33°C
$CaCl_2$	-51°C
Multi Cl	NA

In the case of the magnesium chloride, this deterioration is due to two chemical reactions. First, the magnesium chloride reacts with the calcium hydroxide (portlandite) in the cement paste to form magnesium hydroxide and calcium chloride, Equation 1. This is initially relatively positive, as the magnesium hydroxide, or brucite, precipitates in the pores, slowing down the movement of chloride ions [43]. This precipitation also removes the magnesium hydroxide, which reduces the pH of the pore solution, thereby depassivating the reinforcing steel and increasing the risk of corrosion.

$$MgCl_2 + Ca(OH)_2 \rightarrow Mg(OH)_2 + CaCl_2 \qquad \text{Equation 1}$$

Secondly, once all of the calcium hydroxide has reacted, the magnesium chloride can react with the calcium-silicate-hydrate to form magnesium-silicate-hydrate and calcium chloride, Equation 2.

$$MgCl_2 + C\text{-}S\text{-}H \rightarrow M\text{-}S\text{-}H + CaCl_2 \qquad \text{Equation 2}$$

This magnesium-silicate-hydrate has no strength due to its gelatinous structure which leads to a breakdown of the cement paste which then potentially debonds from the fine and course aggregate [44].

The use of calcium chloride either as an anti-icing agent, or formed as a result of Equation 1, also poses a risk to the structure of the concrete as it can react with calcium hydroxide to form calcium hydroxichloride, Equation 3.

$$CaCl_2 + Ca(OH)_2 \rightarrow 3CaO\cdot CaCl_2\cdot 15H_2O \qquad \text{Equation 3}$$

The resulting calcium hydroxichloride had been shown to be expansive causing structural degradation [41, 45].

2.2.1. Corrosion of steel in concrete

Although steel initially behaves passively in concrete, corrosion often initiates in structures exposed to marine environments or in highway infrastructure. Corrosion is most often due to either carbonation of the concrete, or, more commonly, by sufficient chloride build up at the surface of the reinforcing bars. In the case of highway structures, chlorides are applied to the surface as de-icing or anti-icing salts. As surface chlorides build up, they begin to diffuse through the porous concrete to the reinforcement and ultimately reach the surface of the steel, initiating corrosion, schematically demonstrated in Figure 2-4. For black steel (400W) this requires 0.4% - 0.5% by mass of cementitious [46].

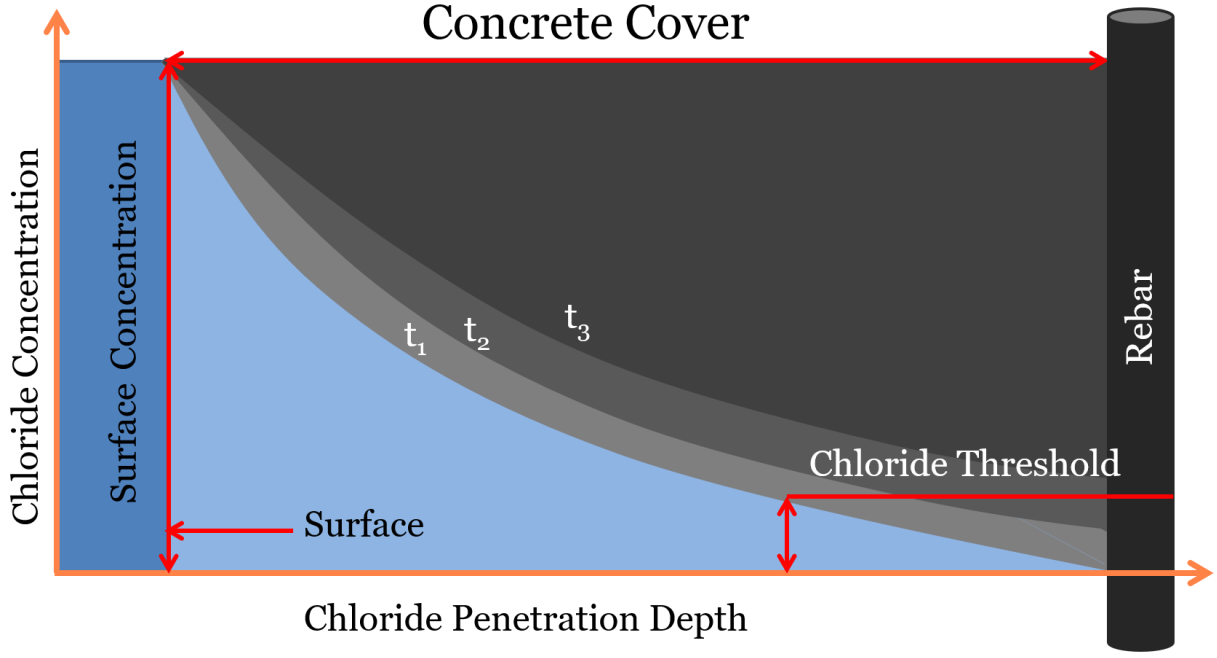

Figure 2-4: Diffusion of chloride into concrete

To model this process, many authors [13, 47, 48] use Fick's second law of diffusion, which states:

$$C(x,t) = C_s\left(1 - ERF\left(\frac{x}{2\sqrt{D \cdot t}}\right)\right) \qquad \text{Equation 4}$$

Where*: C(x,T)* is the unbound chloride concentration (kg/m^3) at a depth *x* at a time t; C_s is the surface chloride content (kg/m^3), ERF is the Gaussian error function, and *D* is the apparent diffusion coefficient (m^2/s).

Although the empirical equation seems simple, the nature of the corrosion becomes difficult to predict once the chloride concentration exceeds a given value. Due to the nature of concrete structures (being man-made, non-homogeneous, and exposed to the ever-changing environment), discrete values of the variables in Equation 4, are unrealistic when used in a model, and should rather be considered stochastically, with a mean and standard deviation, for instance using a Monte Carlo simulation. In addition, the critical chloride threshold of a given steel is also dependent on the nature of the concrete, on the environment and on the surface condition of the steel. As such, special consideration should be given to the model's input values, including: (i) the critical chloride threshold level an individual grade of reinforcement; (ii) the surface chloride content of the concrete based on geographic location; (iii) location of the reinforcement within the structure (iv) the concrete cover to the rebar in question and (v) the location, density, and size of structural cracks. Once each variable is considered individually and quantified within the model, the effects on the overall project and the cost must then be considered.

It should be noted that corrosion of steel within concrete, does not necessarily mean that the structure has failed. Practically, a good definition of failure would describe a state in which the structure is no longer able to safely perform what it was designed to do. In the case of reinforced concrete structures, failure typically occurs when the more voluminous corrosion products induce enough tensile stress in the concrete to cause cracking, spalling, and delamination of the concrete. Graphically, the service life from design to failure is shown in Figure 2-5.

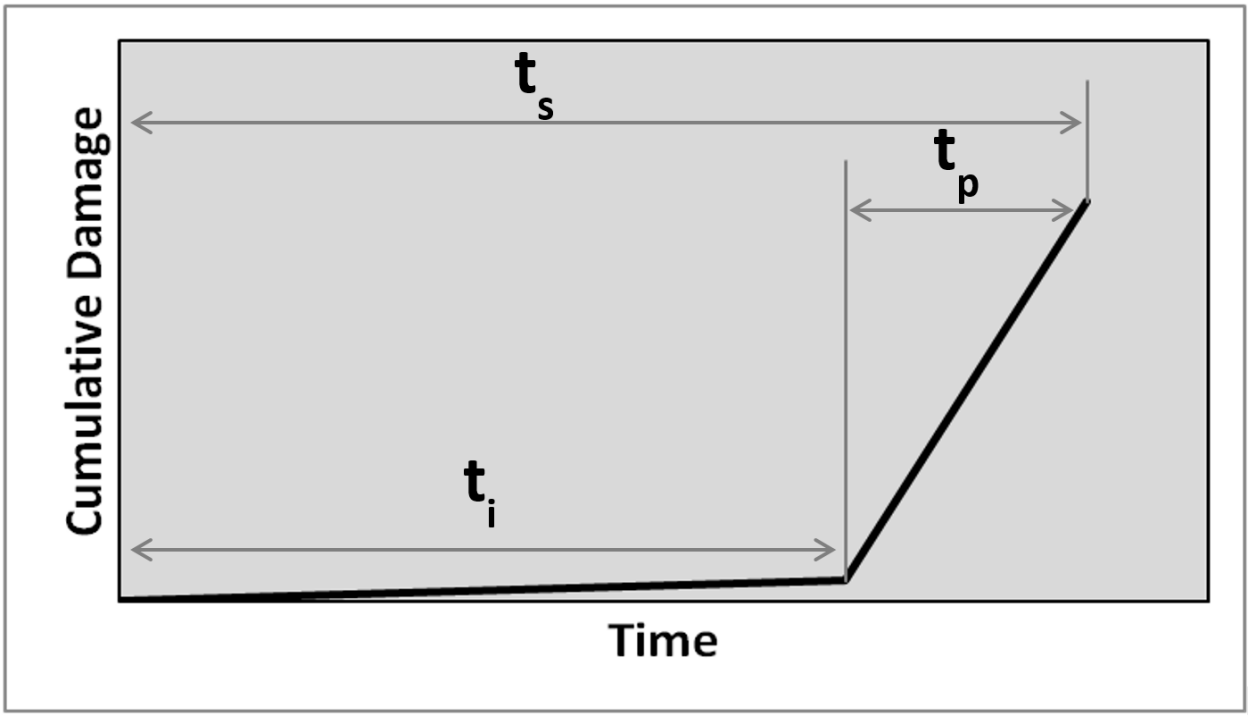

Figure 2-5: Corrosion service life time to failure of steel reinforced concrete structures

where t_i is the time to corrosion initiation, t_p is the "propagation" time from corrosion initiation until cracking, spalling or delamination occurs, and t_s is the total service life.

2.2.1.1. Critical Chloride threshold level

Using Equation 4, once the free chloride concentration surpasses the critical chloride threshold level of the particular grade of steel in the structure, corrosion is assumed to have initiated. The chloride concentration at which corrosion initiates however, is dependent on a number of factors, including the associated cation, with NaCl often having a higher threshold than both $MgCl_2$ and $CaCl_2$[40, 49]. Although this concentration has been evaluated by many researchers for traditional carbon steel, there is a large variance in values reported in the literature for commonly used grades of stainless steel. This variance typically comes from the type of test conducted as well as a statistical anaylsis of the results of that test. Test methods include: rebar in synthetic pore solution [50-53], rebar in concrete or mortar with cast-in chlorides [54, 55], or even specimens removed from the field.

2.2.1.1.1. Synthetic pore solution

The porosity of concrete can vary dramatically, depending on: mix design, cementitious material, availability of water, curing temperature etc. Under normal conditions these pores contain concentrated ionic solutions, typically referred to as pore solutions. These solutions initially passivate embedded reinforcing steel, as the pH often varies between 12.6 and 13.8, often

controlled by the availability of potassium, sodium, and calcium hydroxide in the cement paste [56].

In order to study the chemistry of pore solution, Barneyback and Diamond [57] created a method whereby they could express pore solution from cement paste and analyze its composition. Since then, this method has been used to express pore solution from pastes containing varying cementitious materials and admixed chlorides [58-60], and using solutions based on these compositions to study their effect on corrosion performance. Although the chemical composition varies depending on composition of the initial cementitious materials, most corrosion researchers have made solutions using either saturated $Ca(OH)_2$ with pH ≈12.60 [61-63], a mixture of NaOH and KOH (ASTM A955 [64]), or some combination thereof [51, 65].

2.2.1.1.2. Critical chloride threshold level for corrosion of stainless steel rebar

Currently the MTO has approved UNS S31653 and UNS 32205 to be used in highway infrastructure. The Virginia Department of Transportation, classifies their corrosion resistant reinforcing (CRR) as: Class I – improved corrosion resistance, Class II – moderate corrosion resistance, and Class III – high corrosion resistance [66]. The grades considered are as follows: Class I - UNS S24100, Class II - UNS S32101, and Class III - UNS S24000, UNS S30400, UNS 31603, UNS 31653, UNS 31803 (similar to UNS 32205), and UNS S32304. The different classes of CRR are then allowed to be used in specific applications, Table 2-7.

Table 2-7: Virginia Department of Transportation use of corrosion resistant reinforcement [66]

Functional Classification	CRR Steel		
	Class I	Class II	Class III
Freeway			x
Rural Principal Arterial			x
Rural Minor Arterial		x	
Rural Collector Road	x		
Rural Local Road	x		
Urban Principal Arterial			x
Urban Minor Arterial		x	
Urban Collector Street	x		
Urban Local Street	x		

Previous work by the author [55, 67] compared corrosion behaviour of commercially available stainless steel embedded in concrete embedded in concrete. One set was tested, using linear polarization resistance test in three conditions: transversely cracked concrete, longitudinally cracked concrete, and exposed to multichloride brine. The second set was evaluated using a potentiostatic screening test. The six grades were ranked them based on their performance, Table 2-8.

Table 2-8: Comparative ranking of corrosion resistance of stainless steel between long term and short-term test

	CIST [55]	**Longitudinally cracked concrete** [67]	**Transversely cracked concrete** [67]
S32205	1	1	1
S32101	2	2	3
S31653	3	5	5
S24100	4	4	4
S32304	5	3	2

When monitoring the corrosion of structures containing carbon steel, ASTM C876 [68] defines risk of corrosion based on the steels open circuit potential (OCP) versus a $Cu/CuSO_4$ reference electrode. If the OCP is more positive than -200 mV or more negative than -350 mV, it is deemed to have a low and severe risk of corrosion respectively, Figure 2-6.

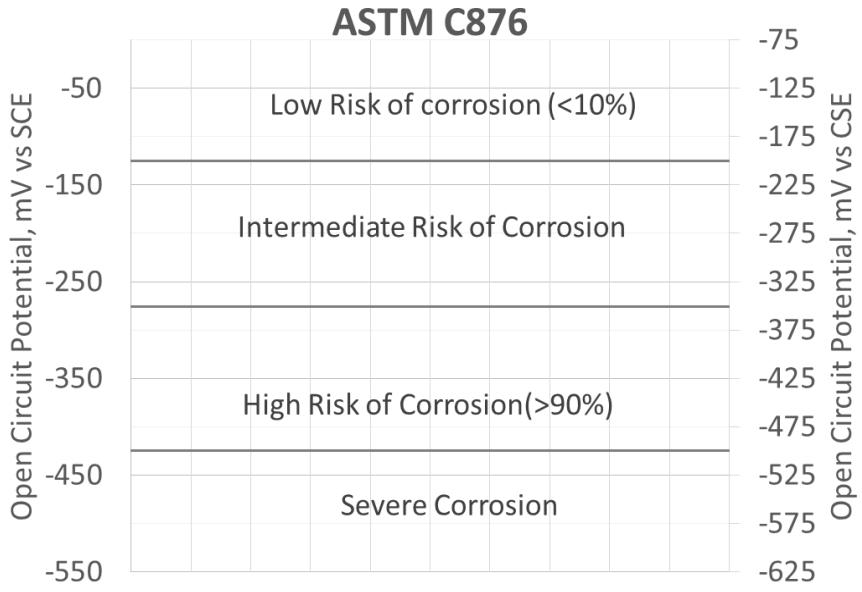

Figure 2-6: ASTM C876: Corrosion potential of uncoated black reinforcing steel in concrete [68]

Similarly, in hopes of creating a similar tool for stainless steel, the author compared the active and passive corrosion properties of 316 and 2205, the two stainless steels the MTO currently has on their designated source for materials (DSM) list, to two proposed alternative steels, 2101 and 2304, Figure 2-7, but due to the large variance in OCP's a standard for all stainless steels is not feasible.

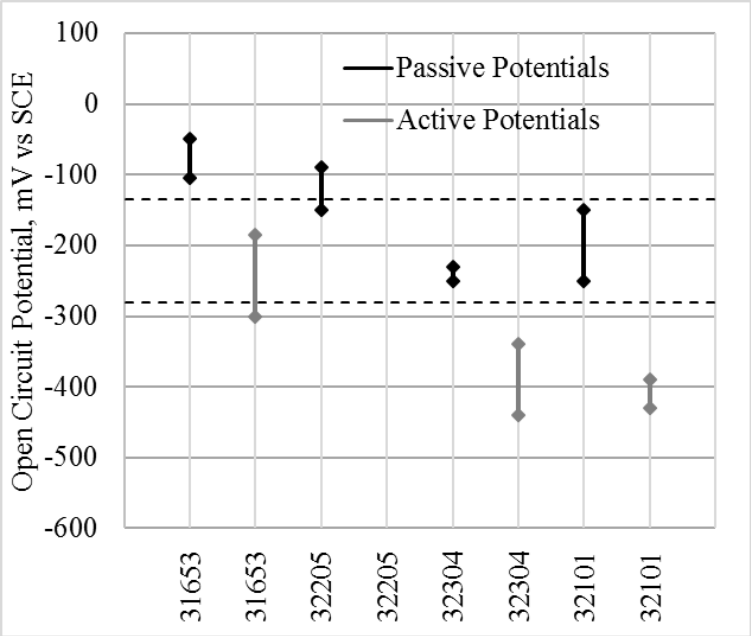

Figure 2-7: Active and passive open circuit potentials 316, 2205, 2304, and 2101 stainless steel [67]

2.2.1.2. Chloride content and apparent diffusion rate

Accurate surface chloride concentrations are required because diffusion and absorption are the most common chloride transportation methods in concrete [5], and diffusion is driven by a concentration gradient. Although diffusion coefficients of sound, un-cracked concrete, have been determined in the lab by many researchers [11, 69, 70], the surface concentrations of structures in the field and the effect of concrete cracks on the average apparent diffusion rate, have not been well documented. Once the surface chloride concentration is determined, Equation 4 can be used to model the chloride ingress in the sound concrete over time, and concentration levels at the depth of reinforcement can be compared to critical chloride threshold levels for the specific grades of steel.

Although the surface chloride concentration can be determined without destructive testing, the apparent diffusion coefficient is often determined using field samples. This coefficient typically requires a core be removed from the exposed structure, and the water soluble and acid soluble chloride contents of samples at 1 mm to 10 mm depth intervals is determined according to ASTM C1218 [71] and ASTM C1152 [72] respectively, example shown in Figure 2-8.

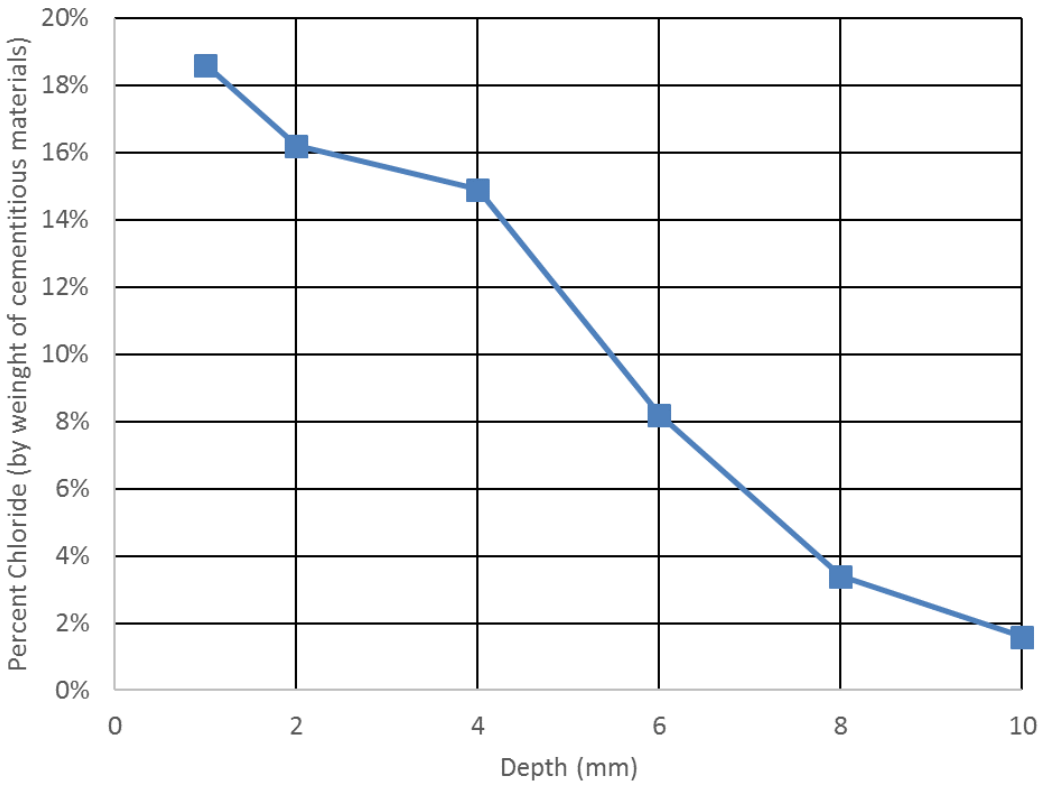

Figure 2-8: Chloride concentration versus depth [70]

2.2.1.3. Concrete cover

The main purposes of concrete cover in modern structures are to limit chloride ingress as well as ensure an adequate bond between the concrete and reinforcing member. This often depends on the application, as well as the exposure class, see Table 2-9 and Table 2-10.

Table 2-9: Concrete cover – CSA A23.3 [73]

	Exposure Class		
Exposure Condition	N*	F-1, F-2, S-1, S-2	C-XL, C-1, C-3, A-1, A-2, A-2
Cast against and permanently exposed to earth	-	75 mm	75 mm
Beams, girders, columns, and piles	30 mm	40 mm	60 mm
Slabs, walls, joists, shells, and folded plates	20 mm	40 mm	60 mm
Ratio of cover to nominal bar diameter	1.0	1.5	2.0
Ratio of cover to nominal maximum aggregate size	1.0	1.5	2.0

Table 2-10: Minimum concrete covers and tolerances, Canadian Highway Bridge Design Code [74]

Environmental exposure		Component	Reinforcement/ steel ducts	Concrete cover and tolerances	
				Cast-in-place, mm	Precast concrete, mm
De-icing chemicals; spray or surface runoff containing de-icing chemicals; marine spray	(1)	Top of bottom slab for rectangular deck	-reinforcing steel	40 +/- 10	40 +/- 10
			-Pretensioning	----	55 +/- 5
			-Post-tensioning	60 +/- 10	60 +/- 10
	(3)	Top surface of structural component	-reinforcing steel	70 +/- 20	55 +/- 10
			-Pretensioning	----	70 +/- 5
	(10)	Precast T-, I- or box-girder	-reinforcing steel	----	35 +10/- 5
			-Pretensioning	----	50 +/- 5
			-Post-tensioning	----	55 +/- 10

If the reinforcing material is not susceptible to chloride or chemical attack, the concrete cover could be reduced. This would allow for a reduction in total concrete volume, reducing the structural dead load. For instance, in the UK, the transportation authorities allow a cover of 30 mm for stainless steel reinforcement if the contractor can meet strict quality control requirements [75]. If GFRP is used as the main reinforcement, the risk of corrosion is removed, and the required cover has the potential to be reduced.

2.3. Gaps in the literature

In order to explain the significance of the research, while addressing the main two objectives, the following will directly correlate the experimental programs conducted to the identified gaps in literature.

2.3.1. The effect of curing- and service-temperature on concrete containing GFRP

- To mitigate the effects of corrosion many designers use GFRP in harsh environment, due to the inherent corrosion immunity of GFRP, with reduced concrete covers. Although this is a rational cost saving measure, the associated stress in the low cover concrete caused by the expansion and contraction of GFRP is unknown. In order to simulate field

observations by the MTO of cracking above GFRP bars in low cover concrete, rapid freeze thaw tests were conducted on concrete with 15 mm and 25 mm concrete cover. Additionally, concrete specimens containing GFRP with 45 mm and 57 mm concrete covers were left in the field and the concrete cover strain monitored.

- Although, as mentioned above, there have been studies determining the effect of test temperature on the bond of GFRP, there were not any completed using high strength concrete that was cured at elevated temperatures. As such, tests were conducted to determine if GFRP at elevated temperatures in plastic concrete experiences a reduction in bond strength when tested at both room temperature and -30°C.

2.3.2. The effect of chloride on properties of concrete

- It has been demonstrated that $CaCl_2$ and $MgCl_2$ can cause degradation of cement paste and mortar [76], but the effect of commercially available anti icing brines on structural concrete has not been studied. In order to determine and compare the degree of this degradation over an extended period of time, concrete exposed to four different chlorides brines currently used by the MTO were tested over a 5-year period.
- Due to the length of time required to initiate corrosion of traditional carbon steel bars in concrete, and the even longer period required to initiate corrosion of stainless-steel bars, many researchers often utilize synthetic pore solutions [42, 77]. These synthetic solutions often do not account for differences in concrete mix design, which can affect the chloride binding and chemical composition of the pore solution. Consequently, cement paste cylinders were cast containing different supplementary cementitious materials with varying water to cementitious materials ratios and admixed chlorides. The cylinders were then slowly crushed, allowing pore solution to be collected and a chemical analysis to be undertaken. This was done at high chloride levels to enable future researchers to determine the critical chloride threshold level of stainless steels in realistic synthetic pore solutions.

Chapter 3 Experimental Procedures

The experimental procedures to determine the effects of curing- and service-conditions on design considerations for reinforced concrete structures have been separated into two groups: first, determining the effect of curing and service temperature; second, determining the effect of salt use. Experiments were designed and conducted to examine both factors, some of which overlapped both groups, as outlined below.

1. The effect of curing- and service-temperatures were evaluated by:
    a. Repeated freezing and thawing behaviour using a modified ASTM C666 Test [14]
    b. GFRP reinforced specimens exposed to a southern Ontario environment
    c. Bond strength measurements using a modified ASTM D7913 Test [15]
    d. Temperature effects on the compressive strength of concrete
2. The effect of salt use was investigated by determining:
    a. The effect of chloride brine exposure on concrete compressive strength
    b. Pore solution composition of cement pastes with admixed chlorides
3. Supplementary testing procedures
    a. Digital image correlation (DIC) determination of the coefficient of thermal expansion of GFRP reinforcing bars
    b. Surface chloride concentration in concrete using X-ray fluorescence (XRF) scanning

3.1. The effect of curing- and service-temperature

The experimental design to consider the effect of curing and service temperature was initially an investigation into the interface between GFRP reinforcing bars and high-performance concrete. Due to the variance in coefficients of thermal expansion between the two materials, it was hypothesized that there would be a breakdown in bond at high or sub-zero temperatures leading to premature failure of the composite material. This was done at the request of the Ministry of Transportation of Ontario because they had observed cracking patterns above GFRP bars in field structures, which they had not experienced with traditional carbon steel bars.

3.1.1. Materials

The two main materials under investigation were concrete and glass fibre reinforced polymers. The concrete mixtures varied based on the test procedure carried out and are described in the corresponding test procedures, whereas the GFRP was supplied by two manufacturers. Sand coated GFRP was supplied by Pultrall Inc., and ribbed GFRP was supplied by Schöck – Combar. They came in both 13 mm (#4) and 16 mm (#5) nominal diameters. Each supplier provided bars in 1220 mm (4 ft) sections, the properties supplied by the producer are provided in Table 3-1 and Table 3-2. Note, the nominal dimensions are used to determine the properties of the GFRP bars

for ultimate tensile capacities, whereas the effective cross sectional area is used when calculating bond strength and apparent horizontal shear strength.

Table 3-1: Mechanical Properties of Pultrall reinforcing bars [78]

	Unit	#4	#5
Ultimate Tensile Strength	MPa	1100	
Youngs Modulus	MPa	60,000	
Resin		Vinyl-Ester	
Mass	g/m	310	442
Effective Cross-Sectional Area	mm^2	145	233
Nominal Cross-Sectional Area	mm	129	199
Effective Diameter	mm	13.59	17.22
Coefficient of thermal expansion (CTE)	Longitudinal (10^{-6}/°C) Transverse (10^{-6}/°C)	6.2 23.8	

Table 3-2: Mechanical Properties of Schöck reinforcing bars [79]

	Unit	12 mm	16 mm
Ultimate Tensile Strength	MPa	>1000	
Youngs Modulus	MPa	>60,000	
Resin		Vinyl-Ester	
Mass	g/m	340	530
Effective Cross-Sectional Area	mm^2	132	201
Core Diameter	mm	13.0	16.0
Exterior Diameter	Mm	14.5	18.0
Coefficient of thermal expansion (CTE)	Longitudinal (10^{-6}/°C) Transverse (10^{-6}/°C)	6.0 22.0	

3.1.2. Understanding the resistance of concrete to rapid freezing and thawing.

In order to test whether the temperature variance typical of the Canadian climate would affect the bond at the interface between GFRP and the concrete, modified ASTM C666 tests were conducted. The ASTM C666 test was modified both by the addition of GFRP to the specimens, where the concrete was not initially reinforced, and by changing the freeze thaw cycling frequency. These tests were undertaken to determine the effect of thermal fatigue on reinforced structures with low concrete covers. The original ASTM C666 was created to determine the durability of concrete when exposed to rapid freezing and thawing cycles [14]. The test consists of submerging a 76.2 mm (3”) wide by 101.6 mm (4”) tall by 406 mm (16”) long specimen (Figure 3-1) in water and freezing the specimen until and internal temperature of -18°C is achieved, then heating the specimen until and internal temperature of +4°C is achieved. The internal temperature of sample specimen with an internal thermal couple, is monitored throughout the cycles to ensure the centre of the concrete specimens achieve the desired temperature.

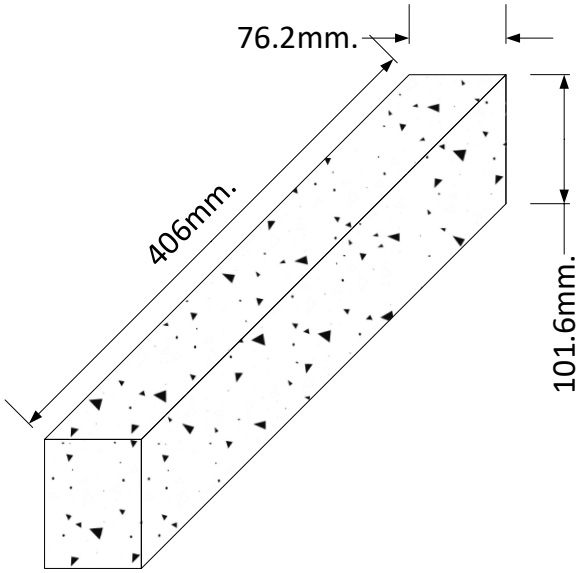

Figure 3-1: ASTM C666 concrete test specimen geometry

Preliminary results indicated there was little degradation, with the initial freeze thaw cycle of 4 to 5 hours, of the concrete specimen. Therefore, the cycles were increased to 24 hours at 20°C and 24 hours at -20°C. After every 50 cycles the specimens were then removed from the chamber and the transverse fundamental frequency, mass, and dimensional measurements are recorded in accordance with ASTM C215 [80], based on Equation 5.

Dynamic Modulus $$E = CMn^2$$ Equation 5

$$C = 0.9464 \cdot \left(\frac{L^3 T}{bt^3}\right)$$ Equation 6

Where: E is the dynamic modulus in MPa, C is a function of specimen geometry $(1/m)$ L, t and b are the specimen length, height and width of the specimen, respectively (m), T is a correction factor using radius of gyration, using research by Pickett [81], M is the mass of the specimen (kg), and n is the transverse fundamental frequency (Hz), from the recorded signal.

It should be noted that the aforementioned equations are based on the fundamental mode of vibration, an assumption for the case of a solid concrete specimen. With the addition of the GFRP, this assumption was confirmed, as follows. An oscilloscope pickup was placed at a free end and the shape of the wave recorded for specimens with and without the embedded rebar. Similarly, the receiver was placed in the centre of the beams and the wave shapes recorded. This wave had an inclined elliptical pattern for the free end, and an elliptical pattern inclined in the opposite direction for the centre, hence it is vibrating in the fundamental mode of vibration [80].

Additionally, the fundamental frequency was determined from first principals, and tested versus experimental data using the following equations.

Natural Frequency	$f_n = \frac{1}{T_n}$	Equation 7
Natural Period	$T_n = \frac{2\pi}{w_n}$	Equation 8
Undamped natural frequency	$w_n = \sqrt{\frac{k}{m}}$	Equation 9
Mass	$m = \rho \cdot L \cdot t \cdot b$	Equation 10

Where: k is stiffness, ρ is density, L is length, b is width, and t is height.

A reduction of the dynamic modulus, P_c, is associated with internal degradation, such as micro-cracking, of the concrete, for which ASTM C215 defines failure as when the dynamic modulus reaches 60% of its original value, Equation 11.

$$P_c = \left(\frac{n_1^2}{n^2}\right) \cdot 100\% \qquad \text{Equation 11}$$

Where:

P_c is: relative dynamic modulus of elasticity, after c cycles of freeze thawing (%)

n is: fundamental transverse frequency at 0 cycles of freeze thawing

n_1 is: fundament transverse frequency after c cycles of freeze thawing

The transverse fundamental frequency is determined in accordance with ASTM C215 [82], by inducing a vibration in the centre of the specimen, Figure 3-2, and measuring the response with a sensor or accelerometer. If the microstructure of the concrete is damaged (ie micro-cracking), the fundamental frequency will change, ultimately leading to a surface crack if damage continues.

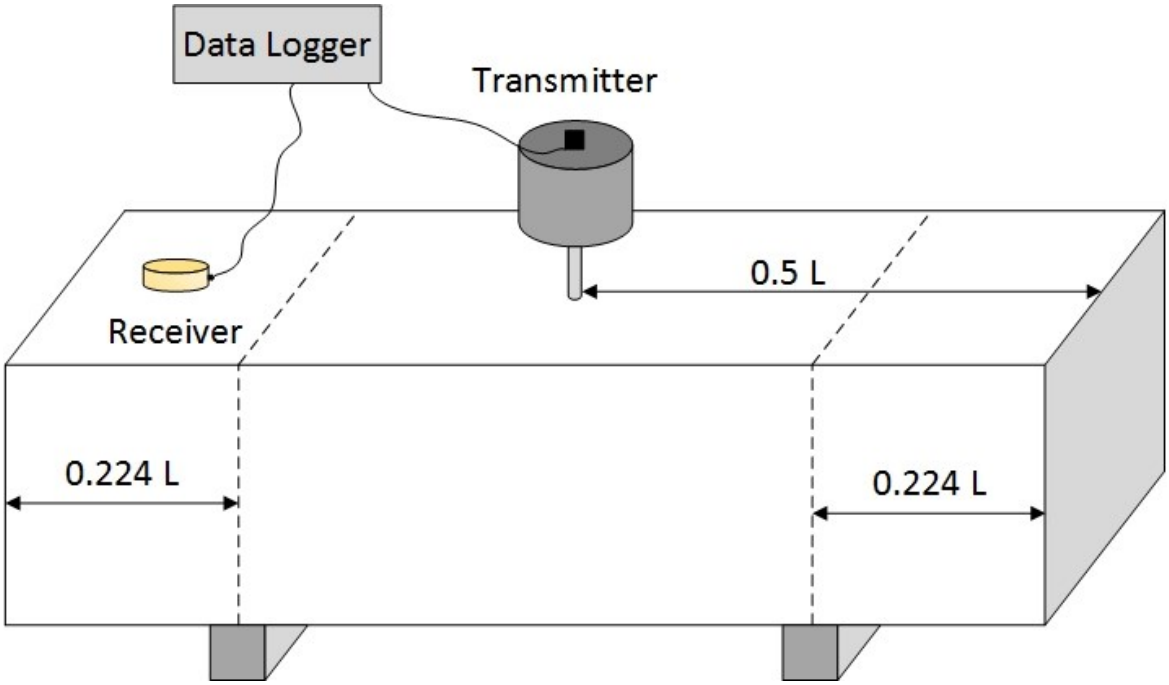

Figure 3-2: Test setup for ASTM C215

The standard test has been conducted on specimens cast with two different GFRP bar diameters,16 mm and 12 mm bars, with either 15 mm or 25 mm concrete covers, Figure 3-3 .

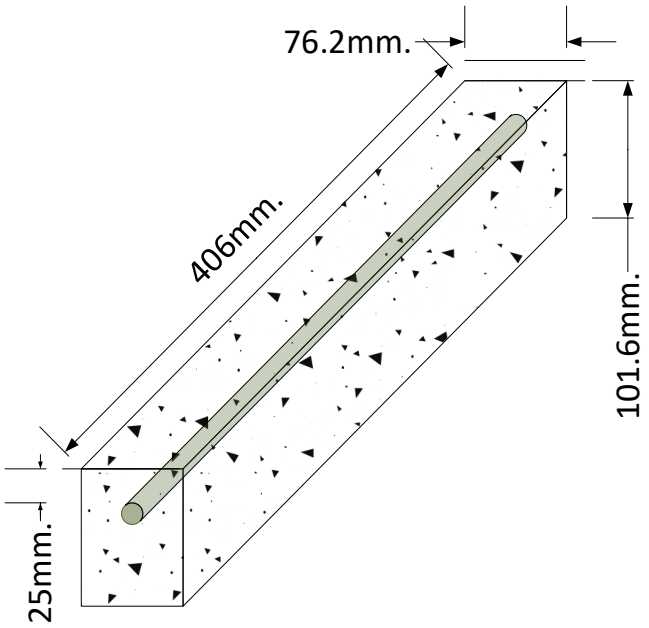

Figure 3-3: Modified ASTM C666 concrete specimen geometries containing GFRP reinforcing bar

Sixteen specimens were cast (4 replicates of each specimen described earlier) using the concrete mix design described in Table 3-3, with a design compressive strength of 40MPa and an 80 mm

slump. Note that for water, the L + abs is the total required water required in order to account for dry aggregate which will absorb some of the admixed water.

Table 3-3: Concrete Mix design used to cast freeze thaw specimens

Constituent	Amount (m^3)	
Gravel (19 or 9mm)	1045	kg
Sand	705	kg
GU Cement	297	kg
Slag or Flyash	98	kg
Euclid Air Extra	237	mL
Superplasticizer	900	mL
Water	158	L + abs
w/c	0.40	ratio

3.1.3. GFRP reinforced specimens exposed to a southern Ontario environment

In order to determine and compare results from the modified ASTM C666 test to in-situ data, as well as determining the effect of GFRP on the strain in the concrete cover, concrete beams containing 13M and 16M Schöck – Combar GFRP were cast. Due to the size requirement of the modified ASTM C666 test and the size of the long-term vibrating wire strain gauges available, the concrete cover was increased from 15 mm and 25 mm to 44.45 mm (1.75”) and 57.15 mm (2.25”), and the strain gauges placed below the GFRP. Initially, four different beams were cast, to ensure data for both bar diameters and concrete covers, with strain gauges and a ponding well, as illustrated schematically in Figure 3-4.

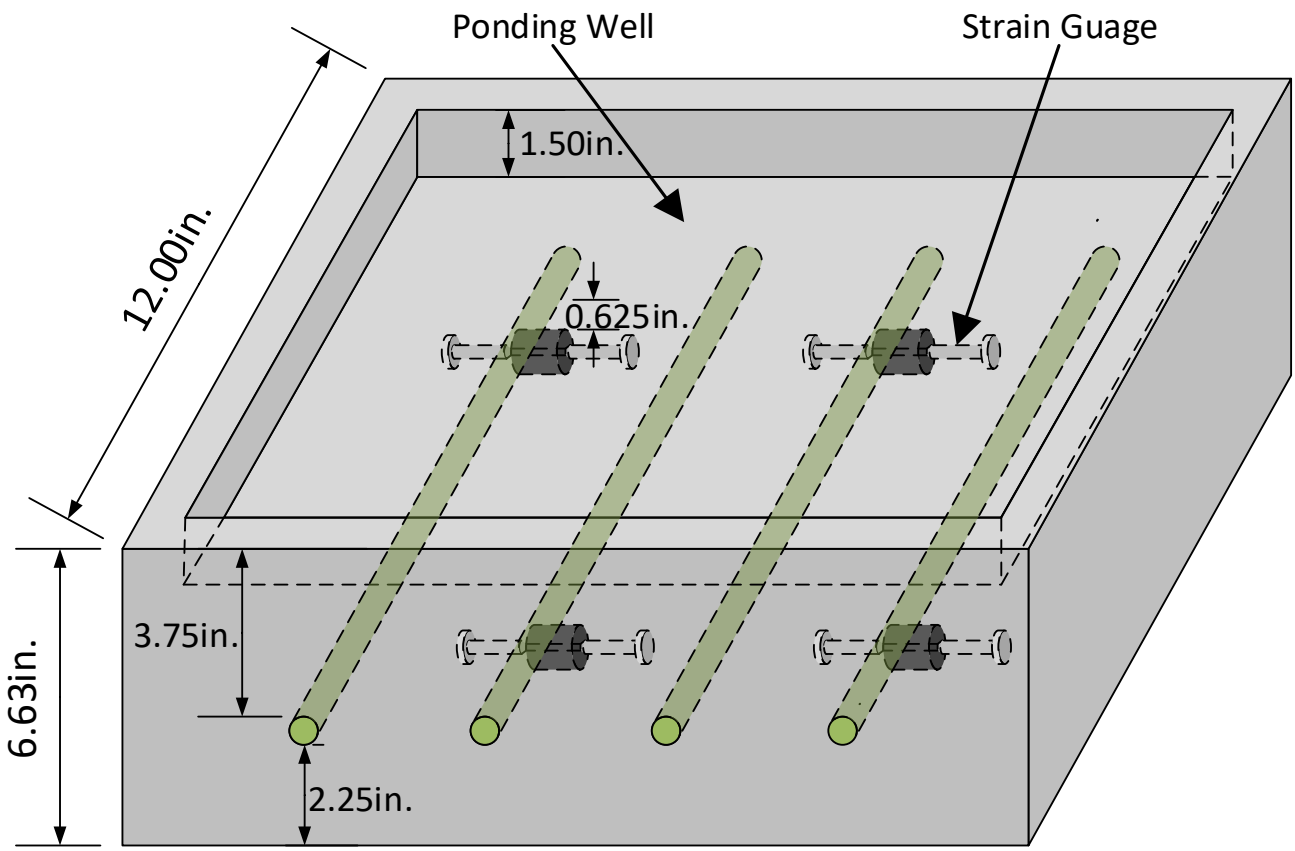

Figure 3-4: Outdoor specimens containing GFRP exposed to freeze thaw cycles and mutli-chloride solution

To ensure adequate compaction of the concrete and consistent wall thickness for the ponding well, the beams were cast upside down on top of an extruded polystyrene (XPS) insulation board, which was wrapped in plastic wrap and oiled to ensure ease of release from the concrete. To fasten the vibrating wire strain gauges at the proper depth, at the mid-height of the concrete cover, stainless steel tie wire was woven through the formwork, tightened to ensure limited sag, and then the strain gauges were fastened to the tie wire, see Figure 3-5.

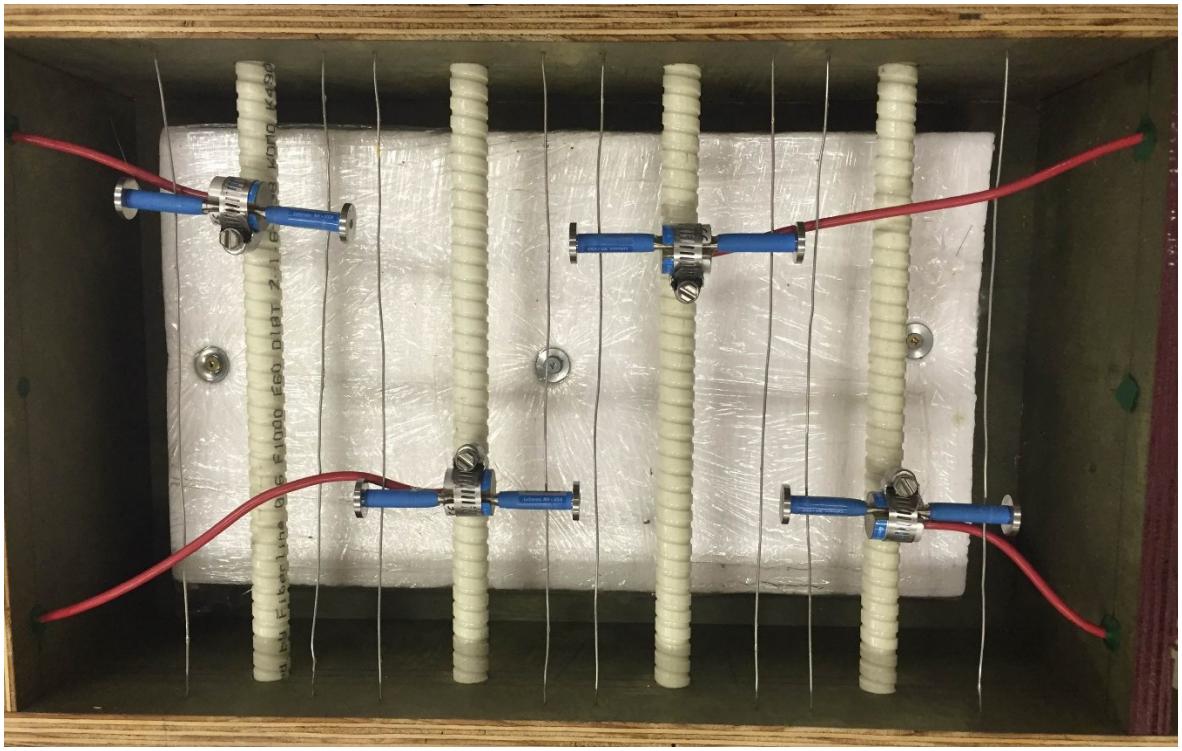

Figure 3-5: Outdoor beam specimen formwork

Later, upon further consideration, it was determined that there was no baseline strain measurement for the concrete mix and specimen geometries. A second pair of beams were cast containing two strain gauges, one above a GFRP bar, as seen below, and one at the same depth but without a bar, see Figure 3-6.

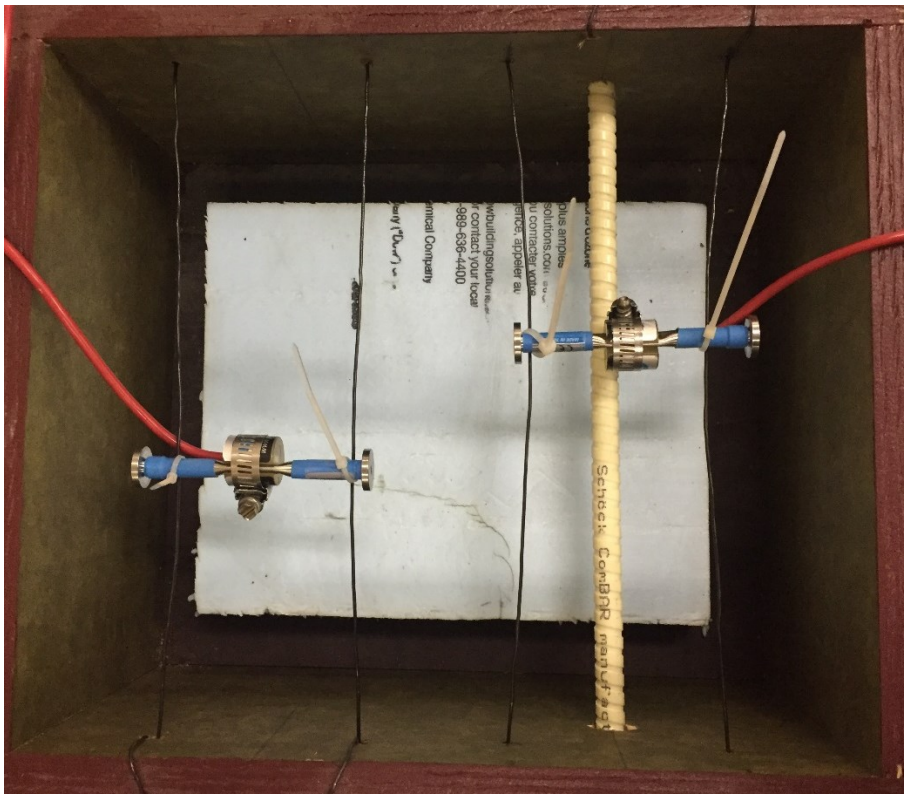

Figure 3-6: Outdoor beam specimen formwork – second cast

The ponding well was provided to determine the effect of chloride contamination on the GFRP and concrete durability. A commercial multi-chloride anti-icing brine was poured into the well 28 days after casting. The chemical composition of the brine is given in in Table 3-4.

Table 3-4: Content, mol/litre, of multi-chloride anti-icing brines, determined by ICP

Brine	Ca mol/l	K mol/l	Mg mol/l	Na mol/l	S mol/l	Sr mol/l	Cl mol/l	Cl^- wt.%
Multi	2006	129	425	1598	36	18	6040	23.1

The first set of specimens was cast on January 15th, 2016 and the second set was cast on April 26th, 2018. Both sets of specimens were moist cured for 4 days at 23°C, then cured for 6 days in ambient lab conditions before being placed in the outdoor testing facility.

Due to the interaction between the concrete and the steel strain gauge, the measured strain must be corrected for temperature due to differences in the coefficient of thermal expansion (CTE) of the two materials. The temperature corrected strain, μ, is given by Equation 12.

$$\mu = (R_1 - R_0)B + (T_1 - T_0)(C_1 - C_2) \qquad \text{Equation 12}$$

Where R_1 is the measured strain, R_O is the strain at 6 days, B is the batch calibration factor, T_1 is the measure temperature, T_O is the calibration temperature at 6 days, C_1 is the CTE of the strain

gauge, and C_2 is the CTE of the matrix in which the strain gauge is placed. In the case of the aforementioned experiment, the batch calibration factor supplied by the strain gauge manufacturer is 1.379 micro-strain/°C for the gauges in the initial cast and 1.369 micro-strain/ °C for those in the second cast. The CTE of the gauge and concrete were considered to be $12.2 \cdot 10^{-6}$/°C and $10 \cdot 10^{-6}$/°C respectively.

To quantify a "large tensile strain", CSA A23.3 [83] first defines the cracking tensile stress of concrete, Equation 13. To convert stress to strain, Equation 15 is utilized. To compare the maximum tensile strain of approximately 200 micro-strain versus a theoretical cracking strain, the 56-day compressive strength, from the first mix, of 43 MPa, Table 3-5, was utilized suggesting a cracking strain of approximately 67 micro-strain, Equation 16. Similarly, when the cracking strain was determined with the results from the second cast, a cracking strain of approximately 66 micro-strain was calculated.

Table 3-5: Compression strength data of outdoor specimens.

Test day	Compressive Strength (MPa)			
	Batch 1		Batch 2	
	μ	σ	μ	σ
7	29.5	1.98	34.9	1.20
28	38.5	0.84	42.8	1.36
56	43.0	1.87	48.9	1.69

Cracking Stress $$f_{cr} = 0.33\sqrt{f_c'} = 0.33\sqrt{42.96} = 2.16MPa$$ Equation 13

Modulus of Elasticity $$E_c = 12411 + 460 \cdot f_c' = 12411 + 460 \cdot 42.96 = 32{,}173MPa$$ Equation 14

Stress vs Strain $$\sigma = E_c \cdot \varepsilon \rightarrow \varepsilon = \frac{\sigma}{E_c}$$ Equation 15

Cracking Strain $$\varepsilon_{cr} = \frac{2.16}{32173} = 67\ micro\ strain$$ Equation 16

3.1.4. Determining the effect of curing and testing temperature on the bond of GFRP in high strength concrete

Northern Ontario structures often experience temperatures well below -30°C, providing a temperature differential between steam curing (~75°C) and service extremes greater than 105°C. Using Equation 17, a bar diameter of 25 mm, CTE $7.2 \cdot 10^{-6}$/°C and $23 \cdot 10^{-6}$/°C for the concrete and GFRP respectively, gives a differential shrinkage between the concrete and GFRP of approximately 0.04 mm. At the interface of the rebar and the concrete, a cracking stress of 2.16 MPa can be reached with a change in temperature of only 45.6 °C, Equation 18.

Reduced bar diameter $$\Delta d_{bar}(\%) = 1 - (\alpha_{GFRP} - \alpha_{conc}) \cdot \Delta T$$ Equation 17

Interface Stress $$\sigma = E_{GFRP-radial}\alpha_T \Delta T$$ Equation 18

Logically, this differential shrinkage will likely detrimentally affect the bond between the two materials. Thus, in order to study the effect of this differential shrinkage, the modified ASTM D7913 tests were completed. They were conducted to test the bond properties of GFRP under elevated curing conditions, simulating the largest temperature change concrete structures in Ontario experience.

ASTM D7913 was designed to measure the bond strength of GFRP bars under normal service conditions. For this project, the standard procedure was modified for use with available equipment, and to simulate current Ontario concrete practices. The modifications are listed below:

1. The test apparatus was designed to be used in the readily available 100 kN MTS frame, which did not have enough height to fit the 1200 mm specimen and bar grip. Therefore the bar length was reduced from 1200 mm (+/- 5 mm) to 915 mm (+/- 5 mm).
2. The compressive strength of the concrete mix was changed from 30 MPa (+/- 3 MPa) to a 50 MPa mix as described below. The mix design provided also specified a higher slump, 180 mm +/- 20 mm and, instead of an ordinary Portland cement concrete, the mix contained high early cement and a 25% cement replacement of ground granulated blast furnace slag. These deviations from ASTM D7913 were made to simulate Ontario concrete mixtures that are subjected to high early heat via steam curing.

3.1.4.1. GFRP rebar Preparation

As previously mentioned, the standard length of the GFRP prescribed by ASTM D7913 was modified from 1200 mm to 915 mm so that a specimen and the test apparatus would fit into the available 100 kN MTS frame. Once the specimens were cut to length, the surfaces of the bars where the wedge collet grips the bar were shaved to the proper diameter (12.2 mm for the 13M bar and 15.4 mm for the 16M bar). This was done by machining a 150 mm long section using a lathe.

3.1.4.2. Concrete Mixture Design

In order to simulate a precast casting environment, where elevated temperatures are used during steam curing, a local pre-caster was contacted and their mix design discussed. The mix design was prepared, based on pre-cast practices, and had cementitious (75% Type 30 (HE) + 25% slag) content of greater than 600 kg/m^3, with a 0.32 w/cm ratio. In order to ensure adequate placement and consolidation of the concrete, a high range water-reducing admixture was used to give a desired slump between 180 mm and 200 mm. An air entraining admixture was used to achieve a desired air content between 5 – 8%. The maximum aggregate in the concrete was 14

mm, slightly smaller than the 19 mm aggregate specified by the precaster and OPSS 1002 [84], to ensure an even aggregate distribution in the small laboratory specimens.

3.1.4.3. Concrete Casting

The pullout testing was separated into two unique test lots. In the preliminary round of testing, casts with six replicates of 12 mm and 16 mm Combar reinforcing bars for the four different curing temperatures were compared to determine the effect of curing temperature on the bond strength of GFRP bars. After analyzing the initial results of five replicates, it was concluded that additional information could be gleaned if the bond strength at -30°C was compared to the bond strength of the same concrete at approximately 23°C. Thus, the second round of testing was composed of casting eight specimens for each curing temperature, bar diameter, and bar manufacturer, and testing four specimens each at -30°C and 23°C. The specimens were cast horizontally, Figure 3-7, into 203 mm by 203 mm cubes, along with fourteen 100 mm ø by 200 mm tall cylinders. To ensure that bond length was five time the diameter of the bar, a PVC conduit was used as a bond break, and the ends sealed with play dough to limit concrete from seeping between the GFRP and the PVC. A thermocouple wire was placed in each specimen and taped to the PVC to monitor the internal temperature of the specimen during the elevated curing process.

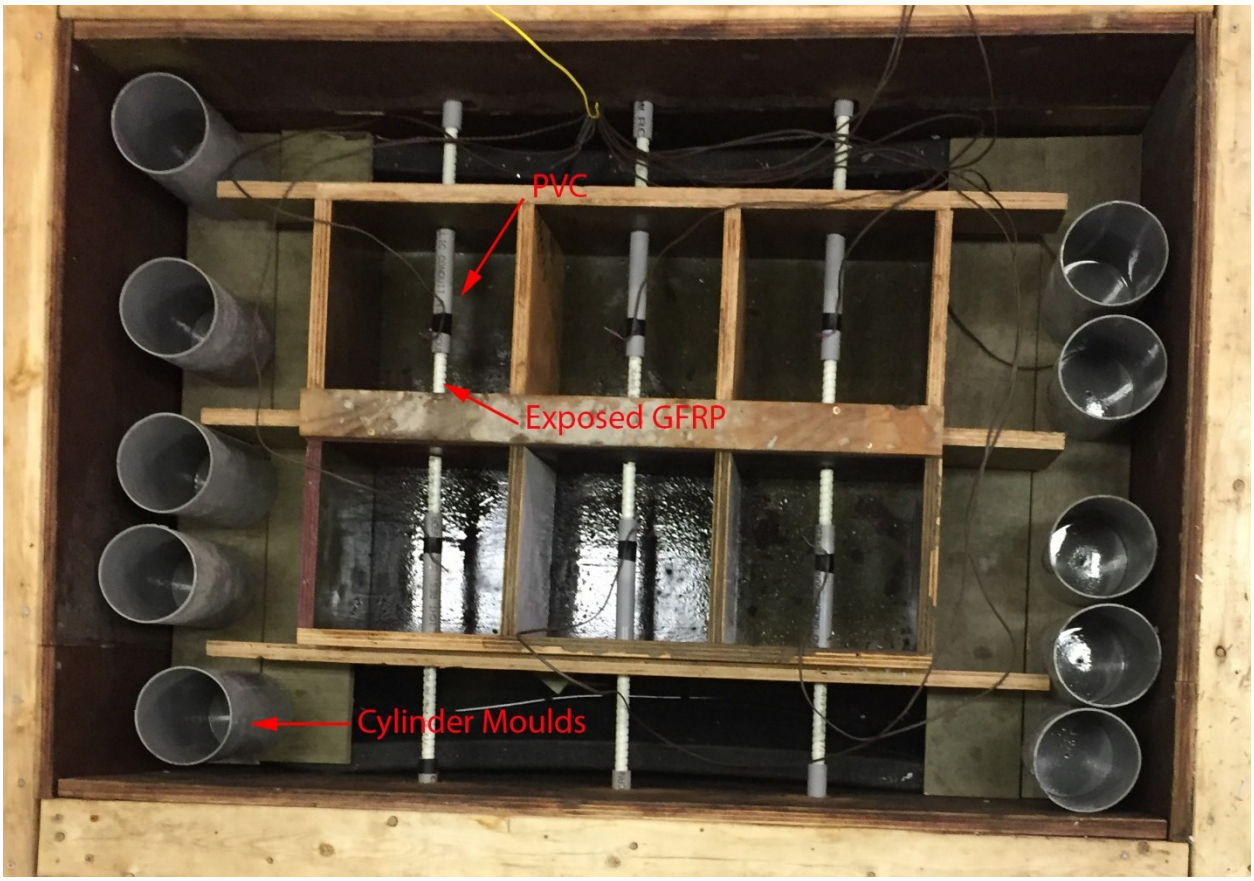

Figure 3-7: Modified ASTM D7913 formwork

3.1.4.4. Concrete curing conditions

To determine the effect of curing temperature, and corresponding temperature differentials between curing and testing temperatures, specimens were cured at 100% relative humidity in a thermal chamber at 60°C, 70°C, or 80°C for a period of 48 hours. Figure 3-8 provides a comparison of internal curing temperature of the three different elevated curing conditions compared to the base case which was cured in ambient lab conditions. Although the maximum temperature of 80°C exceeds the maximum allowable concrete temperature of 70°C specified by the Ontario Provincial Standard Specification (OPSS) 904 [85] to mitigate the risk of delayed ettringite formation, it was used to determine if the larger temperature differential also decreased the bond strength. After 48 hours of elevated curing, the specimens were removed from the thermal chamber and cured at ambient lab conditions for the next 24 days. At that time, four of the eight specimens were placed in a freezer, alongside three concrete cylinders, to bring the internal temperature of the concrete to -30°C, at which time the pullout tests were conducted.

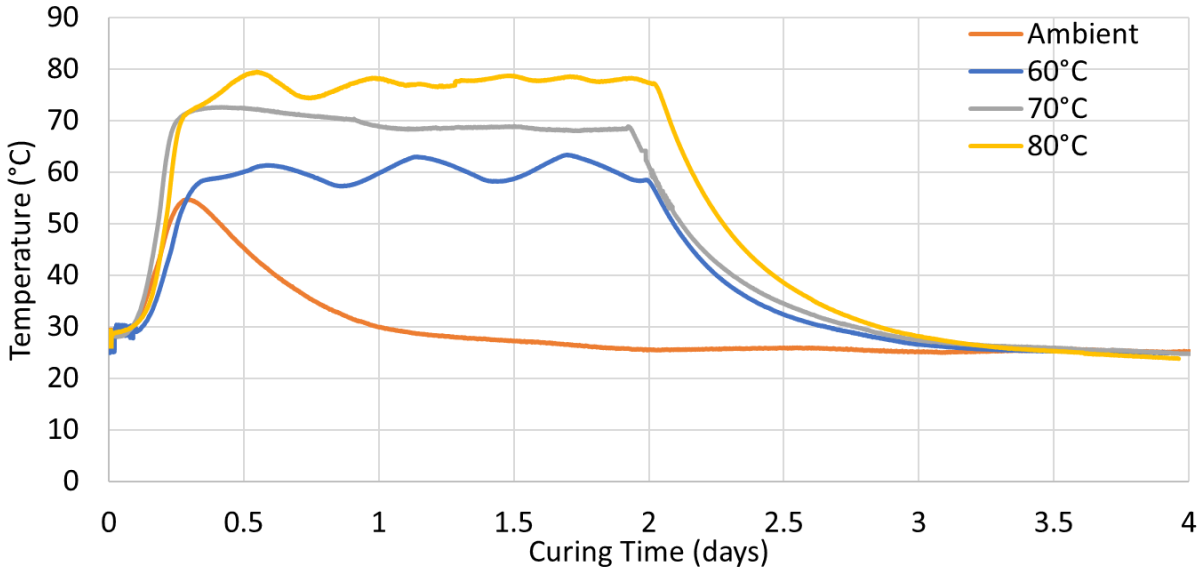

Figure 3-8: Internal temperature of concrete cured at 23°C, 60°C, 70°C, and 80°C

3.1.4.5. Pullout testing

In order to complete the pullout testing, a 25.4 mm (1 inch) thick steel frame was manufactured, shown schematically in Figure 3-9A. The specimens were then placed in the frame and the wedge collet seated on a 1 mm copper sleeve surrounding the machined GFRP surface. The soft copper sleeve was added to account for slight variability in the machined surface and to mitigate slip between the grip and the GFRP, but unfortunately was not 100% successful. Two LVDT's (linear variable differential transducer) were attached to the GFRP both above and below the specimen to monitor any excessive bending in the bar as well as bar stretch before pull-out, Figure 3-9B. The frozen specimens were removed from the freezer directly before testing to ensure the

internal temperature remained as close to -30°C as possible, usually no more than ten minutes from freezer removal until the testing. For comparison purposes, the internal temperature was noted at the beginning and end of the test using the internal thermocouple.

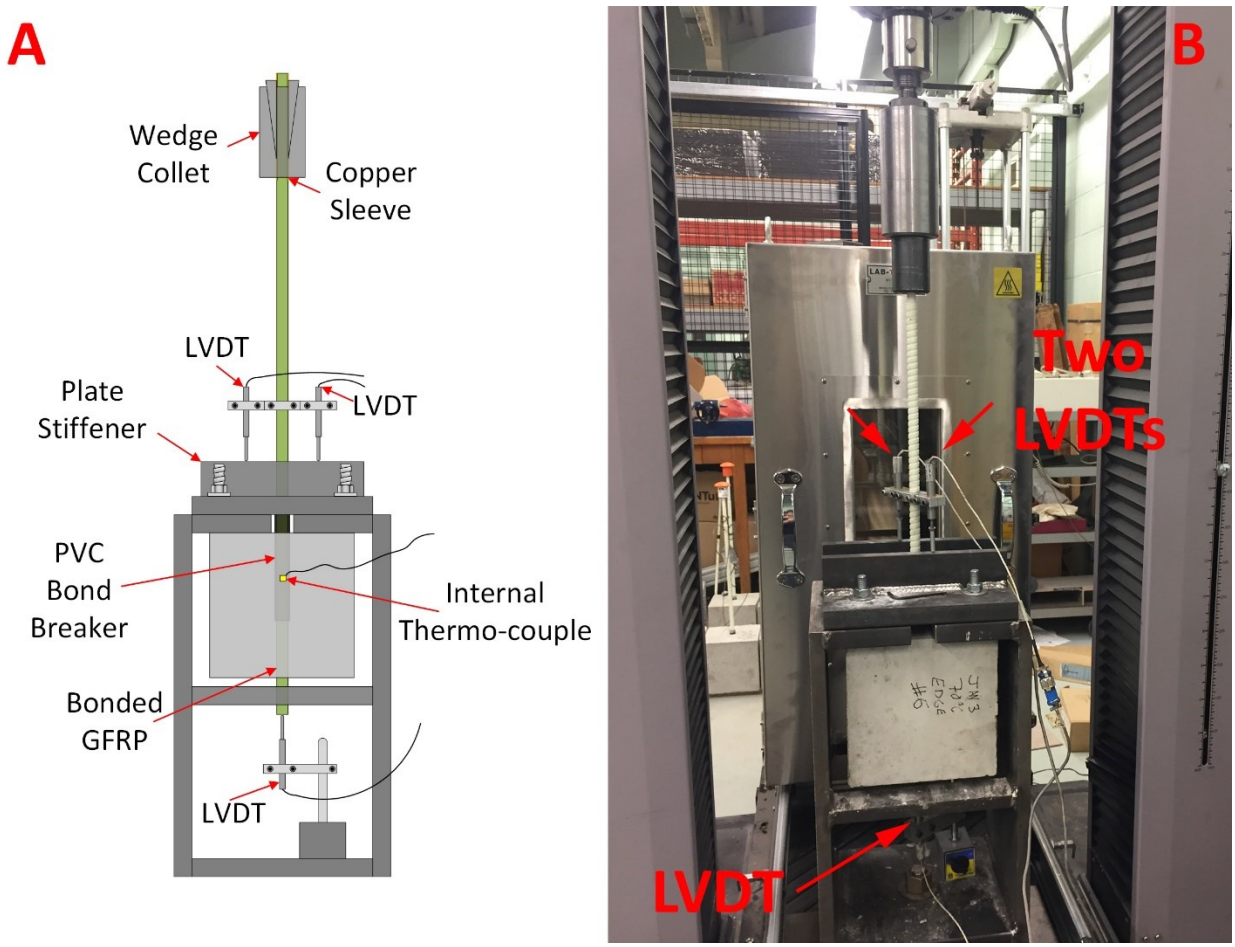

Figure 3-9: Pullout test setup

The pull-out tests were conducted using two separate frames, a 100 kN MTS frame for the 13M bars and a 600 kN MTS frame for the 16M bars, both using a displacement-controlled loading rate of 0.02 mm/s. Before each batch of specimens was tested, the three LVDT's were calibrated to ensure the accuracy of the measurements was within 0.1 mm over a 100 mm range. The load steadily increased until one of three reactions took place. First, a brittle failure of the bond interface could occur, whereby the bond stress peaked and then massive slip of the rebar occurs, an example of which is demonstrated in Figure 3-10. Second, a more controlled failure could occur, whereby the bond stress would peak, and then slowly begin to decrease as the slip increased in a controlled manner, an example of which is found in Figure 3-11. Thirdly, the bond stress would peak as would the slip and then both would decrease. This indicated that bond failure had not occurred, instead that the GFRP had slipped inside of the wedge collet, an example of which is found in Figure 3-12.

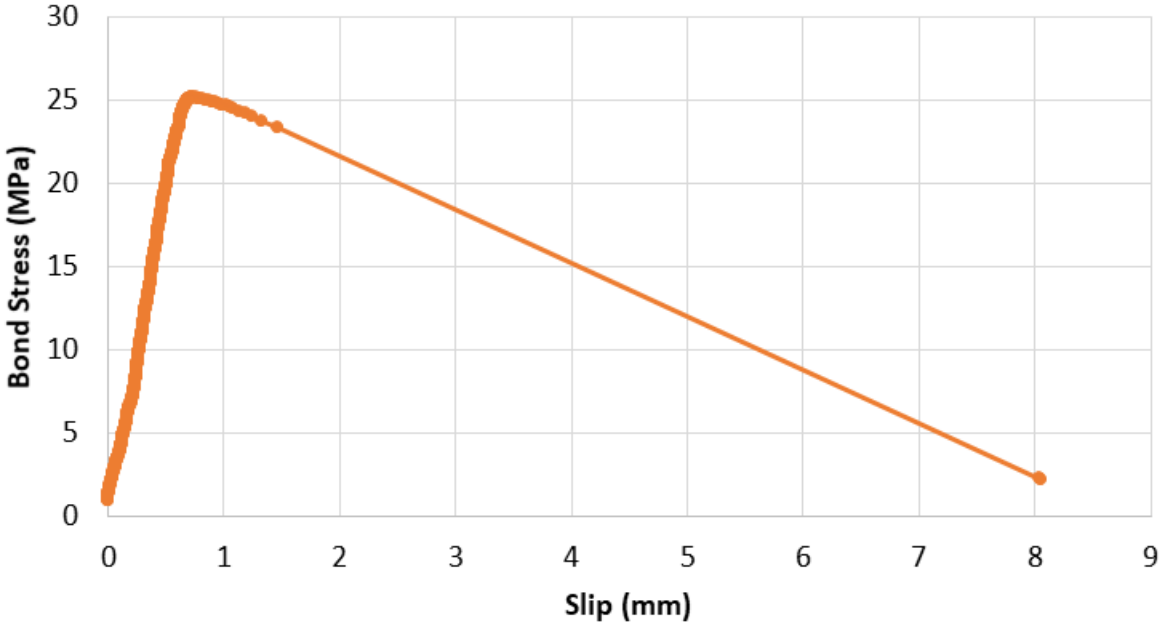

Figure 3-10: Bond stress vs GFRP slip for brittle failure of GFRP – concrete bond

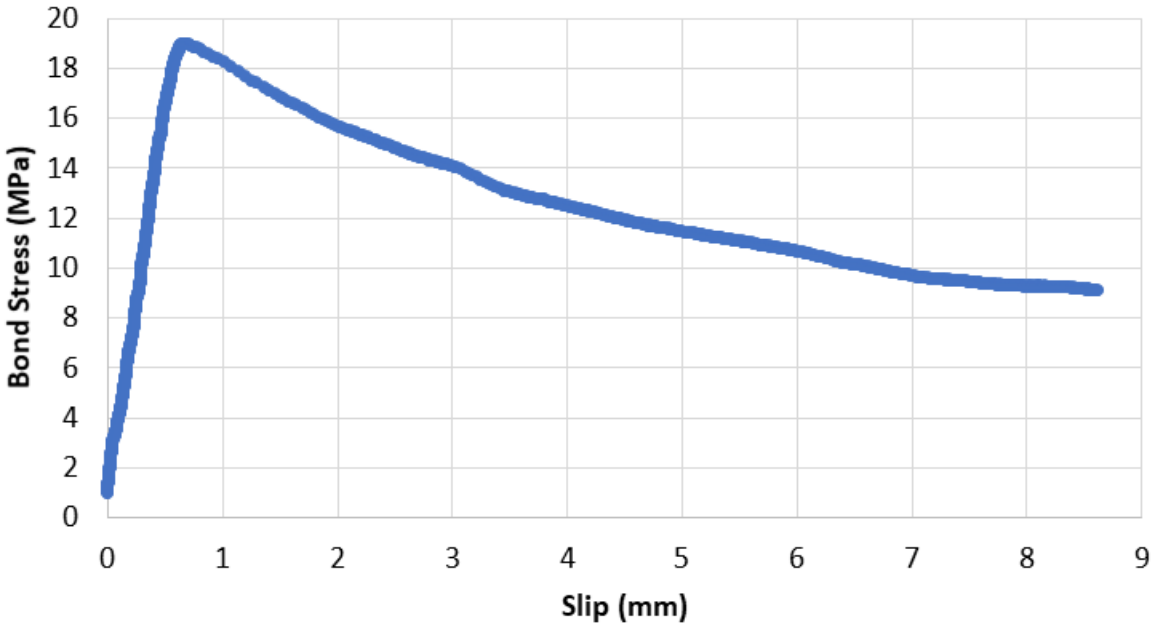

Figure 3-11: Bond stress vs GFRP slip for controlled failure of GFRP – concrete bond

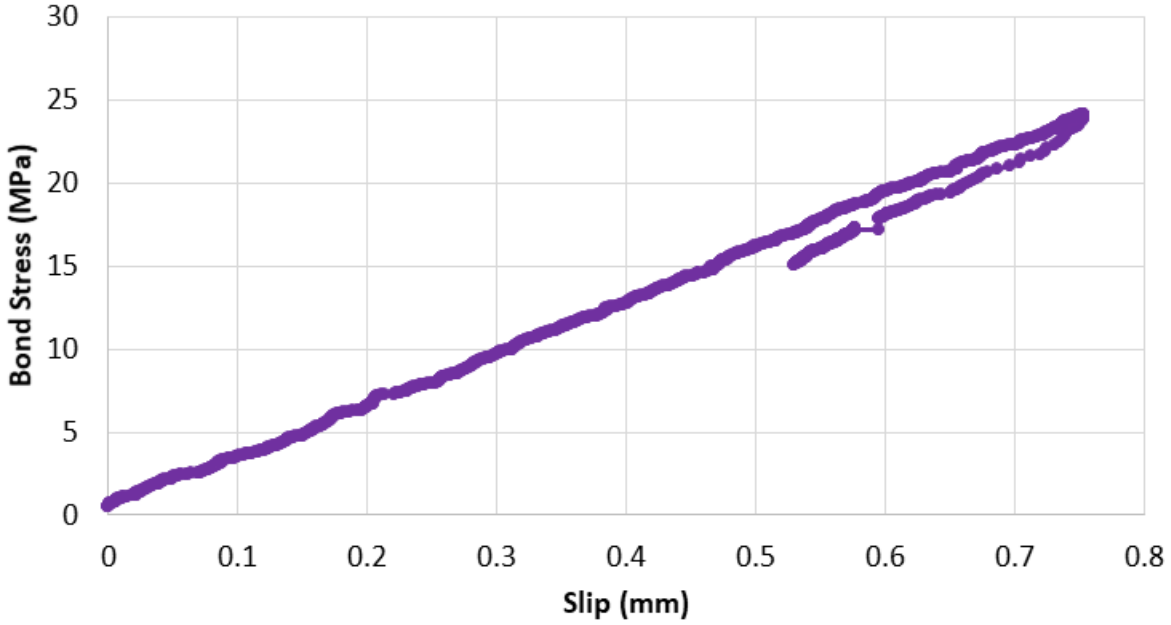

Figure 3-12: Bond stress vs GFRP slip for tests where the wedge collet slips

3.1.5. Effects of temperature on the compressive strength of concrete

Initial pullout tests were completed on both ambient and frozen specimens, whereby a significant increase in the compressive strength of the frozen specimens was observed. In order to determine how and why concrete cured identically, but tested at both ambient lab temperatures and -30°C, had such a large variation in compressive strength, an experimental investigation was undertaken, following Figure 3-13.

As discussed earlier, it was initially assumed that the variation in the compressive strength of concrete was directly related to the free water in the capillary pores. To test this theory, two concrete casts were undertaken using the mix design described in Figure 3-13, with two different water to cementitious materials ratio, 0.32 and 0.45. 160 cylinders, 75 mm ø by 150 mm tall, were cast, ten of which contained thermocouples. After casting, 80 specimens were cured for two days at an elevated temperature of 70°C, while 80 specimens were cured for two days at ambient lab conditions.

After two days curing. the cylinders were removed from the thermal chamber and five samples of both the steam-cured and ambient-cured specimens were set aside. All the remaining cylinders were demolded and labelled, according to their initial two-day curing state and their conditioning state as follows: elevated curing + moist conditioning (ECMC), ambient curing + moist conditioning (ACMC), elevated curing + ambient conditioning (ECAC), ambient curing + ambient conditioning (ACAC). The moist conditioning samples were then placed in the fog room to ensure a 100% relative humidity conditioning, while the remaining ambient conditioned samples were left in the lab. The ten samples which were set aside were end-ground and tested in compression.

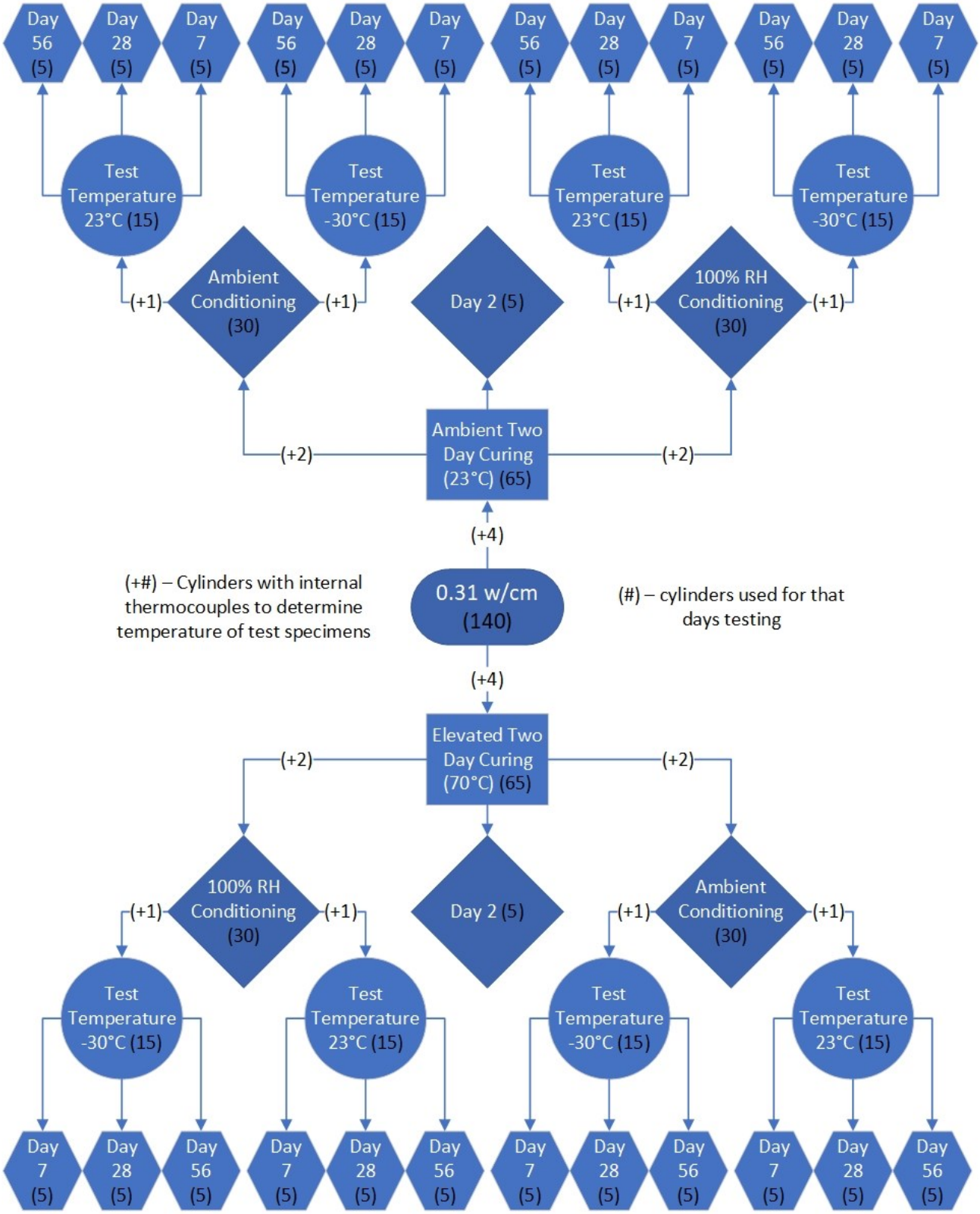

Figure 3-13: Moisture content workflow

After the cylinders were tested, three samples of approximately ten grams of concrete fines (excluding large aggregate where possible) were collected and ground to a fine powder. The five samples were weighed, and were then placed in an oven at 105°C for a period of more than 24 hours. The new weight was recorded when they were removed and the free water determined. To determine the evolution of strength gain and the effects of the different curing conditions, two days prior to standard compressive and moisture content testing (day 5, 26, and 54), the specimens that were to be tested in their frozen state were removed from the conditioning environment. These specimens were end-ground to ensure equal stress when loading, had excess water removed from the surface of the specimens, and were then placed in a freezer at approximately -30°C. The specimens slowly cooled over 48 hours, until the internal temperature was approximately -30°C, see Figure 3-14.

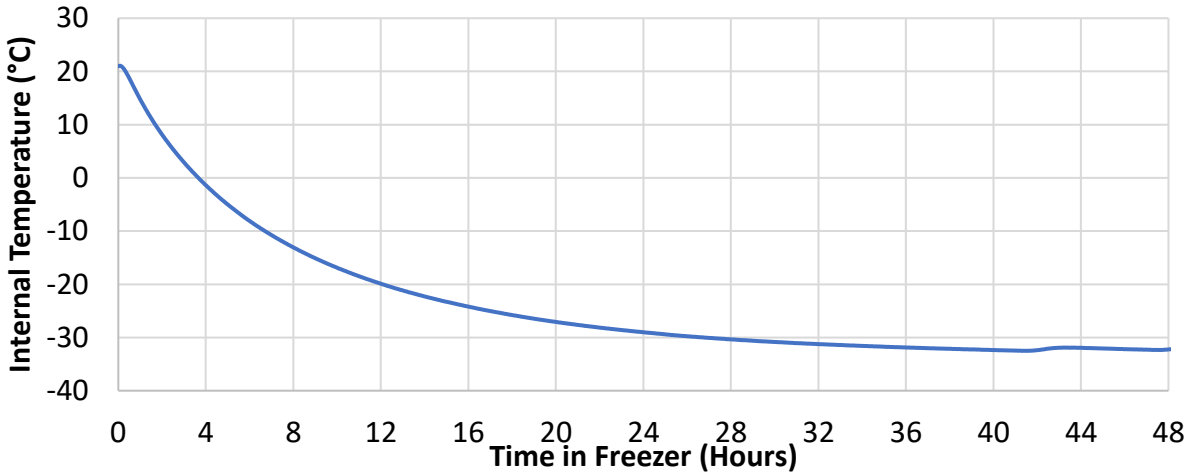

Figure 3-14: Internal temperature vs time exposed to -33°C

On the designated day (day 7, 28, 58), the specimens were removed from the freezer and a compression test conducted. The compression results and the free water content were compared for both the ambient and frozen specimens.

3.2. The effect of salt use on reinforced concrete structures

As mentioned earlier, the use of de-icing salts and anti-icing brines, although necessary, can cause serious material damage and corresponding structural issues. These issues arise both in the form of corrosion of reinforcing steel and concrete structure attack. In order to study, and later model the interaction of the reinforced concrete structure and these chloride containing solutions the following experiments were undertaken.

3.2.1. Effect of chloride brine exposure on concrete compressive strength

Once the chloride begins to migrate through the concrete, it has been shown that $CaCl_2$ and $MgCl_2$ detrimentally affect cementititous materials [76]. In order to expand the literature, the effect of calcium chloride was explored, magnesium chloride, sodium chloride, and a multi chloride brine on a “typical highway structure mix” over long term exposure. This was completed by casting 400

cylinders from one batch of concrete, with a cementitious material (75% ordinary Portland cement and 25% blast furnace slag) content of 355 kg/m^3, a 0.42 w/cm ratio and a specified strength of 30 MPa. Due to the length of time required to cast the 400 cylinders, a second dose of a high range water reducer was added part way through the cast to ensure a consistent fluidity of the mix.

The cylinders were then capped for 24 hours before being demoulded and placed in the humidity chamber for the next 27 days, Figure 3-15, whereby all the cylinders were end-ground. The compressive strength of three cylinders was determined. 79 specimens were re-placed in the humidity chamber and the remaining cylinders were equally divided and immersed in one of four commercial anti-icing brines Figure 3-16, the chemical composition of which is shown in Table 3-6.

Figure 3-15: 400 cylinders in the humidity chamber

Table 3-6: Content, moles/litre (m/L), of major components of the commercial anti-icing brines

Brine	Ca (mol/L)	K (mol/L)	Mg (mol/L)	Na (mol/L)	S (mol/L)	Sr (mol/L)	Cl (mol/L)	Cl^- wt.%
Calcium	3436	123	ND	106	50	21	7603	26.9
Sodium	ND	17	ND	5733	20	ND	5010	17.8
Magnesium	60	33	3497	108	22	ND	6523	21.4
Multi	2006	129	425	1598	36	18	6040	23.1

Figure 3-16: 80 cylinders submerged in the de-icing solution

Every two months for the next five years, three cylinders were randomly chosen and removed from each of the deicing brines and the humidity chamber and tested in compression.

After approximately 2000 days in the chloride brines, two of the remaining cylinders were removed from each solution and transversely dry cut, to avoid dissolving internal chloride. The disks were then analyzed by X-ray fluorescence, at 12.7, 25.4, and 38.1 mm from the surface before being sprayed with either a 0.1M $AgNO_3$ solution or a pH indicator. The $AgNO_3$ solution has been shown to react with the soluble chlorides in the cement paste and precipitate as silver chloride, a white or grey precipitate. The soluble chloride concentration required for the precipitate to form is approximately 0.15% by weight of cement [86].

3.2.2. Pore solution composition of cement pastes with admixed chlorides

As chlorides migrate through the porous cement paste, the concentration at the surface of the reinforcing bars increases until, if the reinforcing material is metallic, corrosion initiates. The amount of chlorides required to initiate corrosion (the critical chloride threshold) depends on the cementitious materials in the concrete as well as the type of reinforcing steel. In the case of stainless steel, this greatly exceeds traditional carbon steel and, if a new corrosion -resistant rebar product is developed for market, it would require decades of exposure in the field to determine the critical chloride threshold. In an attempt to rapidly determine the corrosion resistance of steel reinforcement, researchers often resort to corrosion monitoring in synthetic concrete pore solution [42, 77]. This allows for shorter corrosion initiation times and the ability, by visual inspection, to see exactly when that corrosion initiates. In order to determine the effects that cementitious materials and w/cm ratio have on the chemical composition of cement pore

solution, the solution was expressed from cylinders of known mix design and chloride content and chemically analyzed. The procedure was as follows.

Cement paste cylinders, 50.8 mm ø by 101.6 mm, were cast using ordinary portland cement (GU: (i) without any SCMs; (ii) with 25% replacement by ground granulated blast furnace slag (GU-BFS); (iii) with 25% replacement by Type CH fly ash (GU-FA) and (iv) interground with 7% replacement of silica fume (GU-SF). Chemical analysis of each of the components, provided by the suppliers, are given in Table 3-7.

Table 3-7: Cement and supplementary cementitious materials composition, weight % as provided by the supplier.

Component	Portland cement (GU)	Silica Fume Cement (GU-SF)	Ground Granulated Blast furnace slag	Type CH Fly Ash
LOI	2.04	1.98	1.60	1.25
SiO_2	18.94	25.71	38.66	40.23
Al_2O_3	5.16	4.89	8.9	19.19
Fe_2O_3	2.31	2.32	0.52	8.25
CaO	62.76	56.39	38.53	21.87
MgO	2.31	2.17	11.32	3.99
SO_3	4.03	4.08	2.75	1.70
Total Alkali	0.98	0.97	0.77	1.91

For each of the aforementioned cement paste mixtures, five cylinders were cast with w/cm ratios of 0.40, 0.45, 0.50 and 0.55. For each mix, reagent grade sodium chloride (NaCl) was dissolved in the mixing water in either a 0% or 5% chloride concentration, by mass of cementitious materials. In the case of the 0.40 and 0.50 w/cm mixes additional samples with 2.5% and 7.5% Cl as NaCl were cast. The cement paste cylinders were then sealed and slowly rolled for 24 hours to limit bleeding.

28 days after casting, the hardened pastes were removed from the cylinders and inserted into the pore solution expression chamber, Figure 3-17. A PTFE disc was placed on top of the cylinder to ensure a water tight fit and a nylon disc used to ensure the piston did little damage to the PTFE. A syringe, fitted with a 0.45 μm filter to prevent the inclusion of small solid particles, was then attached at the base of the fluid drain before the piston was inserted and the test commenced.

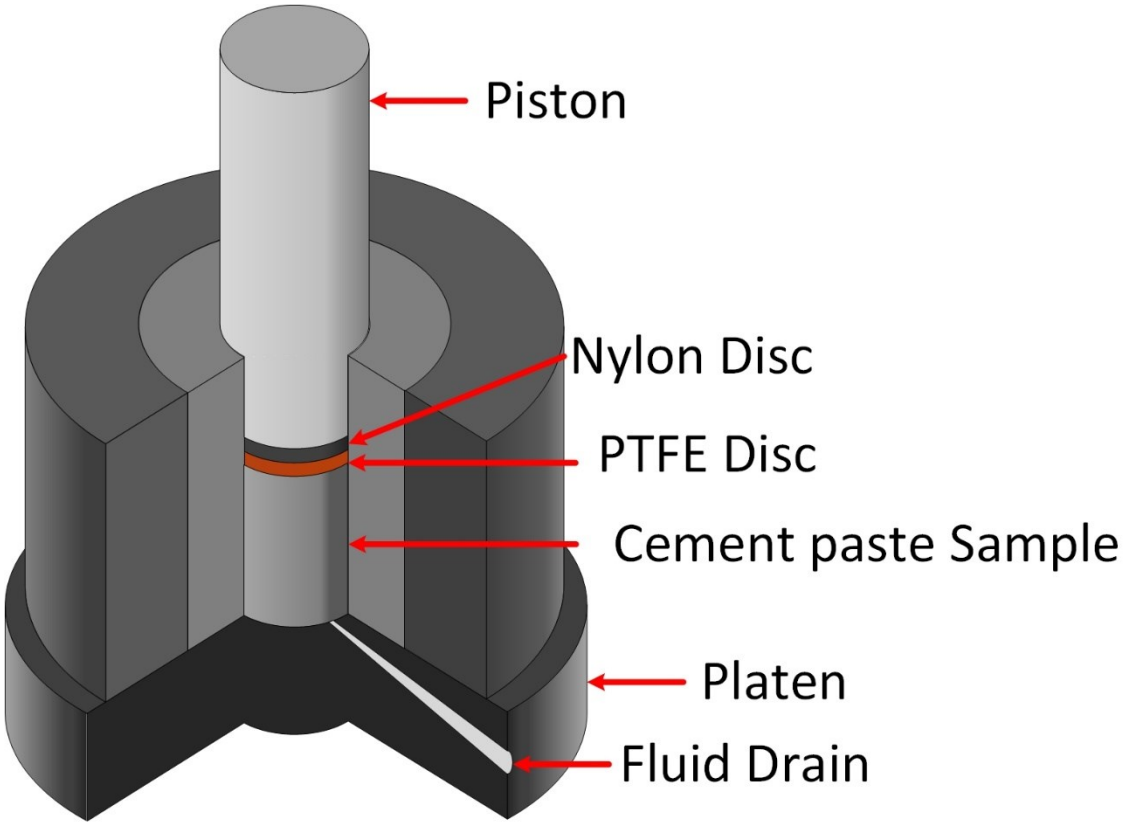

Figure 3-17: Pore solution expression chamber

For each specimen, pressure was applied slowly at increments of 50 kN, up to a max load of approximately 1000 kN, and held between 2-5 minutes between each increment. This was done to ensure constant flow of the pore solution. If the pressure were to be applied too quickly, it the pores would collapse and prevent flow of the pore solution, and then not be available for expression. The expressed pore solutions, typically 2-10 ml, were then sealed to ensure that CO_2 did not react with the $Ca(OH)_2$. The syringes were stored in the dark at ambient temperature until they were sent for analysis. The chemical compositions of three replicate samples were then determined using ion chromatography (IC) for the anions and inductively coupled plasma (ICP – both OES and MS) analysis for the cations. Additionally, where sufficient expressed pore solution allowed, the pH was determined in hopes of identifying the correlation between chloride contents and pH levels.

On the day of pore solution expression, the 5th cylinder was demoulded, ground into a fine powder and weighed. The powdered samples were then placed in an oven at 105°C for 24 hours before being re-weighed, following the recommended procedure of Wong et al. [87], and the evaporable water content, as a weight percentage of the dry cement in the mix, was determined using Equation 19.

$$W_e = \left(\frac{W_w - W_D}{W_w}\right) \cdot \left(1 + \frac{w}{cm}\right) \cdot 100\% \qquad \text{Equation 19}$$

Where W_e is the evaporable water content, W_w is the weight of the wet sample, W_D is the weight of the dry sample, and w/cm is the water to cementitious material ratio.

3.3. Supplemental experimental procedures

3.3.1. Digital Image Correlation determination of the coefficient of thermal expansion of GFRP reinforcing bars

In order to determine the interaction between the GFRP and concrete, the coefficient of thermal expansion of the GFRP was compared to that expected from the concrete. Although the manufacturers supplied values for these coefficients of thermal expansion, Table 3-1 and Table 3-2, a new technique was utilized to confirm these values. Traditionally, the values for CTE are determined using thermomechanical analysis in accordance with ASTM E831 – 06 [88]. The new technique, digital image correlation, DIC, utilizes two cameras, spatially calibrated, to determine the movement between data points on the surface of material being heated or cooled. These cameras are spatially located by analyzing photos of a calibration disc moved throughout the plane in which the specimen will rest. This allows camera triangulation and removes potential distortions. This movement then allows for strains, and correspondingly, stresses to be determined, Figure 3-18**Error! Reference source not found.**.

Figure 3-18: Digital Image Correlation camera setup

To prepare the GFRP for DIC testing, 102 mm (4 inch) long sections were machined using an end mill to create a sample with two flat parallel faces. The flat sections of the two faces were 8 mm and 6mm thick for the 16M bars and 13M bars respectively. Next, 8 mm holes were then drilled through the machined area of the bar to allow a thermocouple to be connected to the surface of the bar. The surfaces were then painted white and speckled with black paint to provide movement reference points for the system, Figure 3-19.

Figure 3-19: Digital Image Correlation sample specimen

Four replicates of each bar size and manufacturer were placed in a freezer at -30°C for 24 hours prior to DIC testing. The specimens were removed from the freezer approximately one minute before the test began and supported by the bottom grip. The images and temperature measurements were recorded at 0.5 frames per second. A typical temperature curve is plotted below, Figure 3-20, and it should be noted that due to the large temperature differential between the freezer and the ambient lab temperature, the specimen temperature increased from approximately -30°C to approximately -25°C in the one minute test setup period.

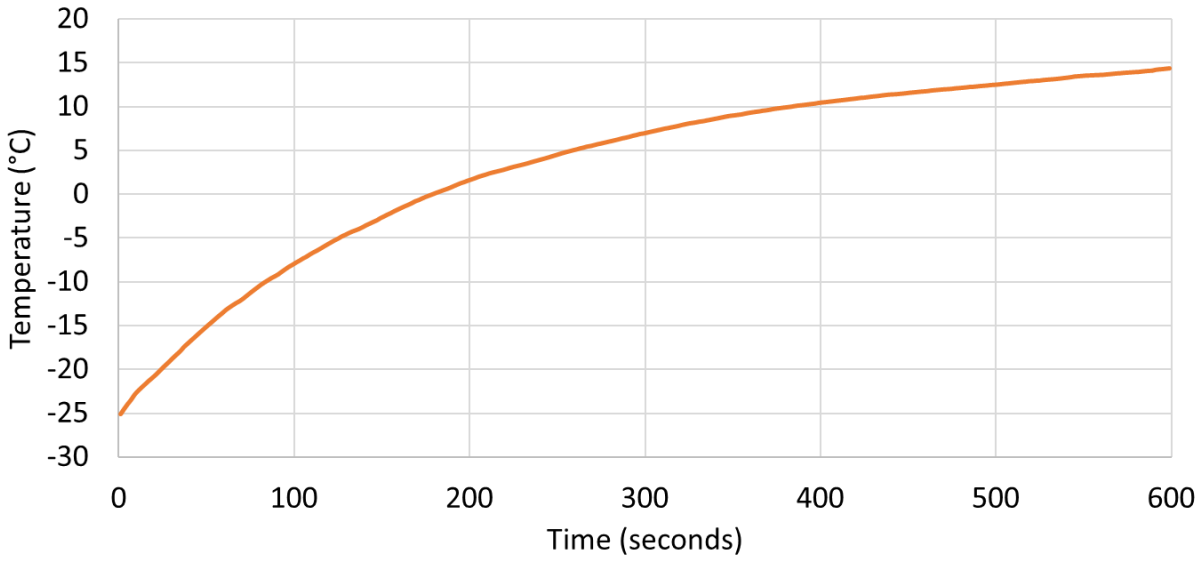

Figure 3-20: Digital Image Correlation test temperature profile

After the DIC experimental procedure took place, transverse strains were analyzed at each quarter-point, as seen in Figure 3-21, and the strains plotted with respect to temperature. The approximate slopes of the plots, using a trendline, were then used to determine the coefficients of thermal expansion.

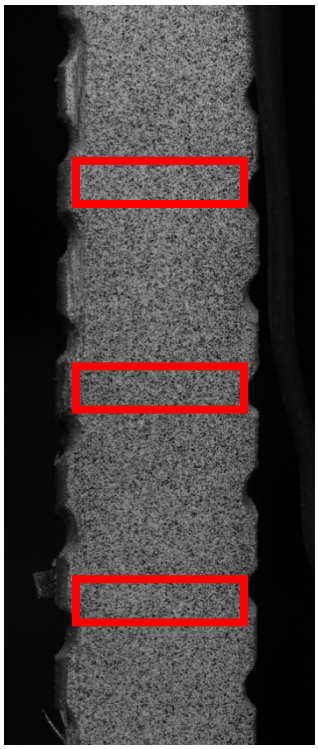

Figure 3-21: Digital Image Correlation strain analysis locations

3.3.2. Chloride concentration using X-ray fluorescence

During winter salt applications, the surface chloride concentration builds up. This concentration is then typically assumed to the be driving force of chloride diffusion which many authors [13, 47, 48] model using an extension of Fick's second law, Equation 4.

Due to the destructive and arduous nature of collecting both surface chloride concentrations and apparent diffusion coefficients, there are few field data available. As such, these data are often limited to specific regions of highway structures. Therefore, in order to be able to collect surface chloride concentrations, rapidly and non-destructively, the use of a portable X-ray fluorescence (XRF) analyzer is proposed.

The XRF analyzer allows the operator to determine the elemental composition of a sample, to a depth of 1 – 5 mm depending on the material density, by directing a high energy X-ray beam at the specific area of the sample in question. The X-rays displace electrons from the inner orbital shells, which are replaced by an electron from a higher orbital shell, releasing fluorescent X-rays with energy corresponding to the specific element, as shown schematically in Figure 3-22**Error!**

Reference source not found.. The analyzer measures the corresponding energy levels and their intensity, and statistically displays the percentage of each element. The technique is limited to elements higher than, and including, aluminum on the periodic table, because of the transmission limits of the beryllium window receiving the emitted X-rays.

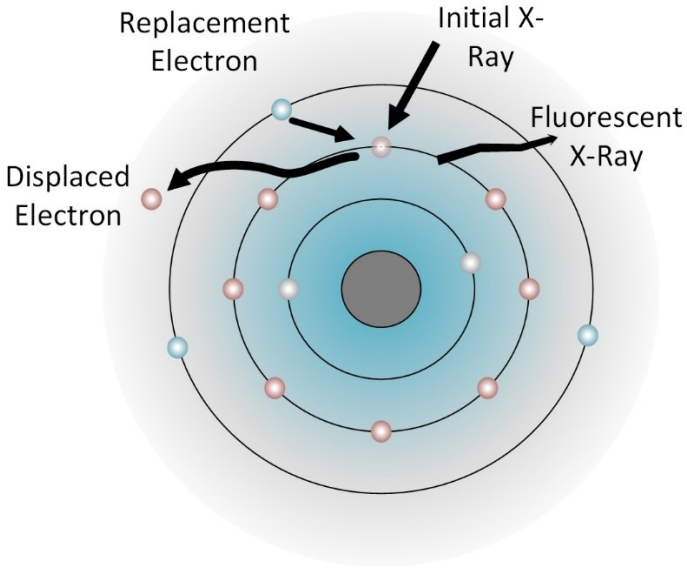

Figure 3-22: Schematic representation of the X-Ray Fluorescence process

In order to calibrate the system to allow analysis of concrete structures, concrete "standard" cylinders with known chloride contents were cast following the mix design in Table 3-3 by dissolving chloride, as sodium chloride, in the concrete mix water. The twelve chloride concentrations added to the concrete to calibrate the XRF unit are given in **Error! Reference source not found.**.

Table 3-8: Cast in chlorides, as $NaCl^-$, mass percentage of cementitious materials

Admixed Chlorides (percent by mass of cementitious materials)												
0.10	0.25	0.50	0.75	1.00	2.00	3.00	4.00	5.00	6.00	7.00	9.00	10.00

After allowing the cylinders to cure a minimum of 28 days, the concrete cylinders were broken into pieces and 75 XRF analyses were conducted on samples of each cylinder. The average measured chloride content, as well as the standard deviation, was determined for each cast in chloride content and plotted in Figure 3-23**Error! Reference source not found.**.

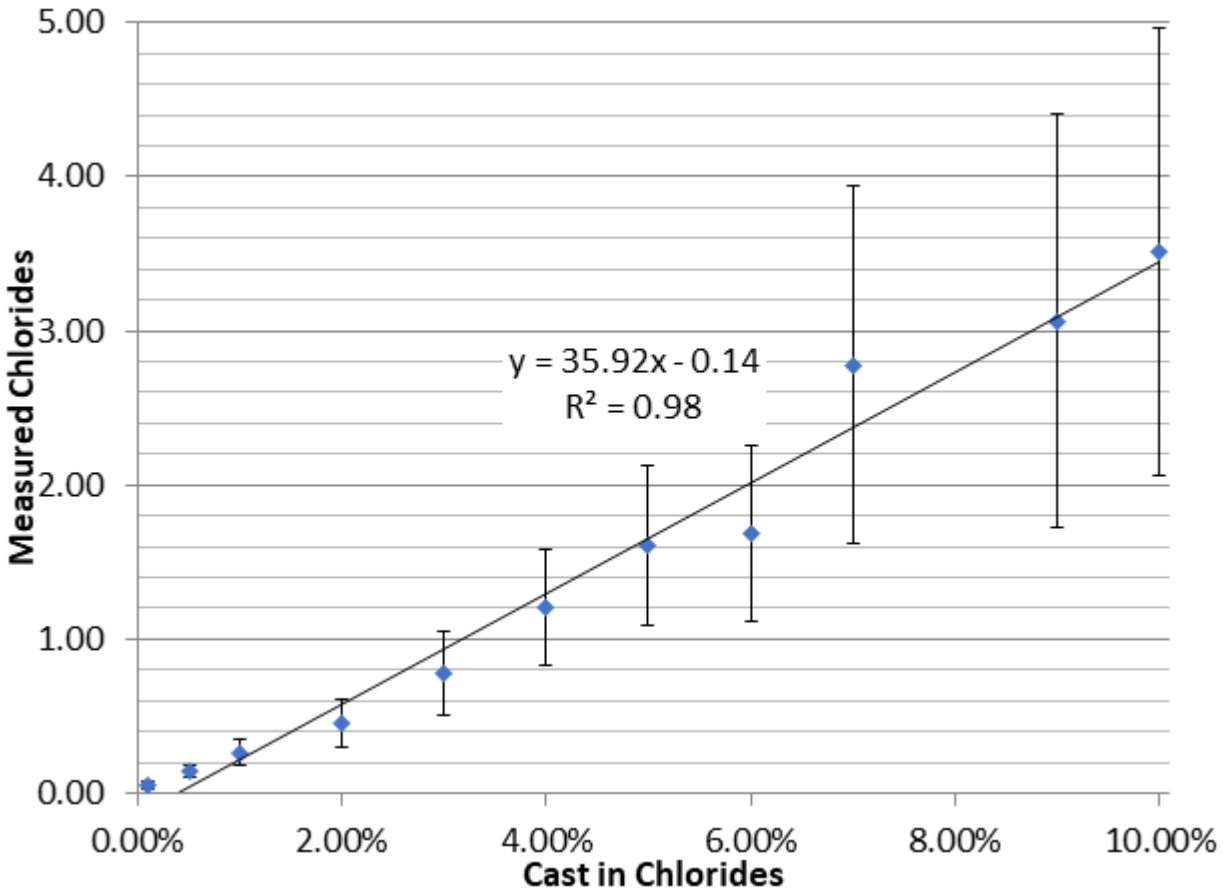

Figure 3-23: Chlorides measured with XRF analyzer versus the amounts cast-in chlorides

This**Error! Reference source not found.** allows XRF owners to quickly scan concrete cores and concrete surfaces to compare their measured data to the curve. This will give an approximate chloride content and can be used as a screening mechanism to determine if the much more rigorous acid-soluble [71] and water-soluble [72] tests to determine chloride content should be conducted.

Chapter 4 Results and Discussion

4.1. The effect of curing and service temperature

4.1.1. Damage of concrete containing GFRP rebars subjected to freeze-thaw cycles

The modified ASTM C666, with prolonged 24 hour freezing and 24-hour thawing cycles, was used to indicate any effect of freeze thaw cycles on the integrity of concrete containing GFRP reinforcing bars. This test was not intended to provide detailed numerical data. Instead the relative dynamic modulus, alongside visual observation, was used to indicate potential concrete degradation. A dramatic decrease in relative dynamic modulus and scaling of the surface of the concrete would indicate that a detailed autopsy should be conducted. The results of dynamic modulus tests were much more consistent over the 300 cycles than the preliminary tests, with very little change occurring in the relative dynamic modulus, Figure 4-1. This is likely because the temperature range (ΔT of 40°C) does not induce enough radial stress to either pull the GFRP away from the concrete, or induce tensile cracking.

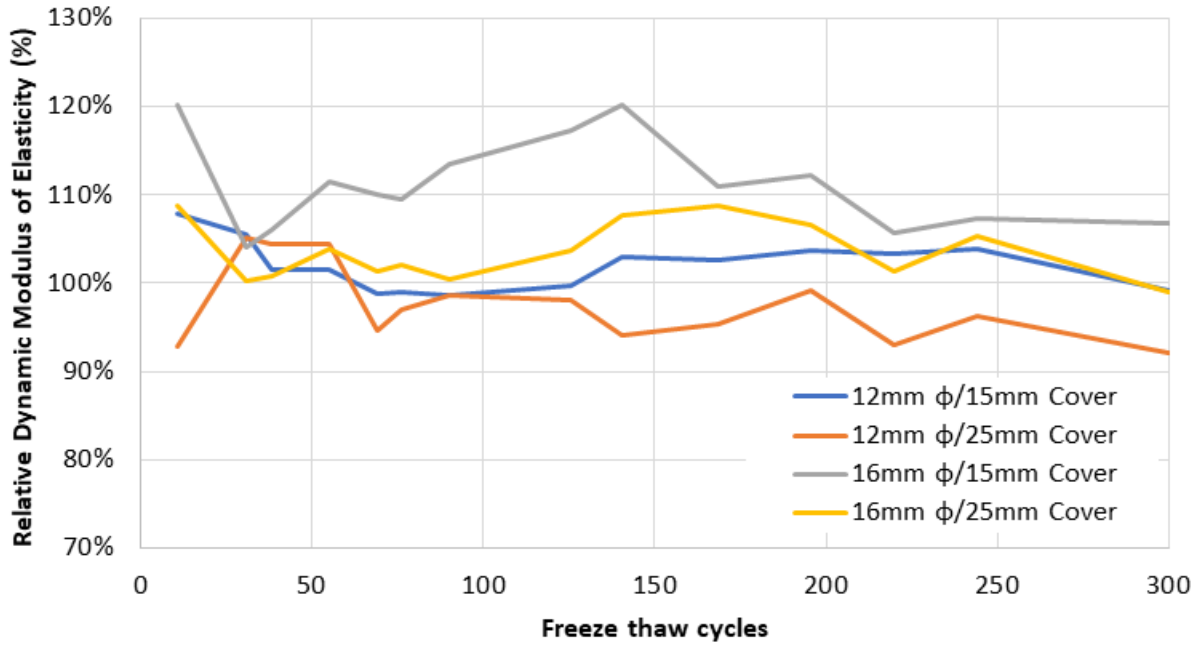

Figure 4-1: Average (of 4 specimens) relative modulus of elasticity versus the number of 24-hour freeze thaw cycles

An analysis of the results indicates the selected test method for determining concrete degradation may not have been ideal, and it appeared that the thermal fatigue cycling did not cause surface damage to the concrete specimens.

4.1.2. Damage of GFRP reinforced specimens exposed to a southern Ontario environment

In order to determine if differential CTE of the GFRP rebars and the concrete posed a significant risk of either microscopic or macroscopic damage to the concrete, the GFRP-reinforced concrete specimens were left in the outdoor testing facility for extended periods of time. The initial cast, without baseline strain measurements, was left for a period of approximately four years. The second cast, used to determine differential strains between concrete containing Schöck – Combar GFRP bars and concrete without reinforcement, was left for approximately 20 months. The temperature corrected strain data for the initial cast are presented in Figure 4-2 and Figure 4-3, and for the second cast in Figure 4-4 to Figure 4-7. Note that tensile strains in the concrete are positive.

Figure 4-2 and Figure 4-3 demonstrate that the 16 mm GFRP bar induced a higher tensile strain than the 12 mm bar, which can be attributed to its larger cross sectional area. These figures also indicate that there was very little compressive strain induced in the concrete after the initial exposure, suggesting that the induced tensile forces during the elevated summer temperatures had caused minimal damage. Alternatively, the GFRP bars had restrained the retractive movement of the concrete and limited the compressive force that the temperature induced.

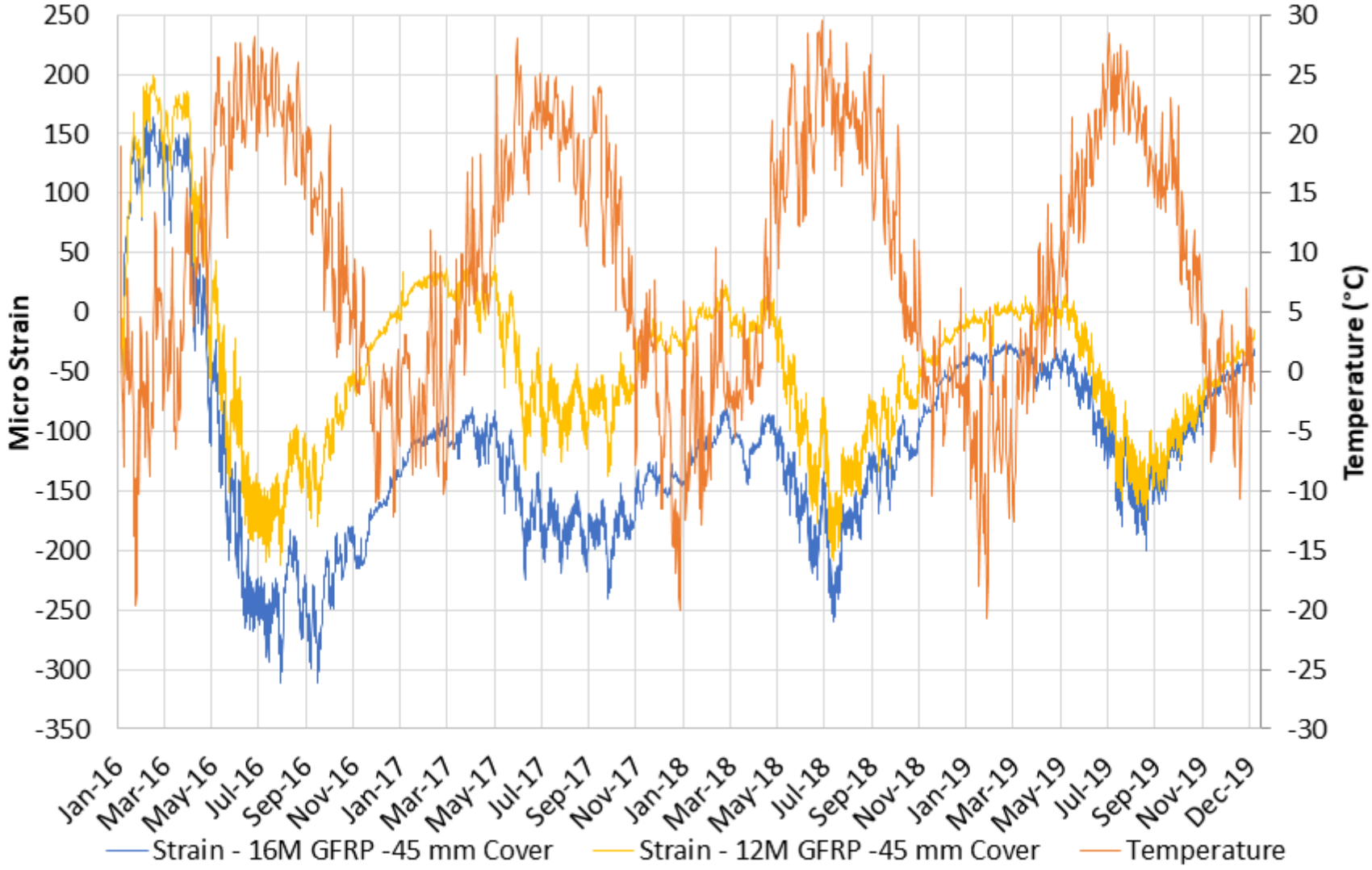

Figure 4-2: Average (of 4 replicates) Strain and internal temperature vs exposure time for specimens containing GFRP with a 1.75" concrete cover

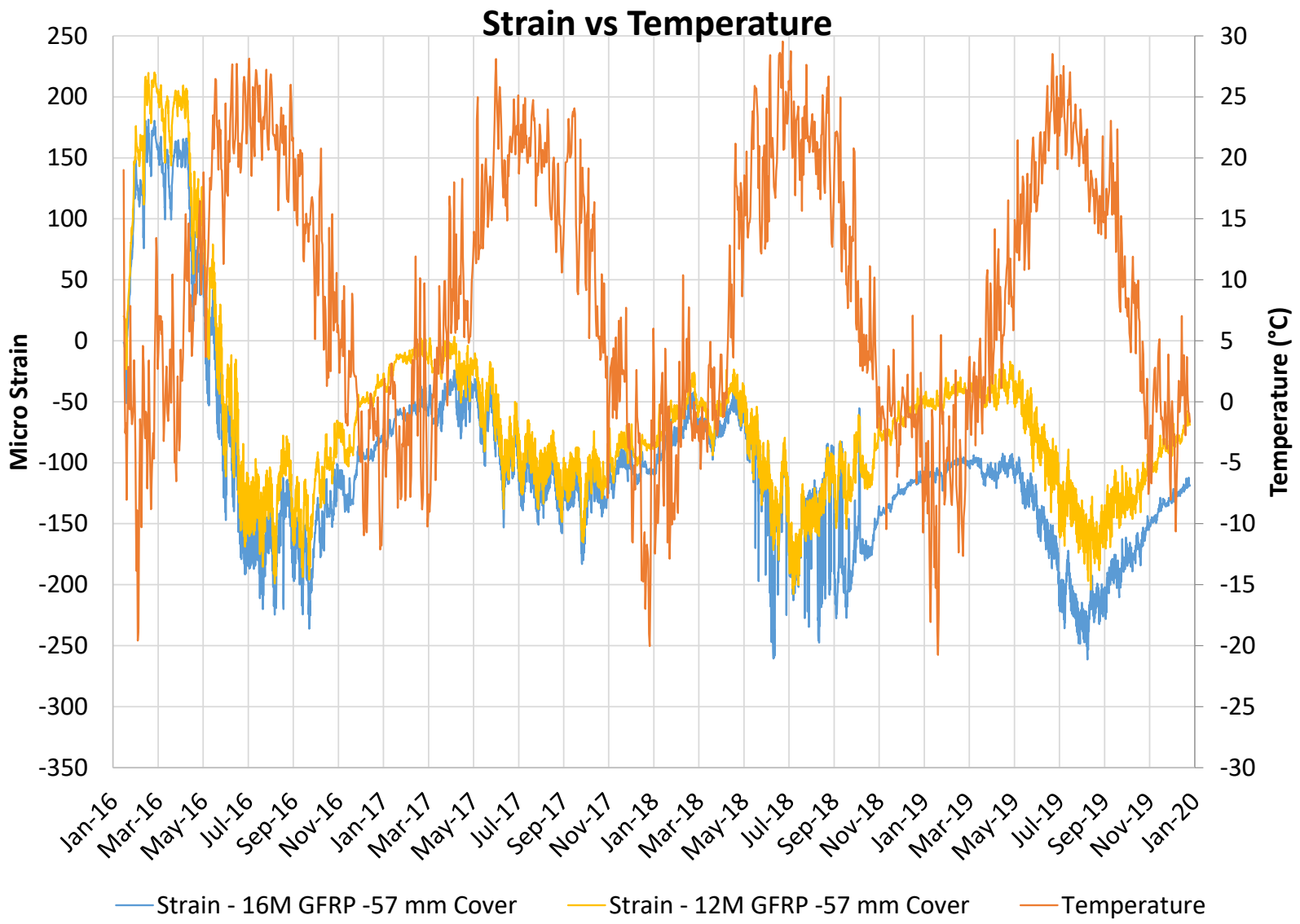

Figure 4-3: Average (of 4 replicates) Strain and internal temperature vs exposure time for specimens containing GFRP with a 2.25" concrete cover

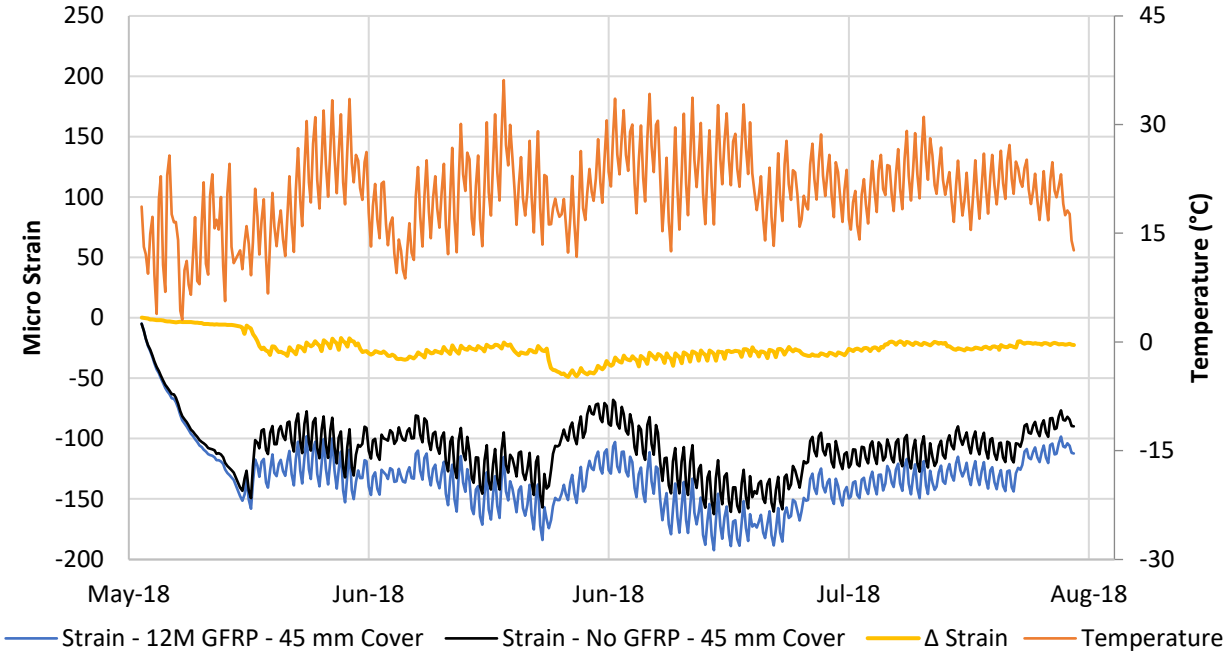

Figure 4-4: Comparative strain data and temperature profile for specimens with a 45 mm concrete cover with and without 12M GFRP reinforcement – May to August 2018

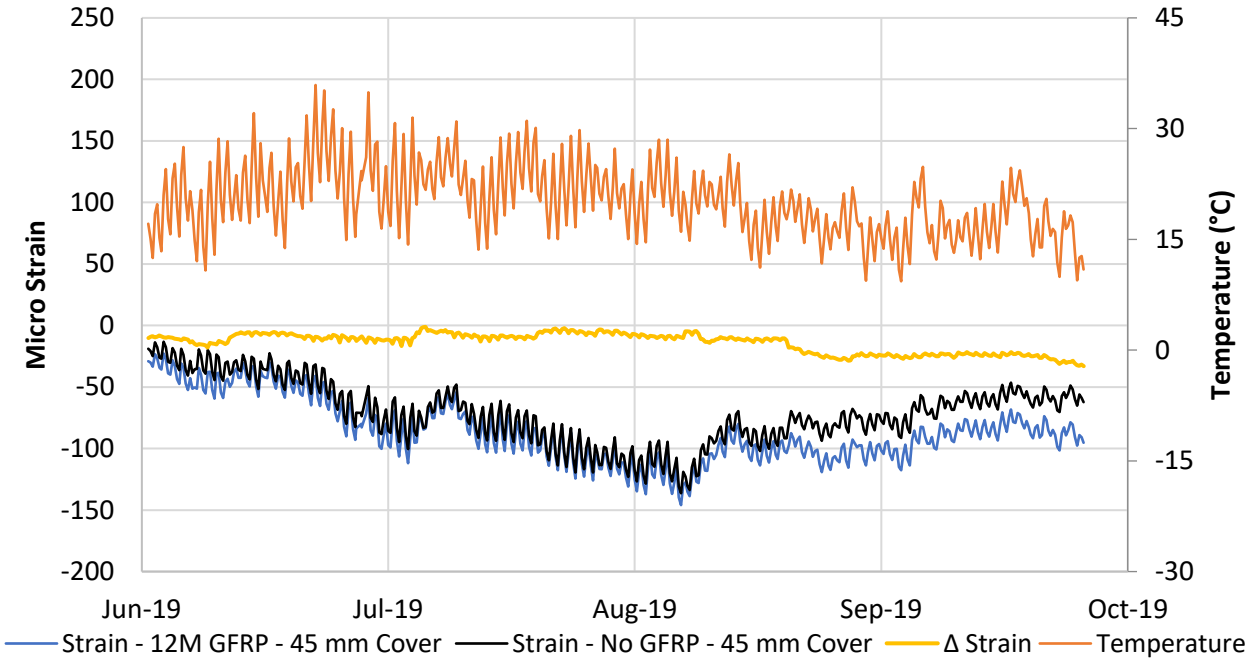

Figure 4-5: Comparative strain data and temperature profile for specimens with a 1.75" concrete cover with and without 12M GFRP reinforcement– June to October 2019

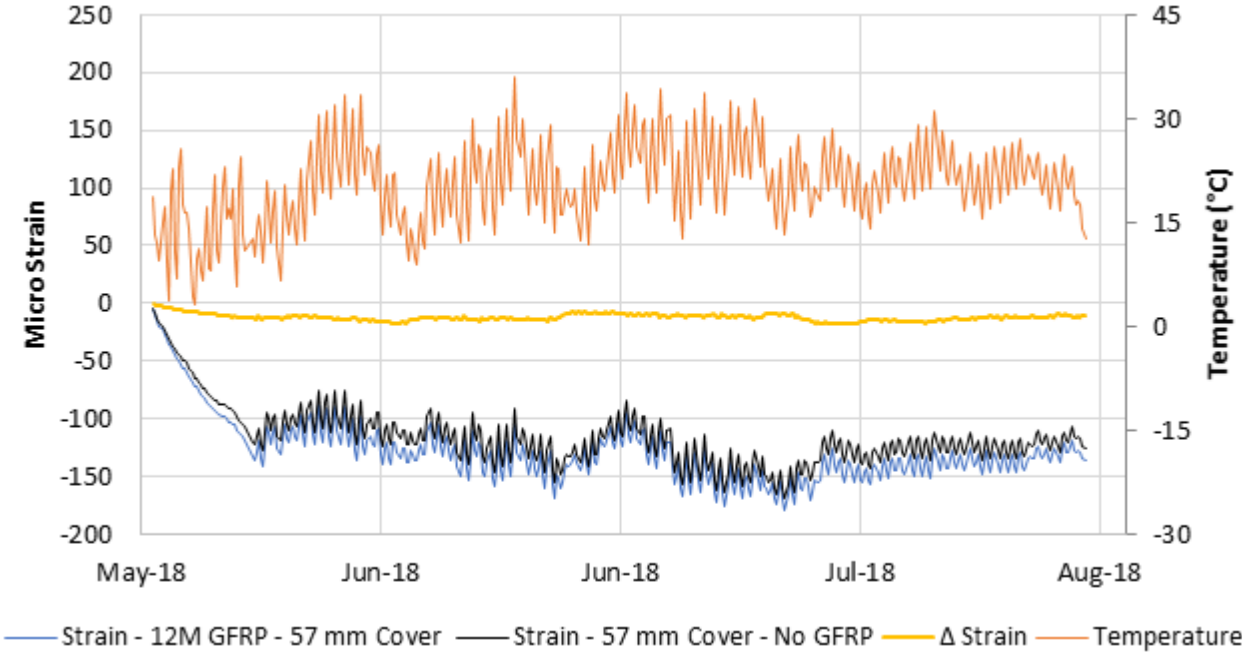

Figure 4-6: Comparative strain data and temperature profile for specimens with a 57 mm concrete cover with and without 12M GFRP reinforcement – May to August 2018

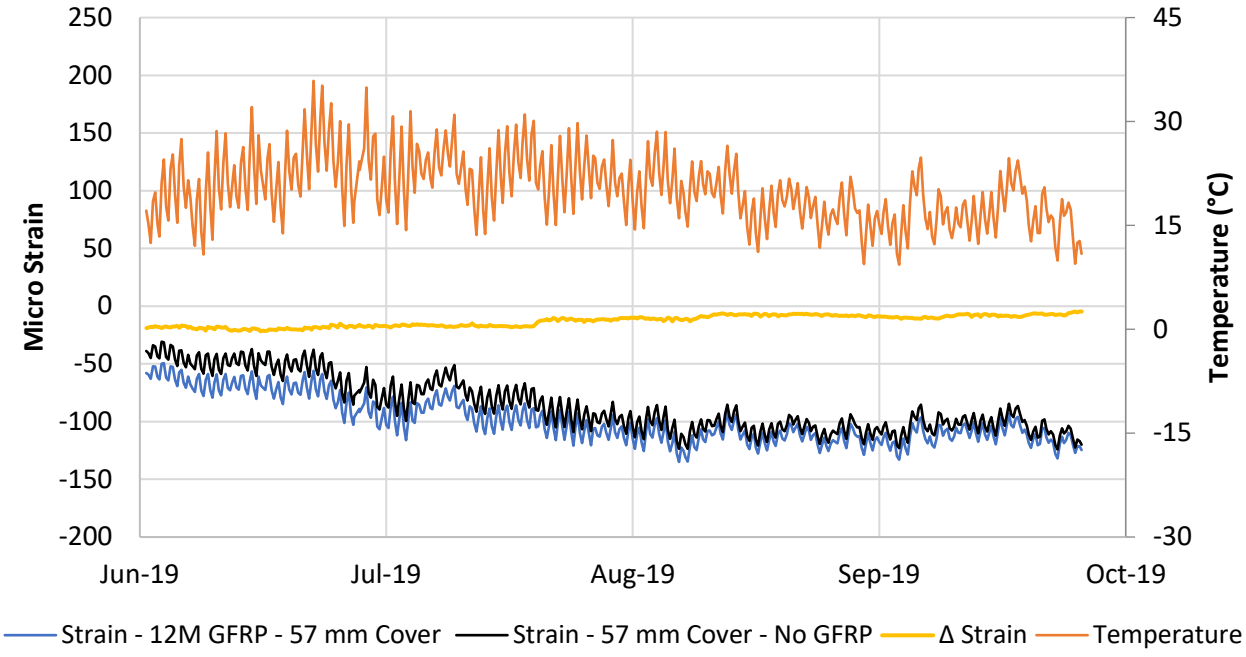

Figure 4-7: Comparative strain data and temperature profile for specimens with a 57 mm concrete cover with and without 12M GFRP reinforcement – June to October 2019

Although data had been collected for the summer months of 2018 and 2019, the strain measurements for the second cast were not continuous due to technical issues with the data loggers. All four figures, Figure 4-4 to Figure 4-7, indicate that the concrete in proximity to the GFRP experienced more tensile strains than concrete without GFRP. The yellow line in each figure represents the difference in strain between those with and without GFRP. It should be noted that the difference in tensile strains in the first year appear to higher than those in the second year, never exceeding 50 micro strain. That, in addition to the results of Equation 16, suggests the improbability of cracking. Inspection of the surfaces of the specimens exposed to the anti-icing brines, Figure 4-8 and Figure 4-9, indicate no surface cracking in relation to the internal GFRP, confirming the results from section 4.1.1, that GFRP does contribute to cracking of the concrete cover.

Although, not directly related to the GFRP reinforcement, significant degradation of the concrete exposed to the multi chloride brine was observed. The composition of the chloride brine, is given in Table 3-6. The major component, calcium chloride reacts with calcium hydroxide to form calcium hydroxichloride, Equation 3, which is known to be expansive and cause structural degradation. The surface scaling confirms results by Cremasco [70] who observed large salt scaling after prolonged multi-chloride exposure. He concluded that this would reduce the service load that a structure could expect to carry as the reduced compressive strength and area reduce the max compressive stress a structure can endure.

Figure 4-8: Ponding well of outdoor specimens exposed to multi chloride brine for more then 3 years

Figure 4-9: Bottom surface of outdoor specimen in Figure 4-8

4.1.3. Bond characteristics of GFRP bars in concrete

The bond strength of GFRP bars in concrete was determined using the procedure prescribed in ASTM D7913. The test was run in two separate trials, with the initial six replicates of Schöck - Combar 12 mm and 16 mm bars tested at room temperature followed by a trial with eight replicates, four of which were tested at room temperature and the remainder tested at -30°C.

4.1.3.1. Initial Results

After the initial pullout tests had been completed, the test specimens were autopsied to determine if the failure mechanism was either bond failure or GFRP slip or if the concrete or the GFRP had caused the bond failure, and to confirm the bond length to determine bond stress at failure. This was done by cutting the concrete sample to the depth of the PVC bond break from two sides, splitting the sample in two, then analyzing the failure surfaces, Figure 4-10.

Figure 4-10: Autopsy of bond test specimen containing 12 mm Schöck – Combar

Once the failure mechanism was determined, the actual bond length was measured with calipers and the percentage of concrete and rib failure estimated, an example of which is demonstrated in Table 4-1.

Table 4-1: Bond length and failure mechanism for 12 mm Schöck – Combar cured at ambient lab temperatures.

Bond Length (mm)	Notes
68.5	Concrete Shear 85% - Rib Shear 15%
64.2	Concrete Shear 80% - Rib Shear 20%
66.8	Concrete Shear 85% - Rib Shear 15%
68.9	Concrete Shear 85% - Rib Shear 15%
64.5	Concrete Shear 80% - Rib Shear 20%
60.2	Concrete Shear 70% - Rib Shear 30%
66.9	Concrete Shear 80% - Rib Shear 20%
66.2	Concrete Shear 80% - Rib Shear 20%

After the bond length was determined the maximum bond stress, τ_m, was calculated using Equation 20:

$$\tau_m = \frac{F}{C_b \cdot l} \qquad \text{Equation 20}$$

Where F is the peak load (N) achieved during the pull-out test, C_b is the effective circumference of the bar (mm – based on diameter provided by the manufacturers), and l is the bonded length (mm).

The initial specimens provided a baseline for bond stress of the Schöck – Combar bars, and the maximum bond stress appeared to be related to the compression strength of the concrete. Both the concrete compression strength and bond stress are presented in Table 4-2 and Table 4-3. It

should be noted that the bond stress for the 12 mm diameter bar appeared to be slightly lower than that of the 16 mm specimens, even with comparable concrete compressive strength.

Table 4-2: Bond strength, concrete compressive strength, and concrete slump values for 12 mm Schöck – Combar cured at: 23°C, 60°C, 70°C, and 80°C.

Curing Temperature		Bond Strength (MPa)	Compressive Strength (MPa)	Slump (mm)
23°C	μ	18.58	73.73	120
	σ	0.99	0.56	-
60°C	μ	16.61	69.83	180
	σ	0.85	0.38	-
70°C	μ	16.5	73.39	260
	σ	0.56	1.37	-
80°C	μ	19.03	74.39	120
	σ	1.12	1.04	-

Table 4-3: Bond strength, concrete compressive strength, and concrete slump values for 16 mm Schöck – Combar cured at: 23°C, 60°C, 70°C, and 80°C.

Curing Temperature		Bond Strength (MPa)	Compressive Strength (MPa)	Slump (mm)
23°C	μ	20.01	68.56	180
	σ	1.20	0.60	-
60°C	μ	20.38	70.48	220
	σ	0.63	0.10	-
70°C	μ	20.37	74.91	260
	σ	0.91	0.49	-
80°C	μ	22.82	75.68	180
	σ	1.01	1.01	-

One aspect of this initial pullout test regiment that should be considered is the proportions of the concrete mix. With a cementitious content greater than 600 kg/m^3, the sticky texture and consistency of the mix, required the placement and finishing techniques to be adjusted each time. This led to slump and air content variations.

4.1.3.2. Full Scale Bond Strength Testing

Full scale testing commenced with Schöck – Combar specimens being cast twice a week for four weeks, followed by four weeks of pullout testing. The 13 mm ribbed bar testing resulted in near 100% success, as only one specimen did not reach bond failure. The data are presented below in Figure 4-11 with error bars indicating the maximum and minimum recorded bond strengths. Note that, contrary to the initial hypothesis, the bond strength increases with decreasing temperature. Additionally, the compressive strength of concrete appears to increase with decreasing temperature.

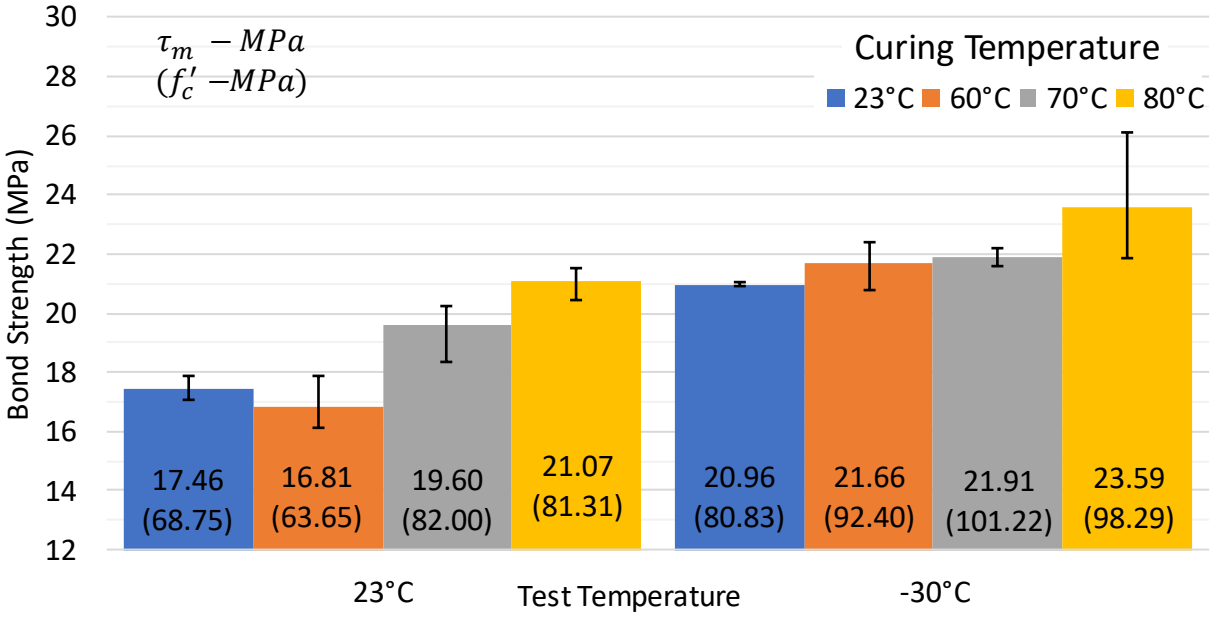

Figure 4-11: Bond strength and compressive strength (number in parentheses) for 12 mm Schöck – Combar pullout specimens cured at 23°C, 60°C, 70°C or 80°C and tested at 23°C and -30°C.

To confirm that the visual observation of increasing bond strength with decreasing test temperature is statistically significant, a t-test was performed using the method discussed in Appendix E – Statistical testing. The summarized results are presented in Table 4-4. The results indicate that for the curing temperatures of 23°C, 60°C, and 70°C that there is statistical evidence that colder test temperatures increase bond strength. The large variance in experimental bond strength data for the 80°C curing temperature combined with the required 95% confidence interval indicate that, although the average bond strength at -30°C was higher than that tested at room temperature, the difference was not statistically significant. The compressive strength increase can also be conclusively linked to the decrease in compressive temperature.

Table 4-4: 12 mm Schöck – Combar T-test results comparing bond strength as well as concrete compressive strength tested at 23° and -30°C across multiple curing temperatures

Curing Temperature	Bond Strength		Compressive Strength	
	P Value	Statistically Significant?	P Value	Statistically Significant?
23°C	0.04%	Yes	0.01%	Yes
60°C	0.01%	Yes	0.02%	Yes
70°C	0.61%	Yes	0.21%	Yes
80°C	7.26%	No	0.01%	Yes

The 16 mm specimens presented issues, because the shaved regions, where the bars were gripped, were not a consistent diameter. This led to only two and one successful bond test for the 70°C curing temperature tested at -30°C and 23°C respectively. The average bond stress data, as well as average compressive strength data are presented in Figure 4-12 with error bars indicating the maximum and minimum recorded bond strengths.

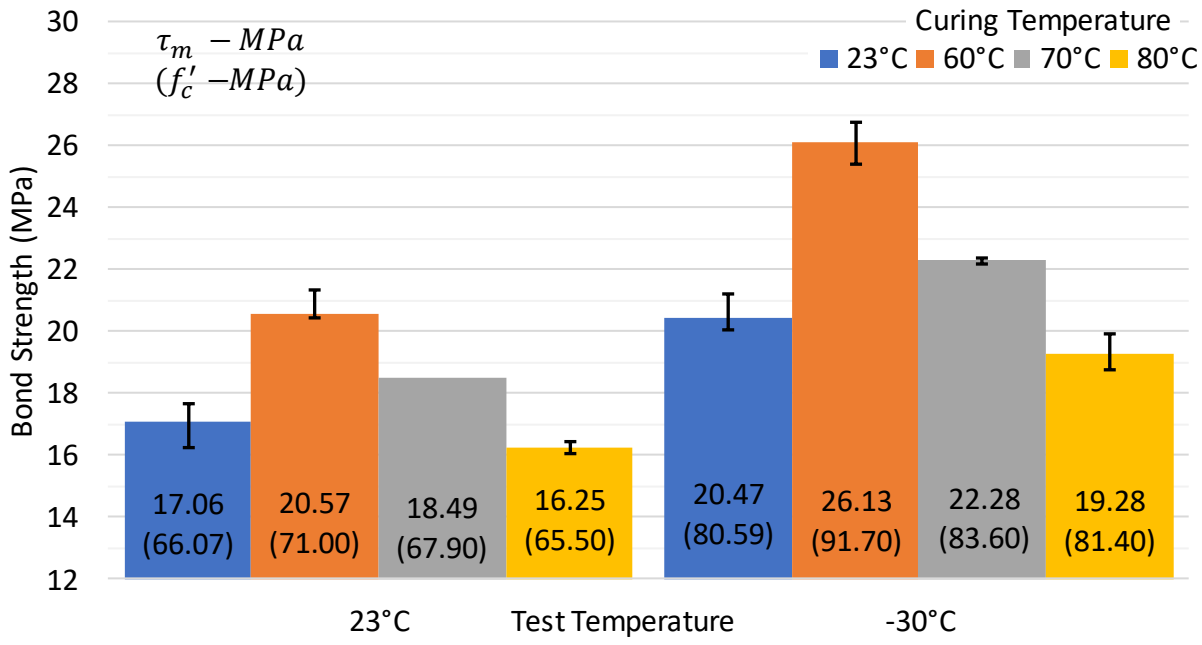

Figure 4-12: Bond strength and compressive strength (number in parentheses) for 16 mm Schöck – Combar pullout specimens cured at 23°C, 60°C, 70°C or 80°C and tested at 23°C and -30°C.

Similar to the 12 mm rebar results, both the bond strength and compressive strength of the 16 mm bars appear to increase significantly with the decreasing test temperature. The data also appear to be less consistant, as there are not continual increases in the bond strength with curing

temperature as was observed in the 12 mm data. Unfortunately, the significance of this could not be tested as each curing temperature represents a different concrete cast.

T-tests were again conducted for the 16 mm bars to determine the significance of the bond and compressive strength results, Table 4-5. Where there were enough successful tests completed, the t-test indicated that both the bond and compressive strength increased with decreasing temperature.

Table 4-5: 16 mm Schöck – Combar T-test results comparing bond strength as well as concrete compressive strength tested at 23° and -30°C across multiple curing temperatures

Curing Temperature	**Bond Strength**		**Compressive Strength**	
	P Value	Statistically Significant?	P Value	Statistically Significant?
23°C	0.02%	Yes	0.02%	Yes
60°C	0.05%	Yes	0.01%	Yes
70°C	NA	NA	0.33%	Yes
80°C	0.00%	Yes	0.01%	Yes

The average, standard deviation, and change in bond strength for the Schöck – Combar reinforcing bars are presented in Table 4-6 to complete the statistical picture. Note that, due to the different concrete casts conducted for each pullout condition, no trend in either compressive or bond strength data, can be compared across different temperatures.

Table 4-6: Average, standard deviation (σ), and change (∆) in bond strength for Schöck – Combar a reinforcing bars.

Curing Temp (°C)	Bond Strength (MPa) - Schöck - Combar GFRP									
	12 mm					16 mm				
	23°C		-30°C			23°C		-30°C		
	Avg	σ	Avg	σ	Δ	Avg	σ	Avg	σ	Δ
23°C	17.46	0.35	20.96	0.29	1.20	17.06	0.65	20.47	0.54	1.20
60°C	16.81	0.67	21.66	0.59	1.29	20.57	0.13	26.13	0.67	1.27
70°C	19.60	0.73	21.91	0.23	1.12	18.49	0.55	22.28	0.14	1.21
80°C	21.07	0.38	23.59	1.56	1.12	16.25	0.22	19.28	0.50	1.19

The Pultrall bars were cast and tested following the same procedure as the Schöck – Combar, with data presented in Figure 4-13 and Figure 4-14. The bond data present the same trend as the Schöck – Combar data, with the bond strength and compressive strength increasing with decreasing test temperature. Note that the bond strength of the Pultrall bars is up to 1.8 times larger than that of the Schöck – Combar. Again, to statistically confirm the visual trends, a t-test was performed which confirms this assumption, Table 4-7 Table 4-8. Again, the larger bars, #5, presented issues with slippage in the grip of the machine, which is why no statistical significance

is shown for the bond strength of specimens cured at 23°C and 60°C. Table 4-9 present the average, standard deviation, and change in bond strength for Pultrall bars.

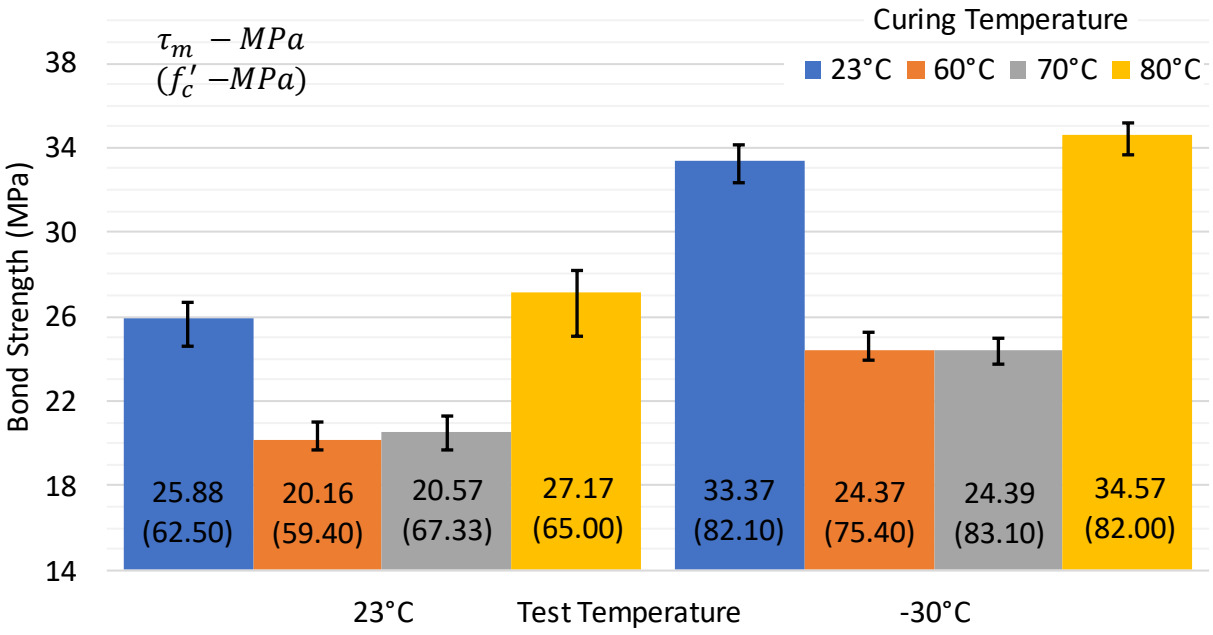

Figure 4-13: Bond strength and compressive strength (number in parentheses) for #4 Pultrall pullout specimens cured at 23°C, 60°C, 70°C or 80°C and tested at 23°C and -30°C.

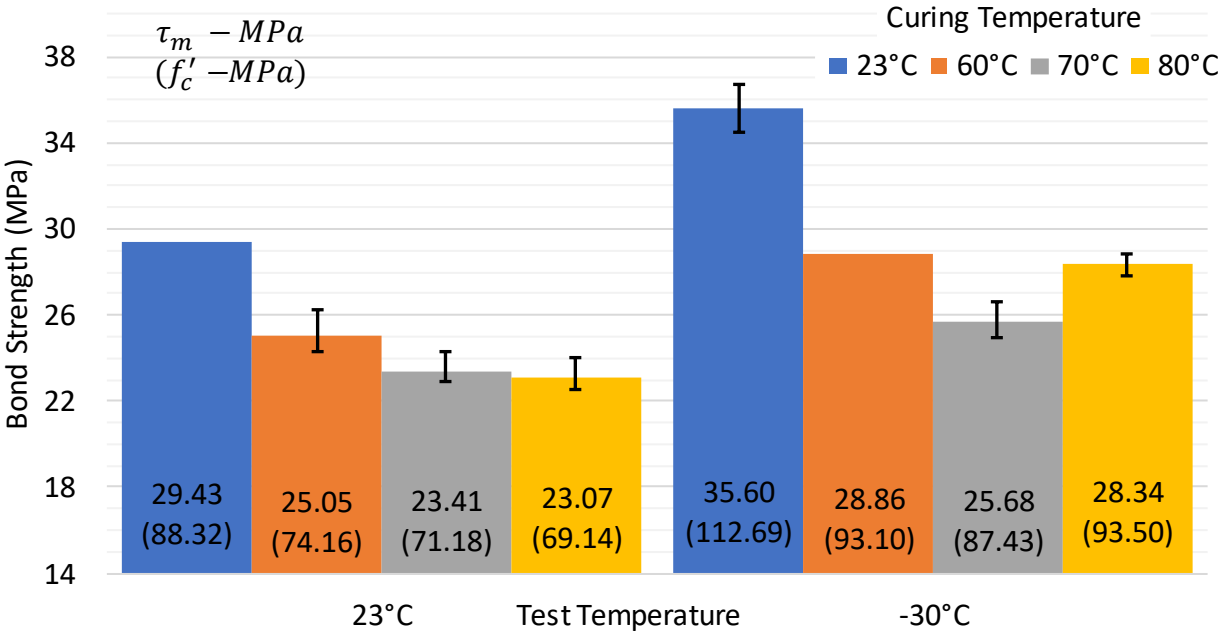

Figure 4-14: Bond strength and compressive strength (number in parentheses) for #5 Pultrall pullout specimens cured at 23°C, 60°C, 70°C or 80°C and tested at 23°C and -30°C.

Table 4-7: #4 Pultrall T-test results comparing bond strength as well as concrete compressive strength tested at 23° and -30°C across multiple curing temperatures

Curing Temperature	**Bond Strength**		**Compressive Strength**	
	P Value	Statistically Significant?	P Value	Statistically Significant?
23°C	0.01%	Yes	0.24%	Yes
60°C	0.01%	Yes	0.11%	Yes
70°C	0.02%	Yes	0.01%	Yes
80°C	0.01%	Yes	0.07%	Yes

Table 4-8: #5 Pultrall T-test results comparing bond strength as well as concrete compressive strength tested at 23° and -30°C across multiple curing temperatures

Curing Temperature	**Bond Strength**		**Compressive Strength**	
	P Value	Statistically Significant?	P Value	Statistically Significant?
23°C	NA	NA	0.00%	Yes
60°C	NA	NA	0.00%	Yes
70°C	0.38%	Yes	0.01%	Yes
80°C	0.01%	Yes	0.00%	Yes

Table 4-9: Average, standard deviation (σ), and change (Δ) in bond strength for Pultrall reinforcing bars.

Curing Temp (°C)	Bond Strength (MPa) – Pultrall GFRP									
	#4					#5				
	23°C		-30°C			23°C		-30°C		
	Avg	σ	Avg	σ	Δ	Avg	σ	Avg	σ	Δ
23°C	25.88	0.99	33.37	0.73	1.29	29.43	0.66	35.60	1.15	1.21
60°C	20.16	0.58	24.37	0.67	1.21	25.05	0.80	28.86	0.88	1.15
70°C	20.57	0.86	24.39	0.50	1.19	23.41	0.56	25.68	0.69	1.10
80°C	27.17	1.41	34.57	0.75	1.27	23.07	0.54	28.34	0.40	1.23

Due to the fact that it was impossible to make all the specimens from the same concrete batch, the compressive strength data do not appear to demonstrate any significant temperature related effects, nor does the concrete cured at 80°C appear to be experiencing any deleterious effects of delayed ettringite formation, although 28 days may not be long enough truly experience those affects.

Figure 4-11 to Figure 4-14 indicate that an increase in concrete compressive strength leads to an increase in bond strength. This trend was initially noted by Okelo and Yuan [89] when they

studied the bond strength of GFRP bars in normal strength concretes (ie $f'_c < 60$ MPa) which they modelled using Equation 21, in which τ is the average bond strength in MPa; f'_c is the specified concrete compressive strength in MPa; and d_b is the effective rebar diameter in millimeters. This equation assumes the average bond strength will be exceeded 75% of the time in the actual structure.

$$\tau = 14.7\frac{\sqrt{f_c'}}{d_b}\ (MPa) \qquad \text{Equation 21}$$

Although this model works well for lower strength concrete, it does not hold true when the compressive strength exceeds 60 MPa due to a change in the bond failure mechanisms that occur at this level. In the present work, it is observed that, as the concrete strength increases, the more likely bond failure is to occur by shearing of the mechanical bond of the GFRP (either sand or ribs) as opposed to concrete crushing noted at lower compressive strengths. When this occurred, the diameter of the bar, either 13 mm or 16 mm, had less effect than in previous studies. This trend was also noted more recently by Lee et al. [90] which they modelled using Equation 22, whereby: $\tau_{b,}$ is the bond strength, α is a coefficient related to the material bonding to the concrete (4.1 for steel or 3.3 for GFRP), and β is a coefficient related to f'_c which again changes based on the use of GFRP or steel. They demonstrated that β could conservatively be assumed as 0.5 for steel, and 0.3 for GFRP.

$$\tau_{b,max} = \alpha(f_c')^{\beta} \qquad \text{Equation 22}$$

When the experimental data presented here were modelled, the results indicated that the coefficient β varied both by manufacturer and test temperature, see Figure 4-15 to Figure 4-18. Upon further refinement, the β coefficient appears to increase for bars from each supplier when frozen, likely due to the cold temperature effects on the vinyl ester resin. Although the data approximately follows similar trends to the equation proposed by Lee et al. [90], the β values proposed seem ultra-conservative. In the present study, all bond strength values fall above the 0.35β value, whereas the bond strength values by Lee et al. appear to follow the average β value of 0.30, with a large number falling below the predicted value.

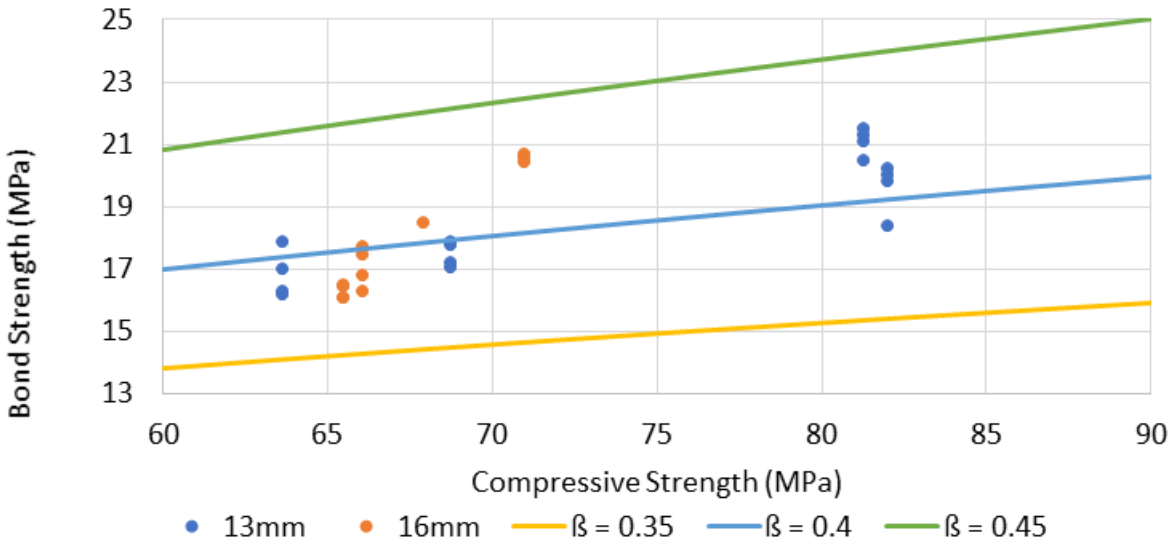

Figure 4-15: Average bond strength vs average compressive strength of Schöck – Combar reinforcing bars tested at 23°C vs those predicted by Equation 22 with different beta coefficients.

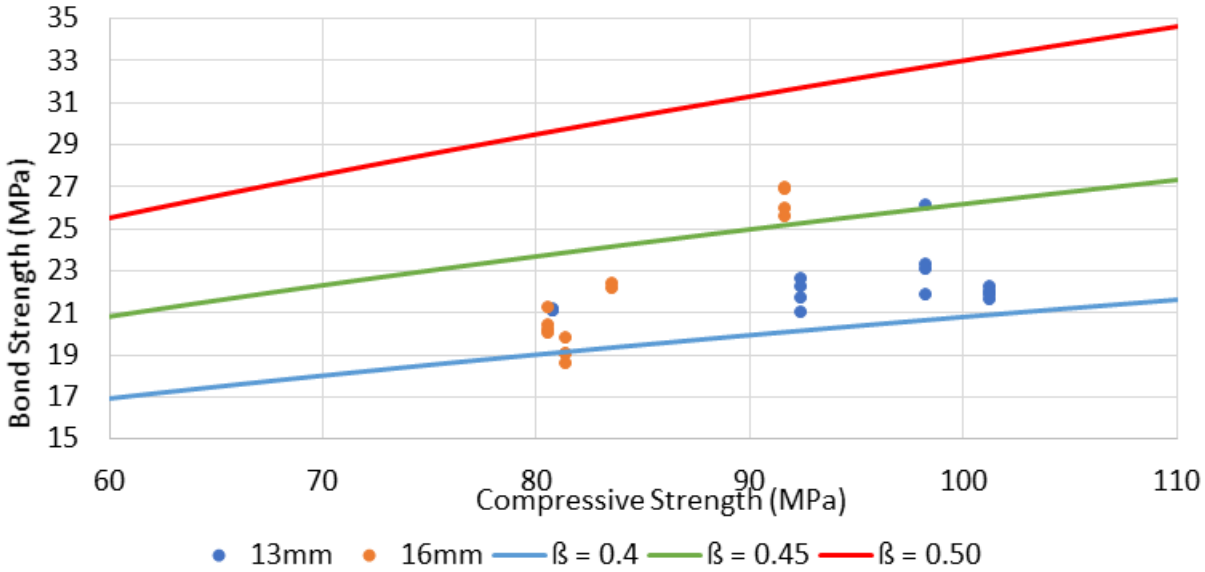

Figure 4-16: Average bond strength vs average compressive strength of Schöck – Combar reinforcing bars tested at -30°C vs those predicted by Equation 22 with different beta coefficients.

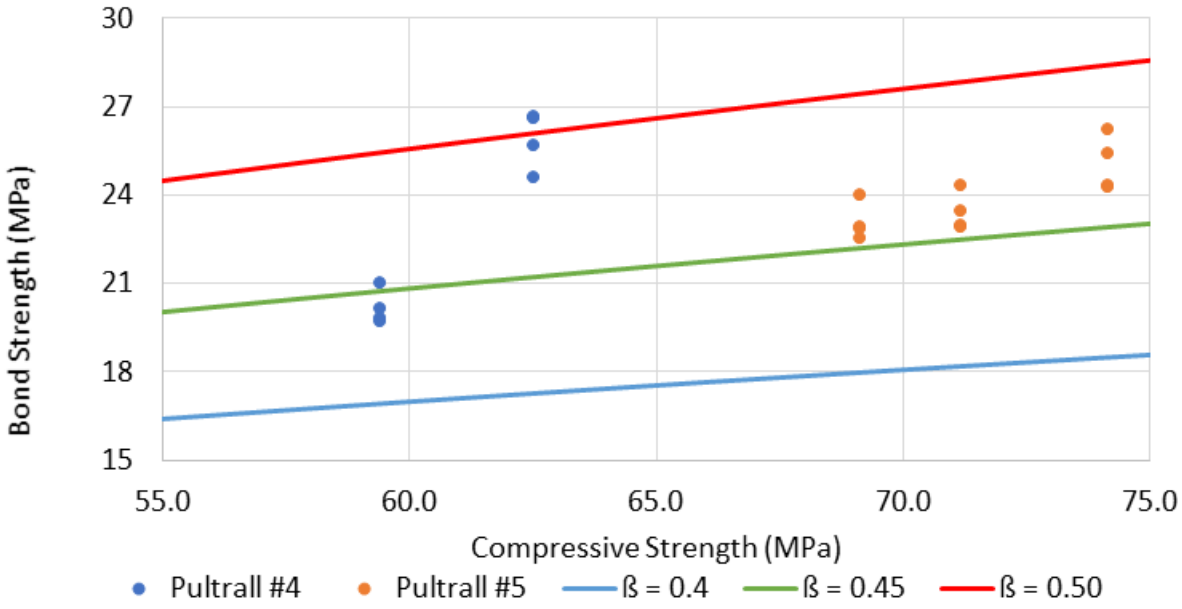

Figure 4-17: Average bond strength vs average compressive strength of Pultrall reinforcing bars tested at 23°C vs those predicted by Equation 22 with different beta coefficients.

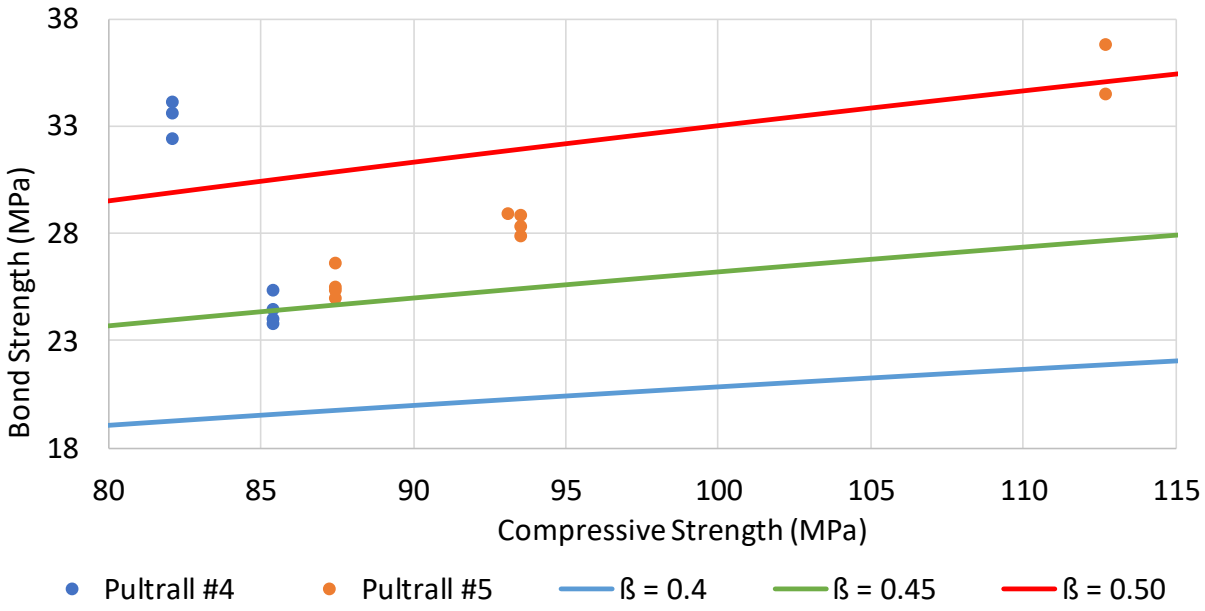

Figure 4-18: Average bond strength vs average compressive strength of Pultrall reinforcing bars tested at -30°C vs those predicted by Equation 22 with different beta coefficients.

Although it has previously been mentioned [89] that once the concrete exceeds 60 MPa, the bond failure mechanism changes from concrete crushing to mechanical bond failure between the glass fibres and the resin matrix, there are inconsistencies between both the extent of the bond failure

as well as the bond failure characteristics between the bar types. This is attributed to the slump of the concrete mix as well as how long the specimens were vibrated, as both variables affect the amount of bleed water that builds up on the underside of the GFRP bar, reducing concrete compressive sterength in that region. Figure 4-19 demonstrates that for the ribbed, Schöck – Combar bars, the percentage of ribs that shear off increases with concrete compressive strength, suggesting that the shear capacity of the vinyl ester resin is the likely cause of failure. By comparison, Figure 4-20 demonstrates less consistency between the concrete compressive strength and the percentage of sheared off Pultrall coating. This is possibly due to the actual stress that the resin experiences in the different loading cases. The Schöck – Combar bars have ribs that cover approximately 60% of the surface whereas the sand coating covers 100% of the surface area in the Pultrall bars. Mathematically, Equation 23 to Equation 26, this means that the vinyl ester at the base of the rib's experiences shear forces approximately 1.67 times larger than those of the sand coated bars and that any defects in this resin are, thus, also increasingly pertinent to the bond strength of the interface.

$$\tau_{\text{Schöck}} = \frac{force}{A_1} \quad \text{Equation 23}$$

$$\tau_{\text{Pultrall}} = \frac{force}{A_2} \quad \text{Equation 24}$$

$$A_1 = A_2 \cdot 60\% \quad \text{Equation 25}$$

$$\frac{\tau_{\text{Schöck}}}{\tau_{\text{Pultrall}}} = 1.66 \quad \text{Equation 26}$$

The other aspect considered is the effect of temperature on the strength of GFRP bars, both in shear and flexure. Numerous researchers have demonstrated that elevated temperatures tend to reduce strength as the temperatures begin to approach the glass transition temperature [91, 92]. Similarly, under freeze thaw conditions, researchers notice that tensile, interlaminar shear, and bond all decrease with increased thermal cycling [93]. This is likely due to internal microcracking between both the resin and the glass fibre as well as between the GFRP bars and the concrete interface. Contrarily, at sustained low temperatures, researchers have noted that flexural, tensile and shear strengths slightly increase which is often related to matrix hardening [94, 95].

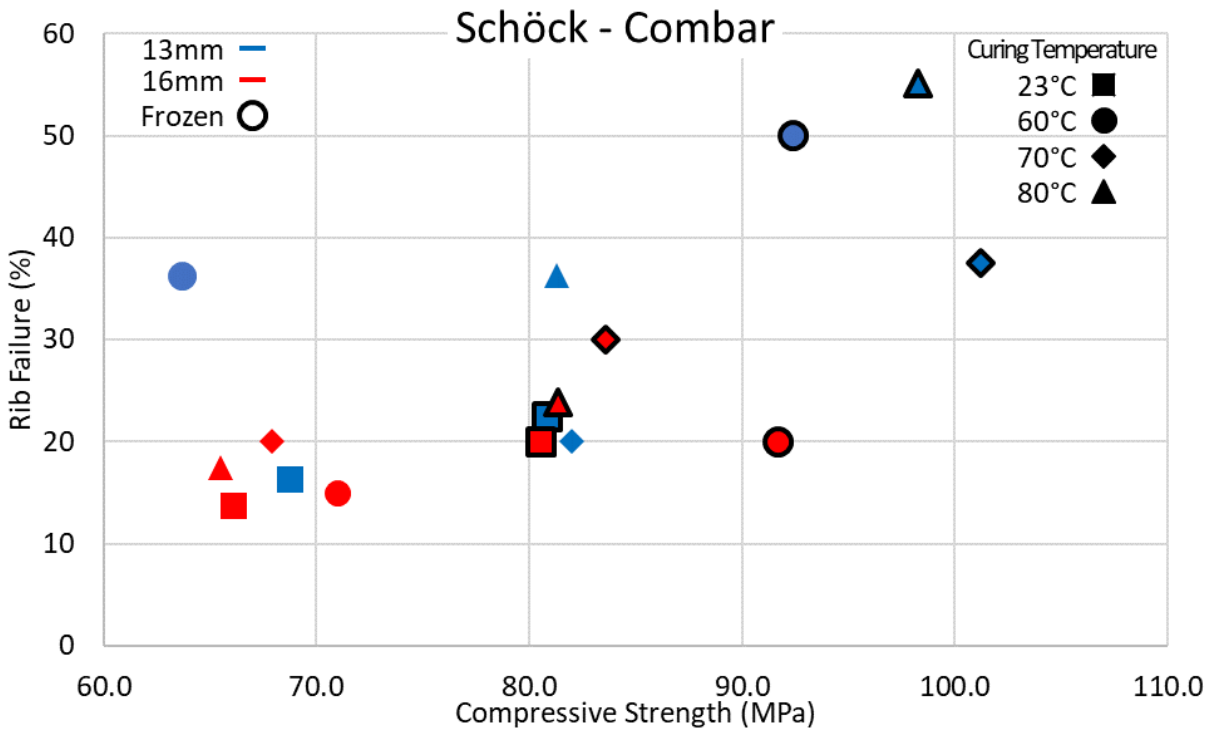

Figure 4-19: Rib shear failure vs concrete compressive strength for pullout test specimens containing Schöck – Combar rebar

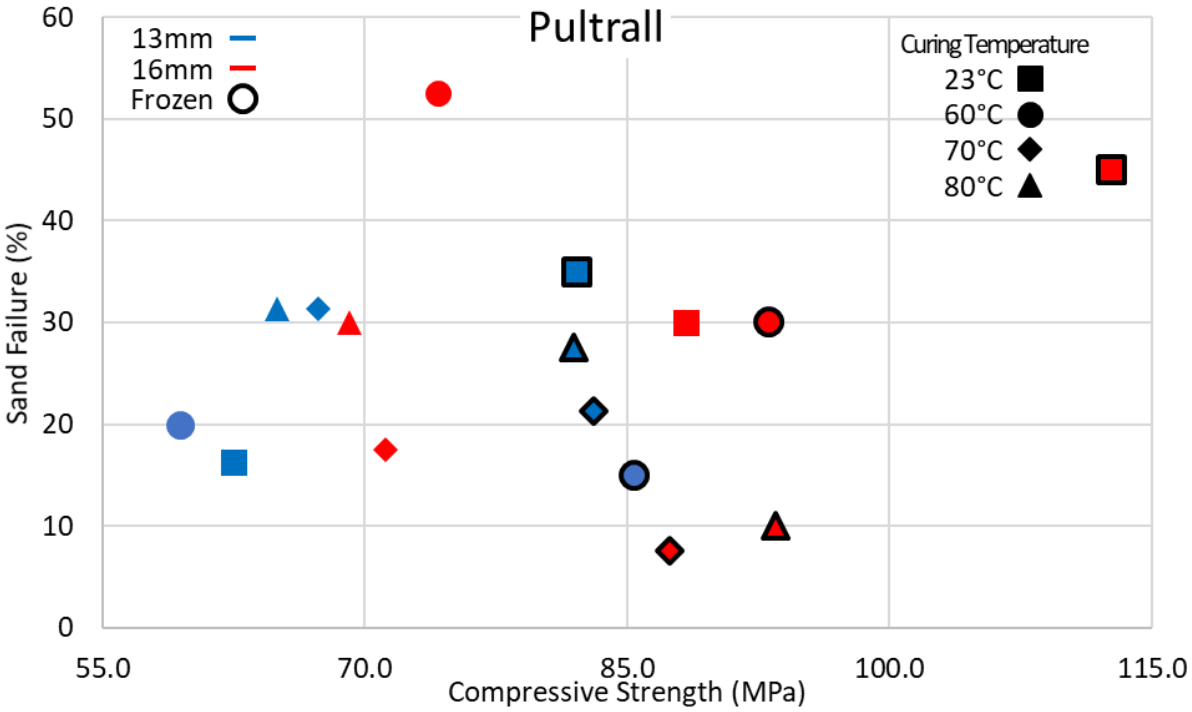

Figure 4-20: Rib shear failure vs concrete compressive strength for pullout test specimens containing Pultrall rebar

It should be noted in nearly all cases the failure mechanism was a combination failure with both rebar surface failing and concrete shearing off. Ideally for code purposes, failure of the concrete is preferable as it is a less brittle failure mechanism. This speaks to the current design codes reluctance to account for compressive strengths higher than 25 MPa. This follows work by Lee et al.[90] which described the bond failure of 36 specimens with concrete compressive strengths ranging between 25 MPa and 93 MPa. They stated that when the bond strength exceeds 25 MPa nearly all of their specimens had complete failure of the bond between the fibre and the mechanical bond layer. This is contrary to the results of the current study as the average sand or rib failure never exceeded 60%, even as the bond stress reached 35 MPa, which could be accounted for by utilizing a higher shear strength resin.

4.1.4. Temperature effects on the compressive strength of concrete

The increase in concrete strength of frozen samples, especially to such a large extent, was not anticipated. Most previous literature studies investigated concrete frozen in the early days of hydration, which limits the rate of chemical reaction and, thus, the amount of C-S-H (calcium silicate hydrate) that forms ultimately resulting in a decrease in strength. Mironov et al. [96] equate this to the fact that, as concrete hydrates, the large macropores transform into micropores. The macropores are much more susceptible to freezing and the frozen water causes more damage if the water does not have a connected pore system for stress relief. Early age strength gain achieved through heat and HE cement promotes a more porous microstructure than concrete mixtures containing regular cement and cured at ambient conditions [97], and can affect the temperature at which internal water freezes. De Fontenay and Sellevold [98] demonstrated that the solution in micropores requires a much lower temperature to freeze than that in macropores due to surface tension of the water. Later, Bager and Sellevold compared the temperatures at which water froze in ambient cured and steam cured high performance mixes. They found that at -20°C, the less porous, ambient cured mix had nearly no frozen water, whereas nearly 60% of the evaporable water of the more porous, steam cured mix had frozen [99]. Logically, they showed that the amount of evaporable water varied based on the w/cm ratio of the mix, but interestingly enough, approximately 10% of the evaporable water never froze even at -55°C.

The compressive test results of the concrete cylinders with the 0.30 w/cm ratio indicate that there is significant early age strength gain at day 2, between 54-75% of the 56-day strength. The use of slag slightly retards early strength gain, since slag reacts more slowly with calcium hydroxide. These strength gains then occur between day 2 and day 7 achieving 85-98% of 56-day strength. The average as well as the maximum and minimum of the five replicates are displayed in Figure 4-21. Note Table 4-10 describes the 4 different curing conditions and the acronyms used in the following figures.

Table 4-10: Curing condition acronyms

ECMC	elevated curing + moist conditioning
ACMC	ambient curing + moist conditioning
ECAC	elevated curing + ambient conditioning
ACAC	ambient curing + ambient conditioning

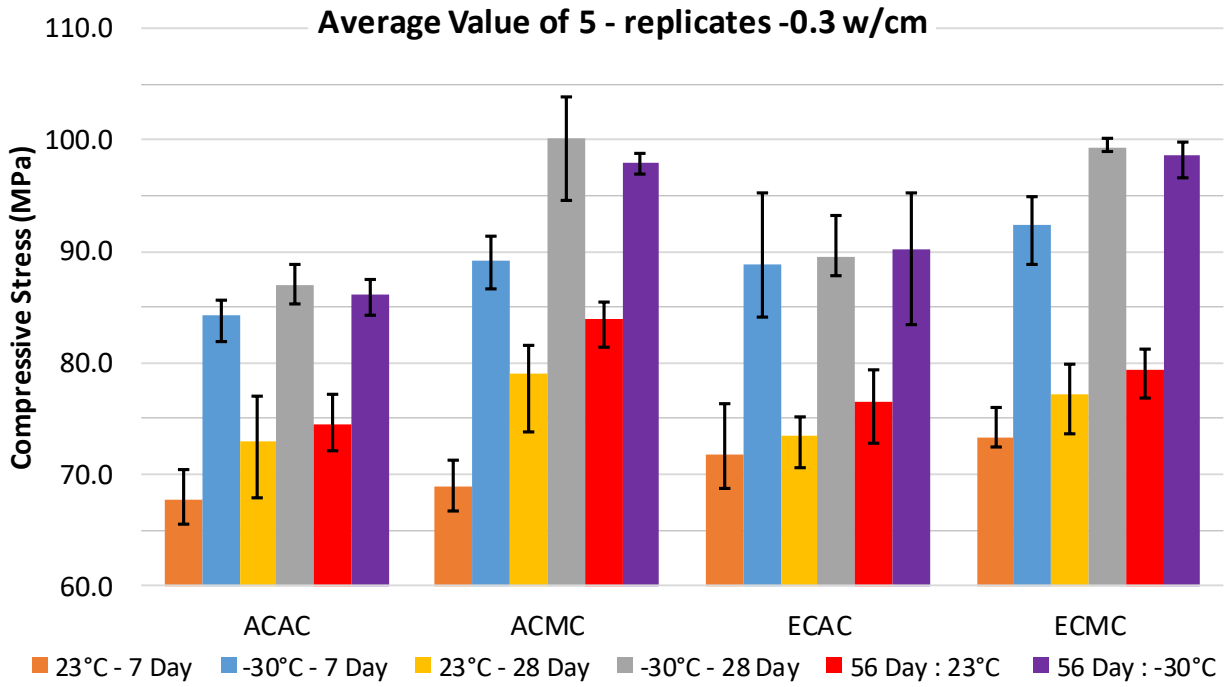

Figure 4-21: Average compressive strength vs curing time for concrete cylinders with a 0.3 w/cm cured at both 23°C and 70°C, conditioned, and then tested at both ambient lab condition and -30°C.

Similar to the bond testing, it is apparent that the compression strength increases with decreasing temperature. To statistically confirm the observation, ANOVA tests were conducted, as descried in Appendix E – Statistical testing. The three hypotheses for the test were as follows: A – The average concrete compressive strengths of concrete tested at 23°C and -30°C are the same, B – The average concrete compressive strengths of the concrete tested on day 7, 28, and 56 are the same, and C - test temperature and test day affect compressive strength independently. The results of the ANOVA tests comparing compressive strengths for different curing conditions are presented in Table 4-11.

Table 4-11: ANOVA test results for concrete with a w/cm ratio of 0.30

23°C vs -30°C	A	P-value	B	P-Value	C	P-Value
ACAC vs ACAC	Reject	0.00%	Reject	0.01%	Accept	5.58%
ACMC vs ACMC	Reject	0.00%	Reject	0.00%	Reject	0.33%
ECMC vs ECMC	Reject	0.00%	Reject	0.07%	Accept	52.73%
ECAC vs ECAC	Reject	0.00%	Reject	0.87%	Accept	16.59%

By rejecting hypothesis A and B the results indicate that compressive strength is affected by both the test temperature (A) and test day (B), which confirms the prior hypothesis. By accepting hypothesis C, it indicates that these two variables are acting independently.

In order to determine if free water had an effect on the compressive strength of concrete, specimens were also cast with the same concrete mix design but with a w/cm ratio of 0.45. The compressive strength result are given in Figure 4-22.

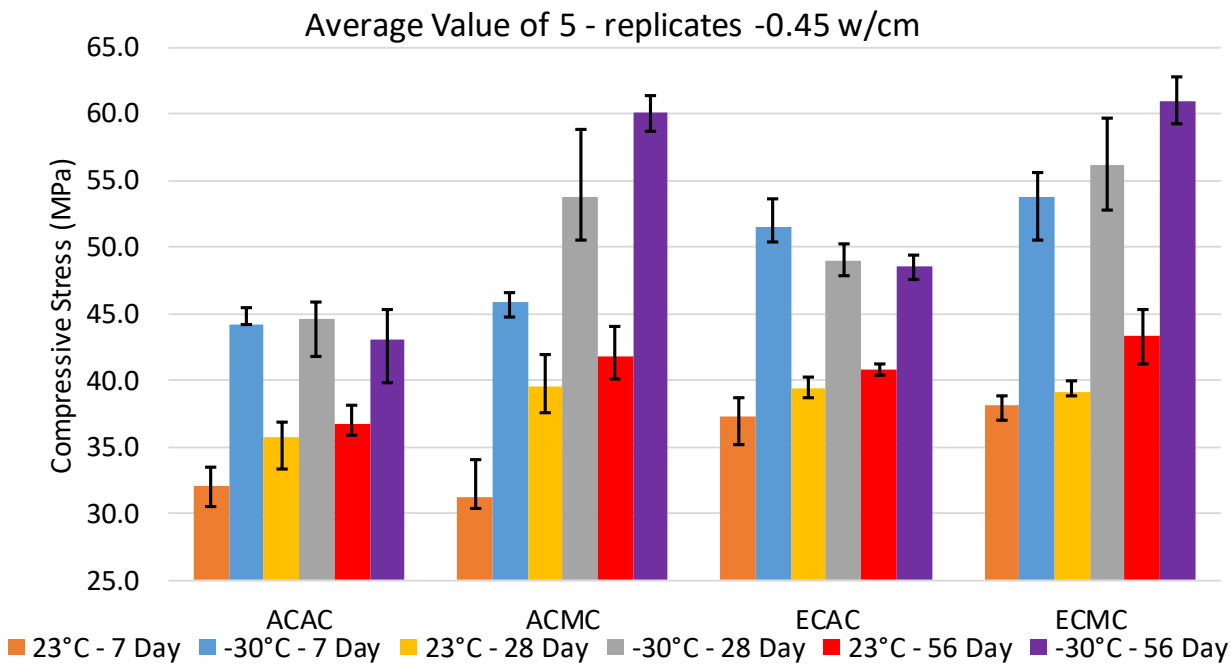

Figure 4-22: Average compressive strength vs curing time for concrete cylinders with a 0.45 w/cm, cured at both 70°C and 23°C, conditioned, and then tested at both ambient lab condition and -30°C.

The ANOVA test again indicated that the test temperature and test day affected the compressive strength results, Table 4-12. In contrast to the 0.30 w/cm mix, by rejecting hypothesis C the test indicates that temperature and time do not act independently, likely to the excess in free water.

Table 4-12: ANOVA test results for concrete compressive strength with a w/cm ratio of 0.45

23°C vs -30°C	A	P-value	B	P-Value	C	P-Value
ACAC vs ACAC	Reject	0.00%	Reject	1.21%	Reject	0.11%
ACMC vs ACMC	Reject	0.00%	Reject	0.00%	Reject	3.86%
ECMC vs ECMC	Reject	0.00%	Reject	0.02%	Reject	0.00%
ECAC vs ECAC	Reject	0.00%	Reject	0.00%	Reject	0.00%

The most apparent difference between the mixtures is the compressive strength. The strength of the 0.45 w/cm ratio mix was as low as 30 MPa at day 7 and as high as 61 MPa at day 56 whereas the strength of the 0.30 w/cm ratio mixture was much higher, ranging between 65 MPa at day 7 and 104 MPa at day 28. This occurred for two reasons. First, the 0.45 w/cm ratio is greater than the approximate 0.42 w/cm ratio, determined by Powers and Brownyard [100], required to fully hydrate cement. This means that there is extra water remaining in pores after hydration, causing a reduction in strength. Second, lower w/cm ratio mixtures increase particle packing by reducing void space, and using the surface tension of water moving to hydrate the cement particles to pull hydration products closer to one another.

These theories are evident when the evaporable water content of the two mixtures is compared, Figure 4-23 and

Figure 4-24. It can be seen that the average (of the 7, 28, and 56 day) evaporable water content of the 0.3 w/cm ratio mix is approximately 5.1%, whereas that of the 0.45 w/cm ratio mix is approximately 9.2%, and appears to be decreasing with time.

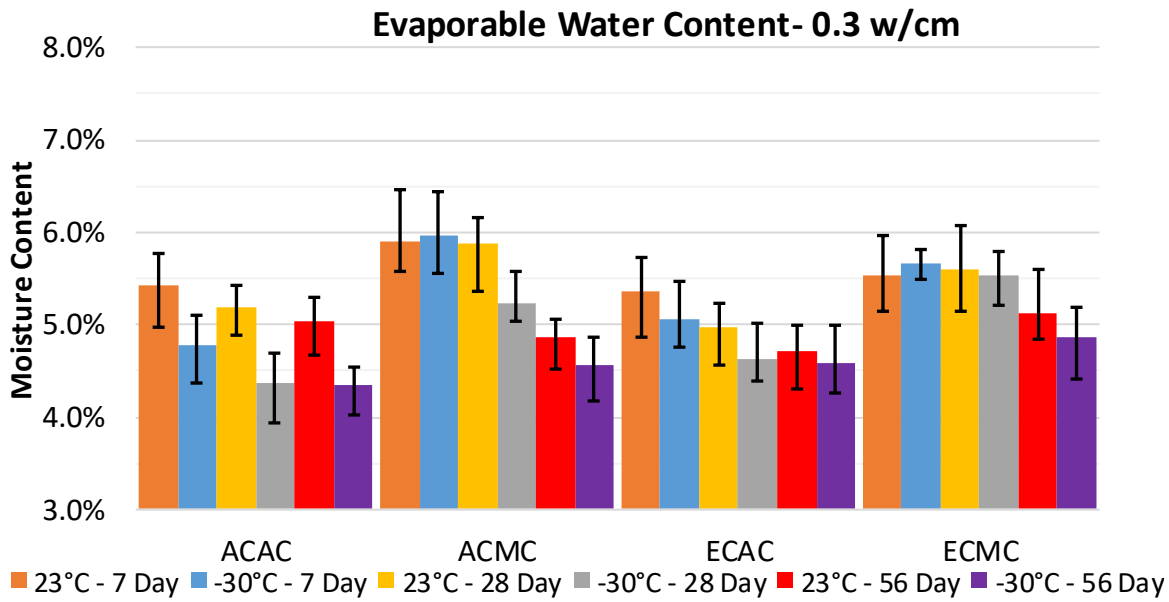

Figure 4-23: Moisture content for concrete cylinders with a 0.3 w/cm cured at both 23°C and 70°C, conditioned, and then tested at both ambient lab condition and -30°C.

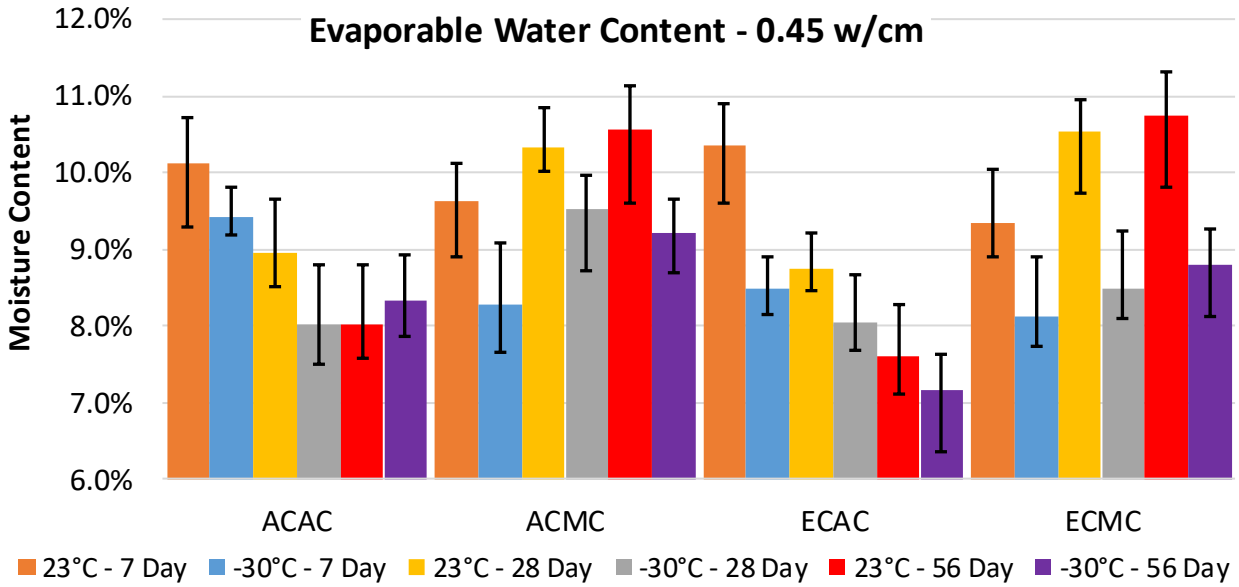

Figure 4-24: Moisture content for concrete cylinders (0.45 w/cm) cured at both 23°C and 70°C, conditioned, and then tested at both ambient lab condition and -30°C.

To statistically confirm the observation, ANOVA tests were conducted. The three hypotheses for the test were as follows: A – The average concrete free water content of concrete cured under different conditions are the same, B – The average concrete free water content of the concrete tested on day 7, 28, and 56 are the same, and C – The curing conditions and test day affect free water content independently. The results of the ANOVA tests comparing compressive strengths for different curing conditions for 0.30 w/cm ratio and 0.45 w/cm are presented in Table 4-13 and Table 4-14 respectively.

Table 4-13: ANOVA test results for concrete moisture content with a w/cm ratio of 0.30

Test at 23°C	A	P-value	B	P-Value	C	P-Value
ACAC vs ACMC	Accept	8.90%	Reject	1.52%	Accept	17.30%
ACAC vs ECAC	Accept	27.72%	Accept	8.03%	Accept	85.93%
ACAC vs ECMC	Accept	29.62%	Accept	20.30%	Accept	70.29%
ACMC vs ECAC	Reject	1.67%	Reject	0.96%	Accept	30.17%
ACMC vs ECMC	Accept	52.05%	Reject	1.57%	Accept	41.58%
ECMC vs ECAC	Accept	6.33%	Accept	11.71%	Accept	63.05%

Table 4-14: ANOVA test results for concrete moisture content with a w/cm ratio of 0.45

Test at 23°C	A	P-value	B	P-Value	C	P-Value
ACAC vs ACMC	Accept	12.19%	Accept	83.77%	Reject	2.62%
ACAC vs ECAC	Accept	8.28%	Reject	0.15%	Accept	51.73%
ACAC vs ECMC	Reject	3.29%	Accept	52.90%	Accept	7.98%
ACMC vs ECAC	Reject	0.31%	Accept	35.97%	Reject	0.34%
ACMC vs ECMC	Accept	43.36%	Accept	15.86%	Accept	84.27%
ECMC vs ECAC	Reject	0.09%	Accept	18.92%	Reject	1.14%

The results indicate that for the 0.30 w/cm ratio that the free water content did not statistically change based on conditioning state, although the ACMC vs ECAC indicated slight significance. Due to the wide range of moisture values taken, it cannot be conclusively stated that the moisture content was reduced over time. Due to the low water content, being less than the 0.42 mentioned earlier, it can be stated that curing conditions and test day affect free water content independently as the moist cured concrete has more water available.

The results are less conclusive for the 0.45 w/cm ratio. The results vary, although they appear to indicate that moisture content does not appear to change with time, verifying the assumption that there is sufficient water in the 0.45 w/cm ratio mix, and that moist curing has less of an affect. It should be noted that these results are short term tests and may not be indicative of the effect of freezing temperatures long term. Over a longer exposure time, the concrete would continue to hydrate, reacting un-hydrated cement and internal water, reducing the porosity. Although the concrete moisture content would fluctuate, based on the surrounding environment, the rate would be reduced due to this decreased porosity.

4.2. The effect of anti-icing brines on concrete properties

4.2.1. Effect of chloride brine exposure on concrete compressive strength

The results of the compression tests of cylinders exposed in the fog room or to NaCl, $MgCl_2$, $MgCl_2$ or multi-chloride brines versus the time of exposure are plotted in Figure 4-25. The compressive strengths of all the samples remained approximately the same over the first six months, at approximately 38 – 40 MPa. Subsequently, the data diverges, with, those cylinders exposed to water in the humidity chamber, increasing over the first 18 months to between 45 and 50 MPa over the next four years. The sodium chloride specimens appear to reach an equilibrium of between 40 and 42 MPa, demonstrating the least long-term detrimental effect of all the anti-icing brines, in agreement with the work of Darwin et al. [101]. The compressive strength of the remaining specimens, those exposed to: magnesium chloride, calcium chloride, or multi chloride

brines, follow a similar trend of deterioration. The multi chloride brine, containing mostly calcium chloride and sodium chloride, Table 3-6, decreases to approximately 35 MPa. Finally, the magnesium and calcium chloride both appear to continue to decrease, in agreement with the work of Collepardi [102]. The way the concrete cylinders failed was also indicative of the compressive strength of the concrete. The moist cured specimens had the highest compressive strength and failed in the most brittle manner, often seeing post peak load drops of 70% and failures which sheared some of the large aggregate. The concrete exposed to magnesium and calcium chloride failed in the least brittle manner, with very little post peak load loss. Instead of shearing the aggregate, the cement paste often failed allowing much of the exposed aggregate to be pulled out of the cement paste binder fully intact.

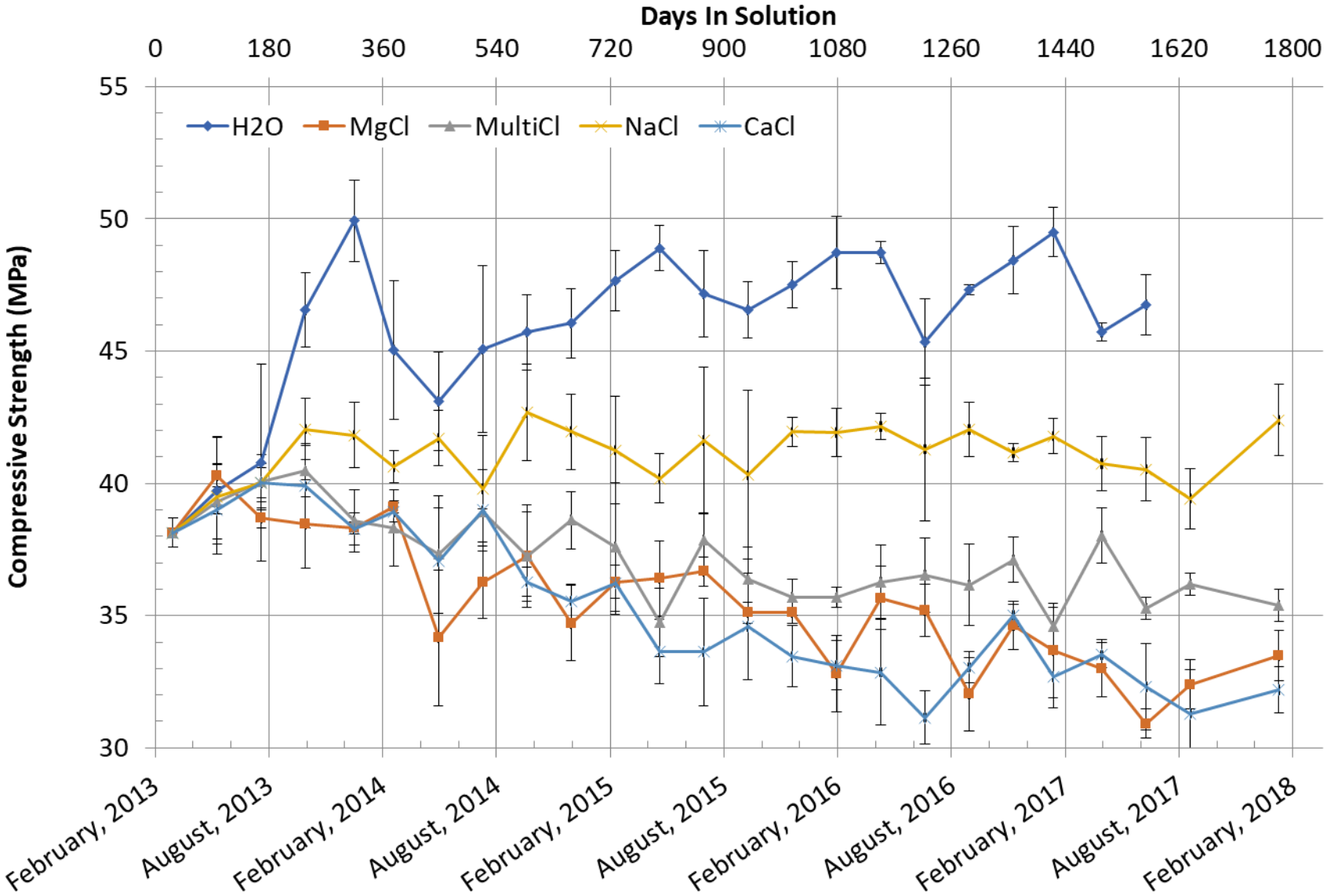

Figure 4-25: Average (of 3 specimens) compressive strength of concrete vs days in solution

The XRF analysis data of the concrete submerged in the different chloride brines, at depths of 12 mm (◊), 25 mm (O) and 38 mm (□) plotted on calibration curve discussed in section **Error! Reference source not found.**, is provided in Figure 4-26. It is evident from this figure that the calcium chloride diffused the farthest into the concrete, whereas the magnesium chloride and multi chloride brine diffused the least. This follows the aforementioned discussion whereby the reaction of magnesium chloride and calcium hydroxide form brucite, clogging the pore network and limiting the further ingress of chlorides. A similar observation is noted in the presence of silver nitrate, Figure 4-27. The colour boundary, i.e. the limit of the $AgNO_3$ precipitate, suggesting 0.15% chloride by weight of cement, also indicates that the chloride ingressed the farthest into the $CaCl_2$ sample, and the least into the $MgCl_2$ sample. It is of interest that although the chloride transport was lowest in the $MgCl_2$ brine, that it still had the lowest compressive strength over time.

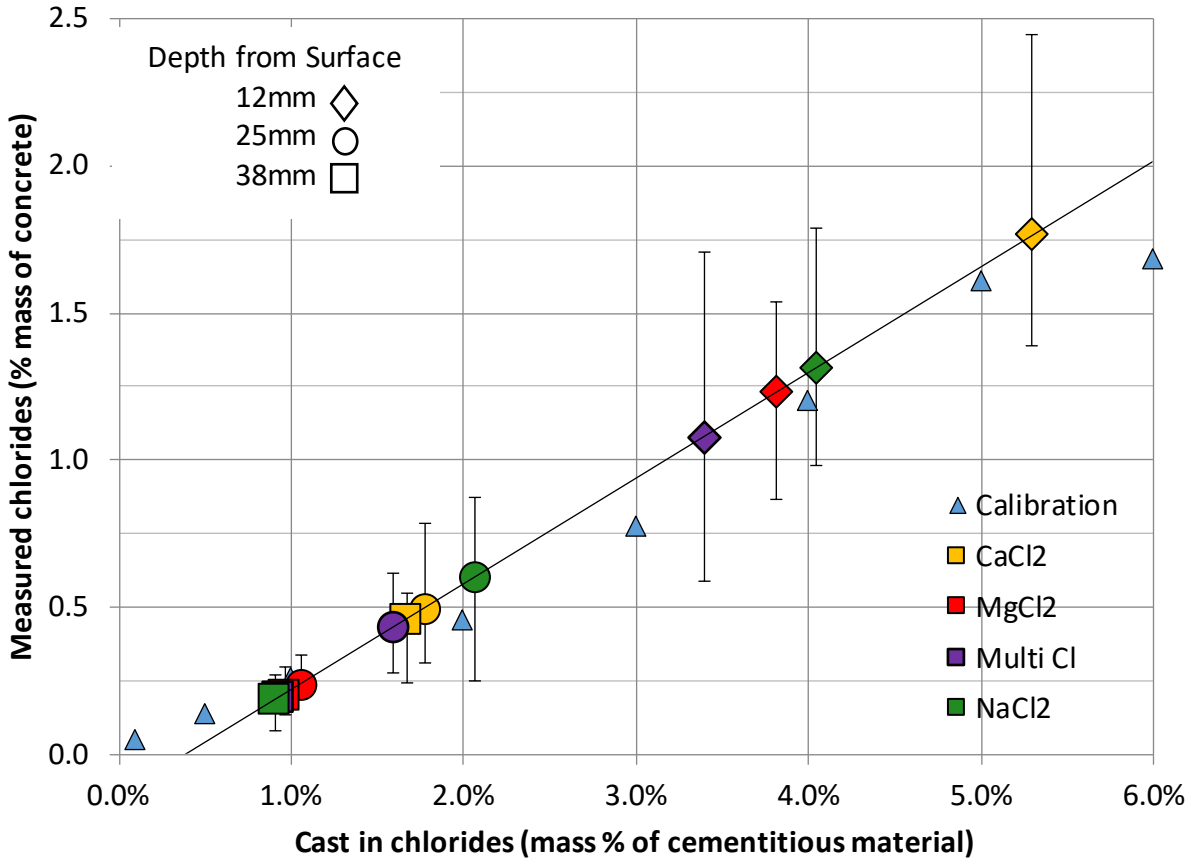

Figure 4-26: Average (of 8 XRF analysis) measured chloride content at depth of 12.7, 25.4, and 38.1 mm from the surface for concrete submerged in $CaCl_2$, $MgCl_2$, Multi Cl, or $NaCl_2$ for 2000 days.

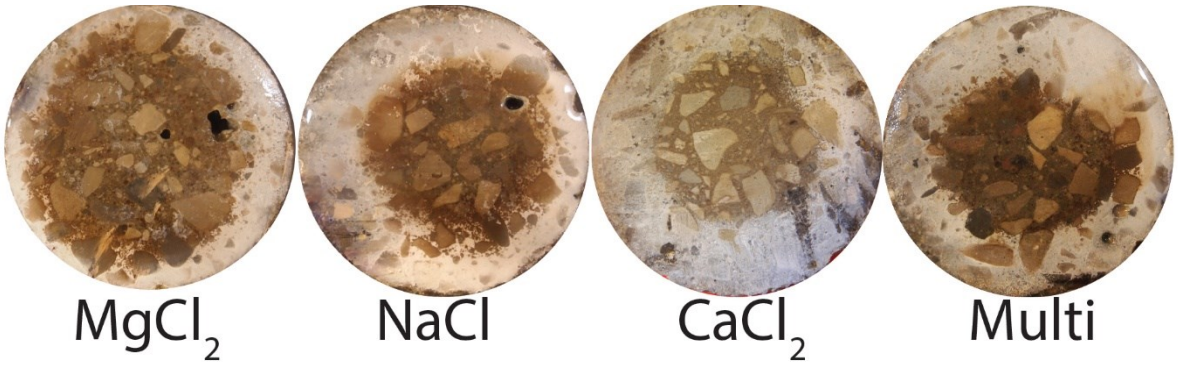

Figure 4-27: Cylinder cross section of concrete submerged in $CaCl_2$, $MgCl_2$, Multi Cl, or $NaCl_2$ for 2000 days, after being sprayed with a 0.1M $AgNO_3$ solution.

4.2.2. Pore solution composition of cement pastes with admixed chlorides

The results below summarize work done conducted with Ibrahim Ogunsanya on four different cement blends, with four w/cm ratios and four NaCl contents. This work has been accepted for publication, [103]

It was previously stated that synthetic pore solution was often used for rapid corrosion testing. The results of these accelerated tests obviously are dependent on the chemical composition of the synthetic pore solutions used. After the ion chromatography (IC) and inductively coupled plasma (ICP) tests were completed the major ions and cations were determined, Table 4-15 to Table 4-18.

Table 4-15: Major components of the pore solution expressed from general use (GU) cement paste, mmol/L

w/cm	Admixed Chloride	Cl	SO_4	S	Na	K	Ca	Al	Si	Fe	Mg
0.40	0.0	2	61	61	164	789	1.28	0.15	0.57	0.08	1.65
	2.5	2622	334	349	2036	946	0.63	0.19	0.78	0.01	1.65
	5.0	4827	572	657	4530	932	0.37	0.02	0.39	0.01	1.65
	7.5	4948	712	825	4859	821	0.64	0.01	0.23	0.01	1.65
0.45	0.0	2	33	33	167	752	0.81	0.20	0.40	0.13	0.06
	5.0	4425	405	423	4509	896	0.31	0.07	0.43	0.01	0.72
0.50	0.0	1	15	16	137	574	1.14	0.14	0.28	0.02	0.70
	2.5	2009	135	135	2434	744	0.83	0.04	0.55	0.08	0.70
	5.0	3934	279	291	3928	777	0.49	0.05	0.39	0.01	1.38
	7.5	5156	486	507	5255	711	0.42	0.03	0.30	0.20	1.38
0.55	0.0	1	12	11	129	530	1.34	0.16	0.26	0.09	0.73
	5.0	3417	180	188	3431	670	0.58	0.05	0.39	0.01	1.38

Table 4-16: Major components of the pore solution expressed from ordinary cement and blast furnace slag cement paste (GU-BFS), mmol/L

w/cm	Admixed Chloride	Cl	SO_4	S	Na	K	Ca	Al	Si	Fe	Mg
0.40	0.0	3	13	37	125	478	1.52	0.09	0.27	0.23	1.65
	2.5	2225	157	285	2157	649	0.83	0.03	0.38	0.11	1.65
	5.0	4851	417	566	4048	683	0.45	0.01	0.41	0.07	1.65
	7.5	5309	622	712	4822	638	0.73	0.01	0.22	0.08	1.11
0.45	0.0	2	10	25	126	477	0.46	0.18	0.32	0.17	0.69
	5.0	3728	235	350	3787	593	0.59	0.03	0.29	0.09	0.69
0.50	0.0	2	5	13	111	403	1.68	0.08	0.18	0.09	0.02
	2.5	1830	120	211	1935	549	0.22	0.23	1.37	0.31	0.03
	5.0	3453	252	432	3587	543	0.74	0.02	0.28	0.32	1.85
	7.5	5132	353	555	5162	519	0.49	0.03	0.27	0.06	0.73
0.55	0.0	1	4	11	100	358	0.98	0.10	0.17	0.05	0.71
	5.0	3065	159	299	3180	489	0.72	0.02	0.30	0.02	1.37

Table 4-17: Major components of the pore solution expressed from ordinary cement and fly ash cement paste (GU-FA), mmol/L

w/cm	Admixed Chloride	Cl	SO_4	S	Na	K	Ca	Al	Si	Fe	Mg
0.40	0.0	2	22	24	185	585	1.08	0.28	0.44	0.16	1.65
	2.5	2153	247	273	2247	715	0.69	0.06	0.75	0.02	1.65
	5.0	4716	554	584	4219	767	0.39	0.03	0.58	0.02	1.65
	7.5	5163	798	785	4811	692	0.58	0.03	0.29	0.03	1.65
0.45	0.0	1	12	13	179	564	1.22	0.34	0.45	0.16	0.70
	5.0	3872	415	412	3955	654	1.29	0.12	0.51	0.07	0.69
0.50	0.0	1	6	6	165	485	1.27	0.22	0.29	0.02	0.02
	2.5	1608	119	120	1685	516	1.18	0.12	0.51	0.35	0.02
	5.0	3388	293	290	3473	580	1.06	0.12	0.55	0.09	1.66
	7.5	4752	514	539	5152	551	1.68	0.04	0.25	0.03	0.90
0.55	0.0	1	3	4	141	415	0.95	0.21	0.25	0.08	0.75
	5.0	3044	226	230	3098	514	1.03	0.08	0.44	0.14	0.69

Table 4-18: Major components of the pore solution expressed from ordinary cement and silica fume cement paste (GU-SF), mmol/L

w/cm	Admixed Chloride	Cl	SO_4	S	Na	K	Ca	Al	Si	Fe	Mg
0.40	0.0	4	38	41	94	341	1.00	0.17	0.46	7.03	1.65
	2.5	2742	262	263	2135	709	2.45	0.05	0.22	2.75	1.65
	5.0	5018	501	512	4024	758	2.38	0.01	0.14	0.49	1.65
	7.5	5772	545	554	4411	690	1.93	0.01	0.11	0.26	1.65
0.45	0.0	3	20	19	86	316	0.06	0.24	0.51	1.47	0.71
	5.0	3953	391	425	4079	675	2.21	0.02	0.27	0.07	0.69
0.50	0.0	3	9	10	75	268	1.08	0.17	0.34	0.80	0.70
	2.5	1687	108	113	1644	511	1.38	0.06	0.43	0.37	1.38
	5.0	3606	278	291	3439	583	1.93	0.03	0.30	0.08	0.71
	7.5	4815	464	485	4922	538	2.92	0.02	0.16	0.04	0.02
0.55	0.0	3	7	7	73	258	0.72	0.18	0.27	0.65	0.02
	5.0	3110	206	216	3041	520	1.79	0.04	0.30	0.13	0.01

As the pore solution was expressed in order to improve the accuracy of synthetic pore solution for rapid corrosion testing, the limitations of this work must be discussed. $NaCl_2$ was used rather than $CaCl_2$ or $MgCl_2$ for a number of reasons:

1. It is the major component of seawater
2. It is the most extensively used de-icing salt globally
3. It is the salt most commonly used in studies of rebar corrosion
4. It is the salt recommended for ASTM G109 and ASTM A955 tests [64, 104]
5. It has been found to bind less chlorides [43, 105]

Although Table 4-15 to Table 4-18 prove a large amount of information, the chloride and sulphate data appear to be the most interesting as they appear to be in correlation with each other. To demonstrate this, the chloride content (wt. %) of the expressed pore solution has been plotted as a function of admixed chloride for both 0.40 w/cm ratio and 0.50 w/cm ratio in Figure 4-28 and Figure 4-29. Similarly, the sulphate content (wt. %) of the solution has been plotted as a function of admixed chloride for both 0.40 w/cm ratio and 0.50 w/cm ratio in Figure 4-30 and Figure 4-31. Upon further investigation it can be seen from both Figure 4-29 and Figure 4-31 that both the sulphate and chloride increase linearly in pastes with w/cm ratios of 0.50. Figure 4-28 also indicates that in pastes with less free water (ie 0.40 w/cm ratios), the chloride content in the pore solution reaches a saturation limit. The variance, from ~17.5% for the GU paste to ~21% for the GU-SF paste, is attributed to the impact of pH on the saturation limit of chlorides in solutions. Vollpracht et al. [106] demonstrated that there is a reduction in pH of pore solutions with the addition of SCM's due to the consumption of calcium hydroxide during the pozzolanic reaction.

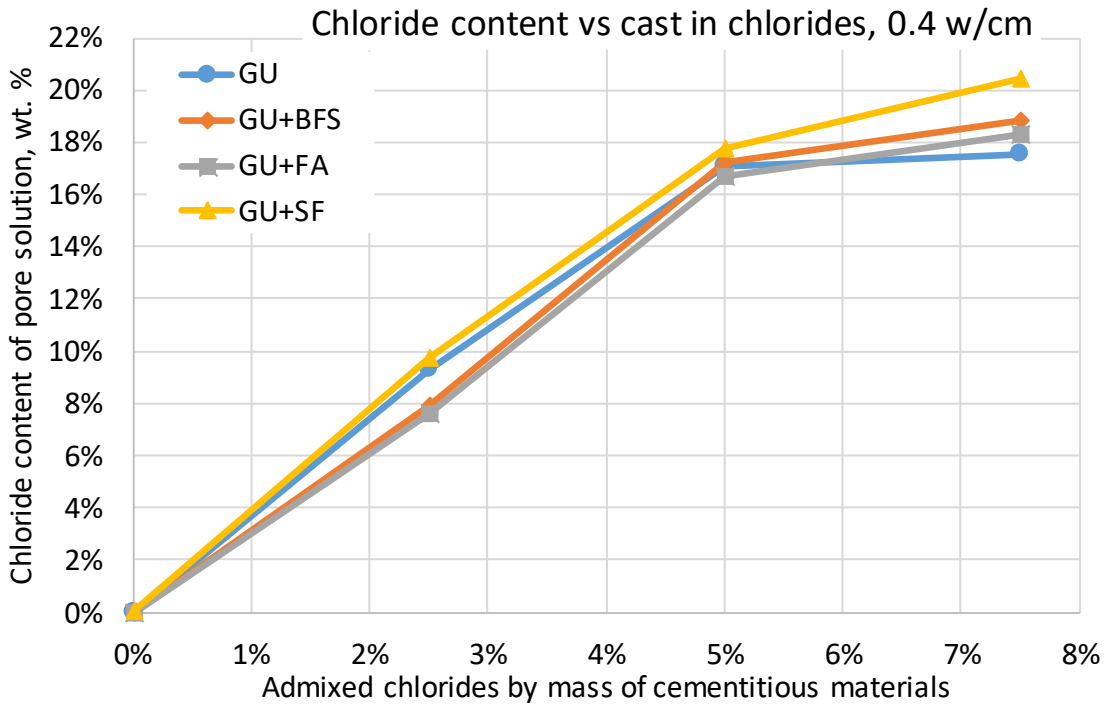

Figure 4-28: Chloride content (wt.%) of the expressed pore solution as a function of the admixed chloride content for mixes with a w/cm ratios of 0.40

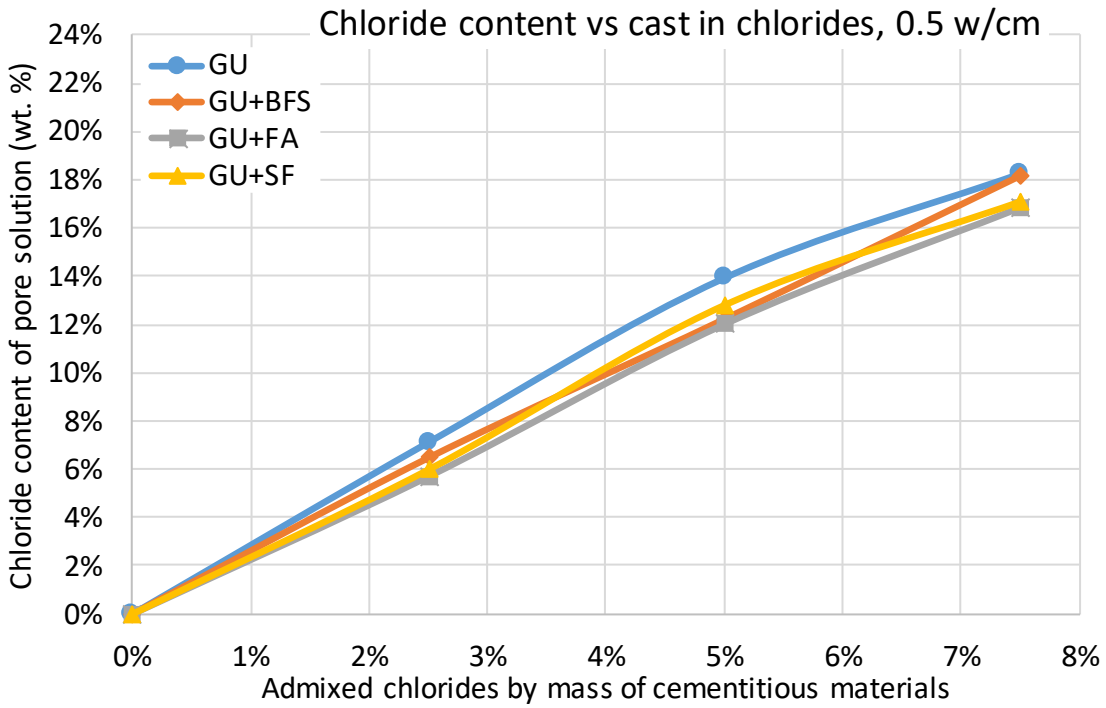

Figure 4-29: Chloride content (wt.%) of the expressed pore solution as a function of the admixed chloride content for mixes with a w/cm ratios of 0.50

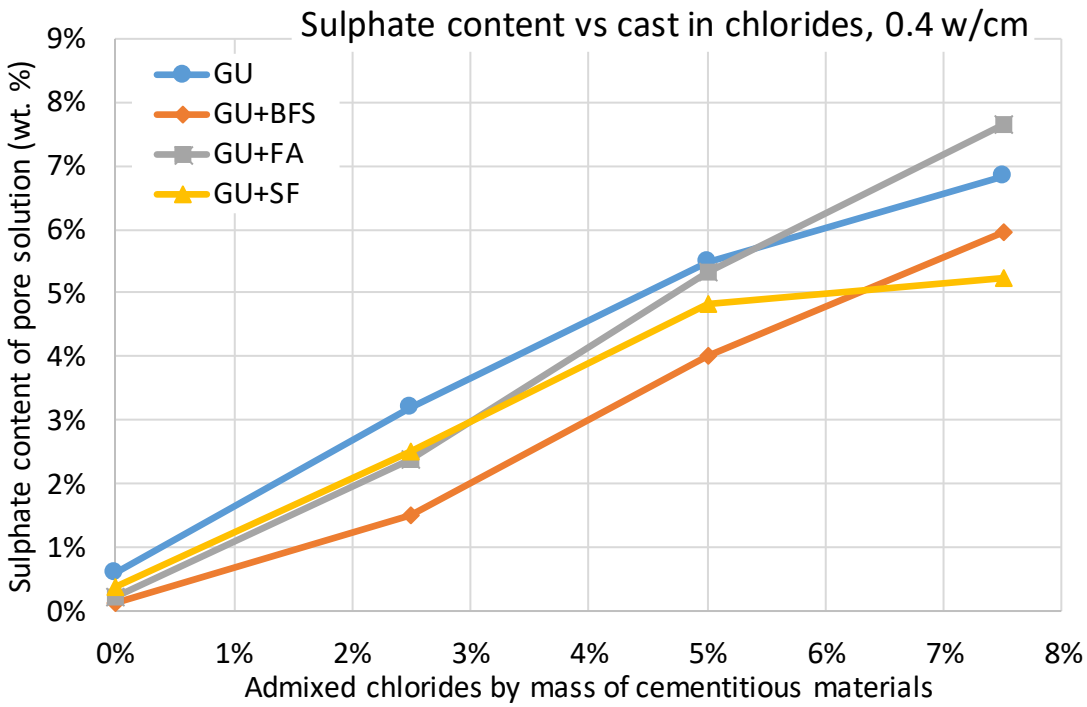

Figure 4-30: Sulphate content (wt.%) of the expressed pore solution as a function of the admixed chloride content for mixes with a w/cm ratios of 0.40

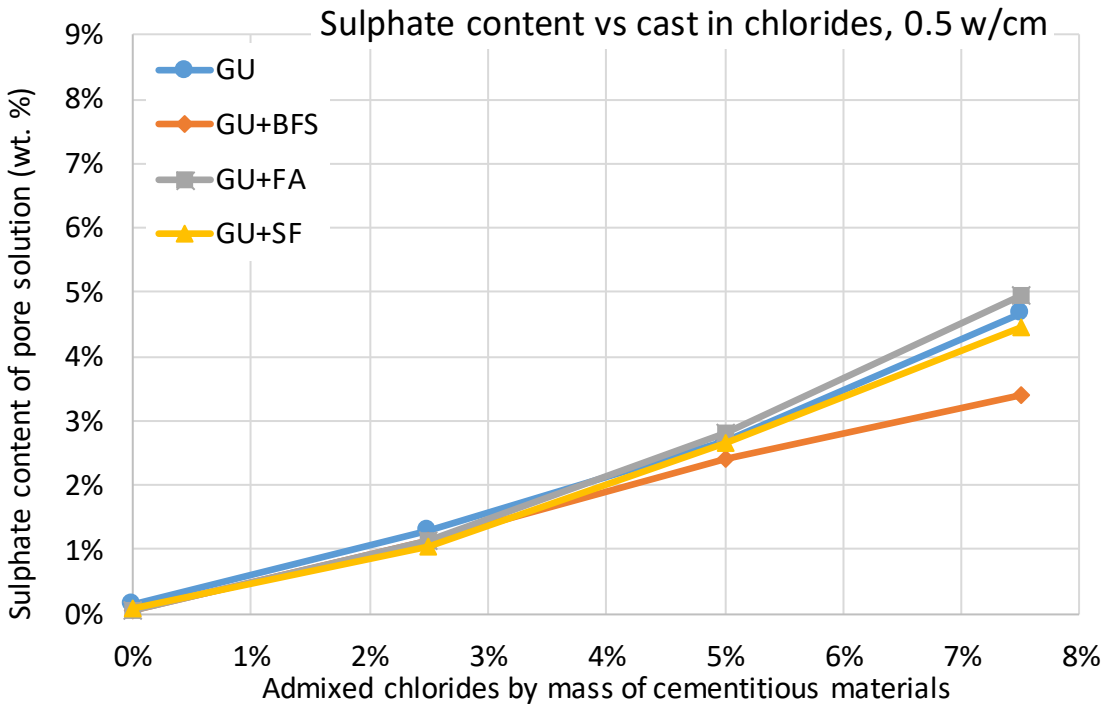

Figure 4-31: Sulphate content (wt.%) of the expressed pore solution as a function of the admixed chloride content for mixes with a w/cm ratios of 0.50

It is also possible that instead of reaching a saturation limit, that the chlorides are instead bound in the different cement phases, or in the form of Friedel's salt. For this to occur, sulphate anions, from the aluminate phases, may substitute chloride anions. Logically, as the GU-FA mix had the highest weight % of aluminates(See Table 3-7), as it had more sulphates available for this exchange, leading to a high sulphate to chloride ratio in the pore solution. Figure 4-27 to Figure 4-31 demonstrate this with relative consistency, especially at higher chloride levels. Simultaneously, when the sulphate and chloride content of the expressed pore solution are plotted versus w/cm ratio for 5% admixed chlorides, Figure 4-32 and Figure 4-33, the GU+FA mix had the lowest chloride content, except at a 0.40 w/cm ratio, and the highest sulphate content.

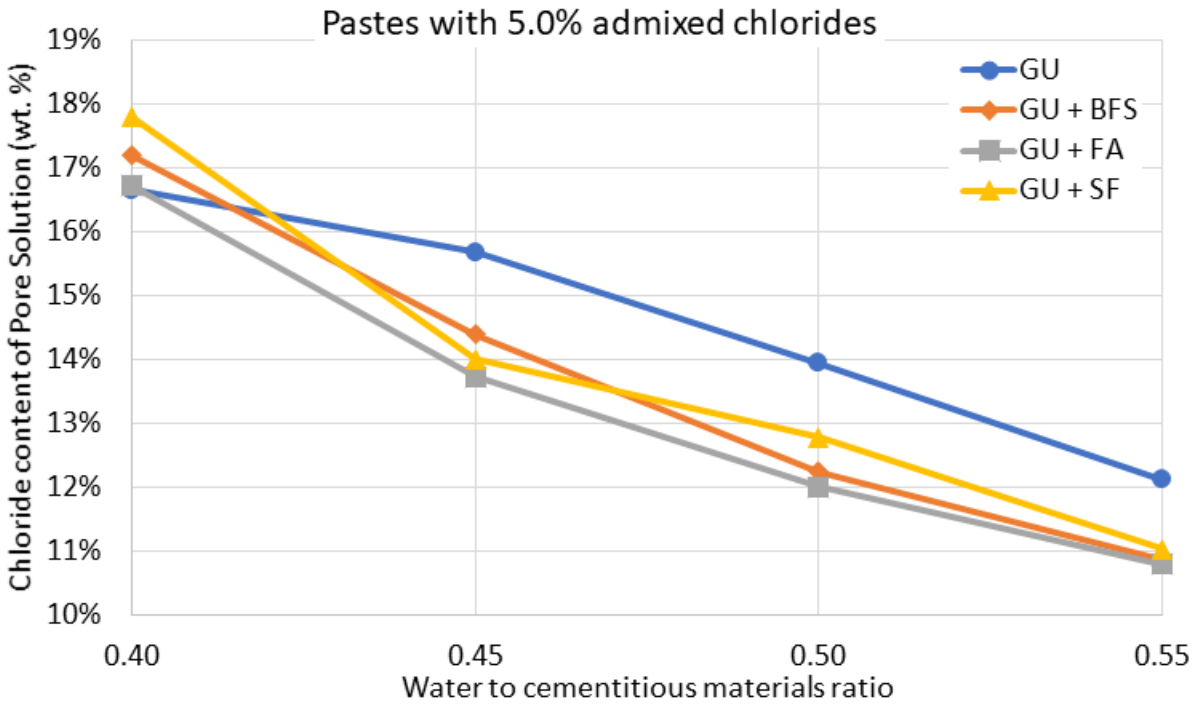

Figure 4-32: The influence of w/cm ratio on the chloride content (wt.%) of the pore solution expressed from pastes containing 5.0% admixed chlorides by weight of cementitious material

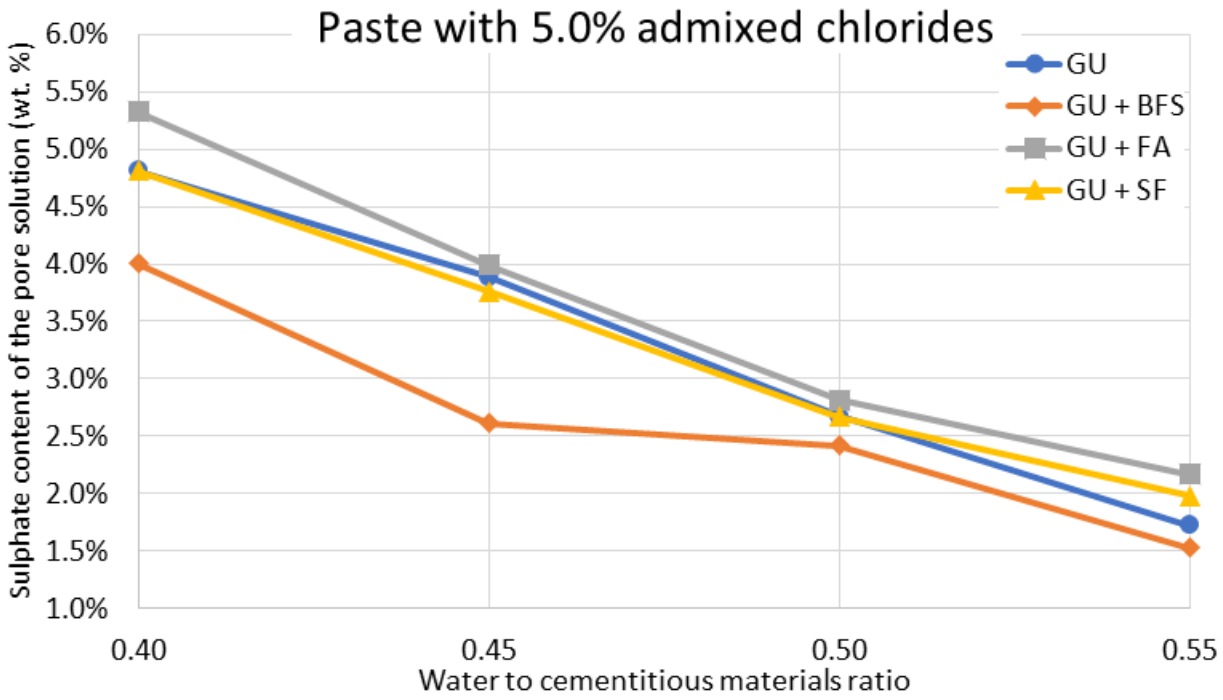

Figure 4-33: The influence of w/cm ratio on the sulphate content (wt.%) of the pore solution expressed from pastes containing 5.0% admixed chlorides by weight of cementitious material

To compare bound and free chlorides and sulphates, the evaporable water content was determined using Equation 19. The free chloride (Cl_{free}) and bound chloride (CL_{bound}) were then determined using Equation 27 and Equation 28.

$$Cl_{free} = Cl_{dissolved} \cdot W_e \qquad \text{Equation 27}$$

$$Cl_{bound} = Cl_{added} - Cl_{free} \qquad \text{Equation 28}$$

Similarly, the free sulphate ($SO4_{free}$) and bound sulphate ($SO4_{bound}$) wasthen determined using Equation 29 and Equation 30.

$$(SO_4)_{free} = (SO_4)_{dissolved} \cdot W_e \qquad \text{Equation 29}$$

$$(SO_4)_{bound} = (SO_4)_{added} - (SO_4)_{free} \qquad \text{Equation 30}$$

The bound chloride vs bound sulphate is plotted in Figure 4-34. Although the bound chloride and bound sulphate do no correspond at a 1:1 ratio, it can be seen that, as the bound chloride in the pore solution increases, the bound sulphate decreases.

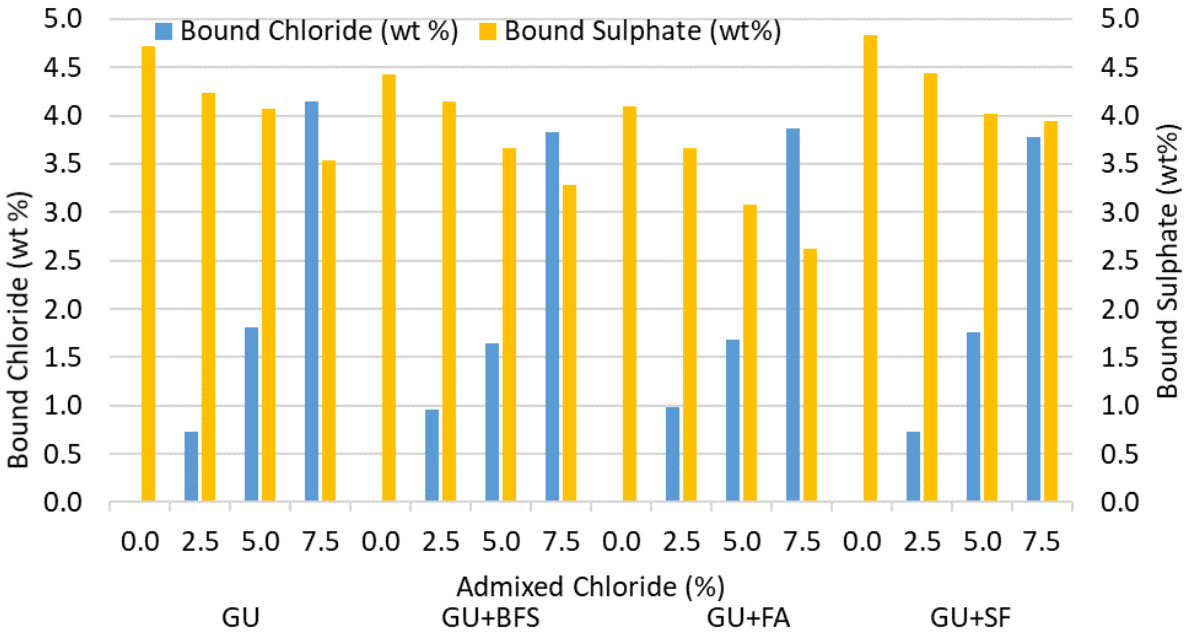

Figure 4-34: Bound chloride vs bound sulphate for cement pastes with 0.40 w/cm ratio

Similarly, Figure 4-35 plots free chloride and free sulphate as wt% of the expressed pore solution for cement pastes with a 0.40 w/cm ratio for different amounts of admixed chlorides. This demonstrates that sulphate content increases with admixed chloride content in the pore solution, ultimately leading to an increase the critical chloride threshold level of carbon steel, as demonstrated by Ogunsanya and Hansson [52].

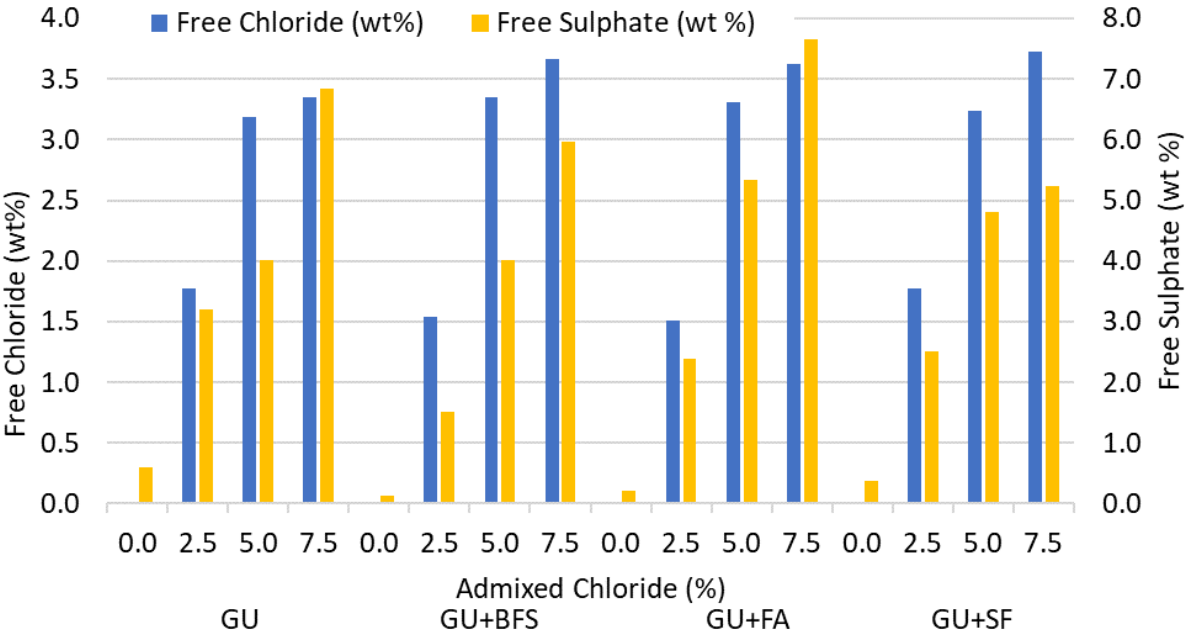

Figure 4-35: Weight % chloride and sulphate in the pore solution of cement pastes with 0.40 w/cm ratio

4.3. Supplemental experimental procedures

4.3.1. Determination of Coefficient of Thermal Expansion

The coefficient of thermal expansion of GFRP bars was determined using the Digital Image Correlation technique. Once the GFRP samples had been prepared and sufficiently frozen, the specimens were removed from the freezer and placed in the frame as demonstrated in Figure 3-18. Each test took 10 minutes allowing the temperature to increase from -30C to 15C. An example of the plot of temperature versus strain for three #5 Pultrall bars is shown in Figure 4-1 with the remaining data presented in Appendix A

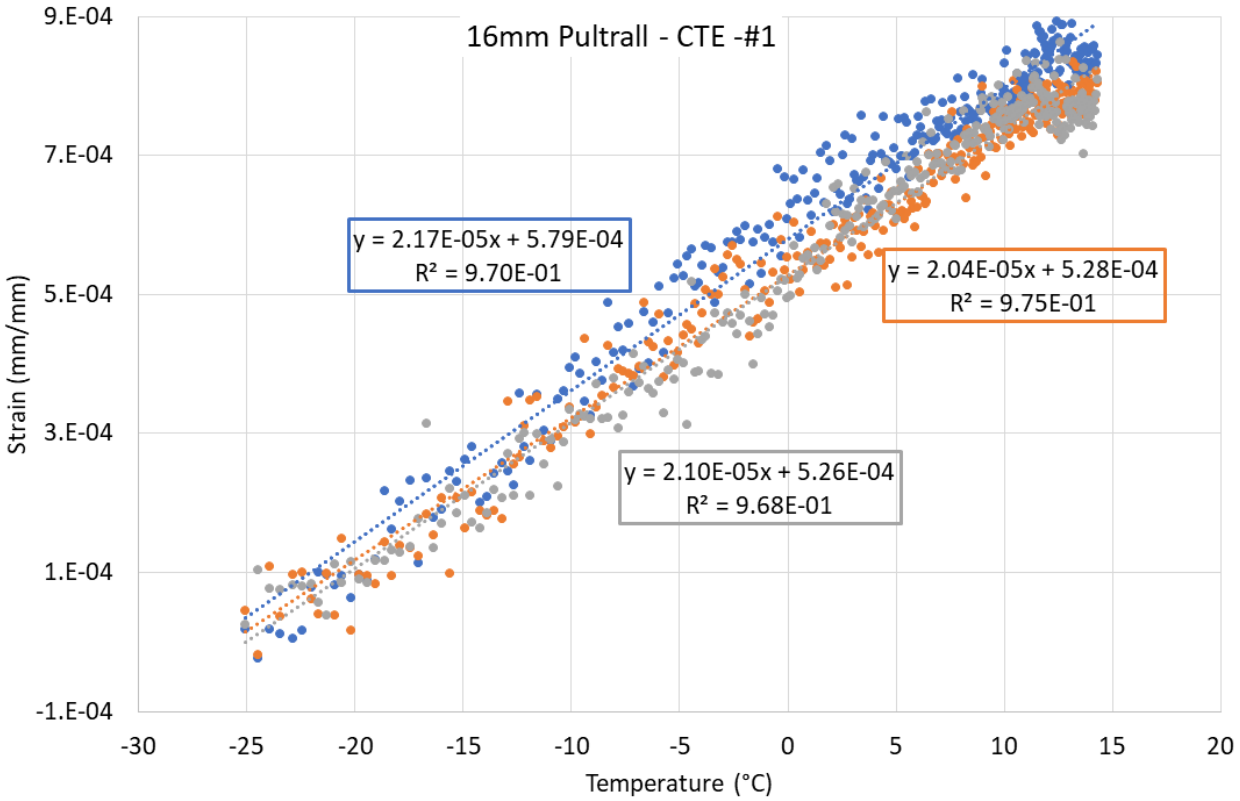

Figure 4-36: Coefficients of thermal expansion for three replicate #5 Pultrall samples.

Due to the extremely low displacement, corresponding with low strains, the data appears noisy, although trends are apparent. The R^2 values were used to demonstrate the consistency of the data after adding a trendline, with a slope that equates to the CTE. This was used to determine the average CTE using twelve data sets for each bar manufacturer and bar diameter, represented in Table 4-19 and

Table 4-20. These coefficients of thermal expansion were then compared with the manufacturer provided data, Table 3-1 and Table 3-2, and found to be lower (between 9% and 23%), although the values reported by the manufacturer are likely upper-end values based on variability between different GFRP batches.

Table 4-19: Coefficient of thermal expansion and coefficient of determination for: #4 (A), and #5 (B) Pultrall bars.

A	CTE	R^2		**B**	CTE	R^2
P13-1	2.22E-05	0.959		P16-1	2.17E-05	0.970
	2.09E-05	0.963			2.12E-05	0.978
	1.85E-05	0.938			2.10E-05	0.968
P13-2	1.91E-05	0.945		P16-2	1.93E-05	0.959
	1.89E-05	0.934			2.19E-05	0.981
	2.19E-05	0.954			2.00E-05	0.946
P13-3	2.02E-05	0.968		P16-3	2.00E-05	0.961
	1.80E-05	0.916			2.19E-05	0.980
	1.77E-05	0.956			2.13E-05	0.979
P13-4	1.93E-05	0.954		P16-4	2.09E-05	0.976
	1.90E-05	0.929			1.94E-05	0.970
	2.08E-05	0.952			2.10E-05	0.975
DIC Average	1.97E-05	0.947		DIC Average	2.08E-05	0.970
DIC Standard Deviation	1.41E-06	0.015		DIC Standard Deviation	8.77E-07	0.010
% Difference	-17.7%			% Difference	-9.1%	

Table 4-20: Coefficient of thermal expansion and coefficient of determination for: 13 mm (A), and 16 mm (B) Schöck - Combar bars.

A	CTE	R^2		**B**	CTE	R^2
C13-1	1.96E-05	0.948		C16-1	1.74E-05	0.957
	1.85E-05	0.955			1.97E-05	0.963
	1.50E-05	0.915			1.83E-05	0.963
C13-2	1.56E-05	0.917		C16-2	1.73E-05	0.968
	1.65E-05	0.912			1.83E-05	0.965
	1.50E-05	0.925			1.80E-05	0.953
C13-3	1.82E-05	0.922		C16-3	2.16E-05	0.975
	1.71E-05	0.916			2.02E-05	0.953
	1.82E-05	0.882			1.91E-05	0.959
C13-4	1.69E-05	0.961		C16-4	1.82E-05	0.932
	1.50E-05	0.949			1.84E-05	0.942
	1.65E-05	0.955			1.94E-05	0.949
DIC Average	1.68E-05	0.930		DIC Average	1.88E-05	0.957
DIC Standard Deviation	1.47E-06	0.023		DIC Standard Deviation	1.19E-06	0.011
% Difference	-23.6%			% Difference	-14.5%	

Chapter 5 Analysis of the impact of Temperature, Salt Use and Rebar Selection on Structure Service Design

5.1. Temperature and salt use

Due to the evolving requirements of structural concrete, their plastic and hardened state properties have drastically changed over the past 100 years. These changes, result in significant improvements including higher strength, elevated early age strength allowing for faster construction sequences as well as the introduction of chemical admixtures which can enhance certain characteristics of the hardened and plastic concrete. Of course, resolving a problem in one area almost always creates new challenges as a consequence. For instance, high early strength concrete is produced at the expense of its durability, as it is more susceptible to thermal shrinking. Mehta and Richards [107] suggest that the method of concrete pouring required a paradigm shift, back to construction practice patterns employed in the 1930's. At the time, construction practice did not require such speed of construction. Instead, it allowed for slower curing concrete, which allowed the concrete to designed more accurately for a required strength. It also resulted in a lower permeability, higher elastic modulus, and lower creep values. Similarly, if the results from both the effects of temperature and salt use on the compressive strength of concrete are compared, two, potentially dangerous observations become apparent, at opposite ends of the spectrum. Either the compressive strength greatly increases or greatly decreases, potentially changing both the design and failure characteristics of the structure. As such, a Monte Carlo simulation was undertaken to determine the effects of concrete variability on the moment resistance of a simplified beam.

As concrete is generally a field cast composite material comprised of highly variable materials, the product created is non-homogeneous as are its characteristics. As such, code writers have identified safety factors to deal with in-situ concrete placing factors including: quality of the supplied concrete, compaction of the placed concrete, the curing process, the ambient temperature and the relative humidity, and the time from batch time to when the concrete was placed. These factors, for instance resistance factors $\phi_s \; and \; \phi_c$, for reinforcing steel and concrete respectively, have been used to control risk related to: strength variability, differences between the dimensions of the design and the as-built structure, as well as simplifying assumptions made in code equations [108]. In the case of CSA A23.3, $\phi_s \; and \; \phi_c$ are 0.85 and 0.65.

5.1.1. Temperature profile

The initial temperature profile of the pullout testing was determined in collaboration with the Ministry of Transportation of Ontario to correspond to temperatures experienced by Ministry owned structures in Ontario's North-West, the largest community being Thunder Bay. Historical temperature data for Thunder Bay for the last 70 years was collected from Environment Canada. The data are plotted below in Figure 5-1, with the black line presenting the average monthly

temperature data, the yellow line presenting the extreme maximum monthly temperature data, and the blue line presenting the extreme minimum monthly temperature data. Although it can be seen from Figure 5-1 that in extreme cases Thunder Bay can experience temperatures lower than -30°C between November and March, they are most commonly experienced in January and February.

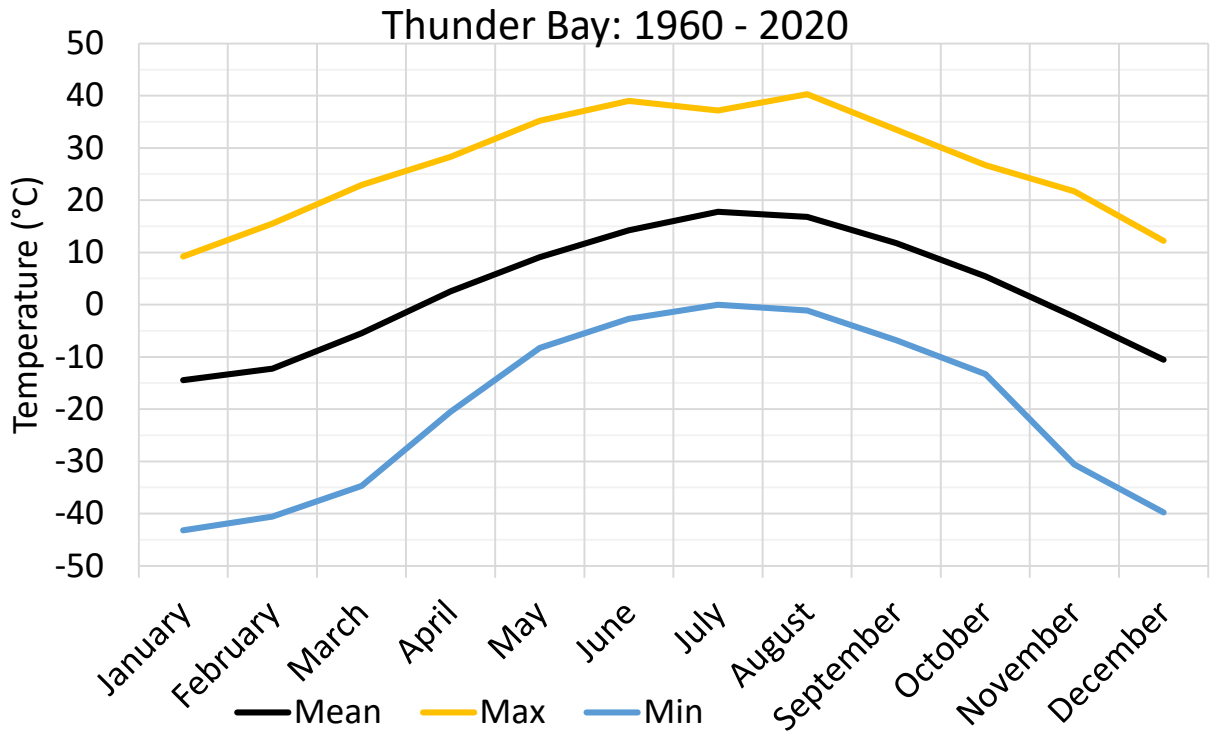

Figure 5-1: Historical temperature data for Thunder Bay Ontario between 1960 and 2020

Table 5-1: Number of occurrences per year of temperatures exceeding -30°C

Environmental Condition		**Occurrences per year**
Temperature exceeds -30°C	μ	7.50
	σ	5.24
Temperature exceeds -30°C two consecutive days	μ	3.15
	σ	2.87

The goal of the simulation was to determine both the effect of the temperature on the overall strength of the structure, as well as the likelihood of failure in a given year based on the temperature effects. It has been assumed that the temperature data follow a Poisson distribution, assuming that cold weather events happen independently of each other, which is a simplification. Using this assumption, it can be statistically determined that the probability of the temperature dropping below -30°C for two consecutive days in a given year is 86%.

5.1.2. Effect of moisture content

The water to cementitious materials ratio of a concrete mix impacts the compressive strength in both ambient and frozen states as demonstrated in 4.1.4. Although the data are limited, the research compared frozen concrete, conditioned at -30°C for 2 days, to the same concrete tested in an ambient condition. The data from section 4.1.4 demonstrate that concrete compressive strength can increase by up to 46% between the unfrozen and frozen state.

Table 5-2: Change in compressive strength between non-frozen and frozen test

	0.3 w/cm			**0.45 w/cm**		
	7 Day	28 Day	56 Day	7 Day	28 Day	56 Day
ACAC	1.24	1.19	1.16	1.38	1.25	1.17
ACMC	1.29	1.27	1.17	1.46	1.36	1.44
ECAC	1.24	1.22	1.18	1.38	1.24	1.19
ECMC	1.26	1.29	1.24	1.41	1.43	1.41

Those data indicate that two identical mixes, where only the initial water to cementitious materials ratio varied from 0.30 to 0.45, had average ambient 56-day compressive strengths of 78.6 MPa and 40.7 MPa respectively. An identical but slightly less significant trend, was experienced by the frozen concrete where the average 56-day compressive strengths were 93.2 MPa and 53.2 MPa respectively.

Moisture content versus compressive strength ratio of the frozen concrete to ambient concrete is graphically presented in Figure 5-2. It is apparent that the excess moisture in the 0.45 w/cm mix has a large impact on the compressive strength ratio.

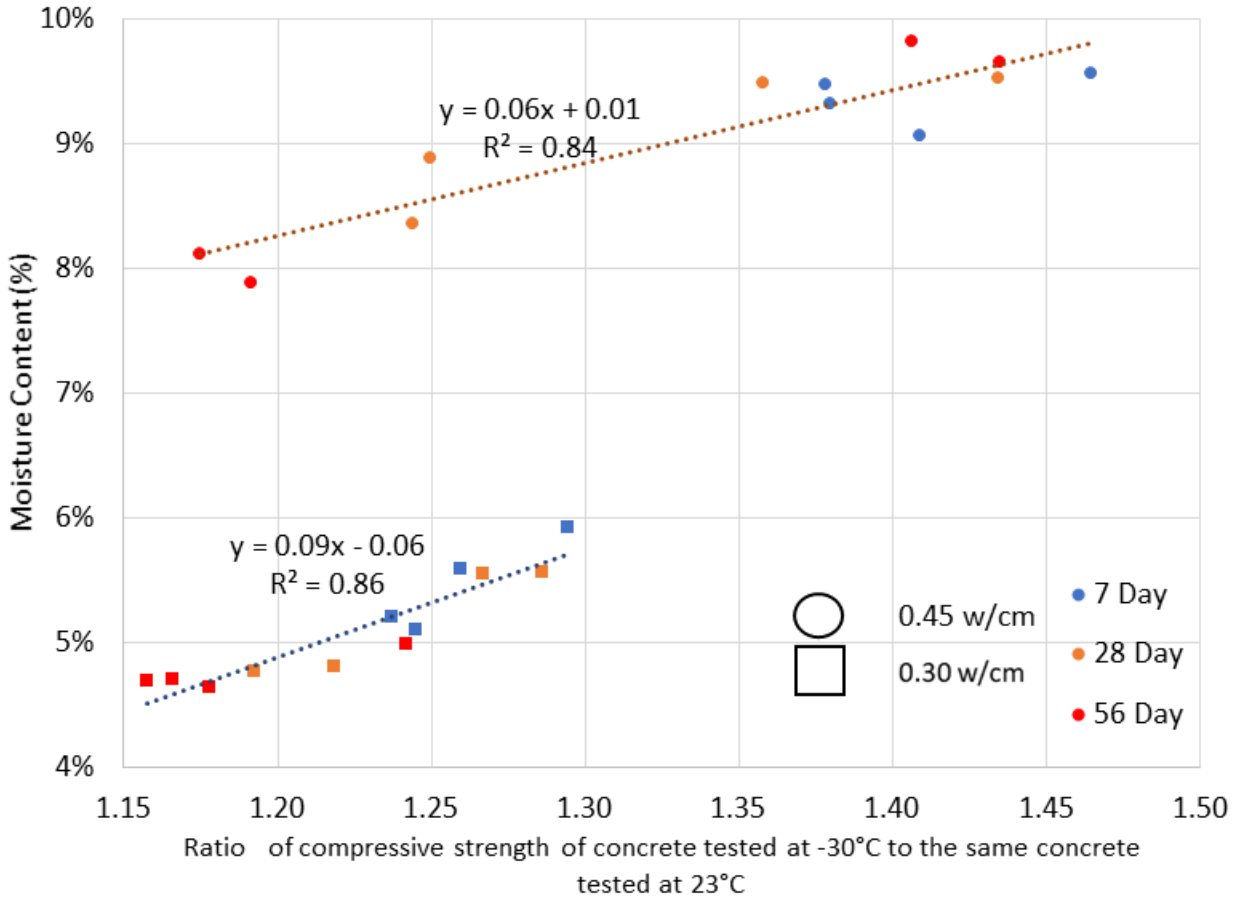

Figure 5-2: Moisture content vs compressive strength ratio of concrete tested at -30°C and 23°C

Table 5-3: Average (of all tests) Moisture Content

Water to cementitious material		Moisture Content
0.45 w/cm	μ	9.09%
	σ	0.62%
0.30 w/cm	μ	5.13%
	σ	0.42%

5.1.3. Effect of field conditions

Due to both curing and placement conditions, concrete compressive strength determined from testing cylindrical specimens is not always a true representation of in situ conditions. Stewart [109] suggested that compression tests are not accurate representations of field conditions, but that the data collected from the cylinder testing should be modified by the following:

$$f'_{field} = k_{cp} k_{cr} f'_{cylidner} \quad \text{Equation 31}$$

Where k_{cp} is a compaction coefficient and k_{cr} is the curing coefficient. Stewart then implies that the curing process is the most limiting part of the process, at a mean reduction of approximately 0.86, but varies from 0.66 to 1.0, with a coefficient of variation of approximately 0.05. The compaction coefficient also limits the assumed field strength but to a lesser extent, with a mean reduction of 0.95, varying from 0.8 to 1.0. He also provided the qualitative evaluation shown in Table 5-4.

Table 5-4: Statistical parameters for k_{cp} [109]

Worker performance		**Compaction Coefficient (k_{cp})**	**Curing Coefficient (k_{cr})**
Poor	μ	0.80	0.66
	σ	0.048	0.033
Fair	μ	0.87	0.84
	σ	0.052	0.042
Good	μ	1.0	1.0
	σ	0.0	0.0

Mirza et al [110] present data, which followed a normal distribution and stated that cored sample strengths varied from standard cylinder strengths at a ratio of 0.74 to 0.96 with the average again of approximately 0.87. This corresponded with the coefficient of variation (COV) of 10% based on their previous studies, but was found to be larger by other researchers. Due to the tight restrictions for contractors placing concrete for MTO owned structures, it was assumed the workmanship varied between the fair and good levels and, for the Monte Carlo simulation, the assumed the values presented in Table 5-5.

Table 5-5: Assumed field condition data used in current Monte Carlo simulation

Field Condition		
k_{cp}	μ	0.94
	σ	0.0281
k_{cr}	μ	0.92
	σ	0.023

5.1.4. Tensile strength of steel and GFRP

There are stringent guidelines for the minimum yield strength of reinforcing steel, usually assumed as 400 MPa. CSA G30.18 [111] states that "99^{th} percentile of steel sampled must exceed 400 MPa". In 1979, Mirza and MacGregor [110] found that, if bars were limited to one supplier, the coefficient of variance (COV) ranged between 3-6 percent. More recently, Bournonville et al. [112] statistically analyzed yield and tensile strengths of grade 60 (60 KSI or approximately 413

MPa) rebar from 29 mills. The average yield strength of all sizes of reinforcing bars was found to be 69.6 ksi (~480 MPa), with a coefficient of ranging between 3.6 and 9.0% (with and average of 7.15%), and a standard deviation of 4976 psi (~34.3 MPa). Although little recent data on the variability of the Youngs modulus were available, it was assumed for the Monte Carlo simulation that the 95th percentile of the modulus exceeded 200 GPa. It was also assumed that the COV of the modulus of elasticity is 2% following the data presented by Allen, [113].

As for GFRP, the strength depends on the manufacturer as can be seen from Table 3-1 and Table 3-2. Statistically, Pilakoutas et al. [114] found that the tensile strength of GFRP follows a normal distribution with a COV of 0.05. Building on this, Silva [115] presented data that suggest the mean tensile strength ranges between 1.15 and 1.20 times the minimum tensile strength of the GFRP, from all manufacturers that they tested. The modulus of elasticity appears to be more consistent than the tensile strength with Johnson [116] reporting an average modulus of 60,090 MPa and a similar COV of 0.045.

Thus, for the modelling in this work, the values presented in Table 5-6 were assumed.

Table 5-6: Properties of tensile reinforcement assumed for Monte Carlo simulation

Parameter		
F_y (MPa)	μ	480
	σ	34.3
Modulus of Elasticity (MPa)	μ	206,580
	σ	4131
$F_{gfrp\text{-}ultimate}$ (MPa)	μ	1265
	σ	63.25
Modulus of Elasticity GFRP (MPa)	μ	60,090
	σ	2720

5.1.5. Compressive strength data

In order to utilize the moisture data from both the low- and high-w/cm mixes in the stochastic model, compressive strength data from a regular concrete, approximately 35 MPa, have been analyzed. The compressive strength data have been collected by the author beginning in 2012 for the low strength mix, and since 2015 for the high strength mix. The mean and standard deviations of mixes are given in

Table 5-7.

Table 5-7: Average compressive strength assumed in Monte Carlo simulation

Mix Design Compressive Strength		Compressive Strength (MPa)
35 MPa	μ (22)	46.8
	σ	3.92

In order to utilize the data in the Monte Carlo simulation, the distribution was determined using the probability paper plot method. The plots for both the 35 MPa and 65 MPa concrete are presented in Figure 5-3 and Figure 5-4 respectively. These figures represent the normal distributions, and when compared, both graphically and through the R^2 value, to the lognormal and Weibull distributions, it is evident that the data can be best described by the normal distribution.

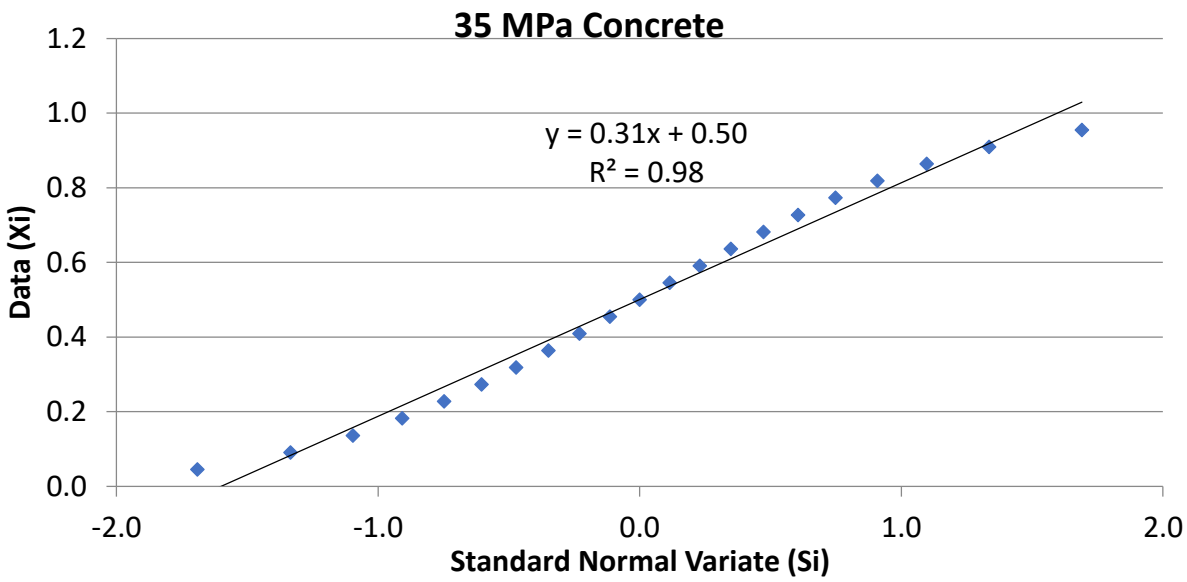

Figure 5-3: Normal Probability Paper Plot for 35 MPa concrete

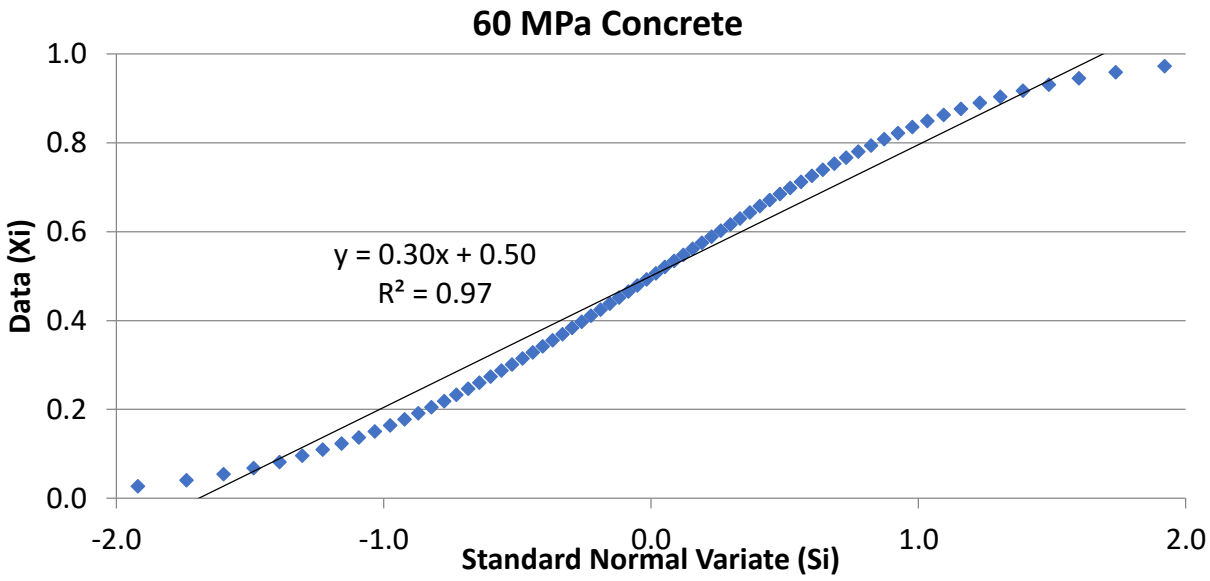

Figure 5-4: Normal Probability Paper Plot for 60 MPa concrete

5.1.6. Detrimental effects of chloride content on compressive strength of concrete

Although the nearly 5-year submersion of cylinders cannot be directly compared to an equivalent structural exposure time, reported in section 4.2.1, evaluation of the 58-year-old Lyn Road bridge deck conducted by WSP in 2016 [117] indicated surface layer chloride contents as high as 0.407% by weight of concrete, Table 5-8. When the 34 year old barrier wall of the HWY 406 overpass over 12-Mile Creek in St. Catherines, Ontario was examined, chloride contents as high as 0.772% were measured, [118].

Table 5-8: Lyn Road Overpass Chloride Measurements

	Depth	**Bridge Deck – Lyn Road bridge**	**Barrier Wall – 12-Mile Creek**
Chloride Content (% Chloride by mass of concrete)	0 – 10 mm	0.407	0.772
	20 – 30 mm	0.258	0.508
	40 – 50 mm	0.124	
	60 – 70 mm	0.074	
	80 – 90 mm	0.078	
	100 – 110 mm	0.085	
	120 – 130 mm	0.027	
	140 – 150 mm	0.021	

If these data are superimposed on Figure 4-26, it can be observed that the chloride has penetrated to nearly the same extend as the 5-year exposure, although the chloride closest to the surface appears to be significantly lower, Figure 5-5. Although Lyn Road Bridge is 58 years old, more detrimental chloride brines had not been applied to the structure for at least the first 20 years, suggesting that structures of similar age in the future may experience chloride contents exceeding those pictured below.

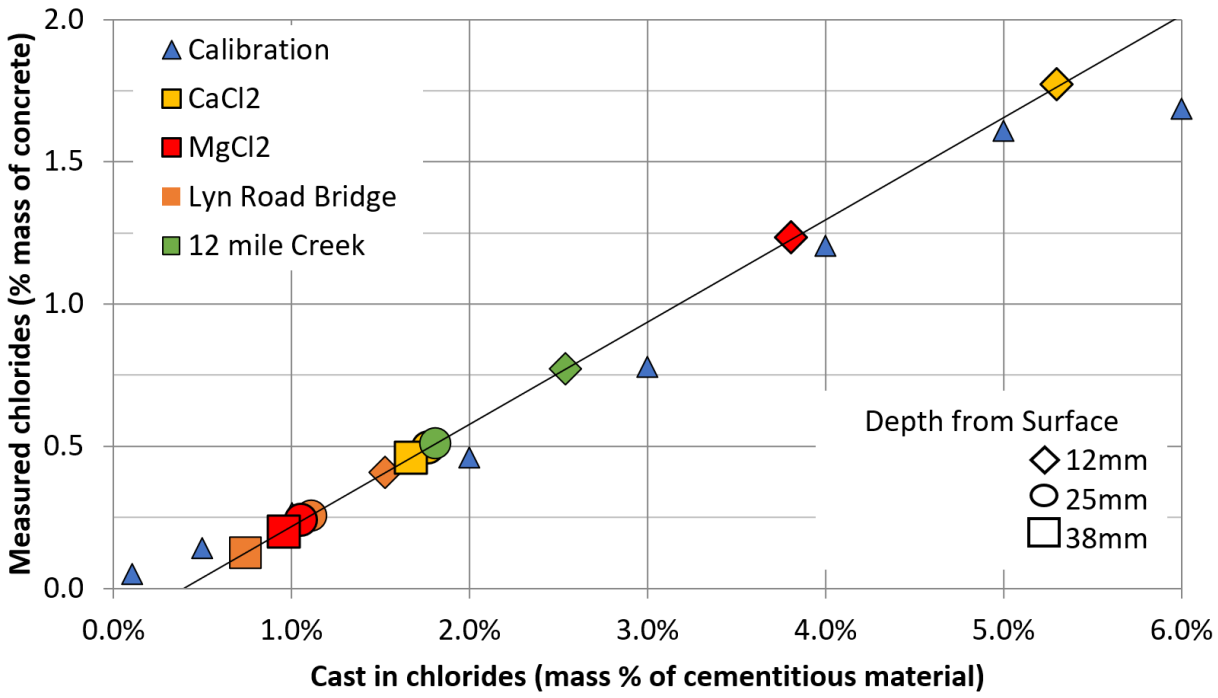

Figure 5-5:Chloride contents, near the surface, of Lyn Road Bridge and 12 Mile Creek Bridge

5.1.7. Bias factor

As mentioned earlier, material properties and as built structures often exceed those specified by either the code or the designer. As such, the use of a bias factor is used to account for this extra variability. CSA S6-14 [74] states that "*the bias factor for a parameter is defined as the ratio of mean real values to the specified values from the code*". For simply supported bridge spans it recommends a bias factor with a mean of 1.05 and a coefficient of variation of 0.075. This statistical parameter is multiplied by the moment resistance when completing a reliability analysis.

5.1.8. Increased compressive strength

If an increase in compressive strength is observed, as in the frozen concrete, thought must be given to the fundamental concrete mechanics. When concrete is reinforced with GFRP, especially in the case of flexural reinforcement in beams, structural engineers design these structures to be over-reinforced. This means that the moment couples between the GFRP and the structure rely

on the concrete crushing before the GFRP fails in a brittle manner. Increased compressive strength with decreasing temperature, combined with the fact that most ready-mix suppliers provide mixes with mean compressive strength values of up to 125% of the specified design strength, can lead to situations in which the structure changes from an over reinforced design to an under-reinforced design. In theory, this could result in catastrophic failure of the GFRP before the concrete fails. Although this failure mechanism is highly undesirable, solace can be taken in the fact that the structural capacity is likely to have greatly increased beyond the design requirements. To analyze the effects of the compressive strength variability on potential structural designs, a statistical failure comparison has been completed using a Monte Carlo simulation for a simple case has been completed below. The design, shown in Appendix B, requires a beam with a 500 mm width and 750 mm depth to carry a load of 500 kN·m assuming a concrete compressive strength of 35MPa and GFRP reinforcement based on the data provided for 16 mm Schöck Combar reinforcing bars. The designed beam cross section is shown in Figure 5-6

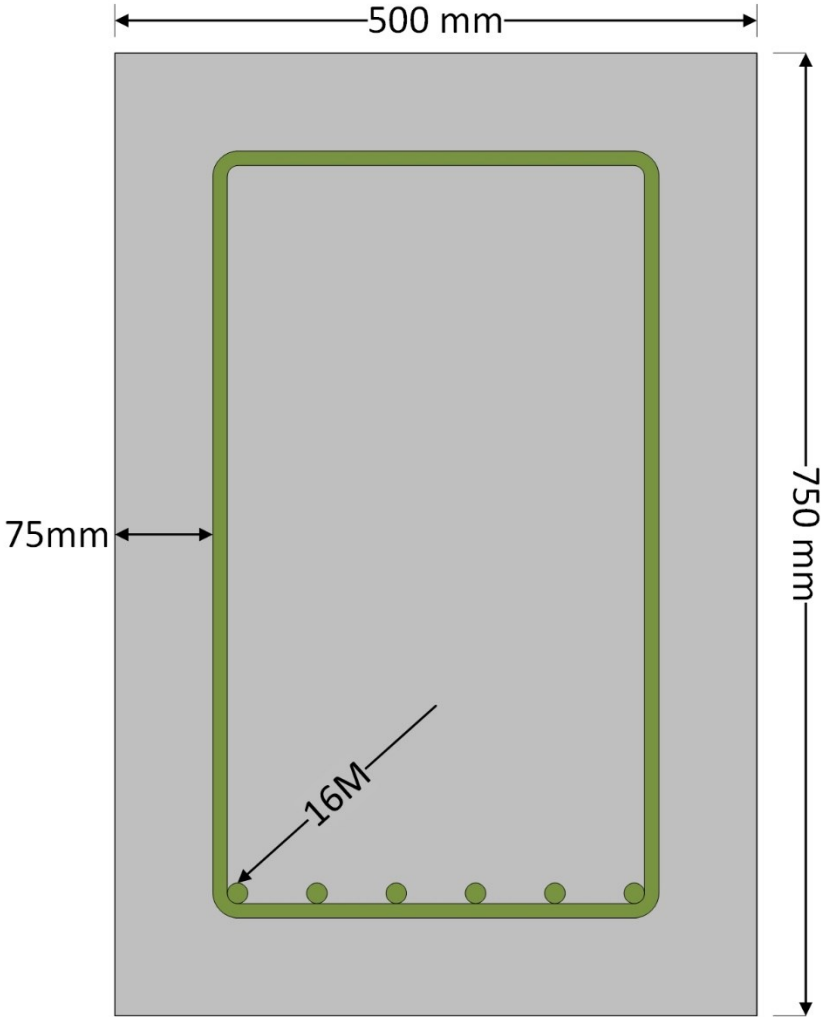

Figure 5-6: Over-Reinforced Beam Cross Section using 16 mm GFRP rebar

5.1.8.1. Monte Carlo Simulation

The Monte Carlo simulation was conducted on the beam from the design example presented in Appendix B, using the parameters outline in Table 5-9.

Table 5-9: Monty Carlo Simulation Parameters

Symbol	Mean	Standard Deviation	COV	Distribution	Units	Description
f'c (35)	46.80	3.92	0.084	Normal	MPa	Compressive Strength
B	1.05	0.0787	0.075	Normal		Bias Factor
k_{cp}	0.95	0.0285	0.03	Normal		Compaction Coefficient
k_{cr}	0.86	0.043	0.05	Normal		Curing Coefficient
w_{free}	9.2	0.6176	0.067	Normal	%	Free Water
f_{frpu}	1265	63.25	0.05	Normal	MPa	GFRP Ultimate Tensile
E_{frp}	60089	2720	0.045266	Normal	MPa	GFRP Modulus of Elasticity

When determining the failure mechanism, the designer often compares the reinforcement ratio (ρ), Equation 32, to the balanced reinforcement ratio (ρ_b). The balanced reinforcement ratio assumes that the tension material reaches ultimate capacity at the same time the concrete begins to crush, which is the most efficient use of both materials. In the case of designs where FRP is utilized, if $\rho > \rho_b$ it is assumed that the concrete crushes before the FRP ruptures, although this is always confirmed using Equation 33, based on Figure 5-7. As such, it should be noted that the reinforcement ratio used in the design is approximately 20% higher than the balanced reinforcement ratio which would provide the designer with an extra factor of safety.

$$\rho = \frac{A_s}{bd} \qquad \text{Equation 32}$$

$$\varepsilon_{frp} = \left(\frac{d}{c} - 1\right)\varepsilon_{cu} < \varepsilon_{frpu} \qquad \text{Equation 33}$$

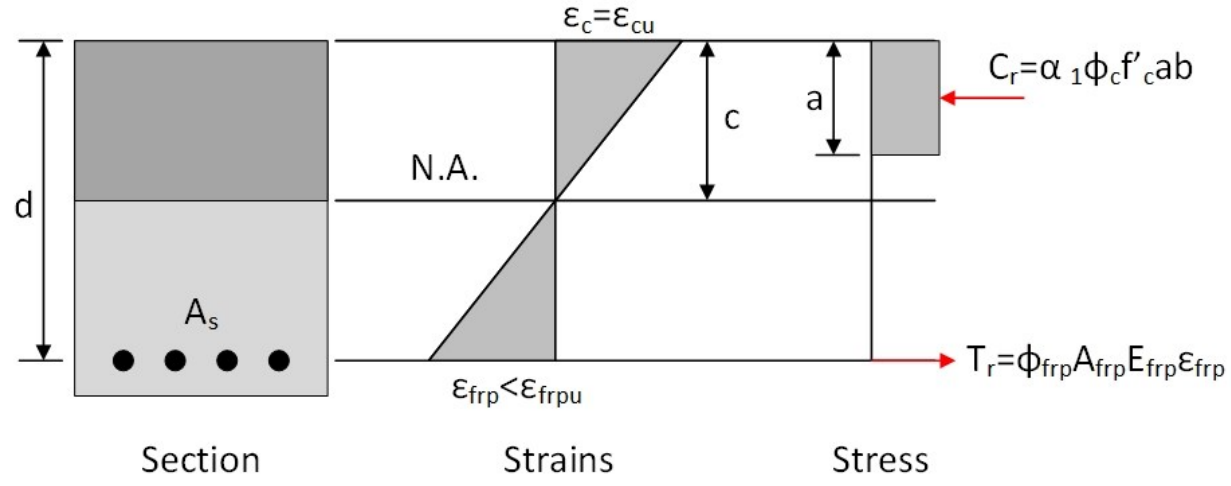

Figure 5-7: Over-reinforced failure

Since the Monte Carlo simulation takes into account the variability in materials and workmanship, the material resistance factors were set to 1.0 for both GFRP and concrete. The results of the analysis are presented in Figure 5-8.

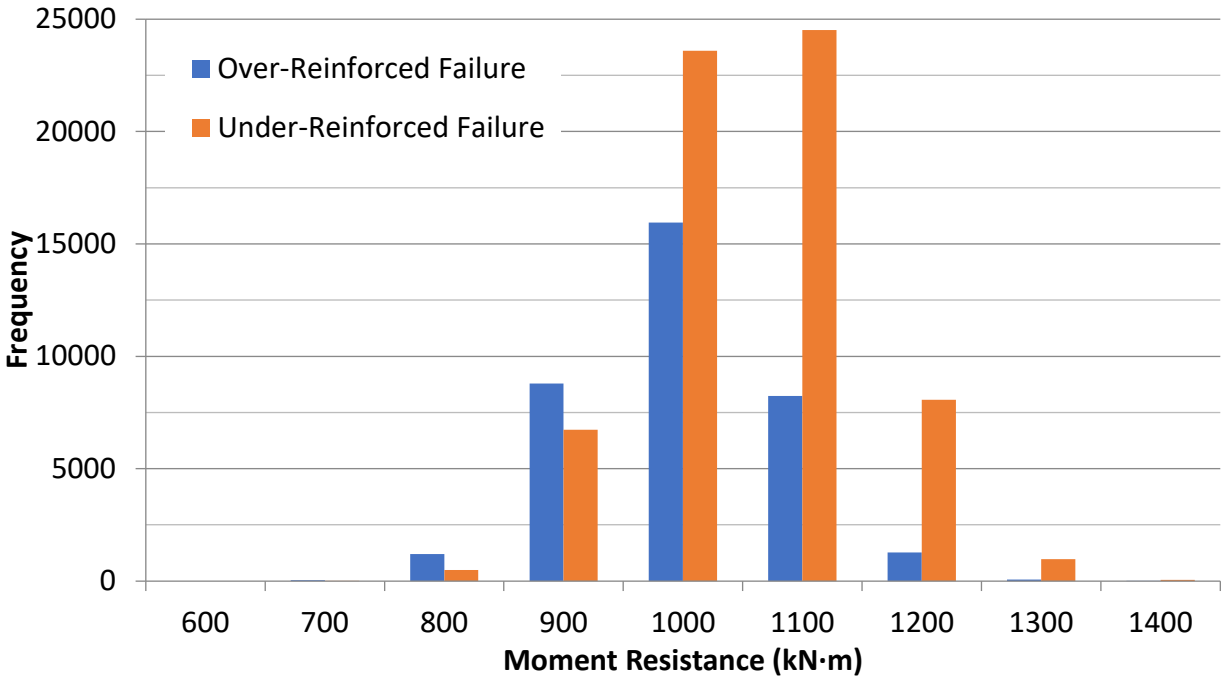

Figure 5-8: Frequency vs moment resistance comparing over- and under-reinforced failures from Monte Carlo simulation assuming code material resistance factors ($\phi_c = 1.0$ and $\phi_{frp} = 1.0$)

The code considers higher variability within the concrete material compared to the FRP, and as such the resistance factor for concrete is slightly lower. By equating both of these, the assumed

concrete capacity increases, and begins to dominate the design with 64.4% of the structures being under-reinforced and 35.6% of the structures being over-reinforced. More importantly, it can be observed that the moment capacity exceeds the required moment resistance of 500 $kN \cdot m$, with the lowest simulation being nearly 1.2 times greater (600 $kN \cdot m$).

By analysing the data, it can be said with certainty, that designers should not be overly concerned by the effect of increased concrete compressive strengths due to moisture in cold climates. It should be noted that this is not a true structural reliability assessment, as there is no comparison between load and resistance. Essentially, the work presented determines statistically how often the moment resistance exceeds the code requirement.

5.1.9. Decreased compressive strength

Similar to the increase in compression strength, if a decrease in compressive strength is observed, thought must be given to the failure mechanism, but also capacity of the structure. When structural engineers utilize steel for flexural reinforcement, they design these structures to be under-reinforced. Essentially, this ensures that the steel yields before the concrete crushes, ensuring the less brittle of the two failure modes.

When determining the failure mechanism, the reinforcement ratio (ρ) is typically compared to the balanced reinforcement ratio (ρ_b). If $\rho < \rho_b$ it is assumed that the steel yields, although yielding is always confirmed using Equation 34, based on Figure 5-9.

$$\frac{c}{d} < \frac{700}{700 + f_y} \qquad \text{Equation 34}$$

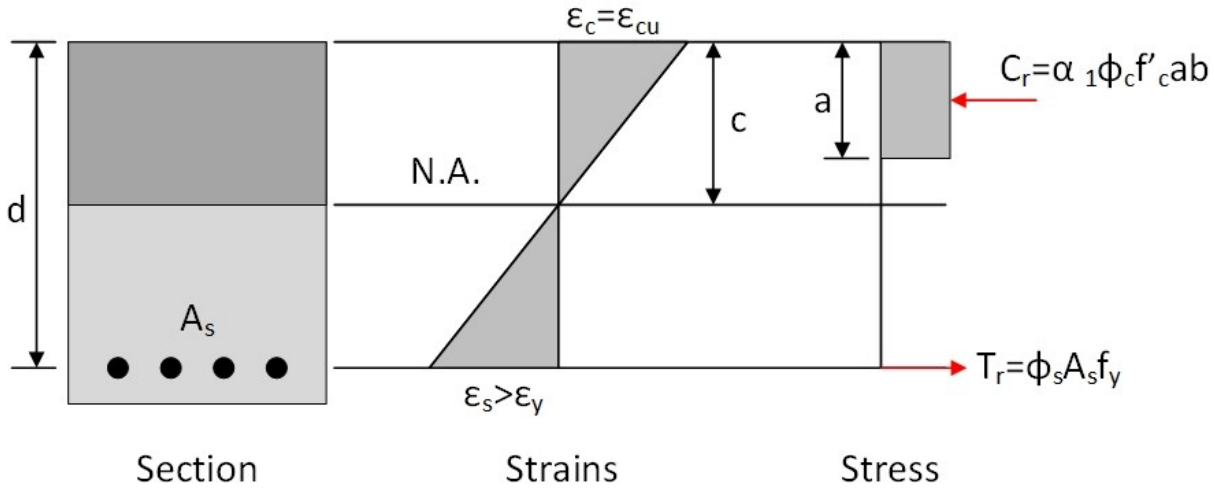

Figure 5-9: Under-reinforced failure

As was the case with the increasing compressive strength, in order to account for risk, the worst-case scenario must be assessed. Although many concrete suppliers mitigate risk by supplying concrete with strengths exceeding 120% of the required compressive strength, this is not always the case. As such, for the following simulation, the 28-day compressive strength of the concrete was assumed to be 105% of the design strength.

From section 4.2.1, it is evident that magnesium and calcium chloride have large, adverse effects on the compressive strength of the concrete. If the compressive strength of concrete submerged in magnesium and calcium chloride for approximately 5 years is compared to the compressive strength of concrete at 28 days, there is an appreciable reduction, from 38.13MPa to 32.20MPa for the calcium chloride exposure. This reduction, of approximately 18%, is not the largest reduction observed, as specimens exposed to magnesium chloride exhibited an average strength of 30.34 MPa in June of 2017, after 4.3 years of exposure. If instead the compressive strength is compared to that of the moist cured concrete after 100 days (μ = 46.69 MPa, σ =2.69 MPa), the reduction is more than 31%. Similarly, to the design example provided for section 5.1.8, a simplified under-reinforced design example is provided in Appendix C. The design required a 500 mm wide by 750 mm deep beam to resist a moment of 1,000 kN·m, using 400 MPa steel, assuming a concrete compressive strength of 30MPa. The designed beam cross section is shown in Figure 5-10.

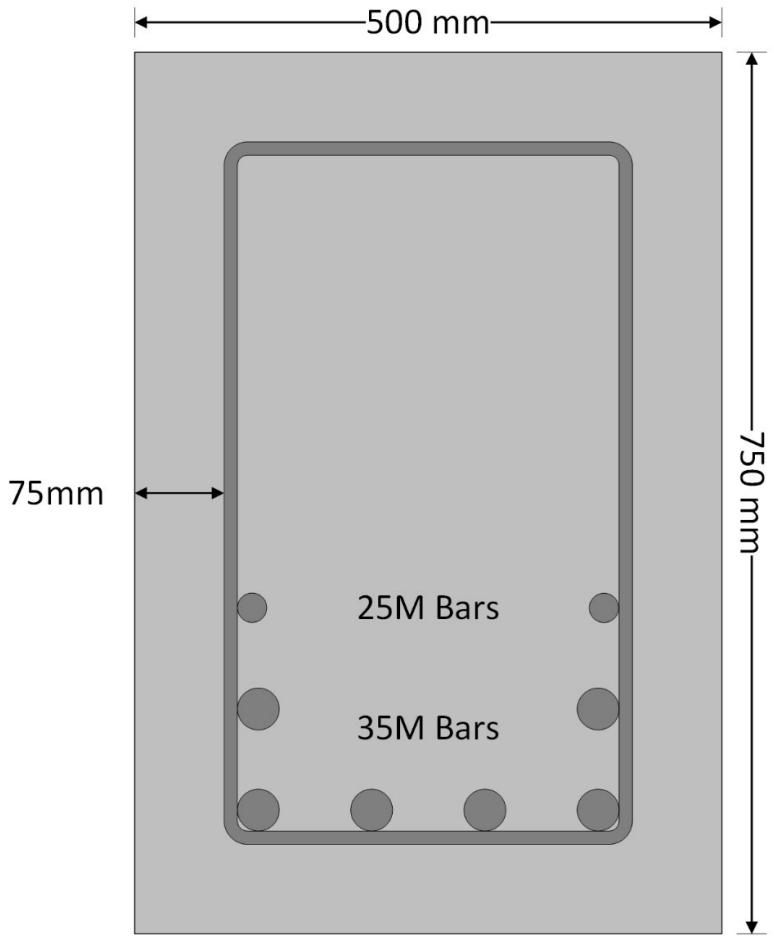

Figure 5-10: Under-Reinforced Beam Cross Section assuming 400 MPa steel reinforcing bars

5.1.9.1. Monte Carlo Simulation

The simulations (100,000) were conducted in a similar manner as the design, assuming a value of 1.0 for the concrete resistance factor (ϕ_c) and the steel resistance factor (ϕ_{frp}), with the mean and standard deviation presented in Table 5-10.

Table 5-10: Monty Carlo Simulation Parameters

Symbol	Mean	Stdev	COV	Dist	Units	Description
F_y	480	34.3	0.071	Normal	MPa	Steel Yield Strength
B	1.05	0.0787	0.075	Normal		Bias Factor
E_{steel}	206580	4131	0.020	Normal	MPa	Modulus of Elasticity
f'c (30)	31.50	2.64	0.084	Normal	Mpa	Compressive Strength
k_{cp}	0.95	0.0285	0.03	Normal		Compaction Coefficient
k_{cr}	0.86	0.043	0.05	Normal		Curing Coefficient

The results indicated that 99.9% of the simulations exceed the 1000 kN·m factored moment, Figure 5-11, with the lowest moment resistance being 902 kN·m and the highest moment resistance being 2220 kN·m with over-reinforced failures occuring 35.7% of the time, Figure 5-12.

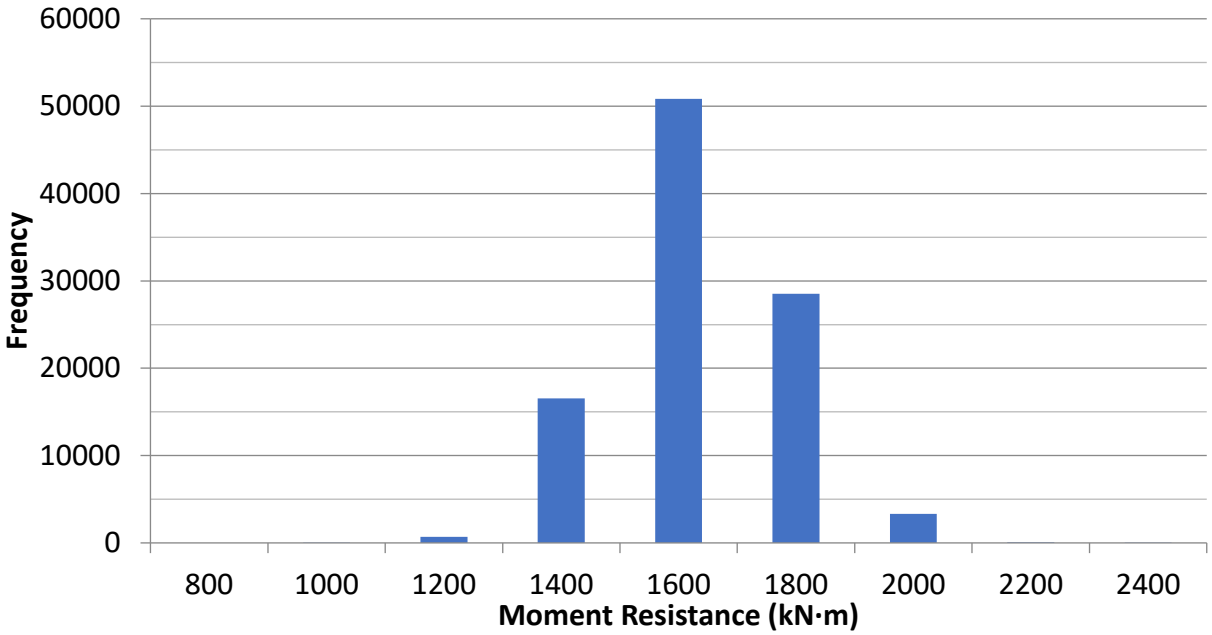

Figure 5-11: Frequency vs moment resistance from Monte Carlo simulation assuming code material resistance factors ($\phi_c = 1.0$ and $\phi_{frp} = 1.0$)

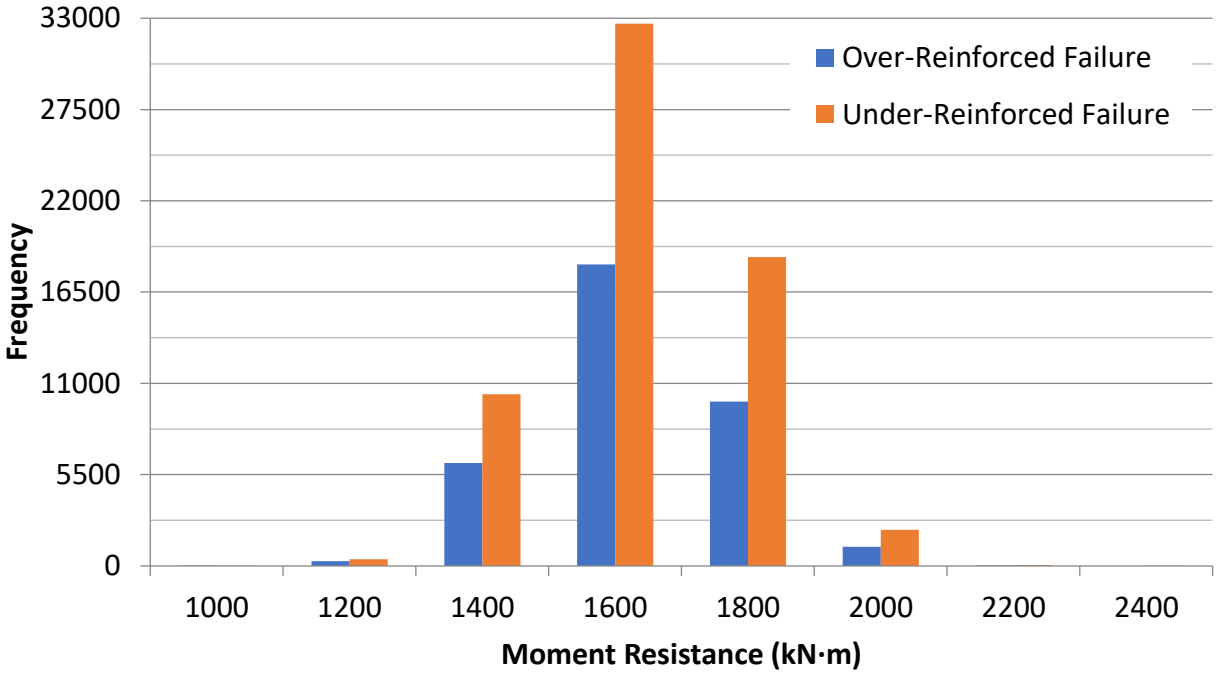

Figure 5-12: Frequency vs moment resistance comparing over- and under-reinforced failures from Monte Carlo simulation assuming code material resistance factors ($\phi_c = 1.0$ and $\phi_{frp} = 1.0$)

To determine the detrimental effect of chloride deterioration on the overall moment resistance of the example structure described above, another Monte Carlo simulation was conducted assuming the same parameters as shown in Table 5-10, whilst also including a chloride reduction coefficient based on the ratio of average compressive strength of the $MgCl_2$ and $CaCl_2$ compared to the wet cured concrete for the last year of testing. The mean and standard deviation reduction values were calculated as 0.697 and 0.0188 respectively. Figure 5-13 compares the pre- and post-chloride exposure moment resistance of the structure.

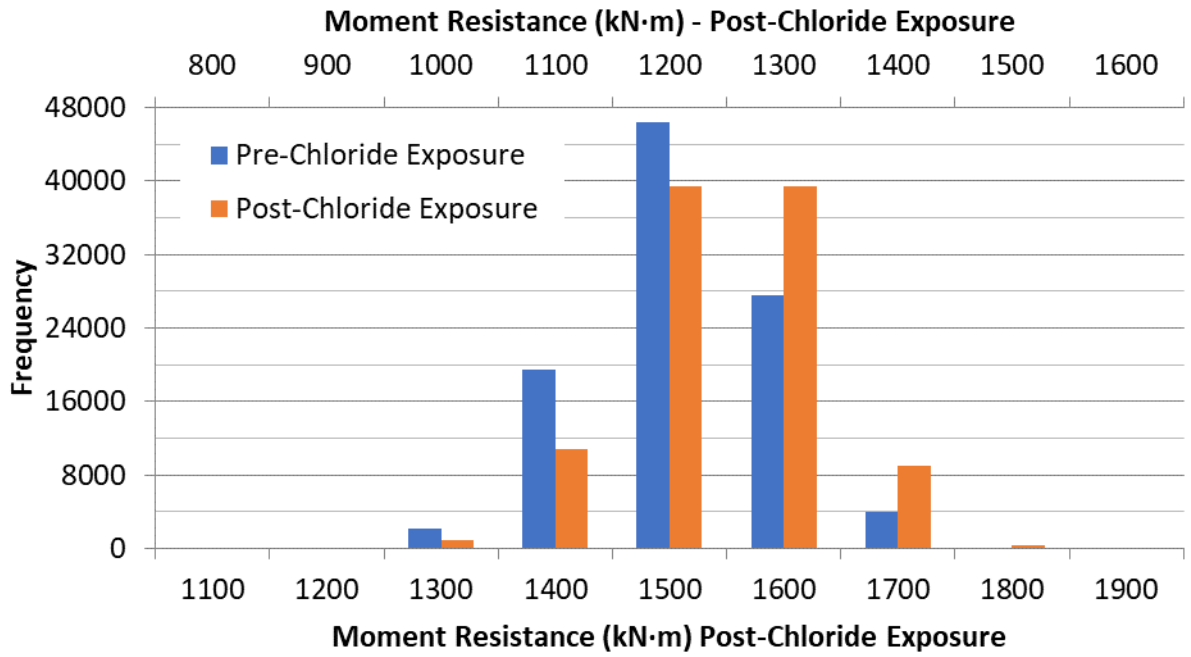

Figure 5-13: Frequency vs Moment Resistance Comparison between Pre- and Post-Chloride ($\phi_s = 1.0$ and $\phi_c = 1.0$)Similarly, when the same simulation is run only changing the resistance factors to 1.0, a moment reduction resistance is noted. The over-reinforced failure now drastically changes from 35.7% to 97.9% for the pre- and post chloride exposure respectively. The average moment resistance also drastically falls from 1462.0 kN·m to 1195.9 kN·m, with 1% now not meeting the 1000 kN·m design requirement. A summary of the significant results is found in Table 5-11.

Table 5-11: Results Summary

	ϕ_c and ϕ_s = 1.0	
	Pre-Chloride	Post-Chloride
M_r (μ) $(kN \cdot m)$	1535.8	1070.2
Over-Reinforced	35734	97901
$M_r < M_f$	0	25448

An assessment of the results could provide a very bleak outlook for concrete structures exposed to chloride. It appears that, with the ϕ_c and ϕ_s = 1.0, there is a drastic reduction in the average moment resistance and an increase in the number of structures no longer meeting the required 1000 kN·m moment. As mentioned earlier, it should be noted that this is not a true structural reliability assessment, as there is no comparison between load and resistance. Essentially, the work presented determines statistically how often the moment resistance exceeds the code requirement.

5.2. Bond and Development length considerations

When structural engineers' design reinforced concrete structures they initially deal with the flexural and shear strength designs. Once those are complete, they must detail how the reinforcement must be placed, determining the spacing, and the development length. The development length describes the amount of rebar that must be embedded in the concrete to establish a bond strength sufficient to ensure the rebar, in the case of steel reinforcing bars, will yield before pulling out of the concrete. This bond is transferred by adhesion, friction, and mechanical interlock [108], see Figure 5-14.

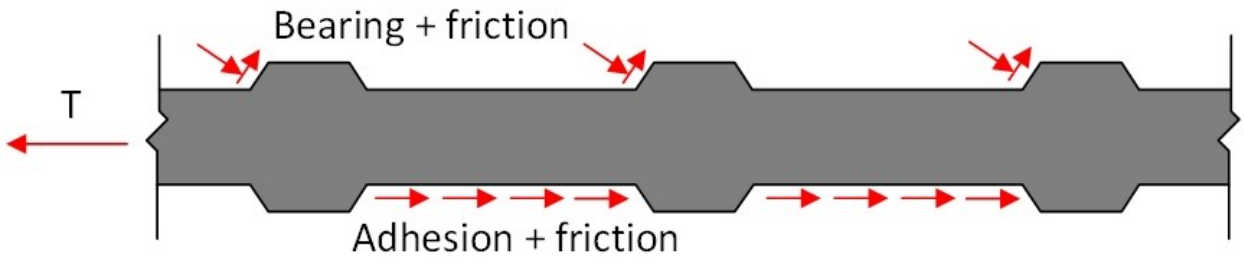

Figure 5-14: Bond Mechanics

Although adhesion plays a role for bond, Achillides and Pilakoutas [119] noted that for FRP rebar adhesion typically accounts for less than 3 MPa of the bond stress, and the adhesion is assumed to fail when the slope of the bond stress vs slip curve changes, and example of which is given in Figure 5-15. The remainder of the bond strength vs free-end slip diagrams can be found in appendix B.

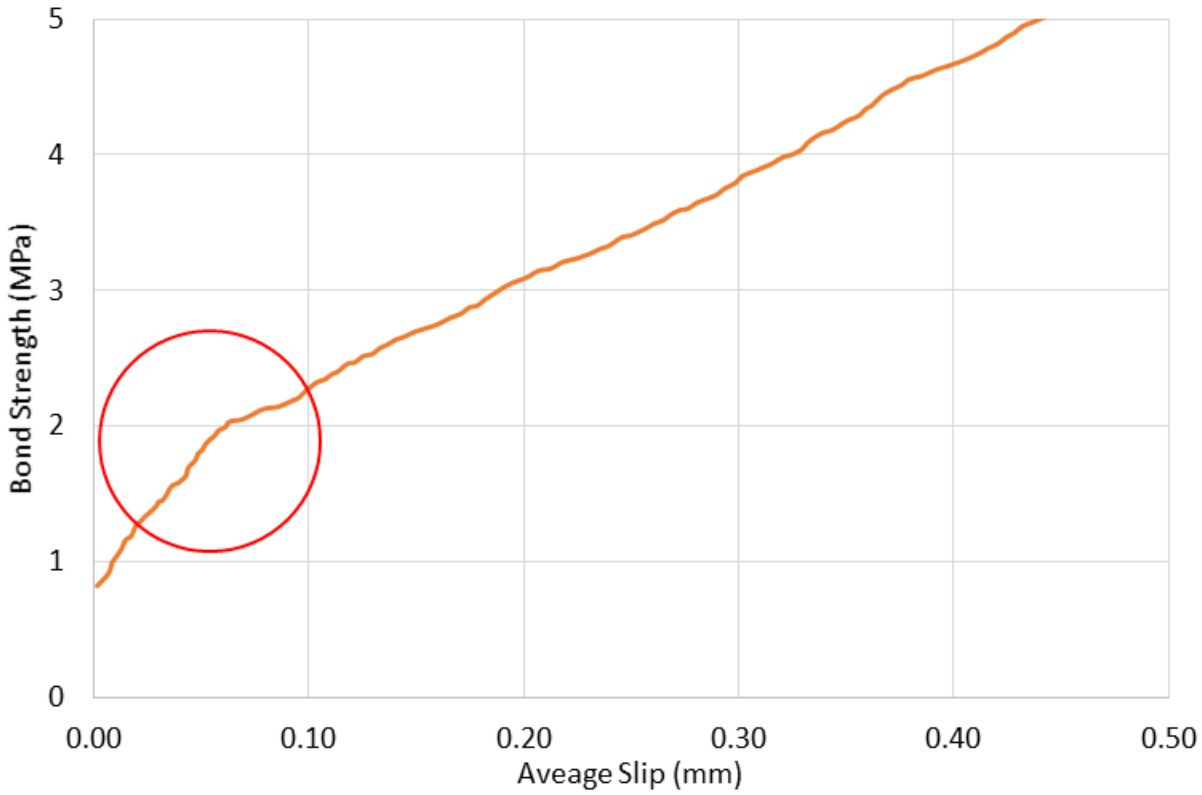

Figure 5-15: Bond strength versus slip; the change in slope encircled, indicates the shear stress at which adhesion is overcome.

For steel reinforcing bars, CSA A23.3 uses Equation 35 [73].

$$l_d = 1.15 \cdot \frac{k_1 \cdot k_2 \cdot k_3 \cdot k_4}{d_{cs} + K_{tr}} \frac{f_y}{\sqrt{f_c'}} A_b \qquad \text{Equation 35}$$

$$d_{cs} \leq \left\{ \begin{array}{c} C_c + \frac{d_b}{2} \\ \frac{2}{3}\ centre\ to\ centre\ spacing \\ 2.5 \cdot d_b \end{array} \right\} \qquad \text{Equation 36}$$

$$K_{tr} = \frac{A_{tr} f_{yt}}{10.5 \cdot s \cdot n} \qquad \text{Equation 37}$$

Where k_1 is a bar location factor, k_2 is the bar coating factor, k_3 is the concrete density factor, k_4 is the bar size factor, d_{cs} is a cover and spacing factor (Equation 36), f_y is the yield strength of the steel, f_c' is the compression strength of concrete, K_{tr} is the transverse reinforcement index, A_{tr} is the area of the stirrups, f_{yt} is the yield strength of the stirrups, s is the stirrup spacing, n is

the number of bars developed, and A_b is the area of the bar. Note that all the modification factors can be found in Table 5-12.

Table 5-12: Modification factors for steel reinforcement

Modification Factor	Value	Comment
k_1	1.3	Horizontal reinforcement with >300mm of concrete below the bar
	1.0	Other cases
k_2	1.5	Epoxy-coated bar with a clear cover $< 3d_b$ or with a clear spacing $< 6d_b$
	1.2	For all other epoxy-coated bar
	1.0	For uncoated bars
k_3	1.3	Low density concrete
	1.2	Semi-low density concrete
	1.0	Normal density concrete
k_4	0.8	For $20M\ bars\ and\ smaller$
	1.0	For $25M\ bars\ and\ larger$

Although most codes have a well-defined development for steel, not many have addressed development length for FRP's. Currently, Eurocode does not explicitly state the development requirements and instead recommend that designers refer to the International Federation for Structural Concrete (FIB) bulletin No. 40 [120]. Bulletin 40 covers the design of concrete reinforced with fibre reinforced polymers, and gives recommendations of using either the Canadian, American, or Japanese code when it comes to the development length of FRP in concrete. Both the American and Canadian code, discussed below, follow very prescriptive measure, whereas the Japanese code often requires the designer to verify bond strength experimentally, and use that to back calculate the development length.

5.2.1. FRP development length according to CSA S806

Similarly to CSA A23.3 development length for steel, CSA S806 [121] quantifies development length for GFRP by Equation 38.

$$l_d = 1.15 \cdot \frac{k_1 \cdot k_2 \cdot k_3 \cdot k_4 \cdot k_5}{d_{cs}} \frac{f_F}{\sqrt{f_c'}} A_b \qquad \text{Equation 38}$$

Where k_1 is a bar location factor, k_2 is the concrete density factor, k_3 is the bar size factor, k_4 is the bar fibre factor, k_5 is the bar surface profile factor, d_{cs} is a cover and spacing factor (Equation

36), f_F is the design stress in tension at ultimate limit state, f_c' is the compression strength of concrete and $\sqrt{f_c'} \leq 5\ MPa$, and A_b is the area of the bar. Note that all the modification factors can be found in Table 5-13.

Table 5-13: Modification factors for FRP reinforcement

Modification Factor	Value	Comment
k_1	1.3	Horizontal reinforcement with >300 mm of concrete below the bar
	1.0	Other cases
k_2	1.3	Low density concrete
	1.2	Semi-low-density concrete
	1.0	Normal density concrete
k_3	0.8	For $A_b \leq 300mm^2$
	1.0	For $A_b > 300mm^2$
k_4	1.0	For CFRP and GFRP
	1.25	For AFRP
k_5	1.0	For surface-roughened or sand-coated surfaces
	1.05	For spiral pattern surfaces
	1.0	For braided surfaces
	1.05	For ribbed surfaces
	1.80	For indented surfaces

The most noteworthy differences between the steel and GFRP development length calculations is the transverse reinforcement index for the steel bars and the limitation of the $\sqrt{f_c'}$ to 5 MPa for FRP bars, essentially limiting the concrete compressive strength to 25 MPa. The lack of a transverse reinforcement index is explained by Wambeke and Shield [122], who demonstrated that, unlike in the case of steel bars, the addition of stirrups did not improve the bond strength of the GFRP bars. Second, limiting the concrete compressive strength suggests the changing failure mechanism from concrete failure to GFRP failure changes the required development length.

5.2.2. FRP development length according to ACI 440

Alternatively, if the American code, ACI 440 [123] is used, Equation 39 is used to define the bar stress.

$$f_{fe} = \frac{0.083\sqrt{f_c'}}{\alpha}\left(\frac{13.6 l_e}{d_b} + \frac{C}{d_b}\frac{l_e}{d_b} + 340\right) \leq f_{fu} \quad \text{Equation 39}$$

$$f_{fu} = C_E \cdot f_{fu}^{*} \quad \text{Equation 40}$$

Where f_{fe} is the bar stress that can be developed by the embedment length l_e, α is a bar location factor (1.0 when there is less than 305 mm of concrete below the horizontal bar, 1.5 when there is more than 305 mm below the horizontal bar), d_b is the bar diameter, c is the concrete cover. and C_E is an environmental reduction factor given in the Table 5-14 below.

Table 5-14: Environmental reduction factor for various fibres and exposure conditions [123]

Exposure Condition	Fibre Type	Environmental reduction factor C_E
Concrete not exposed to earth and weather	Carbon	1.0
	Glass	0.8
	Aramid	0.9
Concrete exposed to earth and weather	Carbon	0.9
	Glass	0.7
	Aramid	0.8

Resolving for the required embedment length to develop the ultimate capacity of the bar:

$$l_e = \frac{\left[\left(\frac{f_{fu}\cdot\alpha}{0.083\sqrt{f_c'}}\right) - 340\right]}{\left(\frac{13.6}{d_b} + \frac{c}{d_b}\cdot\frac{1}{d_b}\right)} \quad \text{Equation 41}$$

ACI 440 describes the transfer of force through bond using Equation 42

$$l_e \pi d_b u = A_f f_f \quad \text{Equation 42}$$

Where u is the bond stress, A_f is the cross sectional area of fibre reinforced polymer, f_{fu} is the stress in the FRP reinforcement in tension.

5.2.3. Analysis of code provisions

In order to assess the development length from the two codes, ACI 440 and CSA S806, as well as compare these values to the data collected, an assessment was done comparing the results from Equation 39, Equation 41, and Equation 42 using the results from 3.3.1. It should be noted that f_c' values and u values used are the average from the lab tests completed, the results of which are plotted in Figure 5-16 to Figure 5-19.

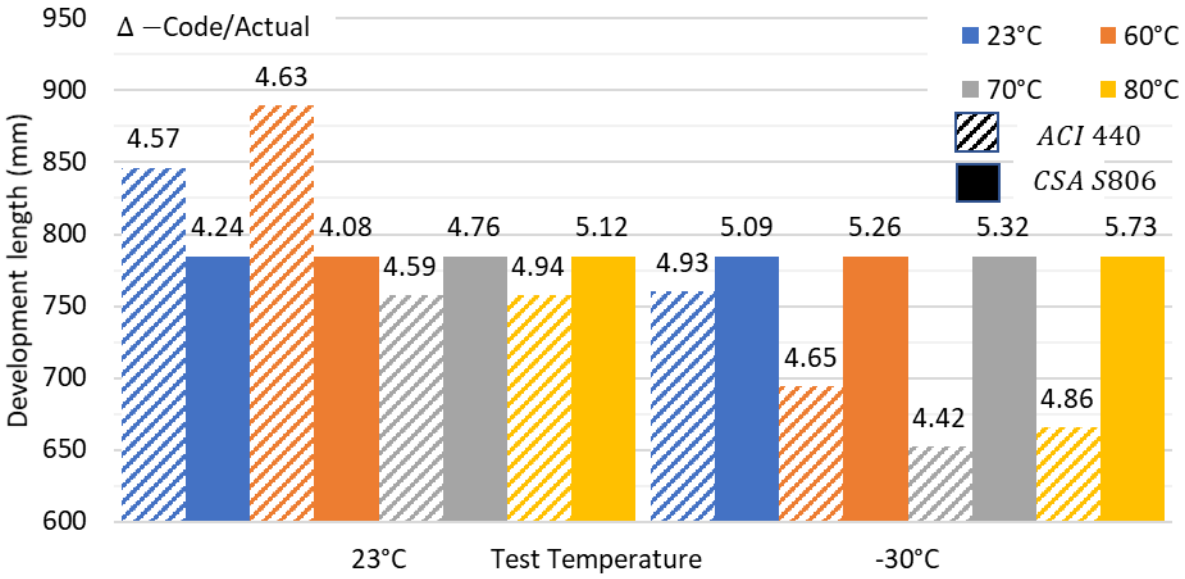

Figure 5-16: Development length according to the ACI (hatched bars) and CSA code (solid bars). The number above column gives the ration of these development lengths to the average of those determined as being actually required from bond strength testing for 12 mm Schöck – Combar.

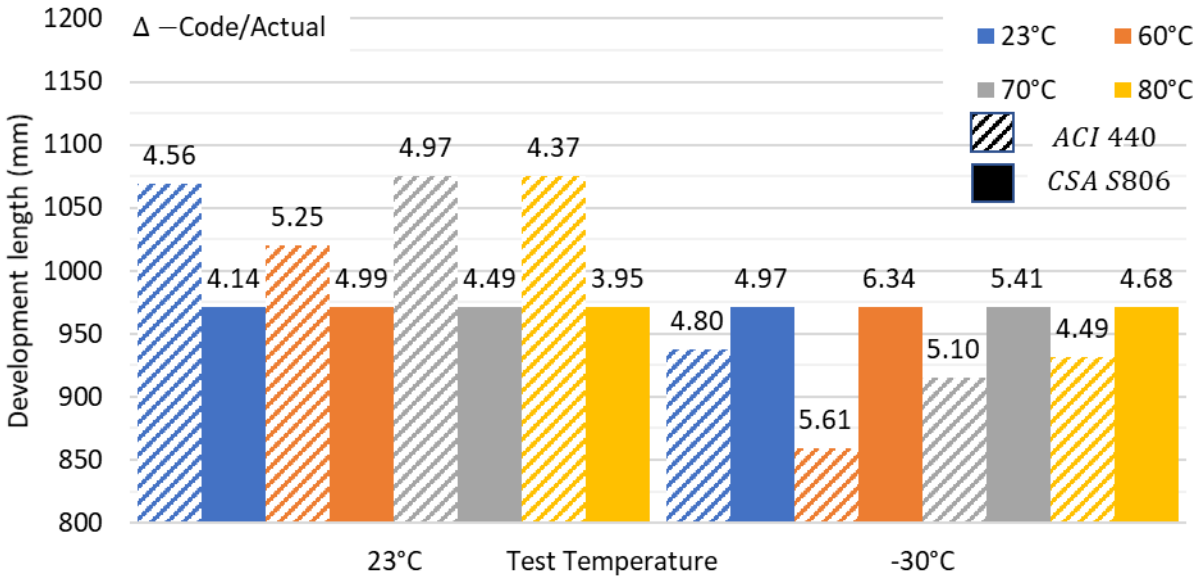

Figure 5-17: Development length according to the ACI (hatched bars) and CSA code (solid bars). The number above column gives the ration of these development lengths to the average of those determined as being actually required from bond strength testing for 16 mm Schöck – Combar.

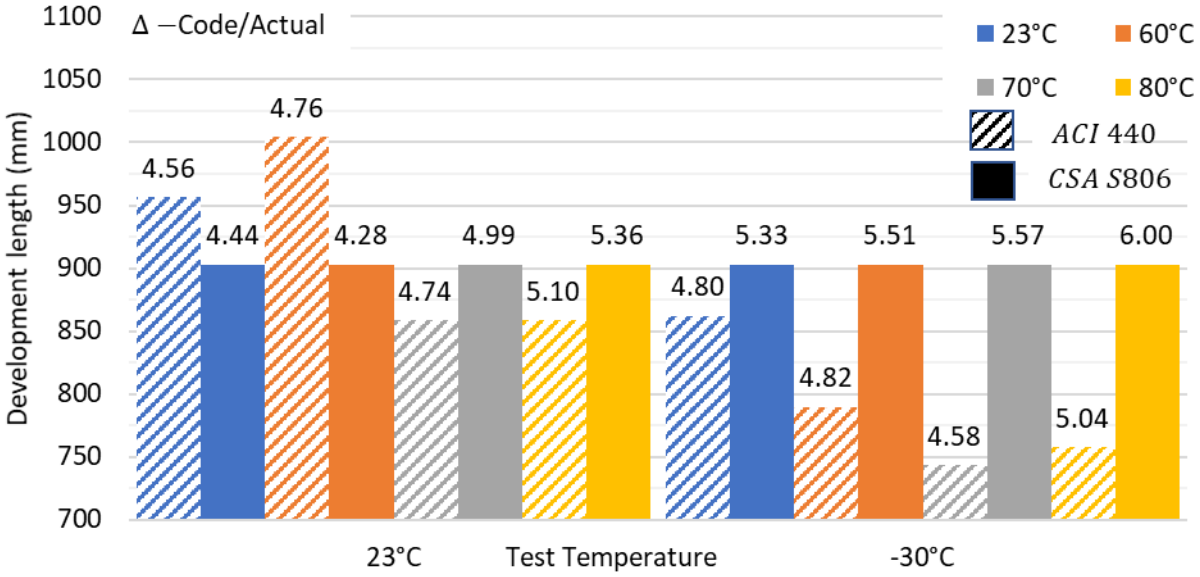

Figure 5-18: Development length according to the ACI (hatched bars) and CSA code (solid bars). The number above column gives the ration of these development lengths to the average of those determined as being actually required from bond strength testing for #4 Pultrall bars

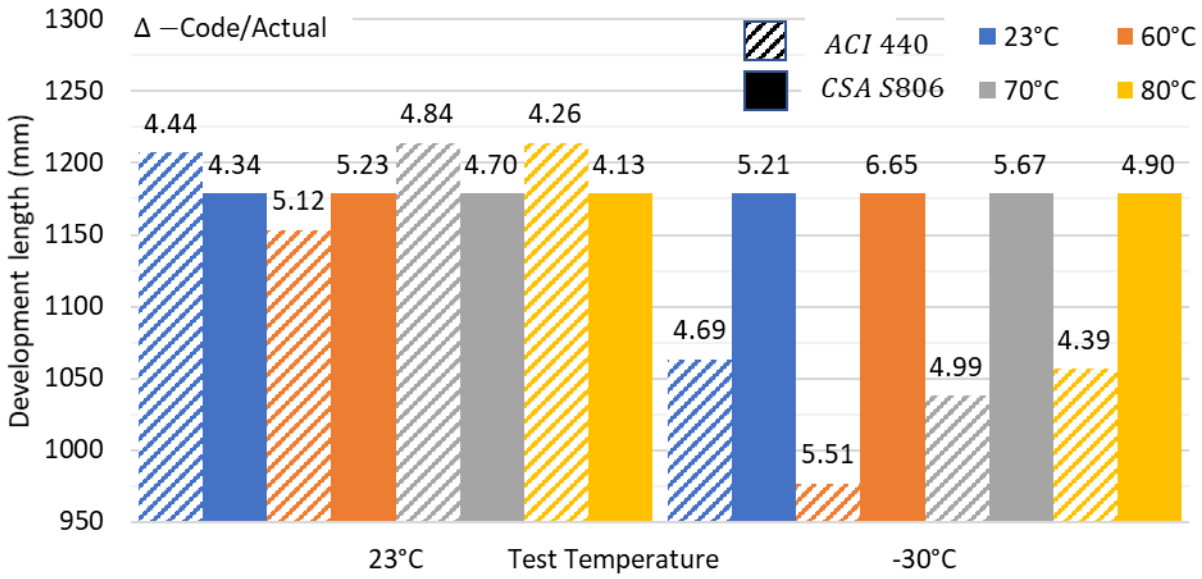

Figure 5-19: Development length according to the ACI (hatched bars) and CSA code (solid bars). The number above column gives the ration of these development lengths to the average of those determined as being actually required from bond strength testing for #5 Pultrall bars

The first thing to note is that the development length, according to CSA S806, depends only on the bar surface finish and diameter as the compressive strength in the concrete exceeds 25MPa. This means that the development length for the Schöck – Combar bars is 785 mm for the 13 mm bar and 971 mm for the 16 mm bar. Similarly, it means the development length for the #4 and #5 Pultrall bars are 903 mm and 1179 mm respectively. If, in turn, the code provisions are compared with the actual test data, by dividing the code data by the lab results, the average ratios for both the Combar and Pultrall bars indicate the conservative nature of the codes. These results are available in Table 5-15 and Table 5-16 respectively.

Table 5-15: Ratio of development length code provisions vs lab data for Schöck – Combar rebar.

	Combar – 13 mm			**Combar – 16 mm**		
	Equation 41	ACI 440	CSA S806	Equation 41	ACI 440	CSA S806
	l_e (mm)	$\frac{experiment}{code}$	$\frac{experiment}{code}$	l_e (mm)	$\frac{experiment}{code}$	$\frac{experiment}{code}$
	185	4.57	4.24	234	4.56	4.14
	192	4.63	4.08	194	5.25	4.99
	165	4.59	4.76	216	4.97	4.49
	153	4.94	5.12	246	4.37	3.95
	154	4.93	5.09	195	4.80	4.97
	149	4.65	5.26	153	5.61	6.34
	148	4.42	5.32	179	5.10	5.41
	137	4.86	5.73	207	4.49	4.68
Avg	160.45	4.70	4.95	203.30	4.89	4.87
Std	17.93	0.18	0.52	27.88	0.40	0.71

Table 5-16: Ratio of development length code provisions vs lab data for Pultrall rebar.

	Pultrall - #4			**Pultrall - #5**		
	Equation 41	ACI 440	CSA S806	Equation 41	ACI 440	CSA S806
	l_e (mm)	$\frac{experiment}{code}$	$\frac{experiment}{code}$	l_e (mm)	$\frac{experiment}{code}$	$\frac{experiment}{code}$
	203.3	4.70	4.44	271.7	4.44	4.34
	211.2	4.76	4.28	225.4	5.12	5.23
	181.1	4.74	4.99	250.7	4.84	4.70
	168.5	5.10	5.36	285.2	4.26	4.13
	169.4	5.09	5.33	226.5	4.69	5.21
	163.9	4.82	5.51	177.4	5.51	6.65
	162.0	4.58	5.57	208.0	4.99	5.67
	150.5	5.04	6.00	240.5	4.39	4.90
Avg	176.26	4.85	5.18	235.67	4.78	5.10
Std	19.70	0.18	0.55	32.32	0.39	0.75

If the two codes are compared, CSA S806 is more conservative, except for the 16 mm Schöck – Combar, where the averages between it and ACI 440 are extremely close. The standard deviation of the CSA provisions compared with the test data are also much higher as the test data varied, sometimes significantly, with compressive strength.

If the actual compressive strength of the concrete is used to compare the CSA development length requirement, the ratio's become much more reasonable for the bars from Schöck – Combar. Figure 5-20 indicates that the development length for 13 mm bars is more conservative, with ratio of modified code to actual bond length of between 2.56 and 2.89. The ratios for the 16 mm bars varied much more significantly, between 2.55 and 3.31 times the experimental values.

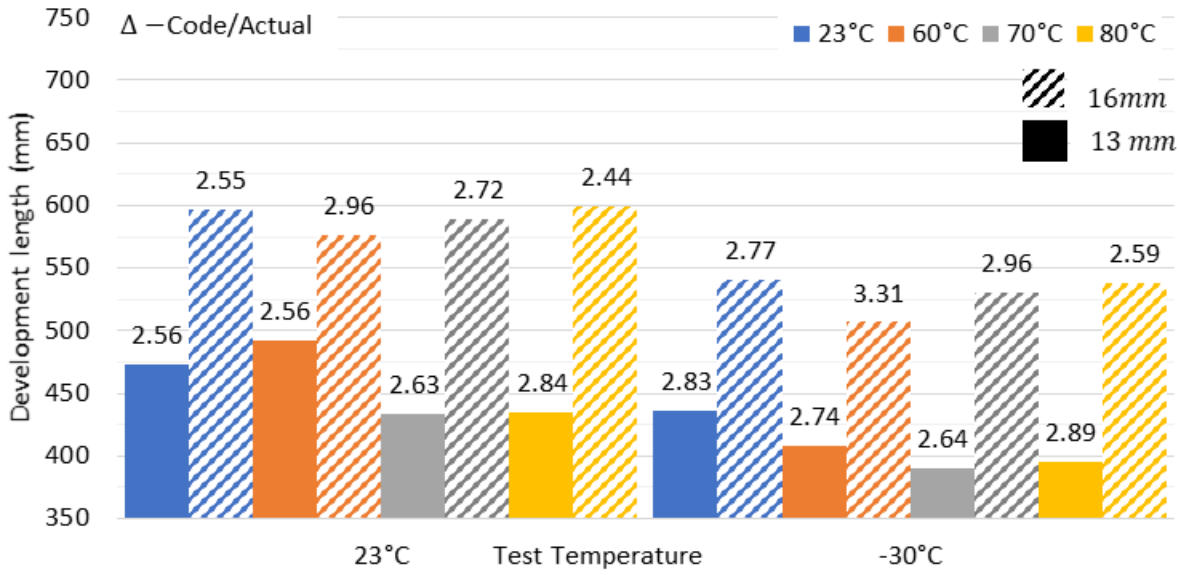

Figure 5-20: Development lengths using the modified CSA code. The numbers above the bars are the ratio of these development lengths to those actually required as calculated from bond strength values for Schöck – Combar bars

Similarly, if the modified code requirements are compared to the experimental data for the bars from Pultrall, the ratios are similar to the Schöck – Combar. The #4 mm bar ratios range from 2.68 to 3.03, whereas the #5 mm bars range from 2.55 to 3.47, Figure 5-21.

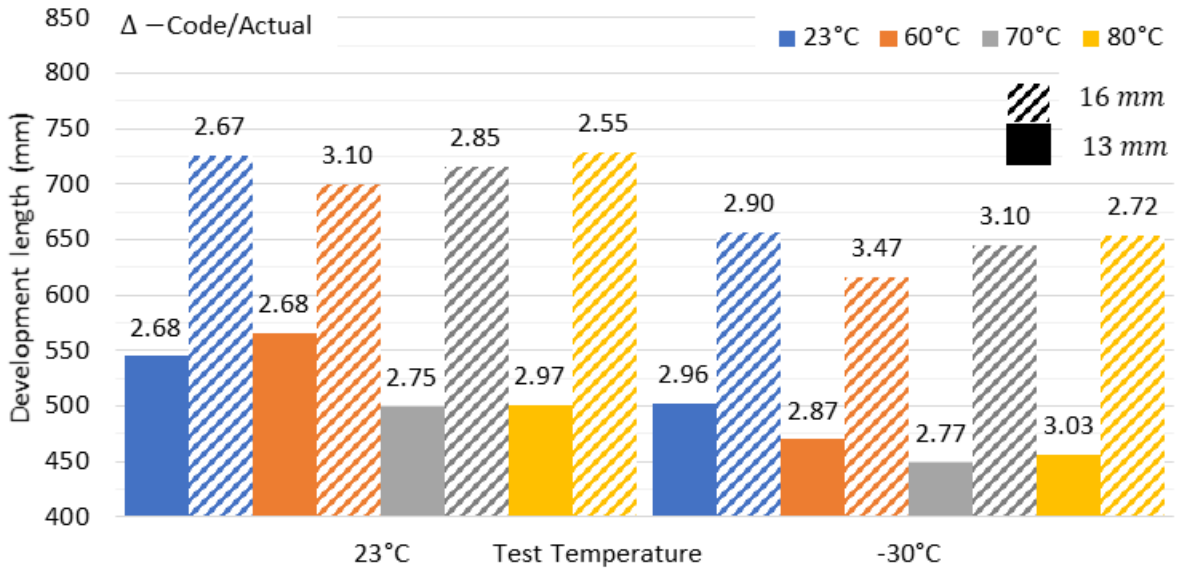

Figure 5-21: Development lengths using the modified CSA code. The numbers above the bars are the ratio of these development lengths to those actually required as calculated from bond strength values for Pultrall bars

The current research has indicated that the both CSA and ACI design codes are very conservative based on the pullout tests conducted. As such and as demonstrated above, the CSA code could be improved by using the actual design strength of the concrete, instead of not allowing bond strength gains for concrete strengths above 25 MPa. Alternatively, the code could add a parameter to account for the shear strength of the GFRP resin in high strength concrete. The resin strength could be correlated to composite failure numbers in order to more accurately account for product variability.

These changes should be considered in light of the confinement provided by the test apparatus, the pullout test method, and the size of the members being tested, which some authors suggest do not accurately represent the structures in the field [122]. Confinement has been shown, in extreme cases, to provided increased bond strength of up to 300% [124]. Typically, confinement provided by transverse reinforcement provides an additional 10 – 15% in bond strength [125]. The pullout method, which does force the surrounding concrete into compression as opposed to the concrete tension experienced in the field, leads to higher bond strengths. Benmokrane et al. [126] noted that, when pullout specimen bond strengths are compared to beam specimen bond strengths, pullout strengths range from 105% to 182% of the beam specimens. Achillides [127] noted similar results, but compared the embedment length. When the embedment length was $5d_b$, he noted increased bond strength increases of 140% between the pullout and beam tests, whereas if the embedment length was increased to $7.5d_b$ the corresponding bond stress increase was 165%. Lastly, the top bar in deep beams often experiences bond strength reductions of up to 30% compared with bottom bars due to bleed water accumulating under the bars [128].

Chapter 6 Conclusions and Recommendations

The following chapter presents conclusions and recommendations based on the laboratory and analytical research presented throughout this manuscript. It is divided into two sections, Section 6.1 reiterating the importance of the research and discussing how the research met the research objectives and Section 6.2 making recommendations for further research as well as design considerations for industry practices.

6.1. Conclusions

6.1.1. Based on experimental research

- After more than 300 24-hour freeze thaw cycles, the relative dynamic modulus of elasticity has not indicated degradation of the concrete caused by differences in coefficients of thermal expansion between the GFRP and concrete. These results, based on specimens with reduced concrete cover, provide evidence that designers need not be wary of the thermal fatigue or differential CTE while using GFRP in thin slabs or in structures, such as barrier walls, where reduced cover may be desirable.

- Concrete specimens exposed to both multi-chloride brine and the southern Ontario climate for nearly 4 years do not appear, at the surface, to have experienced any deleterious effects due to the GFRP reinforcement. This confirms the results from the rapid freeze-thaw cycles. Although the specimens appear to experience relatively large strain measurements, the difference between the strain in the concrete and that in the GFRP-reinforced concrete remained consistently below levels required to induce cracking. However, the effect of multi-chloride brine combined with freeze-thaw cycles can reduce both the compressive strength and the actual cross-sectional dimensions of the concrete. This reduces the bending moment capacity as the internal force couple relies on the maximum compression force the concrete can take.
- Neither service temperature nor curing temperature negatively affected the bond strength of GFRP in high strength concrete in these tests. A decrease in the service, or testing temperature, was found only to increase the compressive strength of concrete. This is attributed to pore water freezing which provides resistance to crushing. Contrary to the initial hypothesis, this increased compressive strength at -30°C, by as much as 1.45 times that of the ambiently tested specimens, always increased bond strength with the GFRP. This bond strength increase was between 10 and 29 percent.
- Contrary to the bond strength equation, Equation 22, which Lee et al. [90] proposed whereby a value for β of 0.3 can be used to GFRP , the author suggests that the coefficient be increased to 0.35 for helical ribbed bars and 0.40 for sand coated bars, based on the results presented in this work. These values, based on tests herein, are more conservative for this data set as no test data actually fall below the proposed values, unlike the initial study.
- In GFRP-reinforced high strength concrete, i.e. with compressive strength higher than 60 MPa, the failure mode is often composite, both rib and sand coating delaminating from the fibrous core and concrete shearing at the GFRP concrete interface. In these cases, the sand coated bars had a higher bond strength than the ribbed bars. The author cannot directly relate this to the shear strength of the vinyl-ester resin, as that value is not known. Instead it is hypothesized that the shear stress experienced in the resin at the base of the rib is 66% larger for the helically ribbed bars than the stress experienced between the sand and bar core of the Pultrall bars, which causes failure at a lower load.
- The concrete specimens exposed to $CaCl_2$, $MgCl_2$, or multichloride brines experienced compressive strength reductions, compared with concrete cured at 100% RH, of up to 30%. When compared to their 28-day strengths, the multichloride, $CaCl_2$ and $MgCl_2$ saw reductions of up to 8%, 18%, and 19% respectively. In the case of $MgCl_2$, a negative reaction between $MgCl_2$ and the $Ca(OH)_2$ and Calcium-silicate-hydrate components of the cement paste causes the formation of $Mg(OH)_2$ and magnesium-silicate-hydrate. The $Mg(OH)_2$ precipitates and reduces the pore solution pH to a level at which steel is not passive and the Mg-S-H which is gelatinous, provides no strength or binding to the

aggregates. In the case of $CaCl_2$, the $CaCl_2$ reacts with the calcium hydroxide to form calcium hydroxichloride which is expansive and causes microcracking of the cement paste component of the concrete.

- The chloride in the pore solution of cement pastes, with and without supplementary cementitious materials, appear to reach a saturation limit when the pore solution chloride concentration exceeds 17.5 wt.% chloride. The actual maximum pore solution chloride concentration was observed to be ~17.5 wt.% for GU, 18.3 wt.% for GU-FA, 18.8 wt.% for GU-BFS and 20.5 wt.% for GU-SF, all at a cast in chloride content of 7.5% by mass of cementitious material. This indicated that concrete containing different SCM's will, if exposed to similar levels of chloride, bind different amount of chloride, leading to more or less aggressive corrosion conditions.
- While an increased chloride content in pore solution was expected with an increase of admixed chloride, the observed increasing level of sulphates was not. This sulphate release, likely due to an anion exchange between the chloride and sulphates in the aluminate phases, causes higher concentration of sulphates in the pore solution and less chloride as the chloride was then physically bound in different cement phases.

6.1.2. Based on analytical modelling

- As indicated by the experimental results, the compression strength of concrete increases in a frozen state. A statistical analysis using variability in: (i) material properties, (ii) workmanship, (iii) moisture content, and (iv) curing practices indicated, logically, that when the compressive strength increased that the moment resistance of the structure also increased. Notably, this increase lead to a change in failure mechanism from the desirable over-reinforced structure, in the case of GFRP reinforced structures, to an under-reinforced structure. Although this more brittle failure mechanism is not recommended, the increased capacity was well above the design requirements, indicating that failure is much less likely to occur.
- The ingress of $MgCl_2$ and $CaCl_2$ can lead to compressive strength reductions of nearly 30%. Using Monte Carlo simulation, a significant reduction in the structural capacity of the member is to be expected. Similar to when the concrete strength increases, the failure mechanism of the structure is predicted to change. When designing with steel, this means that the structure goes from an under-reinforced failure, where the steel yields, to an over reinforced structure, where the concrete crushes. Consequently, design considerations should be made to structures in high chloride application zones to ensure public safety.
- When CSA and ACI development length requirements are compared to bond strength results of the experimental program, a large difference is noted, as high as 6 times the experimental result. This, in the case of the Canadian code, is reduced by limiting the concretes contribution to the bond strength to a max compressive strength of 25 MPa.

The code sets this limit because when the compressive strength of the concrete exceeds 25 MPa, researchers have often recorded composite failures, where both the GFRP and concrete fail at their interface. The experimental results presented here indicate that, for compressive strength exceeding 60 MPa, composite failures do occur, but only with a much larger load than the code allows. As such, the code should consider design changes for high strength concrete mixes.

6.2. Recommendations

6.2.1. Improved test matrix to determine the bond strength of GFRP in high strength concrete

The most difficult part of analyzing the statistical significance of bond strength of GFRP in high strength concrete was the lack of repeatability. Due to space and equipment constraints multiple concrete batches were used to compare the different curing programs and different testing temperatures. This allowed for limited comparison on the effects of the curing temperature, and was unable to indicate if the 80°C curing temperature posed a threat to the compressive strength. Ideally, all four curing temperatures for each bar supplier and bar diameter would be cast simultaneously, and cured in four different environmental conditioning chambers. The number of replicates for each testing condition would also be increased to seven, from four. This would increase the probability of five successful tests, and limit the effect of samples failing by grip slippage instead of bond failure.

6.2.2. Comparative bond strength across multiple test procedures

As is always the case in engineering research, the researchers are trying to predict structural service conditions with efficient and repeatable lab testing. The applicability of pullout testing has been discussed in depth in the body of this text. Therefore, a comparative study of pullout in high strength concrete, should be conducted whereby pullout in beams deeper than 300 mm would be tested to observe the effect of confinement, embedment length, bleed water, and bar diameter on bond strength of GFRP bars in concrete.

6.2.3. Improved analytical model for decreased compressive strength caused by chloride ingress

The model, presented in section 5.1.9, followed the design code in using an equivalent stress block analysis to determine the compression force in the concrete and corresponding equal force in the tensile reinforcement. This is, traditionally, a conservative simplification of the area under a parabolic curve. In order to increase the accuracy of the statistical model, two improvements could be made. Firstly, the compression force in the concrete can be determine using Simpsons Rule, based on a Thorenfeldt stress-strain curve. Secondly, consideration should be given to how the chloride penetration front affects the compressive strength of the concrete using the considerations of Equation 43, based on Figure 6-1.

$$f'_{c1} < f'_{c2} < f'_{c3} < f'_c$$ Equation 43

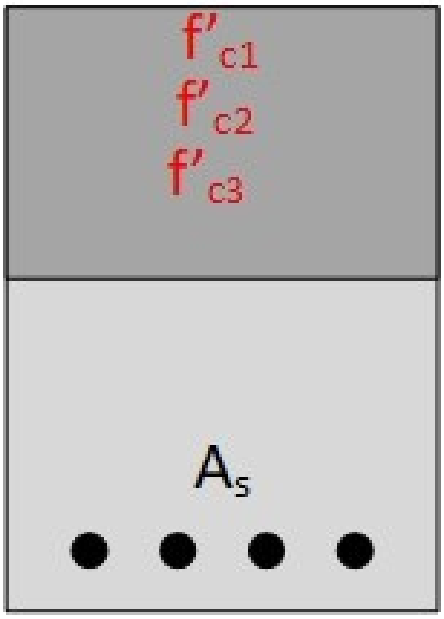

Figure 6-1: Variations in compressive strength

Essentially, experiments must be conducted to correlate $MgCl_2$ and $CaCl_2$ concentrations to tested reductions in compressive strengths. This, alongside field data from structural condition surveys, could determine the actual stress in the concrete using the corresponding transformed section analysis.

6.2.4. Improved test matrix to determine the effect of temperature on compressive strength of concrete

Although a large increase in the compressive strength of concrete subjected to -30°C was observed over the 56-day duration, a larger scale matrix could help determine the effect of: test temperature, concrete age and freeze-thaw cycling, as well as different moisture contents. This in turn would could include a longitudinal study to determine these effects over a period of years, which could in turn be incorporated into a mechanistic model.

References

1. Kosmatka, S.H., B. Kerkhoff, and W.C. Panarese, *Design and Control of Concrete Mixtures*. Fourteenth ed. 2002, 5420 Old Orchard Road Skokie, Illinois Portland Cement Association.
2. Hassoun, M.N. and A. Al-Manaseer, *Structural Concrete: Theory and Design*. 2015: Wiley.
3. Mahgnusson, C.E. and G.H. Smith. *Electrolytic Corrosion of reinforced concrete*. in *American Institute of Electrical Engineers*. 1911.
4. Brown, H.H., *Serious injury to a reinforced concrete building by electrolysis.* Engineering News Record, 1911: p. 95.
5. Poulsen, E. and L. Mejlbro, *Diffusion of Chloride In Concrete: Theory and Application*. 2006, 270 Madison Ave, New York: Taylor and Francis.
6. Diamond, S., *Effects of two Danish flyashes on alkali contents of pore solutions of cement-flyash pastes.* Cement and Concrete Research, 1981. **11**(3): p. 383-394.
7. Marcotte, T.D., *Characterization of chloride-induced corrosion products that form in steel-reinforced cementitious materials*. 2001, UWSpace.
8. Marcotte, T.D. and C.M. Hansson, *Corrosion products that form on steel within cement paste.* Materials and Structures, 2007. **40**(3): p. 325-340.
9. Knudsen, A., F. Jensen, O. Klinghoffer, and T. Skovsgaard. *Cost-effective enhancement of durability of concrete structures by intelligent use of stainless steel reinforcement*. in *Conference on Corrosion and rehabilitation of reinforced concrete structures, Florida*. 1998.
10. Koch, G.H., M. Brongers, N.G. Thomspon, Y.P. Virmani, and J.H. Payer, *Corrosion Cost and Preventive Strategies in the United States*. 2002, Research, Developmet, and Technology Turner-Fairbank Highway Research Center: 6300 Georgetown Pike McLean, VA 22101 - 2296
11. Kirkpatrick, T.J., R.E. Weyers, C.M. Anderson-Cook, and M.M. Sprinkel, *Probabilistic model for the chloride-induced corrosion service life of bridge decks.* Cement and Concrete Research, 2002. **32**(12): p. 1943-1960.
12. Bentz, E.C., *Probabilistic modeling of service life for structures subjected to chlorides.* ACI Materials journal, 2003. **100**(5): p. 391-397.
13. Hartt, W.H., *Service Life Projection for Chloride-Exposed Concrete Reinforced with Black and Corrosion Resistant Bars.* Corrosion, 2012. **68**(8): p. 754-761.
14. ASTM International, *ASTM C666: Standard Test Mehod for Resistance of Concrete to Rapid Freezing and Thawing*. 2008, ASTM International: West Conshohocken, PA.
15. ASTM International, *ASTM D7913: Standard Test Method for Bond Strength of Fiber-Reinforced Polymer Matrix Composite Bars to Concrete by Pullout Testing*. 2014, ASTM International: West Conshohocken, PA.
16. Hooton, R.D. and M.P. Titherington, *Chloride resistance of high-performance concretes subjected to accelerated curing.* Cement and Concrete Research, 2004. **34**(9): p. 1561-1567.
17. Ontario Provincial Standard Specification, *Material Specification for Concrete - Materials and Production*. 2014, Ministry of Transportation of Ontario: Toronto, Ontario.
18. Ontario Provincial Standard Specification, *Construction specification for concrete structures*. 2014, Ministry of Transportation of Ontario: Toronto, Ontario.

19. Ontario Provincial Standard Specification, *Construction specification for prestressed concrete - precast members*. 2012, Ministry of Transportation of Ontario: Toronto, Ontario.
20. Canadian Standards Association, *Precast Concrete - Materials and Construction*. 2016, Canadian Standards Association, : Mississauga, Ontario, Canada. p. 91.
21. Verbeck, G.J. and R.H. Helmuth. *Structures and physical properties of cement paste*. in *5th International Conference on the Chemistry of Cement*. 1968. Tokyo.
22. Taylor, H.F.W., C. Famy, and K.L. Scrivener, *Delayed ettringite formation.* Cement and Concrete Research, 2001. **31**(5): p. 683-693.
23. Heinz, D. and U. Ludwig, *Mechanism of Secondary Ettringite Formation in Mortars and Concretes Subjected to Heat Treatment.* ACI Symposium Publication, 1987. **100**.
24. Eglinton, M., *7 - Resistance of Concrete to Destructive Agencies*, in *Lea's Chemistry of Cement and Concrete (Fourth Edition)*, P.C. Hewlett, Editor. 1998, Butterworth-Heinemann: Oxford. p. 299-342.
25. Aslanova, L.G. and O.A. Resnyansky. *non-metallic (FRP) reinforcement for concrete structures*. in *Second International RILEM sysmposium*. 1995. Ghent, Belgium: Chapman and Hall.
26. Wallenberger, F.T., J.C. Watson, and H. Li, *Glass Fibers*. 2001, American Society of Metals International ;: Novelty Ohio, USA. p. 27 - 35.
27. Benmokrane, B., O. Chaallal, and R. Masmoudi, *Glass fibre reinforced plastic (GFRP) rebars for concrete structures.* Construction and Building Materials, 1995. **9**(6): p. 353-364.
28. Fiberline. *Safe and Health Production environment*. 2016 June 22, 2016]; Available from: https://fiberline.com/safe-and-healthy-production-environment.
29. American Concrete Institute 440 committee - Fiber Reinforced Polymer Reinforcement, *Guide for the Design and Construction of Structural Concrete Reinforced with FRP Bars*. 2006, American Concrete Institute;: Farmington Hills, MI, USA;.
30. Katz, A., N. Berman, and Lawrence C. Bank, *Effect of High Temperature on Bond Strength of FRP Rebars.* Journal of Composites for Construction, 1999. **3**(2): p. 73-81.
31. Robert, M. and B. Benmokrane, *Behavior of GFRP Reinforcing Bars Subjected to Extreme Temperatures.* Journal of Composites for Construction, 2010. **14**(4): p. 353-360.
32. Wright, W., B. Lattimer, M. Woodworth, M. Nahid, and E. Sotelino, *Highway Bridge Fire Hazard Assessment*. 2013, Virginia Polytechnic Institute and State University: Blacksburg, VA. p. 492.
33. Bai, Y., W.R. Burkett, and P.T. Nash, *Rapid Bridge Replacement under Emergency Situation: Case Study.* Journal of Bridge Engineering, 2006. **11**(3): p. 266-273.
34. Sousa, J.M., J.R. Correia, S. Cabral-Fonseca, and A.C. Diogo, *Effects of thermal cycles on the mechanical response of pultruded GFRP profiles used in civil engineering applications.* Composite Structures, 2014. **116**: p. 720-731.
35. Karbhari, V.M., J.W. Chin, D. Hunston, B. Benmokrane, T. Juska, R. Morgan, J.J. Lesko, U. Sorathia, and D. Reynaud, *Durability Gap Analysis for Fiber-Reinforced Polymer Composites in Civil Infrastructure.* Journal of Composites for Construction, 2003. **7**(3): p. 238-247.

36. Alves, J., A. El-Ragaby, and E. El-Salakawy, *Durability of GFRP Bars’ Bond to Concrete under Different Loading and Environmental Conditions.* Journal of Composites for Construction, 2011. **15**(3): p. 249-262.
37. Oswald, C.J., G. Giberson, E. Nicholls, C. Wellen, and S.R. O'ni, M., *Spatial distribution and extent of urban land cover control watershed-scal chloride retention.* Science of the Total Environment, 2019. **652**: p. 278-288.
38. Sutter, L., K. Peterson, S. Touton, T. Van Dam, and D. Johnston, *Petrographic evidence of calcium oxychloride formation in mortars exposed to magnesium chloride solution.* Cement and Concrete Research, 2006. **36**(8): p. 1533-1541.
39. Prannoy Suraneni, Jonathan Monical, Erol Unal, Yaghoob Farnam, and W. Jason, *Calcium Oxychloride Formation Potential in Cementitious Pastes Exposed to Blends of Deicing Salt.* Materials Journal, 2017. **114**(4).
40. Hansson, C.M., Frølund, Th. and Markussen, J.B., *The Effect of Chloride Cation Type on the Corrosion of Steel in Concrete by Chloride Salts.* Cement and Concrete Research, 1985. **15**: p. 65-73.
41. Poursaee, A., A. Laurent, and C.M. Hansson, *Corrosion of steel bars in OPC mortar exposed to NaCl, MgCl2 and CaCl2: Macro- and micro-cell corrosion perspective.* Cement and Concrete Research, 2010. **40**(3): p. 426-430.
42. Hunt, M.J. and C.M. Hansson, *The Influence of the Cations in Anti-Icing Brines on the Corrosion of Reinforcing Steel in Synthetic Concrete Pore Solution.* CORROSION, 2015. **71**(6): p. 749-757.
43. Kurdowski, W., *The protective layer and decalcification of C-S-H in the mechanism of chloride corrosion of cement paste.* Cement and Concrete Research, 2004. **34**(9): p. 1555-1559.
44. Lee, H., R.D. Cody, A.M. Cody, and P.G. Spry. *Effects of Various Deicing Chemicals on Pavement Concrete Deterioration*. in *Mid-Continent Transportation Symposium*. 2000. Ames, Iowa, United States of America.
45. Julio-Betancourt;, G.A. and R.D. Hooton, *Calcium and magnesium chloride attack on cement-based materials: formation, stability, and effects of oxychlorides*, in *2nd RILEM International Workshop on Concrete Durability and Service Life Planning - ConcreteLife'09*, K. Kovler, Editor. 2009, RILEM Publications SARL. p. 432-439.
46. Glass, G.K. and N.R. Buenfeld, *The Presentation of the Chloride Threshold Level for Corrosion of Steel in Concrete.* Corrosion Science, 1997. **39**(5): p. 1001-1013.
47. Sagüés, A.A., K. Lau, R.G. Powers, and R.J. Kessler, *Corrosion of Epoxy-Coated Rebar in Marine Bridges—Part 1: A 30-Year Perspective.* Corrosion, 2010. **66**(6): p. 065001-065001-13.
48. Lu, Z.-H., Y.-G. Zhao, Z.-W. Yu, and F.-X. Ding, *Probabilistic evaluation of initiation time in RC bridge beams with load-induced cracks exposed to de-icing salts.* Cement and Concrete Research, 2011. **41**(3): p. 365-372.
49. De Weerdt, K., A. Colombo, L. Coppola, H. Justnes, and M.R. Geiker, *Impact of the associated cation on chloride binding of Portland cement paste.* Cement and Concrete Research, 2015. **68**: p. 196-202.
50. Goñi, S. and C. Andrade, *Synthetic concrete pore solution chemistry and rebar corrosion rate in the presence of chlorides.* Cement and Concrete Research, 1990. **20**(4): p. 525-539.

51. Kouřil, M., P. Novák, and M. Bojko, *Threshold chloride concentration for stainless steels activation in concrete pore solutions.* Cement and Concrete Research, 2010. **40**(3): p. 431-436.
52. Ogunsanya, I. and C. Hansson, *Detection of the critical chloride threshold of carbon steel rebar in synthetic concrete pore solutions.* RILEM Technical Letters, 2019. **3**(0).
53. Ogunsanya, I. and C. Hansson, *Detection of the critical chloride threshold of stainless steel rebar in synthetic concrete pore solutions.* In Press, 2019(0).
54. Alonso, C., C. Andrade, M. Castellote, and P. Castro, *Chloride threshold values to depassivate reinforcing bars embedded in a standardized OPC mortar.* Cement and Concrete Research, 2000. **30**(7): p. 1047-1055.
55. Niejenhuis, C.B.V., T.W. Bandura, and C.M. Hansson, *Evaluation of the Proposed European Test Procedure for Ranking Stainless Steel Rebar.* CORROSION, 2016. **72**(6): p. 834-842.
56. Scott, A. and M.G. Alexander, *Effect of supplementary cementitious materials (binder type) on the pore solution chemistry and the corrosion of steel in alkaline environments.* Cement and Concrete Research, 2016. **89**: p. 45-55.
57. Barneyback, R.S. and S. Diamond, *Expression and analysis of pore fluids from hardened cement pastes and mortars.* Cement and Concrete Research, 1981. **11**(2): p. 279-285.
58. Page, C.L. and Ø. Vennesland, *Pore solution composition and chloride binding capacity of silica-fume cement pastes.* Matériaux et Construction, 1983. **16**(1): p. 19-25.
59. Luo, R., Y. Cai, C. Wang, and X. Huang, *Study of chloride binding and diffusion in GGBS concrete.* Cement and Concrete Research, 2003. **33**(1): p. 1-7.
60. Anders, K.A., B.P. Bergsma, and C.M. Hansson, *Chloride concentration in the pore solution of Portland cement paste and Portland cement concrete.* Cement and Concrete Research, 2014. **63**: p. 35-37.
61. Bertolini, L., F. Bolzoni, T. Pastore, and P. Pedeferri, *Behaviour of Stainless Steel in Simulated Concrete Pore Solution.* British Corrosion Journal, 1996. **31**(3): p. 218-222.
62. Bertolini, L. and M. Gastaldi. *Corrosion resistance of austenitic and low-nickel duplex stainless steel bars*. in *Eurocorr 2009*. 2009. Nice, France.
63. Hurley, M.F. and J.R. Scully, *Threshold chloride concentrations of selected corrosion-resistant rebar materials compared to carbon steels.* Corrosion 2006. **62**(10): p. 892-904.
64. ASTM, *A955M - Standard Specification for Deformed and Plain Stainless Steel Bars for Concrete Reinforcement*. 2010, American Society for Testing and Materials: Philadelphia, PA.
65. Randström, S., M. Almén, R. Petersson, and M. Adair, *Reproducibility of critical chloride threshold levels for stainless steel reinforcement*, in *Structural Faults and Repair*. 2010: Edinburgh, UK.
66. Structure and Bridge Division, *Corrosion Resistant Reinforcing Steels (CRR): Plan modifications for projects with CRR*. 2016, Virginia Depatment of Transportation,. p. 11.
67. Van Niejenhuis, C.B., S. Walbridge, and C.M. Hansson, *The performance of austenitic and duplex stainless steels in cracked concrete exposed to concentrated chloride brine.* Journal of Materials Science, 2015. **51**(1): p. 1-13.
68. ASTM International, *Standard Test Method for Corrosion Potentials of Uncoated Reinforcing Steel in Concrete*. 2009, ASTM International,: West Conshohocken, PA.

69. Zemajtis, J., *Modeling the Time to Corrosion Initiation for Concretes with Mineral Admixtures and/or Corrosion Inhibitors in Chloride-Laden Environments*, in *Civil Engineering*. 1998, Virginia Tech: Blacksburg, Virginia, United States. p. 140.
70. Cremasco, M., *Analysis of the effects of anti-icing agents on the mechanical properties of concrete*, in *Mechancial Engineering*. 2012, University of Waterloo: Waterloo. p. 250.
71. ASTM International, *ASTM C1218: Standard Test Method for Water-Soluble Chloride in Mortar and Concrete*. 2015, ASTM International: West Conshohocken, PA.
72. ASTM International, *ASTM C1152: Standard Test Method for Acid-Soluble Chloride in Mortar and Concrete*. 2004, ASTM International: West Conshohocken, PA.
73. CSA, *Concrete Design Handbook*. 2018, Cement Association of Canada: Ottawa, Ontario, Canada.
74. CSA, *Canadian Highway Bridge Design Code*, in *8.11 Durability*. 2006, The Canadian Standards Association: Mississauga, Ontario, Canada.
75. Scottish Executive Development Department, *Use of Stainless Steel Reinforcement in Highway Structures*. 2002.
76. Ghazy, A. and M.T. Bassuoni, *Resistance of concrete to different exposures with chloride-based salts.* Cement and Concrete Research, 2017. **101**: p. 144-158.
77. Williamson, J. and O.B. Isgor, *The effect of simulated concrete pore solution composition and chlorides on the electronic properties of passive films on carbon steel rebar.* Corrosion Science, 2016. **106**: p. 82-95.
78. Pultrall, *Fibreglass reinforcing bars*. 2018: Thetford Mines, Quebec, Canada.
79. ComBAR®, S., *ComBAR® by Fiberline - technical information*. 2015.
80. ASTM International, *ASTM C215-14: Standard Test Mehod for Fundamental Transverse, Longitudinal, and Torsional Resonant Frequencies of Concrete Specimens*, in *C215-14*. 2014, ASTM International: West Conshohocken, PA.
81. Pickett, G., *Equations for computing elastic constants from flexural and torsional resonant frequencies of vibration of prisms and cylinders*. 1900.
82. ASTM International, *ASTM C6215-14: Standard Test Mehod for Fundamental Transverse, Longitudinal, and Torsional Resonant Frequencies of Concrete Specimens*. 2014, ASTM International: West Conshohocken, PA.
83. CSA, *Design of Concrete Structures*. 2015, Canadian Standards Association, : Mississauga, Ontario, Canada. p. 297.
84. Ontario Provincial Standard Specification Provision 1002, *Material Specification for Aggregates*, in *Concrete*. 2013, Ontario Provincial Standard Specification.
85. Ontario Provincial Standard Specification Provision 904, *Construction Specification for Concrete Structures*. 2012, Ontario Provincial Standard Specification.
86. Otsuki, N., S. Nagataki, and K. Nakashita, *Evaluation of the AgNO3 solution spray method for measurement of chloride penetration into hardened cementitious matrix materials.* Construction and Building Materials, 1993. **7**(4): p. 195-201.
87. Wong, H.S. and N.R. Buenfeld, *Determining the water–cement ratio, cement content, water content and degree of hydration of hardened cement paste: Method development and validation on paste samples.* Cement and Concrete Research, 2009. **39**(10): p. 957-965.

88. ASTM International, *Standard Test Method for Linear Thermal Expansion of Solid Materials by Thermomechanical Analysis*. 2006, ASTM International: West Conshohocken, Pennsylvania, United Stated of America.
89. Okelo, R. and R.L. Yuan, *Bond Strength of Fiber Reinforced Polymer Rebars in Normal Strength Concrete.* Journal of Composites for Construction, 2005. **9**(3): p. 203-213.
90. Lee, J.Y., T.Y. Kim, T.J. Kim, C.K. Yi, J.S. Park, Y.C. You, and Y.H. Park, *Interfacial bond strength of glass fiber reinforced polymer bars in high-strength concrete.* Composites Part B: Engineering, 2008. **39**(2): p. 258-270.
91. Ferrier, E., O. Rabinovitch, and L. Michel, *Mechanical behavior of concrete–resin/adhesive–FRP structural assemblies under low and high temperatures.* Construction and Building Materials, 2016. **127**: p. 1017-1028.
92. Yan, F., Z. Lin, and M. Yang, *Bond mechanism and bond strength of GFRP bars to concrete: A review.* Composites Part B: Engineering, 2016. **98**: p. 56-69.
93. Won, J.-P. and C.-G. Park, *Effect of Environmental Exposure on the Mechanical and Bonding Properties of Hybrid FRP Reinforcing Bars for Concrete Structures.* Journal of Composite Materials, 2005. **40**(12): p. 1063-1076.
94. Wu, H.-C., G. Fu, R.F. Gibson, A. Yan, K. Warnemuende, and V. Anumandla, *Durability of FRP Composite Bridge Deck Materials under Freeze-Thaw and Low Temperature Conditions.* Journal of Bridge Engineering, 2006. **11**(4): p. 443-451.
95. Kreibich, U.T., F. Lohse, and R. Schmid, *Polymers in Low Temperature Technology*, in *Nonmetallic Materials and Composites at Low Temperatures*, A.F. Clark, R.P. Reed, and G. Hartwig, Editors. 1979, Springer US: Boston, MA. p. 1-32.
96. Mironov, S.A., B.A. Krylov, and O.S. Ivanova, *Curing time of concrete prior to freezing.* Hydrotechnical Construction, 1967. **1**(4): p. 319-325.
97. Bray, W.H. and E.J. Sellevold, *Water sorption properties of hardened cement paste cured or stored at elevated temperatures.* Cement and Concrete Research, 1973. **3**(6): p. 723-728.
98. le Sage de Fontenay, C. and E.J. Sellevold, *Ice Formation in Hardened Cement Paste - I. Mature Water-Saturated Pastes*, P.J. Sereda and G.G. Litvan, Editors. 1980, ASTM International: West Conshohocken, PA. p. 425-438.
99. Bager, D.H. and E.J. Sellevold, *Ice formation in Hardened Cement Paste - II. Steam Cured Pastes with Variable Moisture Contents*, in *Durability of Building Materials and Components*, Sereda; and Litvan;, Editors. 1980, American Society for Testing and Materials: Ottawa, Canada. p. 439 - 454.
100. Powers, T.C. and T.L. Brownyard, *Studies of the Physical Properties of Hardened Portland Cement Paste.* ACI Journal Proceedings, 1946. **43**(9): p. 101-132.
101. David Darwin, JoAnn Browning, Lien Gong, and Sean Hughes, *Effects of Deicers on Concrete Deterioration.* Materials Journal, 2008. **105**(6): p. 622-627.
102. M. Collepardi, L. Coppola, and C. Pistolesi, *Durability of Concrete Structures Exposed to CaCl 2 Based Deicing Salts.* American Concrete Institute - Special Publication, 1994. **145**: p. 107-120.
103. Van Niejenhuis, C.B., I. Ogunsanya, and C.M. Hansson, *Analysis of pore solution of different cements with and without admixed chlorides.* ACI structural and materials journal,, 2020. **In Pres - January 2020**.

104. ASTM International, *Standard Test Method for Determining Effects of Chemical Admixtures on Corrosion of Embedded Steel Reinforcement in Concrete Exposed to Chloride Environments*. 2013, ASTM International: West Conshohocken, Pennsylvania, United Stated of America.
105. Delagrave, A., J. Marchand, J.-P. Ollivier, S. Julien, and K. Hazrati, *Chloride binding capacity of various hydrated cement paste systems.* Advanced Cement Based Materials, 1997. **6**(1): p. 28-35.
106. Vollpracht, A., B. Lothenbach, R. Snellings, and J. Haufe, *The pore solution of blended cements: a review.* Materials and Structures, 2016. **49**(8): p. 3341-3367.
107. Mehta, P.K. and W.B. Richard, *Building Durable Structures in the 21st Century.* Concrete International, 2001. **23**(3): p. 57-63.
108. MacGregor, J. and M. Bartlett, *Reinforced Concrete: Machanics and Design - First Canadian Edition*. 1999: Pearson.
109. Stewart, M., *Workmanship and its Influence on Probabilistic Models of Concrete compressive strength.* ACI Materials Journal, 1995. **92**(4): p. 361-372.
110. Mirza, S.A. and J.G. MacGregor, *Variability of Mechanical Properties of Reinforcing Bars.* Journal of the Structural Division, 1979. **105**(5): p. 921-937.
111. CSA, *Carbon steel bars for concrete reinforcement*. 2014, Canadian Standards Association: Mississauga, Ontario, Canada.
112. Bournonville, M., J. Dahnke, and D. Darwin, *Statistical Analysis of the Mechanical Properties and Weight of Reinforcing Bars.* 2004.
113. Allen, D.E., *Statistical study of the mechanical properties of reinforcing bars.* Building Research Note; no. BRN-85, 1972.
114. Pilakoutas, K., K. Neocleous, and M. Guadagnini, *Design Philosophy Issues of Fiber Reinfored Polymer Reinforced Concrete Structures.* Journal of Composites for Construction, 2002. **6**(3): p. 154-161.
115. Silva, E., S. Diniz, and S. Ribeiro, *Probabilistic Assessment of Serviceability of FRP-Reinforced Concrete Beams*, in *Structural Engineering Department*. 2017, Federal University of Minas Gerais: Federal University of Minas Gerais.
116. David Tse Chuen Johnson, *Investigation of glass fibre reinfroced polymer reinforcing bars as internal reinforcement for concrete structures*, in *Civil Engineering*. 2009, University of Toronto: Toronto, Canada.
117. WSP, *Site No. 16-118, Lyn Road Overpass, Highway 401, Kingston Ontario*. 2016, WSP: Markham, Ontario.
118. Bridge Check Canada Ltd, *Detailed Condition Suvey Report - HWY 406 over 12 mile creek*. 2016: Vaughan Ontario.
119. Achillides, Z. and K. Pilakoutas, *Bond Behavior of Fiber Reinforced Polymer Bars under Direct Pullout Conditions.* Journal of Composites for Construction, 2004. **8**(2): p. 173-181.
120. The International Federation for Structural Concrete, *FRP reinforcement in reinforced concrete structures*. 2007: fib Bulletin No. 40. p. 160.
121. CSA, *Design and construction of building structures with fibre-reinfroced polymers*. 2012, Canadian Standards Association: Mississauga, Ontario, Canada.
122. Wambeke, B.W. and C.K. Shield, *Development Length of Glass Fiber-Reinforced Polymer Bars in Concrete.* ACI Structural Journal, 2006. **103**(1): p. 11-17.

123. ACI - 440 Committee, *Guide for the Design and Construction of Structural Concrete Reinforced with FRP Bars*. 2006, American Concrete Institue: Farmington Hills, MI, USA.
124. Malvar, L.J., *Bond Stress-Slip Characteristics of FRP Bars*. 1994, Office of Naval Research: Naval Facilities Engineering Service Centre, Port Hueneme, CA.
125. Quayyum, S., *Bond behaviour of fibre reinforced polymer (FRP) rebars in concrete*, in *Civil Engineering*. 2010, University of British Columbia.
126. B. Benmokrane, B.T. and Chaallal, *Bond Strength and Load Distribution of Composite GFRP Reinforcing Bars in Concrete.* ACI Materials Journal, 1996. **93**(3).
127. Achillides, Z., *Bond behaviour of FRP bars in concrete*, in *Civil and Structural Engineering*. 1998, University of Sheffield: University of Sheffield.
128. Tighiouart, B., B. Benmokrane, and D. Gao, *Investigation of bond in concrete member with fibre reinforced polymer (FRP) bars.* Construction and Building Materials, 1998. **12**(8): p. 453-462.

Appendix A - DIC test data

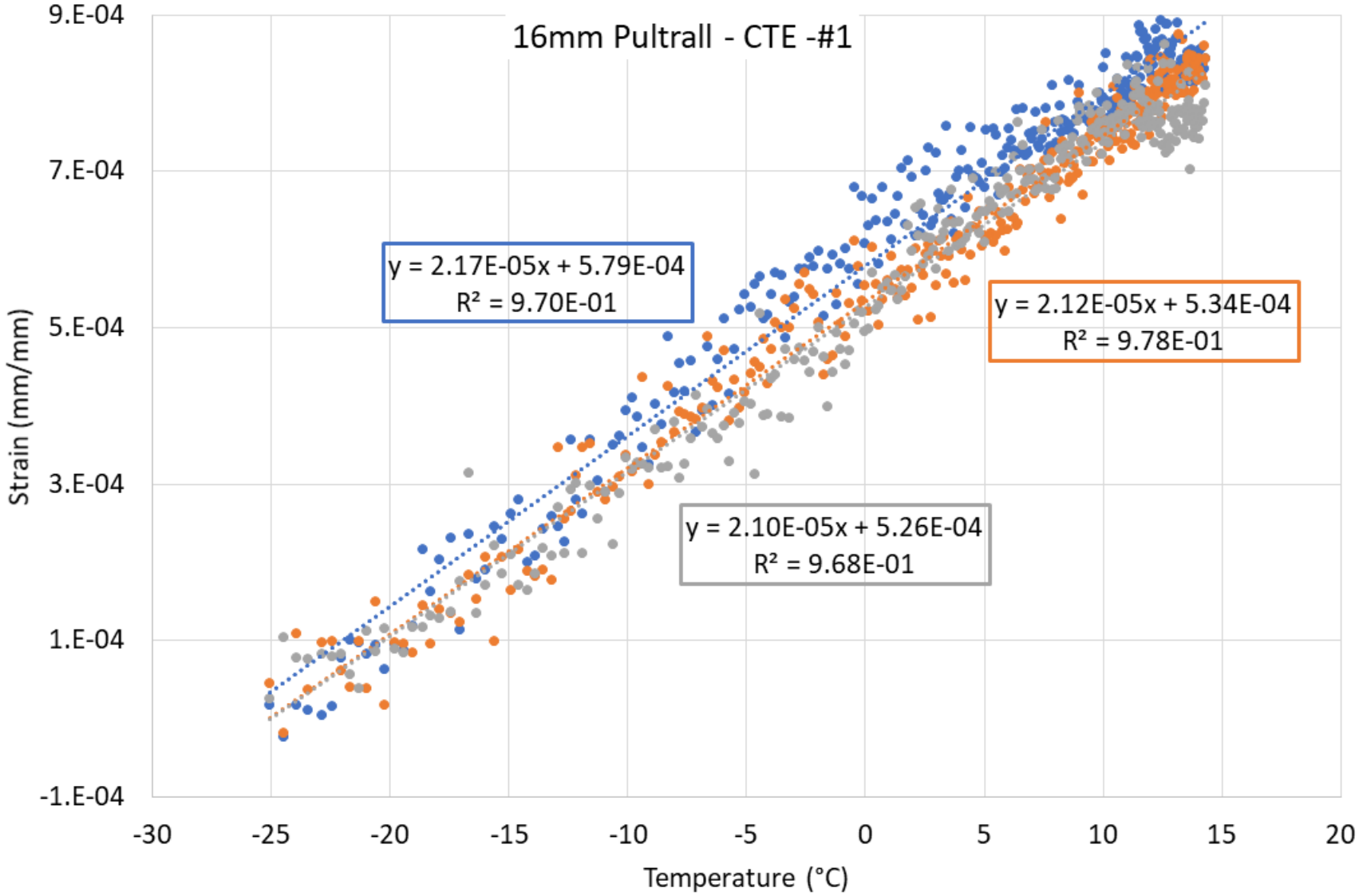

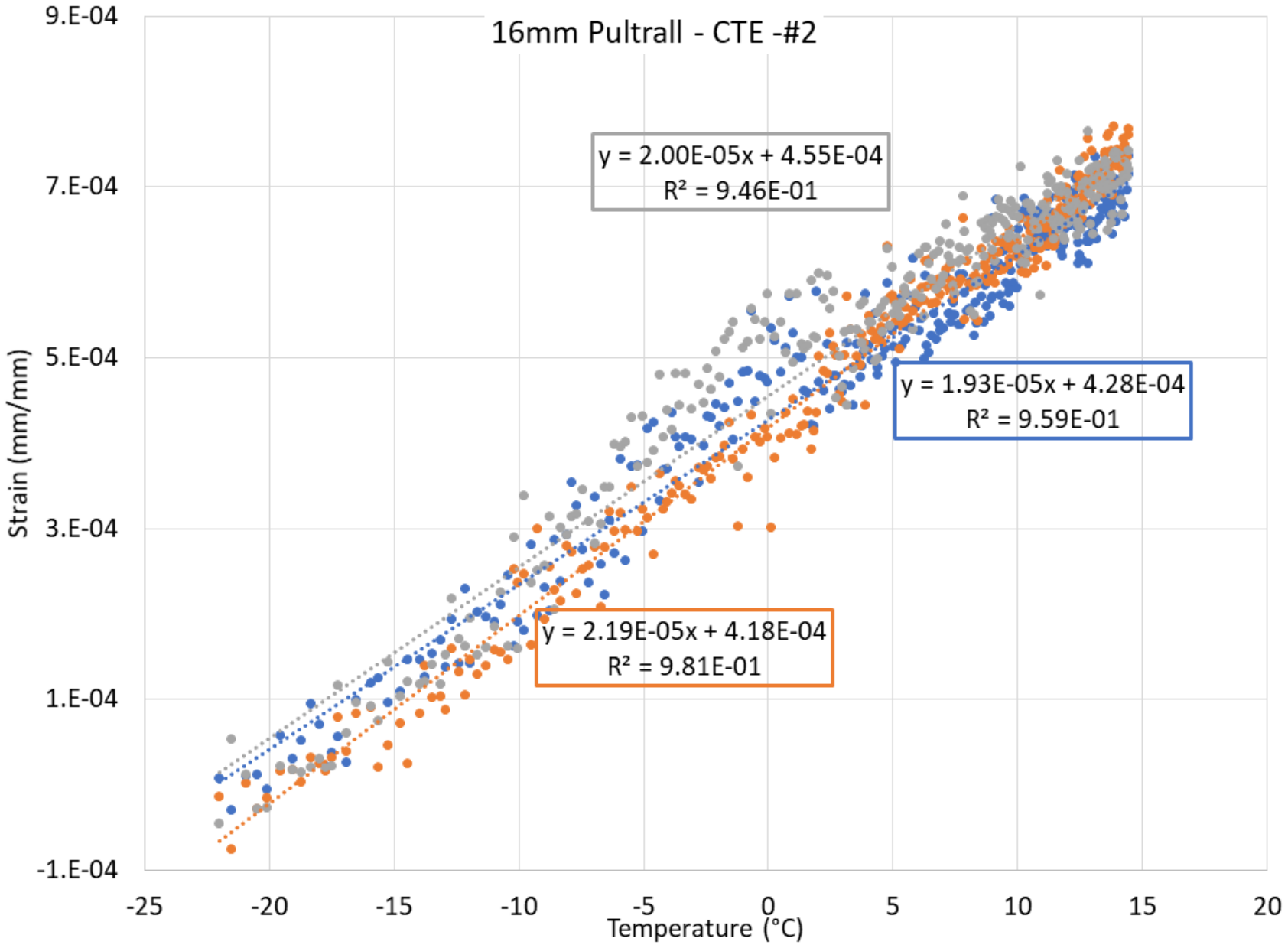
16mm Pultrall - CTE -#2
y = 2.00E-05x + 4.55E-04
R² = 9.46E-01
y = 1.93E-05x + 4.28E-04
R² = 9.59E-01
y = 2.19E-05x + 4.18E-04
R² = 9.81E-01
Strain (mm/mm)
9.E-04
7.E-04
5.E-04
3.E-04
1.E-04
-1.E-04
-25
-20
-15
-10
-5
0
5
10
15
20
Temperature (°C)

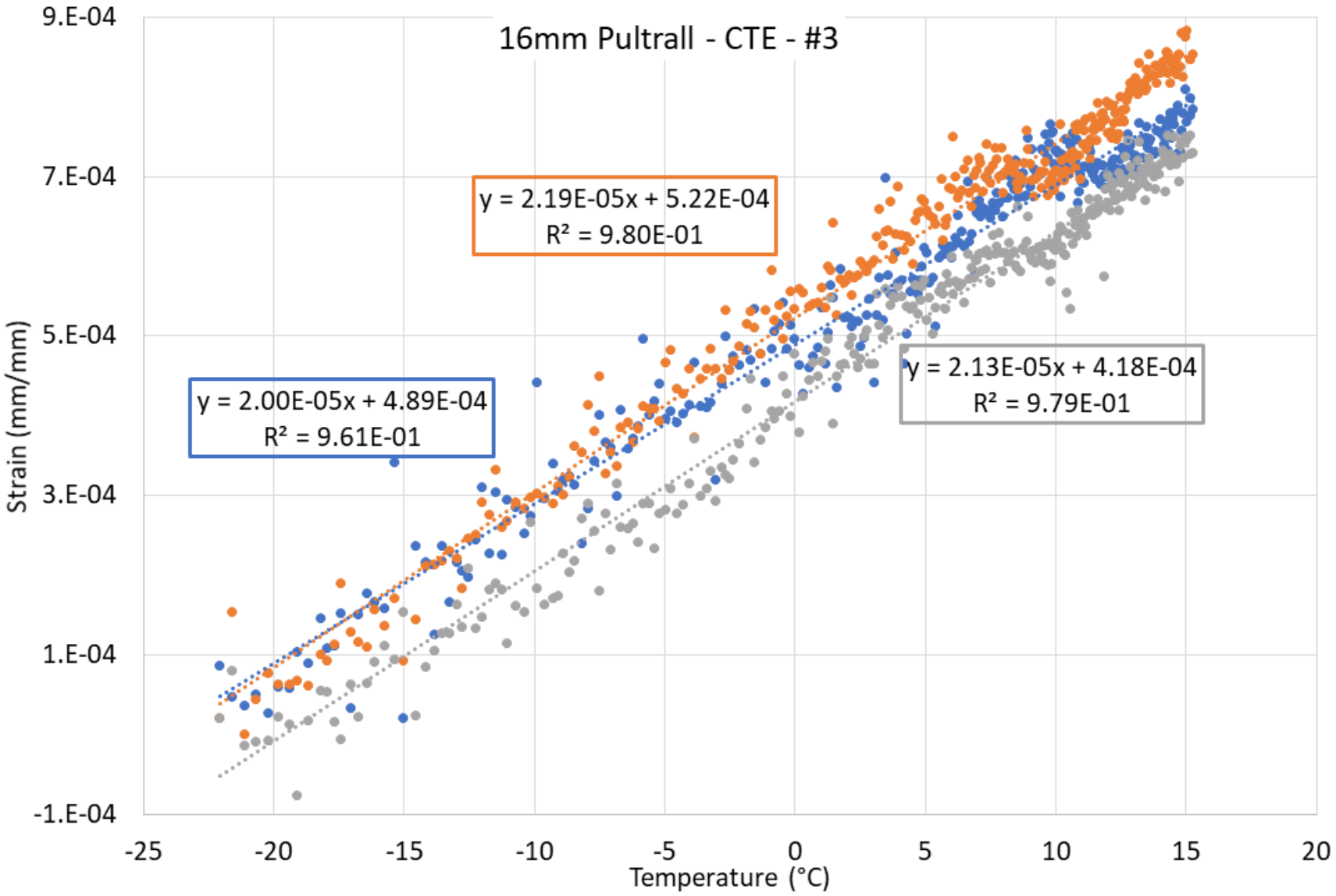
16mm Pultrall - CTE - #3
y = 2.19E-05x + 5.22E-04
R² = 9.80E-01
y = 2.00E-05x + 4.89E-04
R² = 9.61E-01
y = 2.13E-05x + 4.18E-04
R² = 9.79E-01
Strain (mm/mm)
9.E-04
7.E-04
5.E-04
3.E-04
1.E-04
-1.E-04
-25
-20
-15
-10
-5
0
5
10
15
20
Temperature (°C)

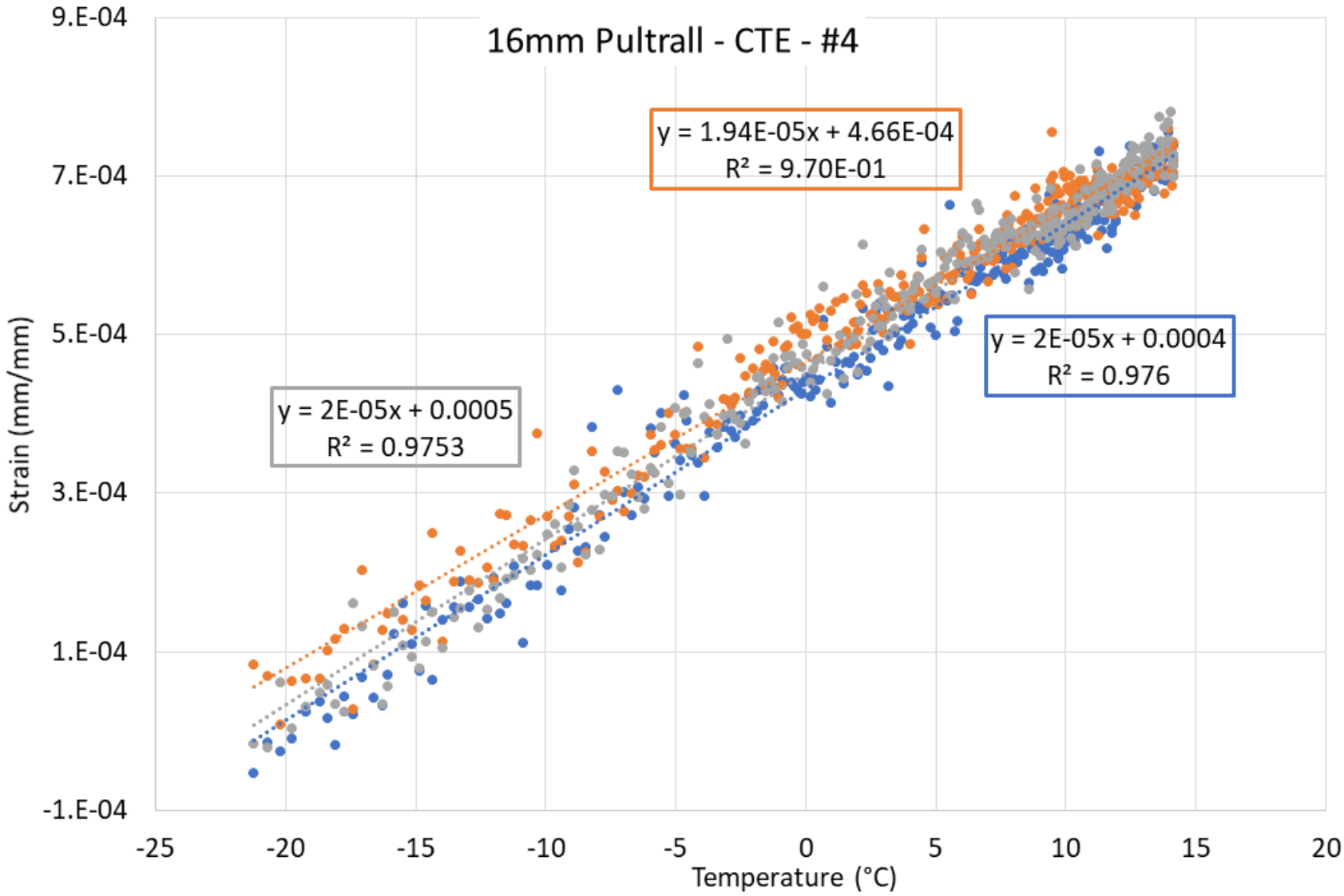
16mm Pultrall - CTE - #4
y = 1.94E-05x + 4.66E-04
R² = 9.70E-01
y = 2E-05x + 0.0004
R² = 0.976
y = 2E-05x + 0.0005
R² = 0.9753
Strain (mm/mm)
9.E-04
7.E-04
5.E-04
3.E-04
1.E-04
-1.E-04
-25
-20
-15
-10
-5
0
5
10
15
20
Temperature (°C)

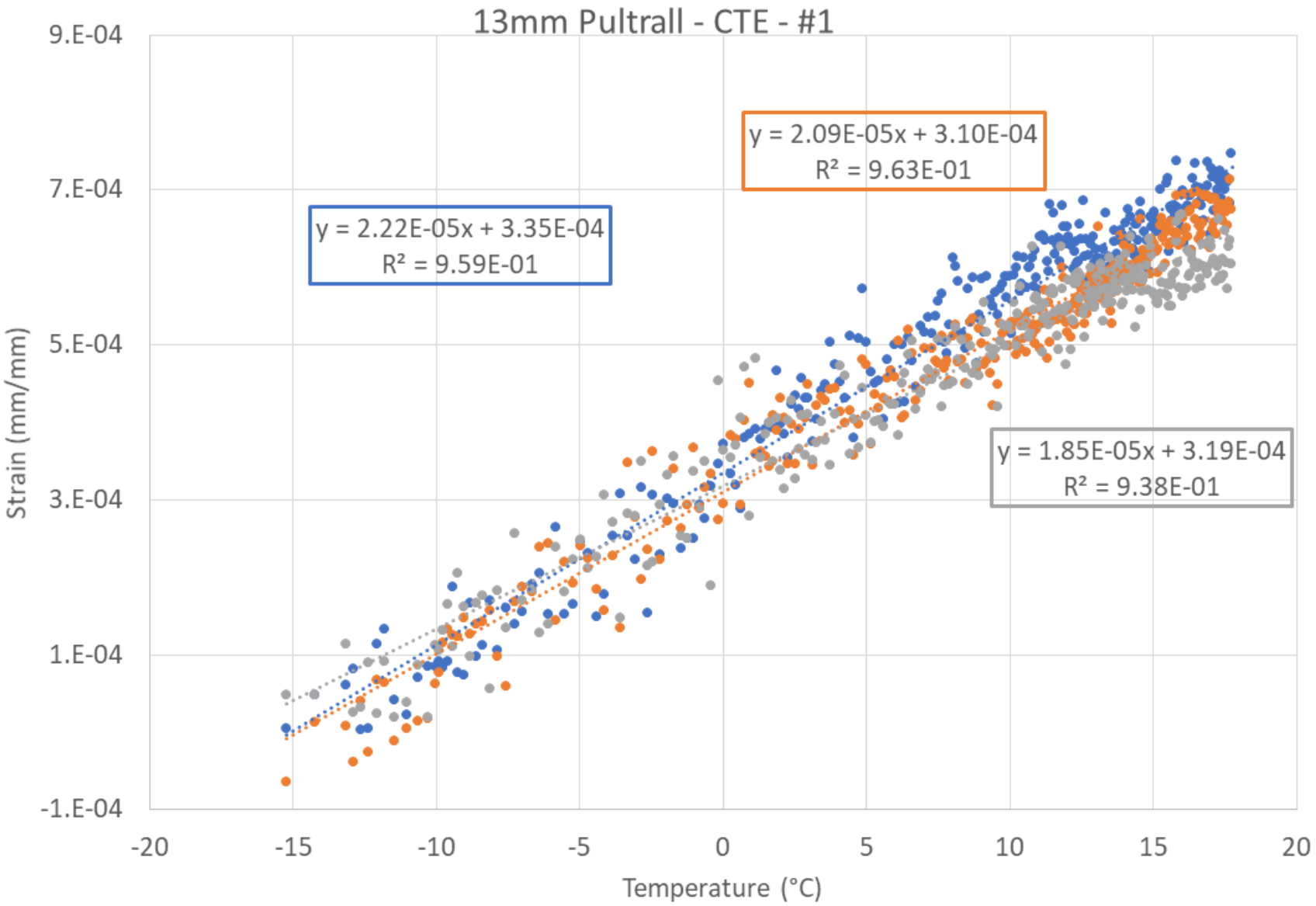
13mm Pultrall - CTE - #1
y = 2.09E-05x + 3.10E-04
R² = 9.63E-01
y = 2.22E-05x + 3.35E-04
R² = 9.59E-01
y = 1.85E-05x + 3.19E-04
R² = 9.38E-01
Strain (mm/mm)
9.E-04
7.E-04
5.E-04
3.E-04
1.E-04
-1.E-04
-20
-15
-10
-5
0
5
10
15
20
Temperature (°C)

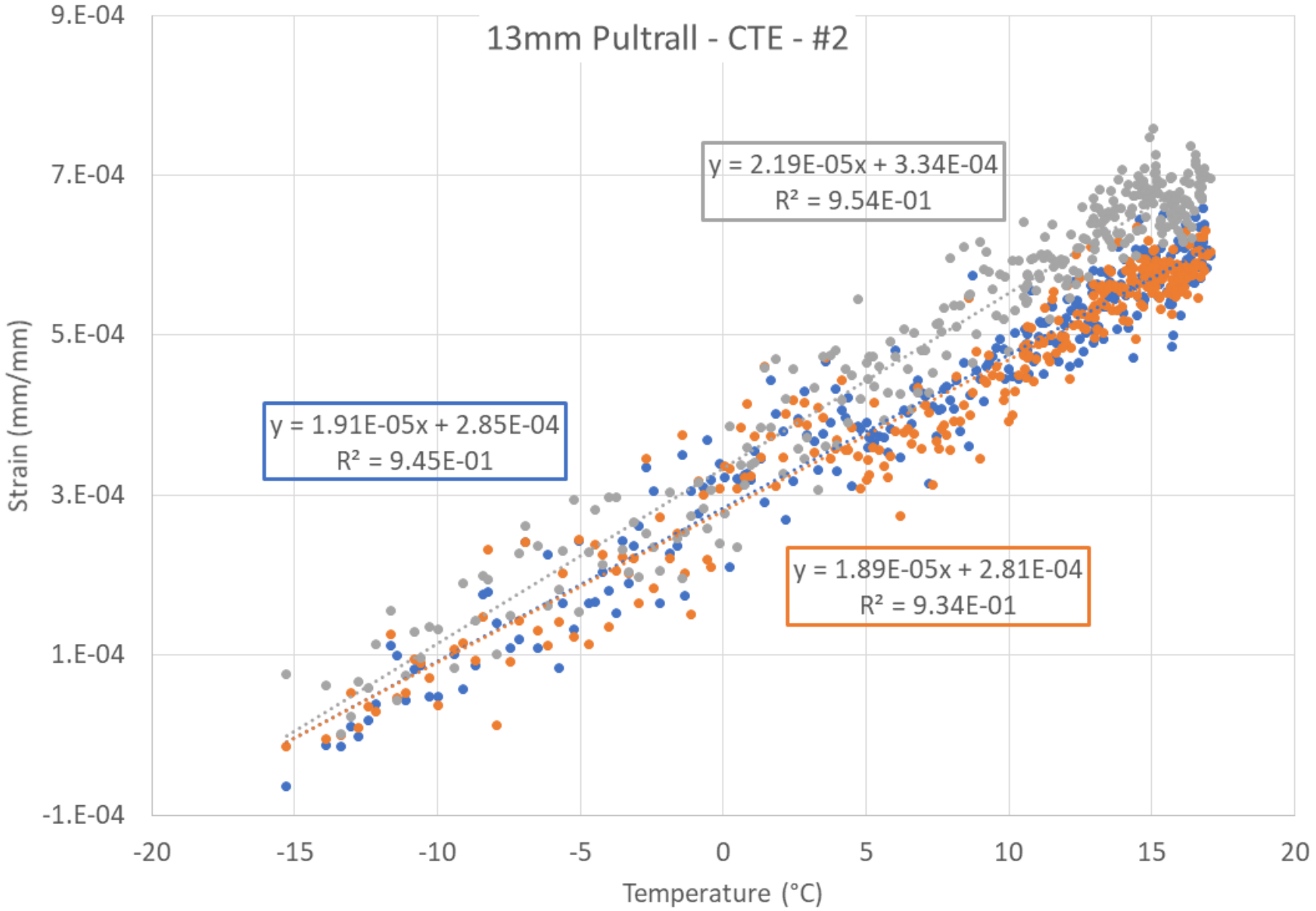
13mm Pultrall - CTE - #2
y = 2.19E-05x + 3.34E-04
R² = 9.54E-01
y = 1.91E-05x + 2.85E-04
R² = 9.45E-01
y = 1.89E-05x + 2.81E-04
R² = 9.34E-01
Strain (mm/mm)
9.E-04
7.E-04
5.E-04
3.E-04
1.E-04
-1.E-04
-20
-15
-10
-5
0
5
10
15
20
Temperature (°C)

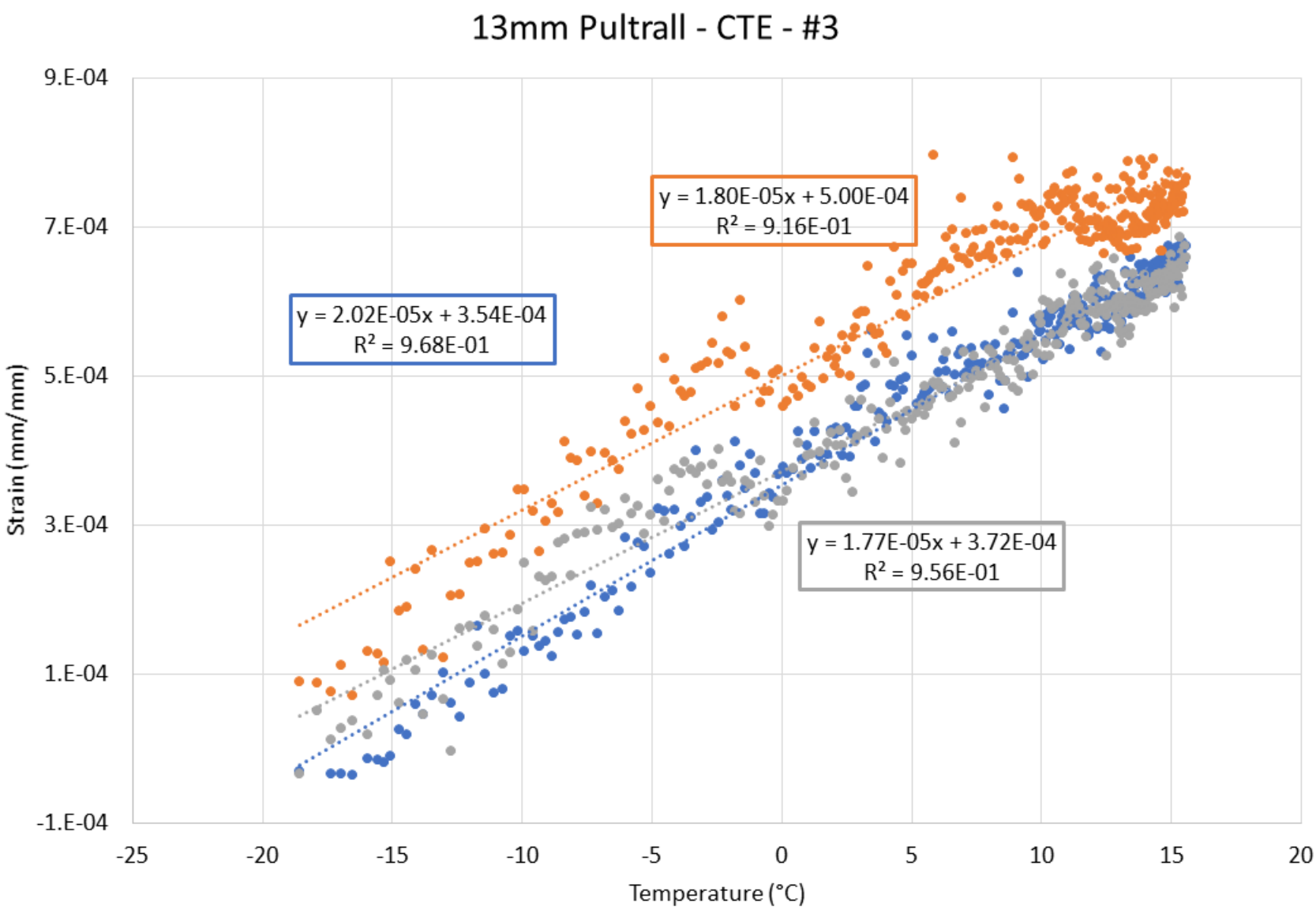
13mm Pultrall - CTE - #3
y = 1.80E-05x + 5.00E-04
R² = 9.16E-01
y = 2.02E-05x + 3.54E-04
R² = 9.68E-01
y = 1.77E-05x + 3.72E-04
R² = 9.56E-01
Strain (mm/mm)
9.E-04
7.E-04
5.E-04
3.E-04
1.E-04
-1.E-04
-25
-20
-15
-10
-5
0
5
10
15
20
Temperature (°C)

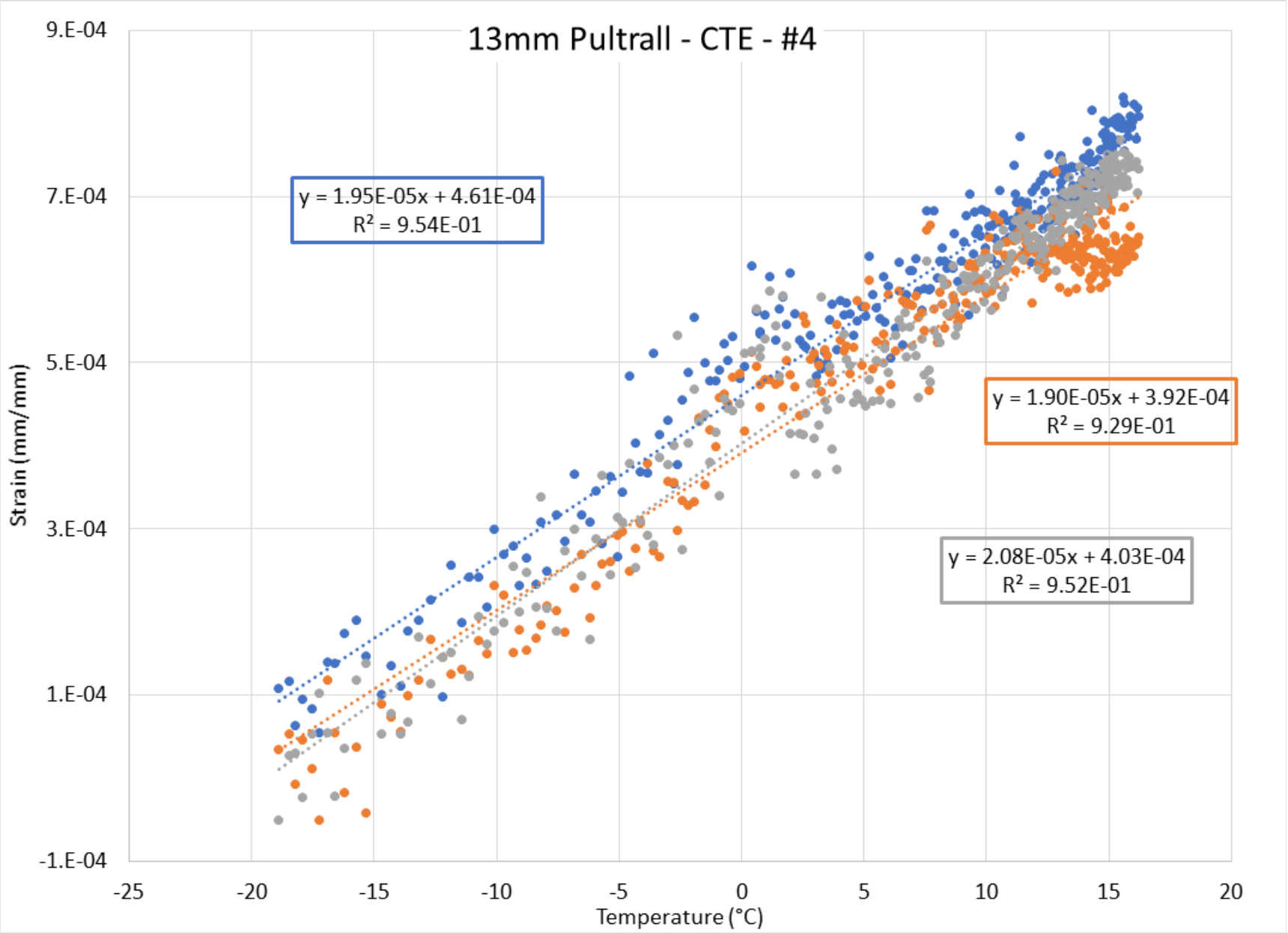
13mm Pultrall - CTE - #4
y = 1.95E-05x + 4.61E-04
R² = 9.54E-01
y = 1.90E-05x + 3.92E-04
R² = 9.29E-01
y = 2.08E-05x + 4.03E-04
R² = 9.52E-01
Strain (mm/mm)
9.E-04
7.E-04
5.E-04
3.E-04
1.E-04
-1.E-04
-25
-20
-15
-10
-5
0
5
10
15
20
Temperature (°C)

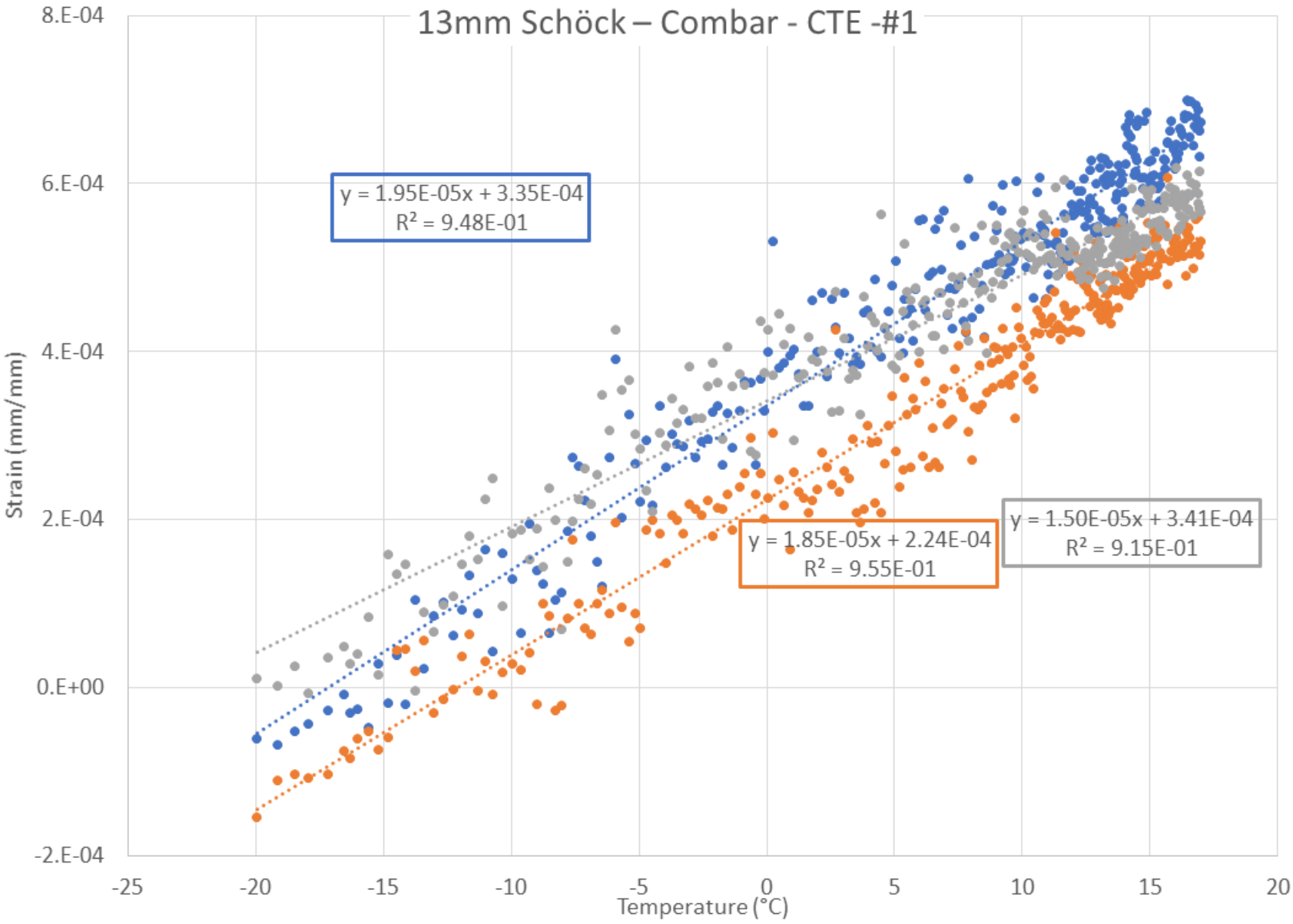
13mm Schöck – Combar - CTE -#1
y = 1.95E-05x + 3.35E-04
R² = 9.48E-01
y = 1.85E-05x + 2.24E-04
R² = 9.55E-01
y = 1.50E-05x + 3.41E-04
R² = 9.15E-01
Strain (mm/mm)
8.E-04
6.E-04
4.E-04
2.E-04
0.E+00
-2.E-04
-25
-20
-15
-10
-5
0
5
10
15
20
Temperature (°C)

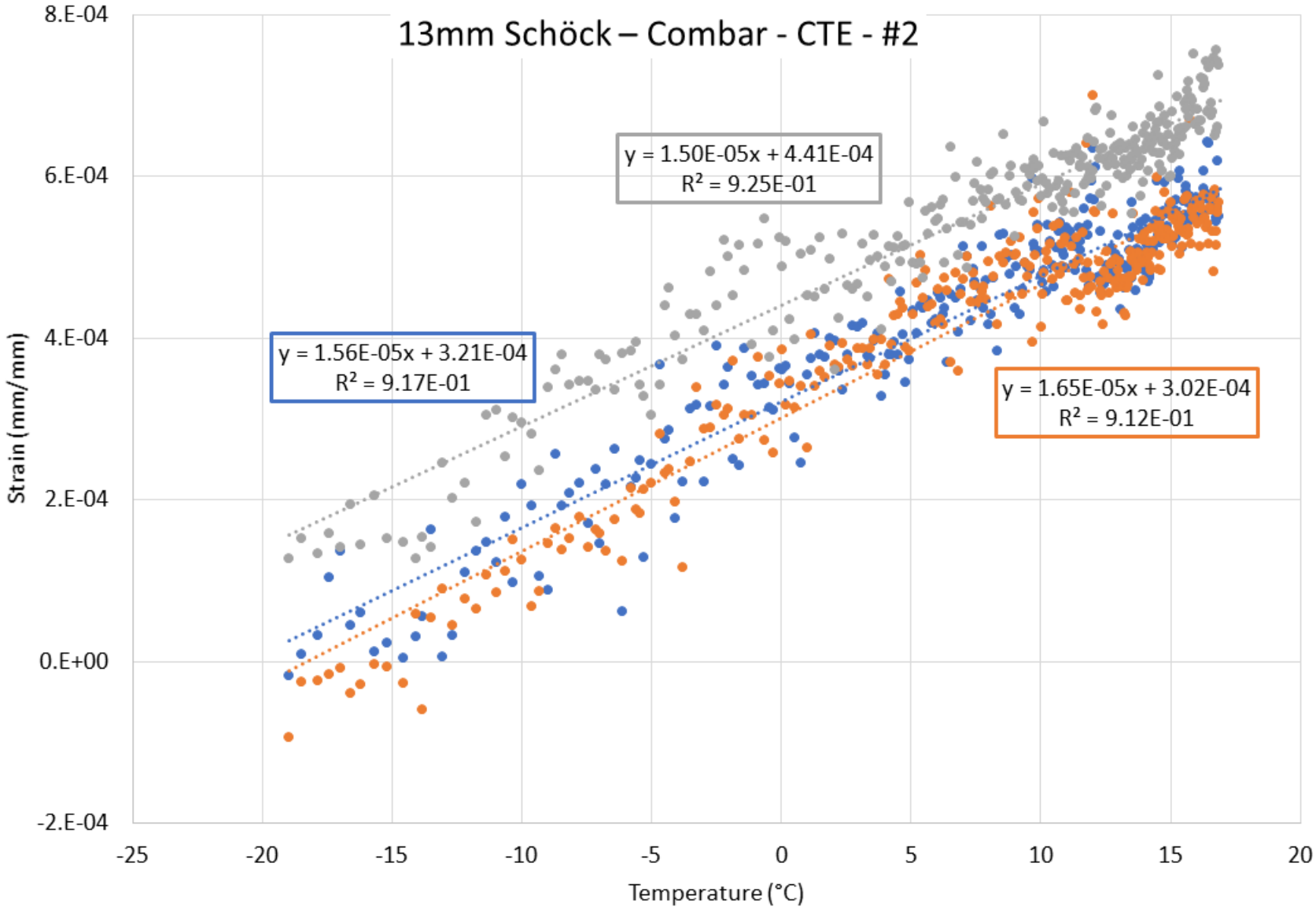
13mm Schöck – Combar - CTE - #2
y = 1.50E-05x + 4.41E-04
R² = 9.25E-01
y = 1.56E-05x + 3.21E-04
R² = 9.17E-01
y = 1.65E-05x + 3.02E-04
R² = 9.12E-01
Strain (mm/mm)
8.E-04
6.E-04
4.E-04
2.E-04
0.E+00
-2.E-04
-25
-20
-15
-10
-5
0
5
10
15
20
Temperature (°C)

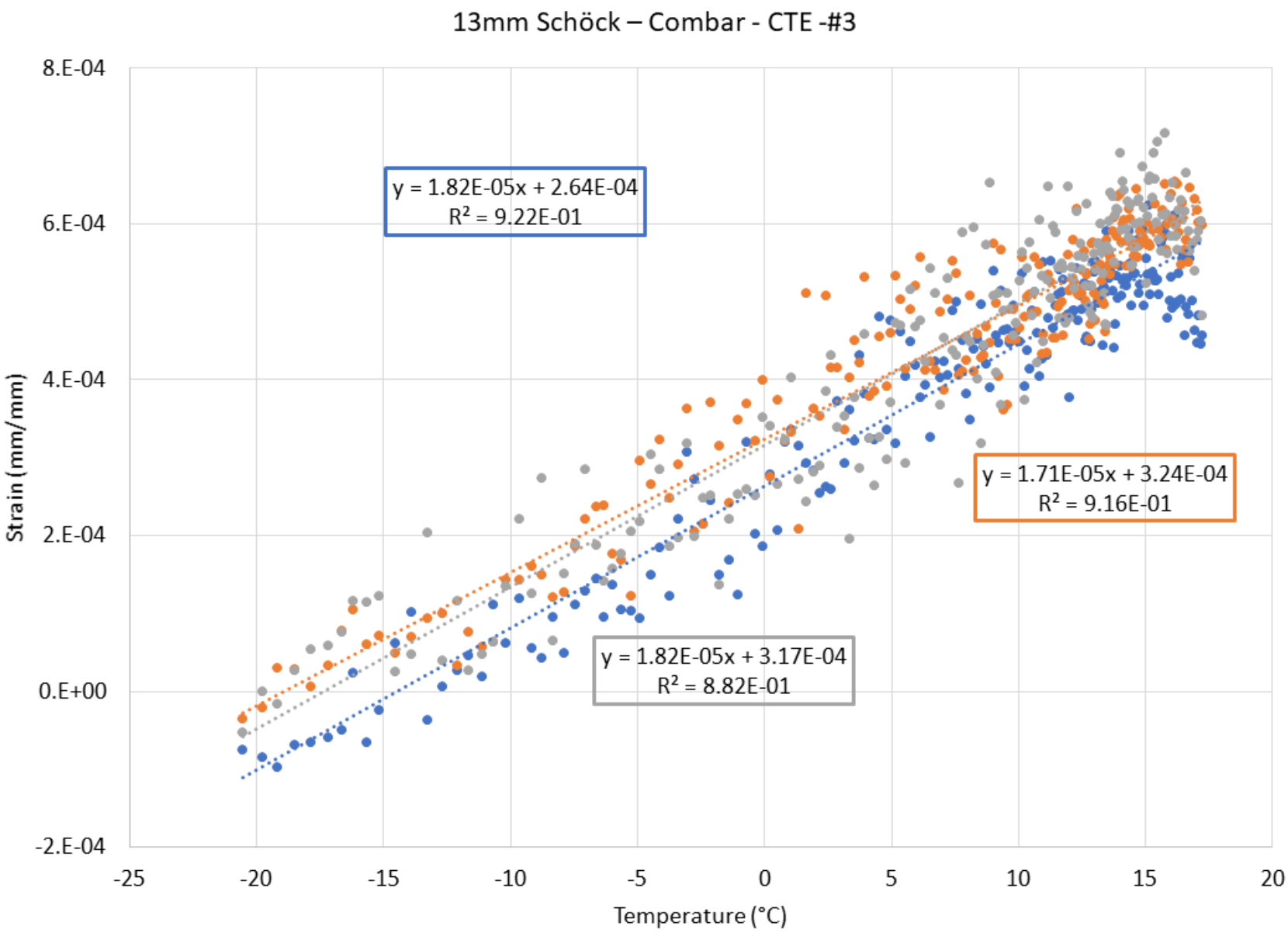
13mm Schöck – Combar - CTE -#3
y = 1.82E-05x + 2.64E-04
R² = 9.22E-01
y = 1.71E-05x + 3.24E-04
R² = 9.16E-01
y = 1.82E-05x + 3.17E-04
R² = 8.82E-01
Strain (mm/mm)
8.E-04
6.E-04
4.E-04
2.E-04
0.E+00
-2.E-04
-25
-20
-15
-10
-5
0
5
10
15
20
Temperature (°C)

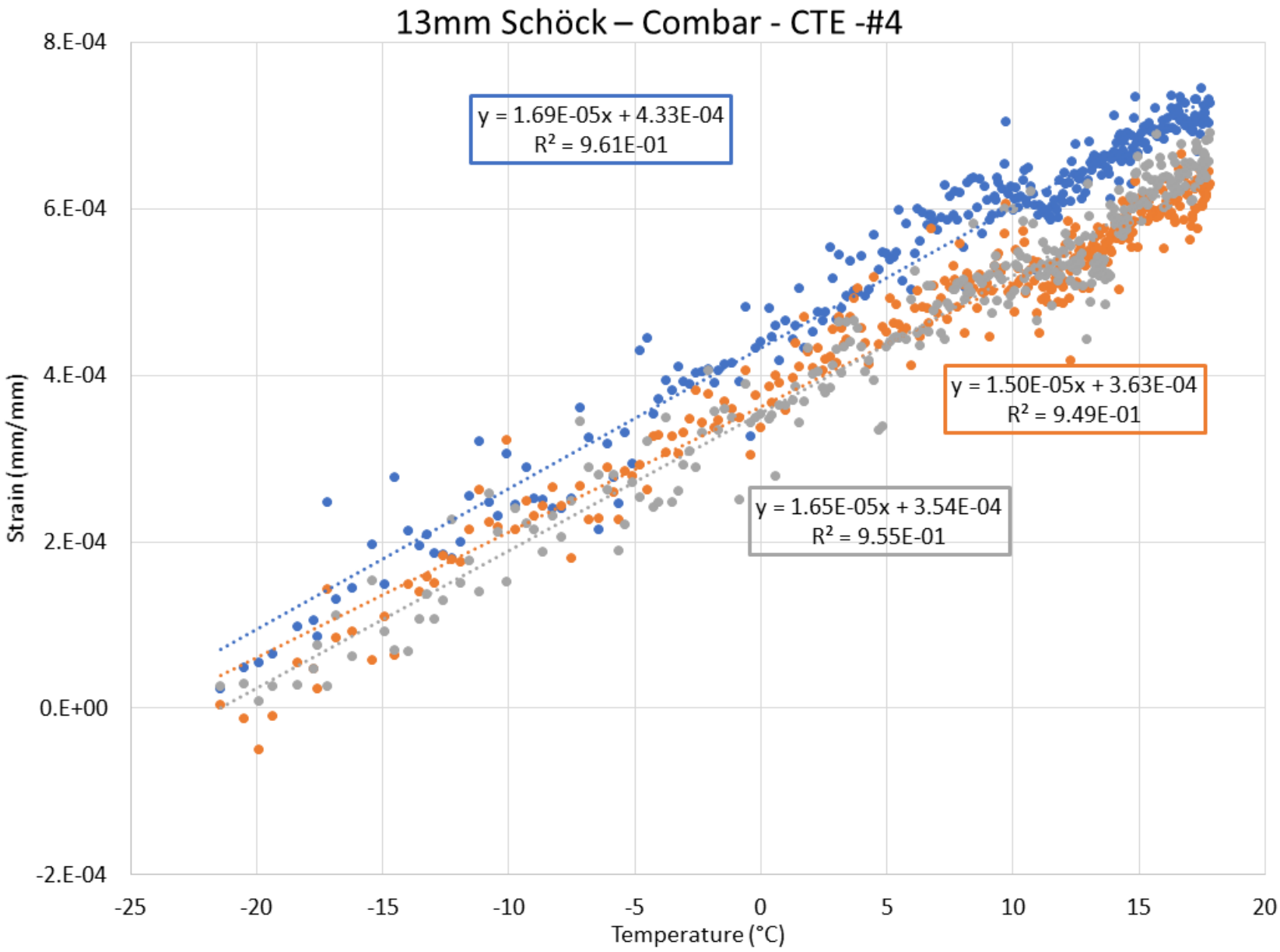
13mm Schöck – Combar - CTE -#4
y = 1.69E-05x + 4.33E-04
R² = 9.61E-01
y = 1.50E-05x + 3.63E-04
R² = 9.49E-01
y = 1.65E-05x + 3.54E-04
R² = 9.55E-01
Strain (mm/mm)
8.E-04
6.E-04
4.E-04
2.E-04
0.E+00
-2.E-04
-25
-20
-15
-10
-5
0
5
10
15
20
Temperature (°C)

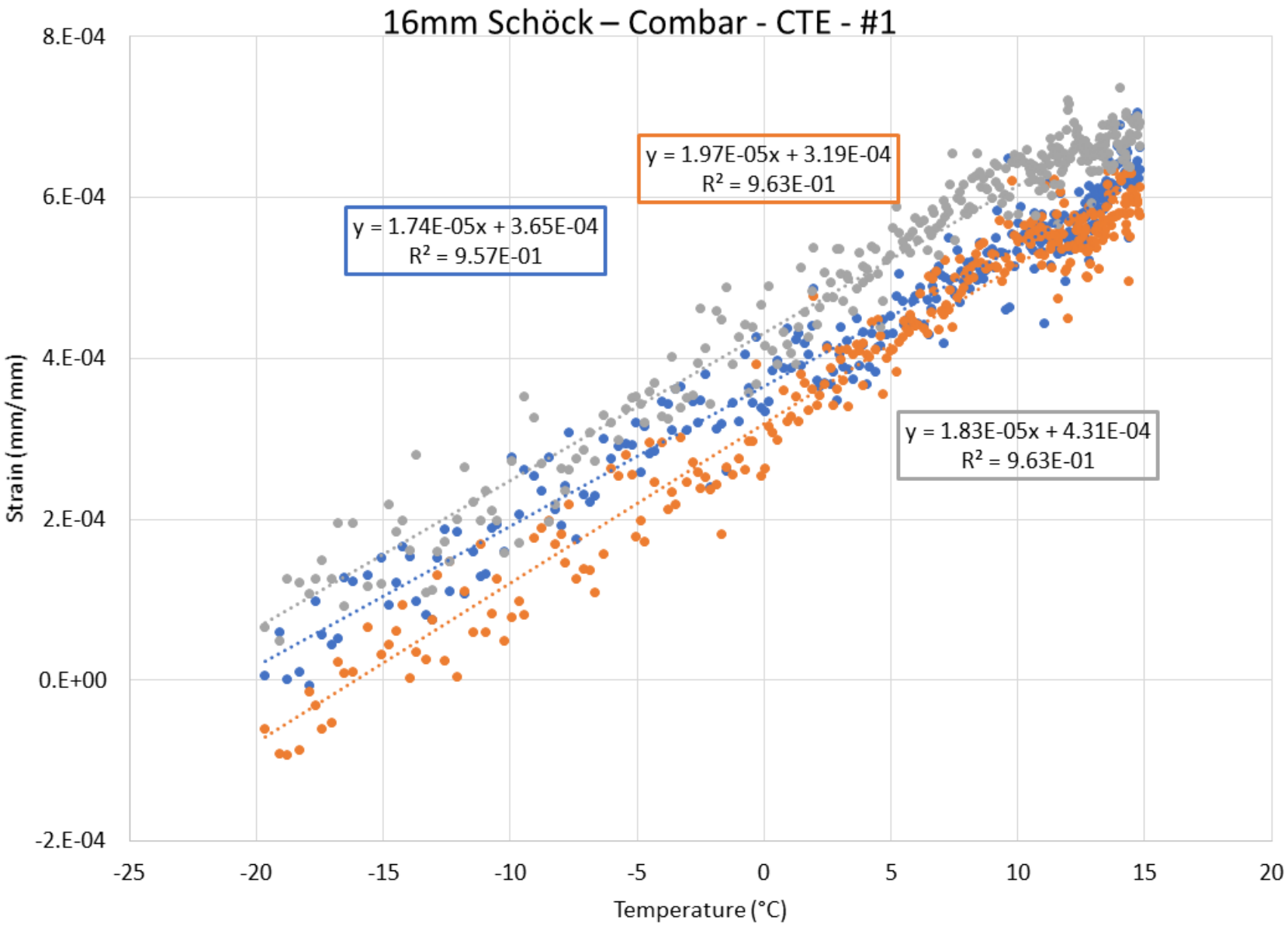
16mm Schöck – Combar - CTE - #1
y = 1.97E-05x + 3.19E-04
R² = 9.63E-01
y = 1.74E-05x + 3.65E-04
R² = 9.57E-01
y = 1.83E-05x + 4.31E-04
R² = 9.63E-01
Strain (mm/mm)
8.E-04
6.E-04
4.E-04
2.E-04
0.E+00
-2.E-04
-25
-20
-15
-10
-5
0
5
10
15
20
Temperature (°C)

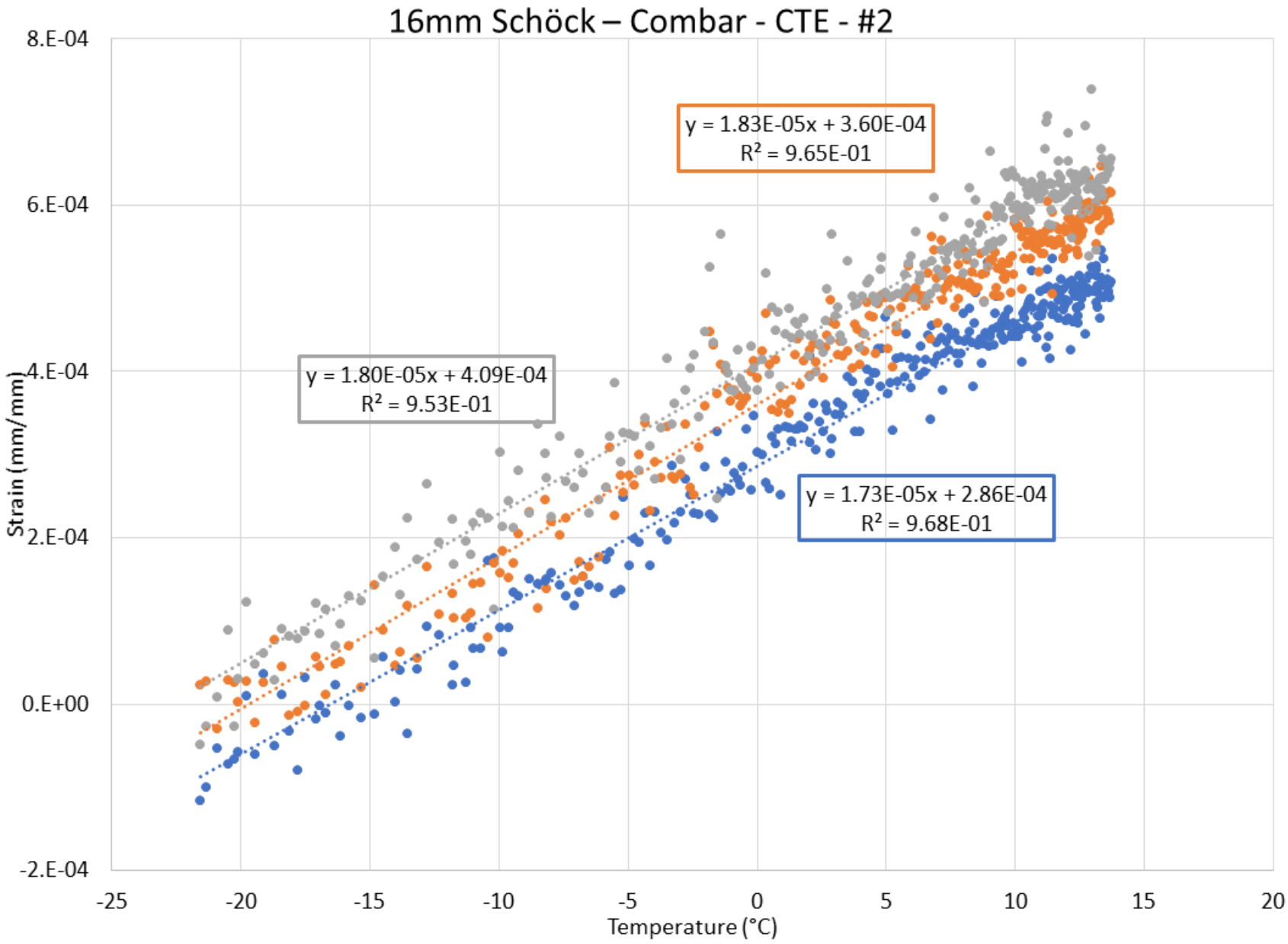
16mm Schöck – Combar - CTE - #2
y = 1.83E-05x + 3.60E-04
R² = 9.65E-01
y = 1.80E-05x + 4.09E-04
R² = 9.53E-01
y = 1.73E-05x + 2.86E-04
R² = 9.68E-01
Strain (mm/mm)
8.E-04
6.E-04
4.E-04
2.E-04
0.E+00
-2.E-04
-25
-20
-15
-10
-5
0
5
10
15
20
Temperature (°C)

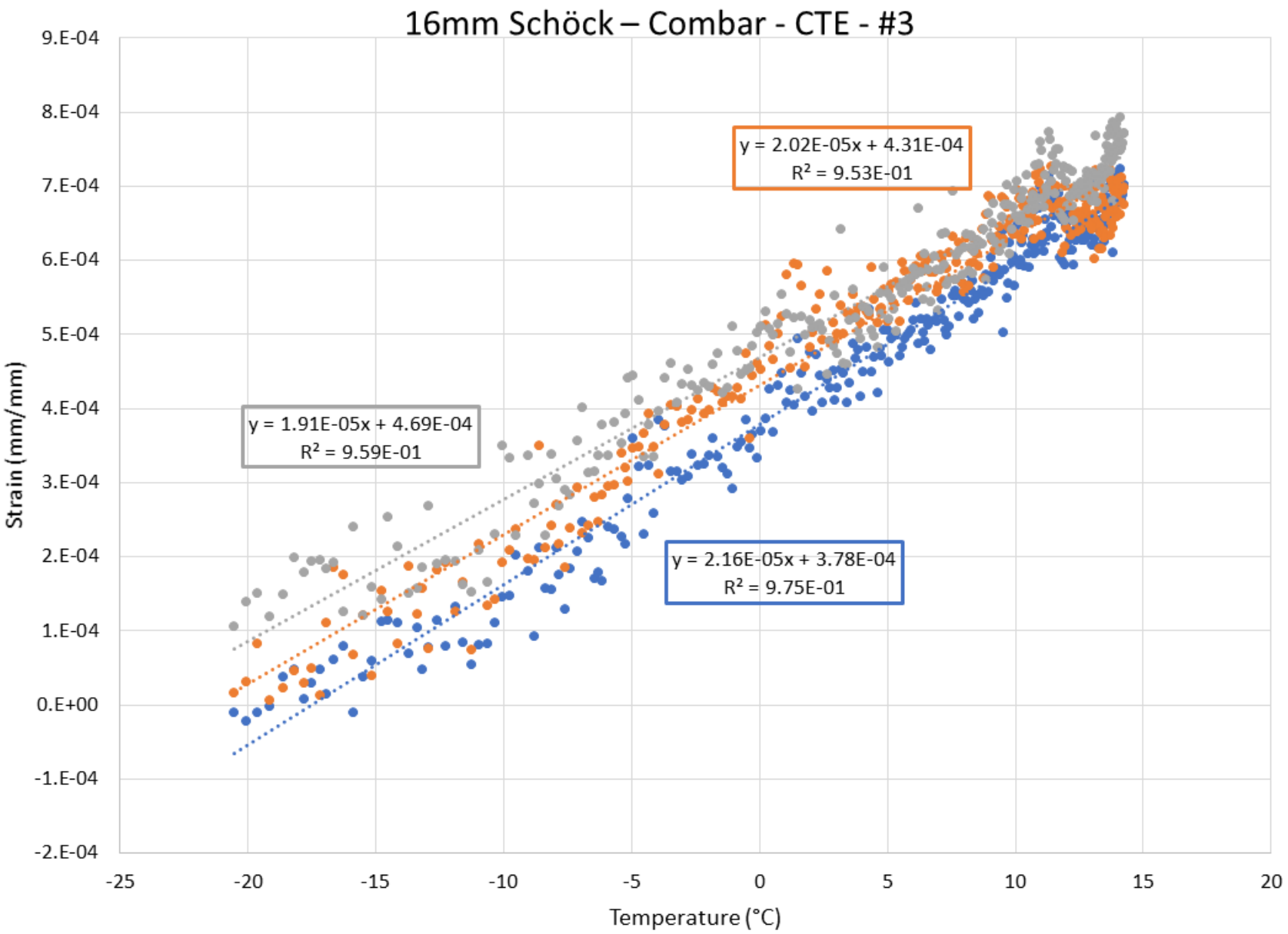
16mm Schöck – Combar - CTE - #3
y = 2.02E-05x + 4.31E-04
R² = 9.53E-01
y = 1.91E-05x + 4.69E-04
R² = 9.59E-01
y = 2.16E-05x + 4.78E-04
R² = 9.75E-01
Strain (mm/mm)
Temperature (°C)
9.E-04
8.E-04
7.E-04
6.E-04
5.E-04
4.E-04
3.E-04
2.E-04
1.E-04
0.E+00
-1.E-04
-2.E-04
-25
-20
-15
-10
-5
0
5
10
15
20

Appendix B - Simplified Over-Reinforced beam design example

Design a 500 mm wide by 750 mm deep beam using 16 mm Pultrall reinforcing bars to resist a moment of 500 kN·m assuming a concrete compressive strength of 35MPa. The list, and description, of variable is provided in the List of Variables found on page xx.

Given:

$$A_b = 199mm^2, f_{frpu} = 1000\ MPa, E_{frp} = 60\ GPa, \varepsilon_{fpru} = \frac{1100}{60{,}000} = 0.01666$$

Check ρ_b

$$\rho_b = \alpha_1\beta_1\ \frac{\phi_c}{\phi_{frp}}\left(\frac{\varepsilon_{cu}}{\varepsilon_{cu}+\varepsilon_{frp}}\right)\frac{f_c'}{f_{frpu}} \rightarrow 0.80(0.88)\frac{0.65}{0.75}\left(\frac{0.0035}{0.0035+0.0166}\right)\frac{35}{1100} \rightarrow 0.311\%$$

Assume a $\rho = \approx 1.20\rho_b = 6 - 16M\ bars$

Check spacing for 1-layer

$$s = \frac{500 - 2(75) - 2(17.22) - 6(18)}{5} = 41.5$$

$$s_{min} = max\begin{Bmatrix}1.4d_b = 1.4(18) = 25.2mm\\ 1.4a_g = 1.4(19) = 26.6mm\\ 30mm\end{Bmatrix} \rightarrow 30mm$$

$$d = 750 - 75 - 13.6 - \frac{18}{2} = 644 \approx 640$$

Set $M_r = M_f$

$$M_r = M_f \rightarrow T_r = C_r$$

$$T_r = \phi_{frp}A_{frp}E_{frp}\left(\frac{\beta_1 d}{a} - 1\right)\varepsilon_{cu}$$

$$C_r = \alpha_1\phi_c f_c' ab$$

$$\alpha_1\phi_c f_c' ab = \phi_{frp}A_{frp}E_{frp}\left(\frac{\beta_1 d}{a} - 1\right)\varepsilon_{cu} - quadratic\ for\ a$$

$$\alpha_1\phi_c f_c' b(a^2) + \phi_{frp}A_{frp}E_{frp}\varepsilon_{cu}(a) - \phi_{frp}A_{frp}E_{frp}\beta_1 d\varepsilon_{cu} = 0$$

$$0.80(0.88)35(500)a^2 + 0.75(1194)60{,}000(0.0035)a - 0.75(1194)60{,}000(0.88)640(0.0035) = 0$$

$$a = 98.6mm$$

$$c = \frac{a}{\beta_1} = \frac{98.6}{0.88} = 111.8$$

$$\varepsilon_{frp} = \left(\frac{d}{c} - 1\right)\varepsilon_{cu} = \left(\frac{640}{111.8} - 1\right)0.0035 = 0.0166 < \varepsilon_{frpU} = 0.0183$$

$$\rho = \frac{A_{fpr}}{bd} = \frac{1194}{500 \cdot 640} \rightarrow \rho = 0.373\%$$

$$f_{frp} = E_{frp}\varepsilon_{frp} = 60{,}000 \cdot 0.0169 = 1{,}000\ MPa < 1100$$

$$M_r = T_r\left(d - \frac{a}{2}\right) = \phi_{frp}A_{frp}f_{frp}\left(d - \frac{a}{2}\right)$$

$$M_r = 0.75(1194)1{,}000\left(644 - \frac{98.6}{2}\right) = 532\ kN \cdot m > 500 \therefore OK$$

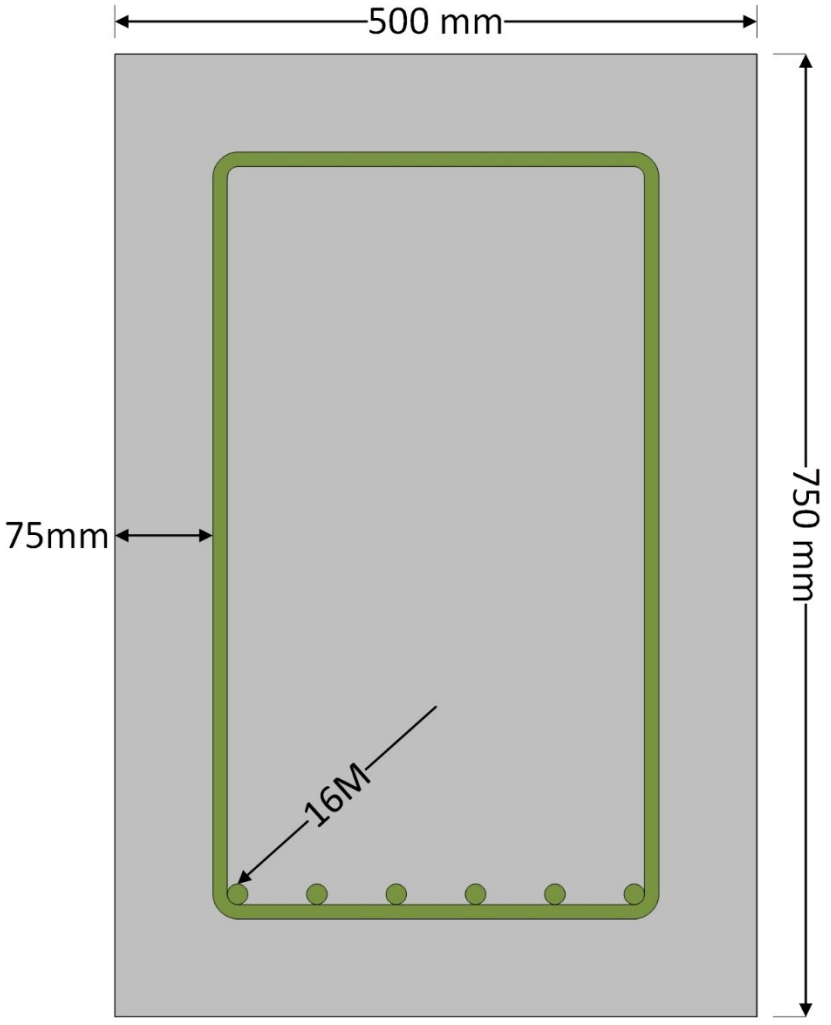

Appendix C - Simplified Under-Reinforced beam design example

Design a 500 mm wide by 750 mm deep beam using 400 MPa reinforcing bars to resist a moment of 1,000 kN·m assuming a concrete compressive strength of 30MPa.

Given:

$$f_y = 400\ MPa, E_{frp} = 60\ GPa, \varepsilon_{fpru} = \frac{400}{200{,}000} = 0.002$$

Check ρ_b

$$\rho_b = \alpha_1\beta_1\ \frac{\phi_c}{\phi_s}\left(\frac{\varepsilon_{cu}}{\varepsilon_{cu}+\varepsilon_s}\right)\frac{f_c'}{f_y} \rightarrow 0.805(0.895)\frac{0.65}{0.85}\left(\frac{0.0035}{0.0035+0.0026}\right)\frac{30}{400} \rightarrow 2.63\%$$

Type equation here.

Check spacing for 1-layer – assuming 35M bar

$$s = \frac{500 - 2(75) - 2(11.3) - 4(35.7)}{3} = 61.5$$

$$s_{min} = max\begin{Bmatrix}1.4d_b = 1.4(35.7) = 50mm\\ 1.4a_g = 1.4(19) = 26.6mm\\ 30mm\end{Bmatrix} \rightarrow 50mm$$

Assume at least 2 layers required

$$d = 750 - 75 - 11.3 - 35.7 - \frac{50}{2} = 603 \approx 600$$

$$M_r = K_r b d^2 \rightarrow K_r = \frac{M_r}{bd^2} = 5.55$$

$$\rho = 2.28\% \rightarrow A_s = 6{,}840\ mm^2$$

3 layers of steel with 25M and 35M steel - see figure below

$$d_{avg} = 598.4mm$$

$$T_r = C_r$$

$$T_r = \phi_s A_s f_y \rightarrow 0.85 \cdot 7000 \cdot 400 \rightarrow 2380\ kN \cdot m$$

$$C_r = \alpha_1\phi_c f_c' ab$$

$$a = \frac{\phi_s A_s f_y}{\alpha_1\phi_c f_c' b} \rightarrow \frac{2380}{7848} \rightarrow 303.2mm$$

$$c = \frac{a}{\beta_1} \rightarrow \frac{303.2}{0.895} \rightarrow 338.8mm$$

$$\frac{c}{d} \leq \frac{700}{700 + f_y} \rightarrow \frac{338.8}{598.4} = 0.566 < 0.636$$

$$M_r = T_r\left(d - \frac{a}{2}\right) = 2380\left(598.8 - \frac{303.2}{2}\right) \rightarrow M_r \cong 1064\ kN \cdot m > 1000\ \therefore, ok$$

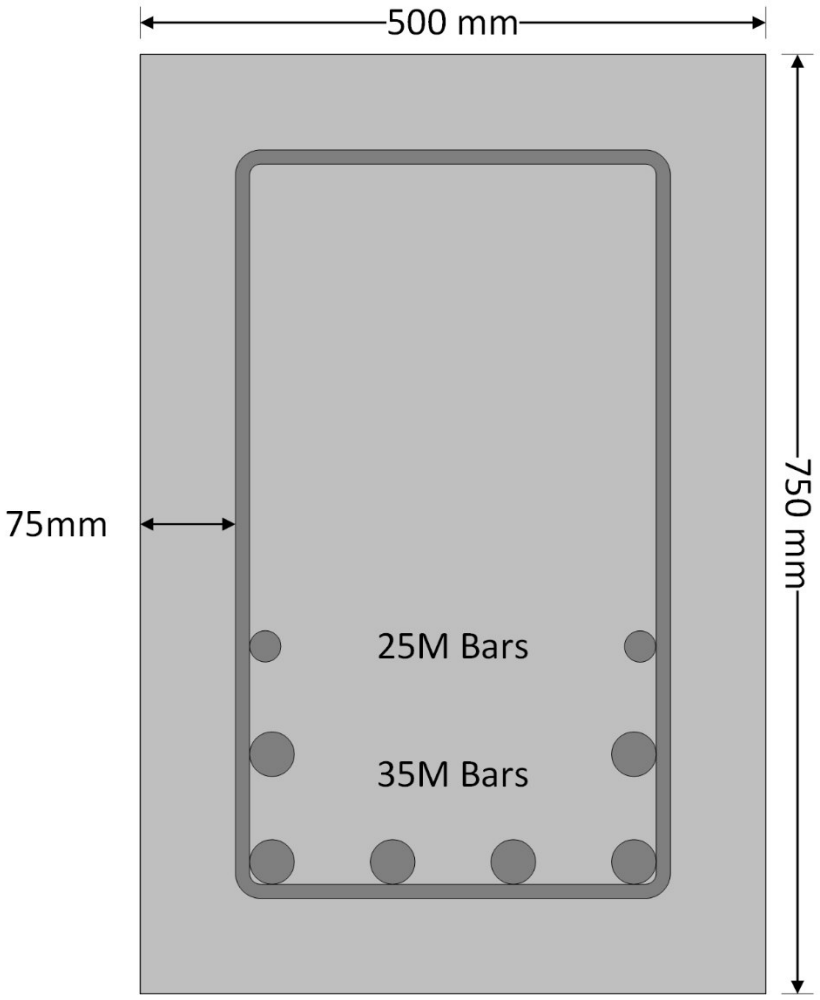

Appendix D - Bond stress vs slip curves

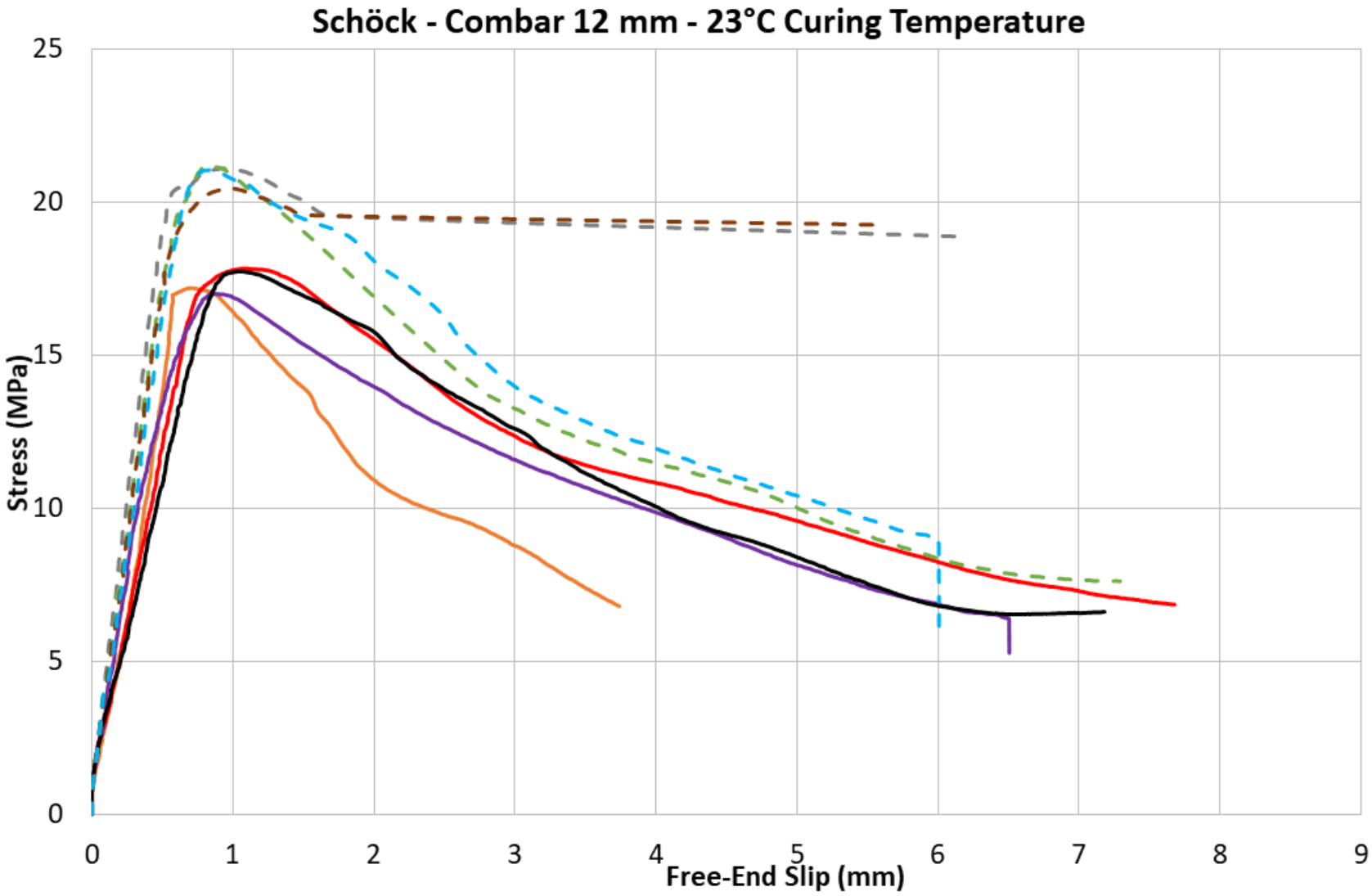

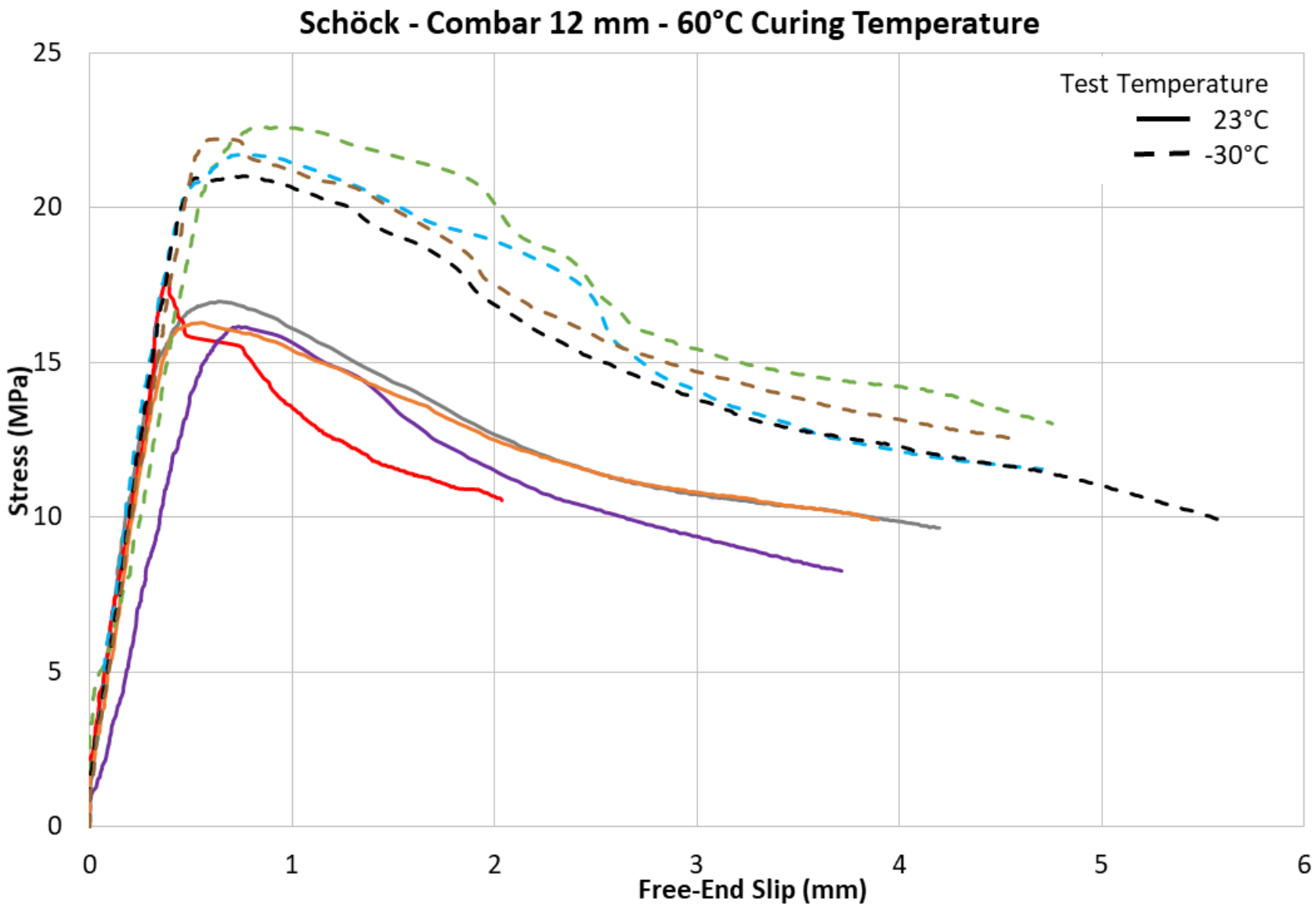
Schöck - Combar 12 mm - 60°C Curing Temperature
Test Temperature
23°C
-30°C
Stress (MPa)
Free-End Slip (mm)
0
5
10
15
20
25
0
1
2
3
4
5
6

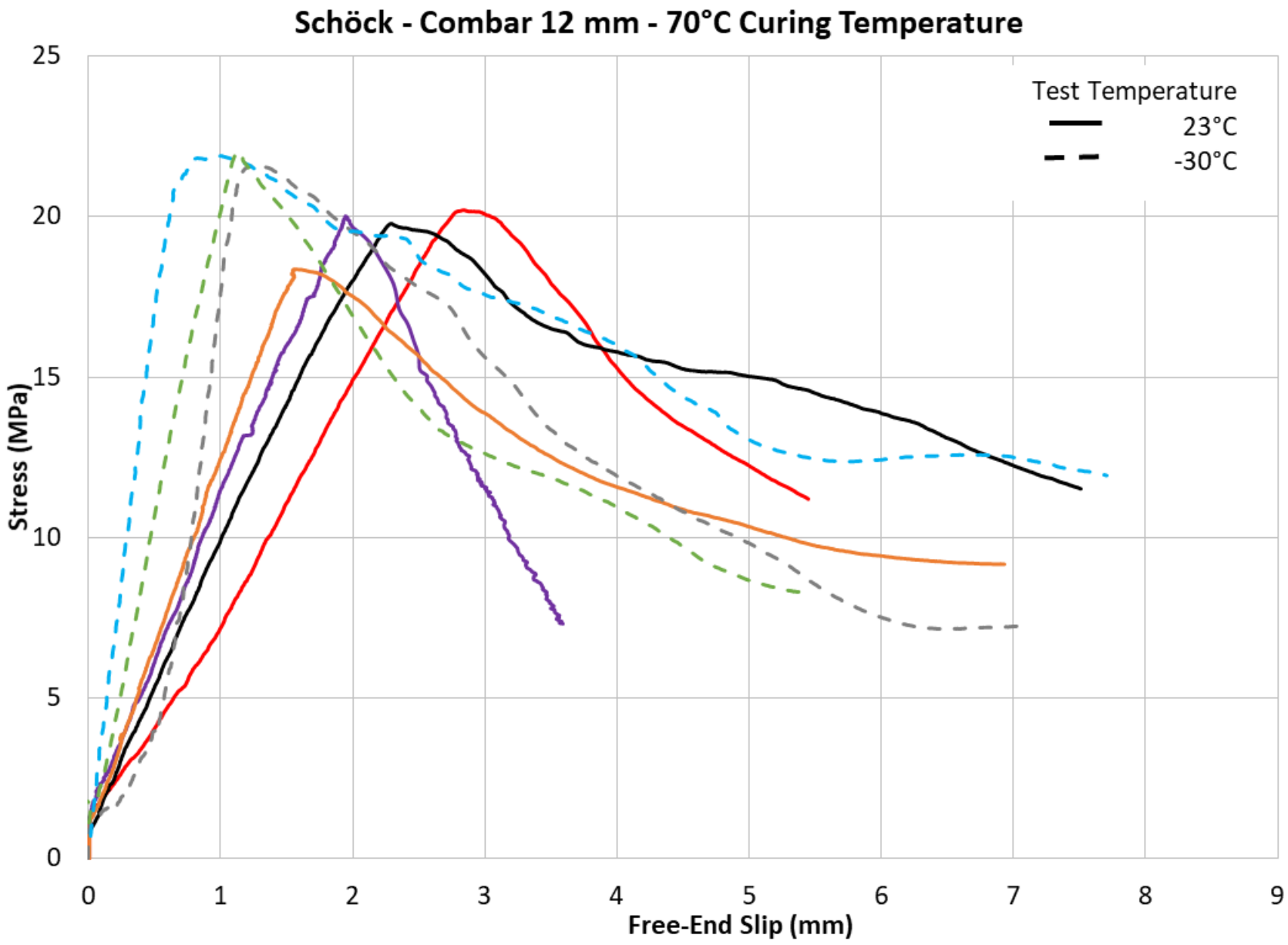
Schöck - Combar 12 mm - 70°C Curing Temperature
Test Temperature
23°C
-30°C
Stress (MPa)
Free-End Slip (mm)
0
5
10
15
20
25
0
1
2
3
4
5
6
7
8
9

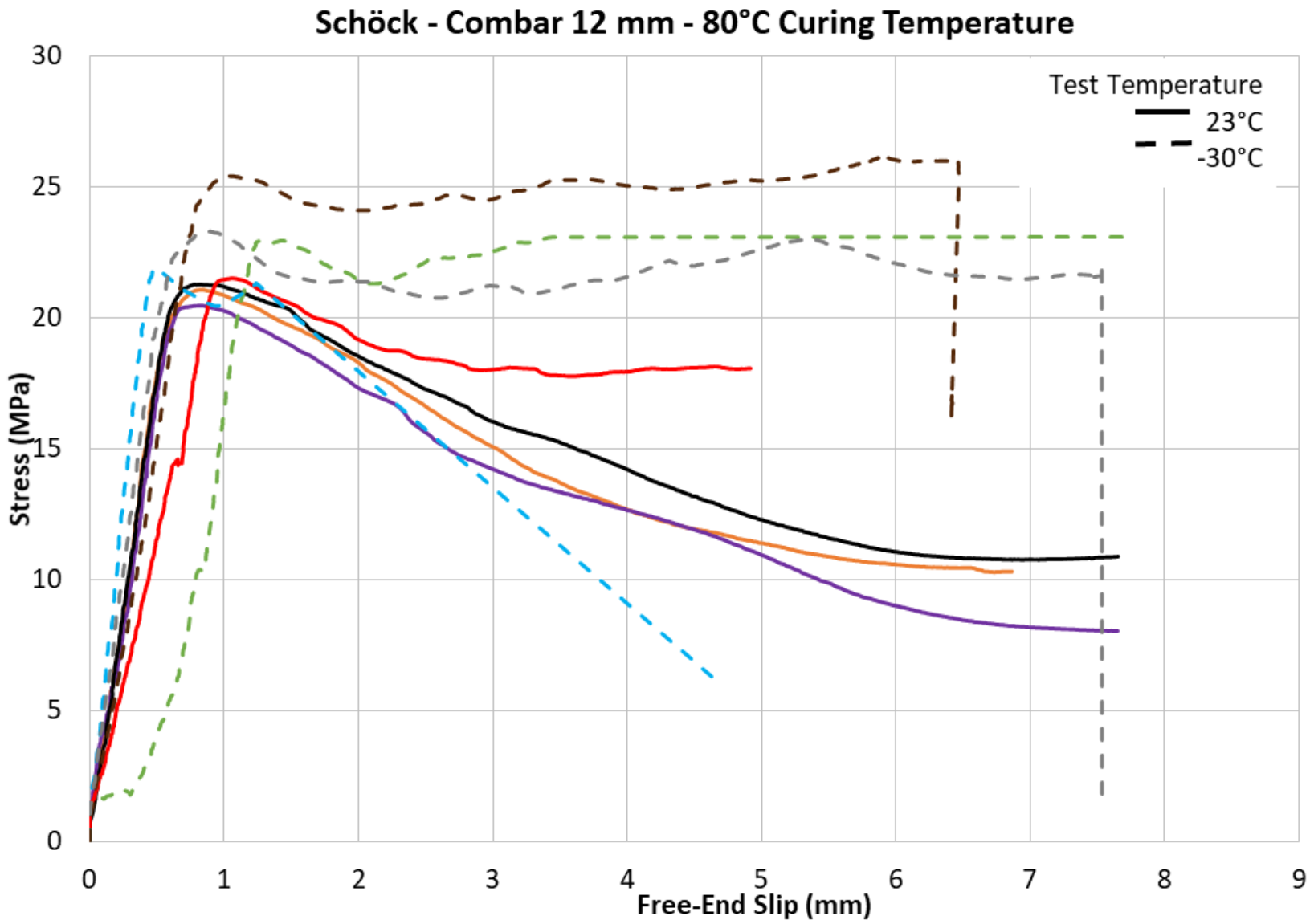
Schöck - Combar 12 mm - 80°C Curing Temperature
Test Temperature
23°C
-30°C
Stress (MPa)
Free-End Slip (mm)
0
5
10
15
20
25
30
0
1
2
3
4
5
6
7
8
9

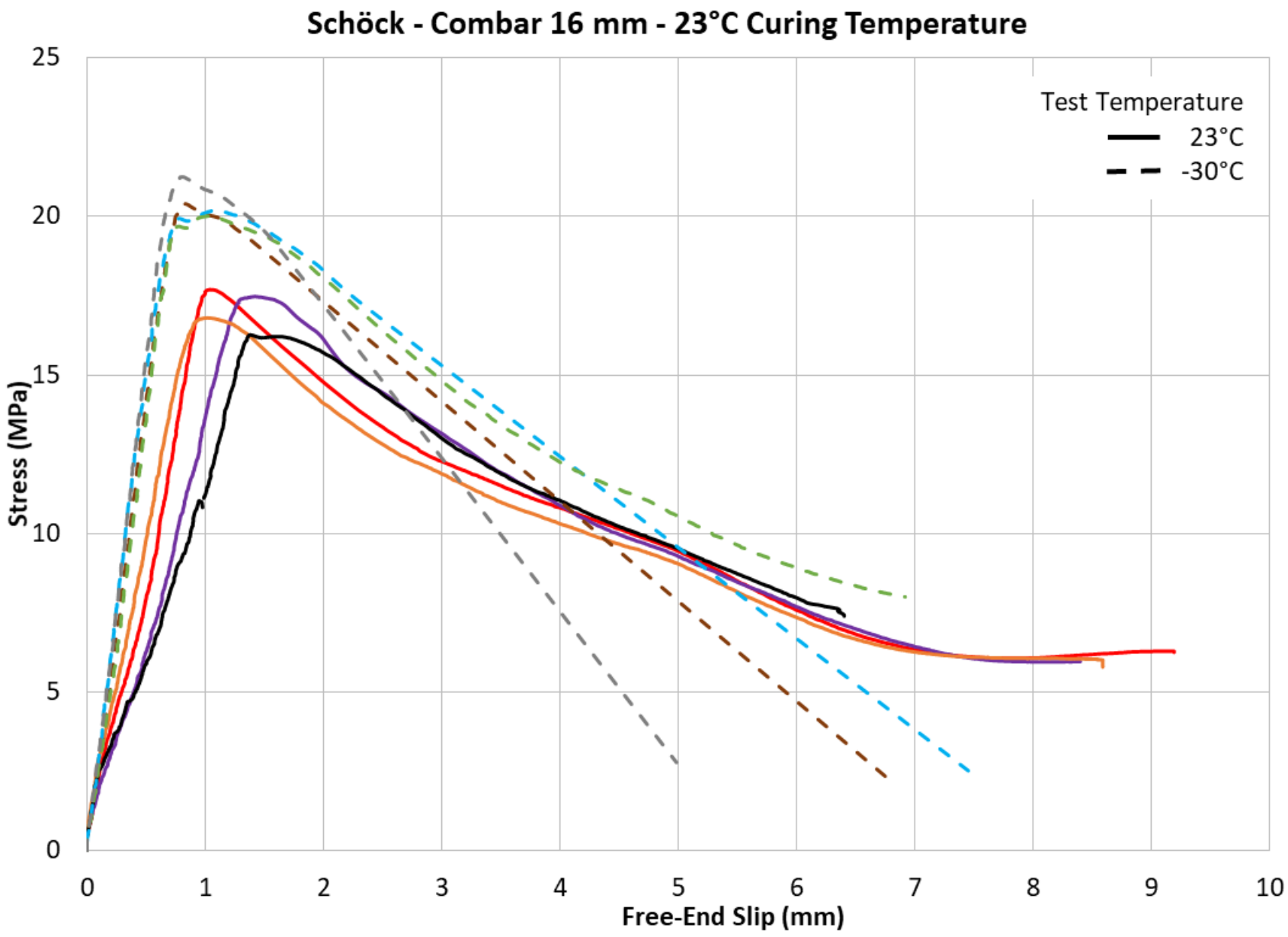
Schöck - Combar 16 mm - 23°C Curing Temperature
Test Temperature
23°C
-30°C
Stress (MPa)
Free-End Slip (mm)
0
5
10
15
20
25
0
1
2
3
4
5
6
7
8
9
10

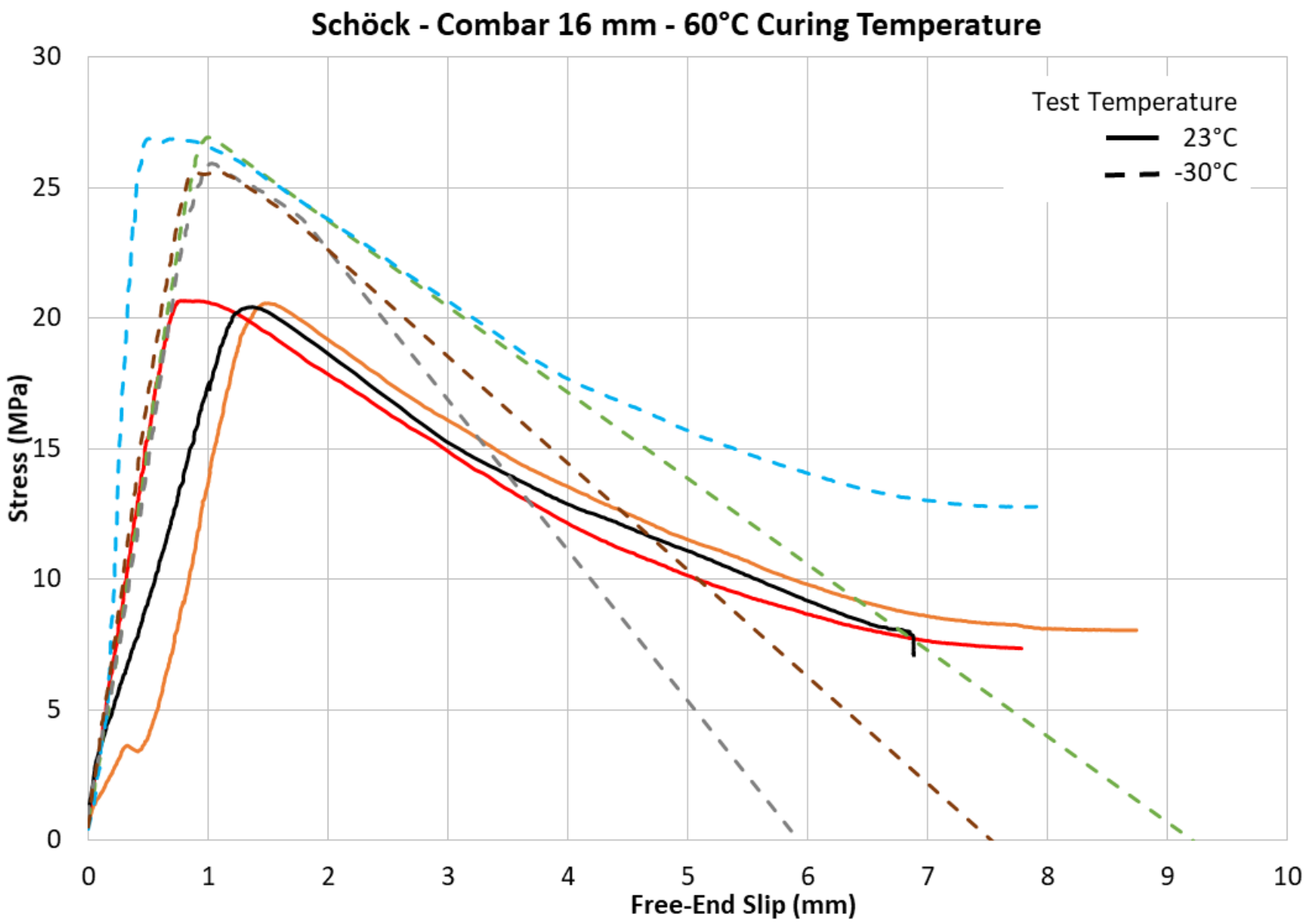
Schöck - Combar 16 mm - 60°C Curing Temperature
Test Temperature
23°C
-30°C
Stress (MPa)
Free-End Slip (mm)
0
5
10
15
20
25
30
0
1
2
3
4
5
6
7
8
9
10

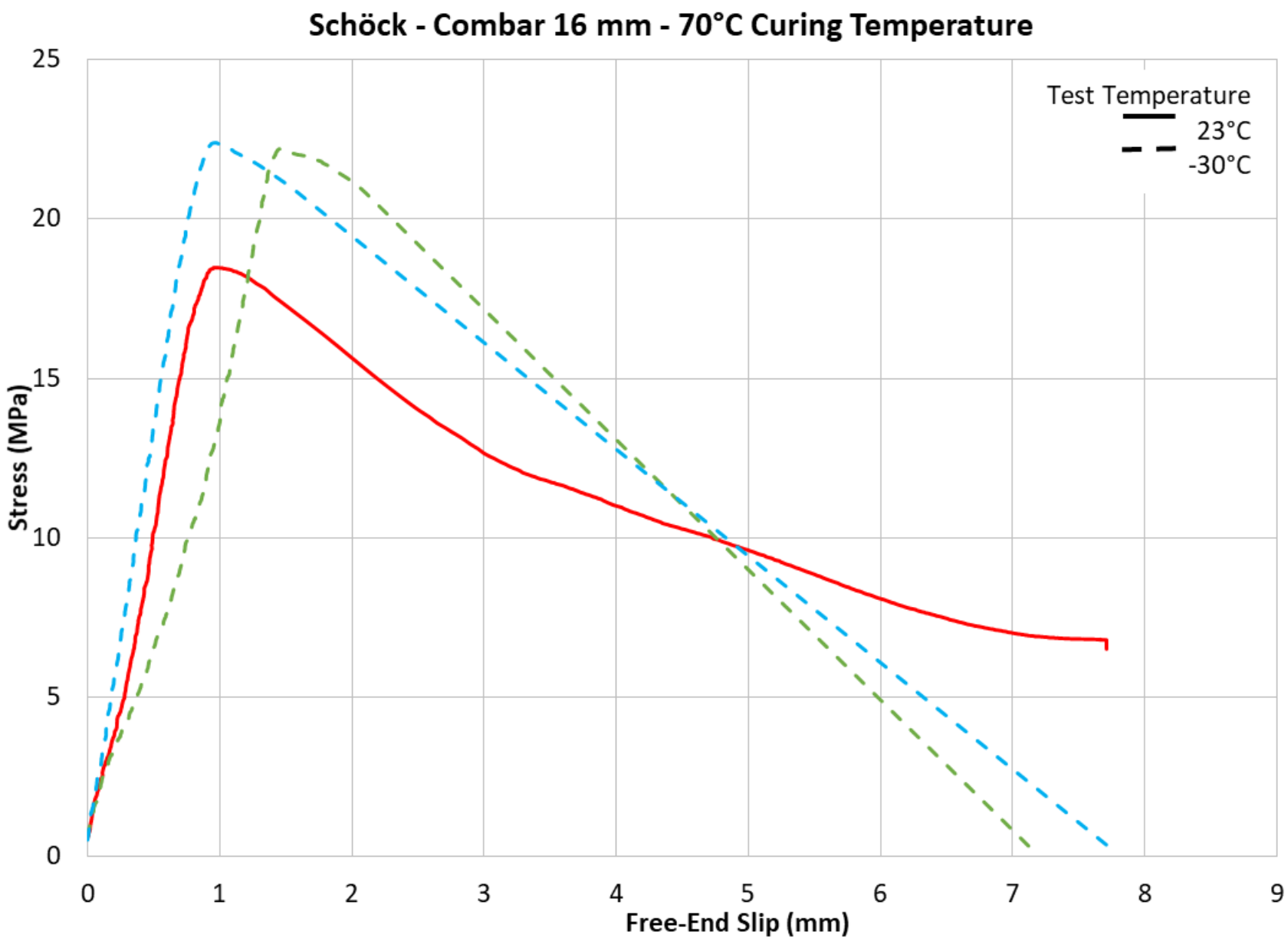
Schöck - Combar 16 mm - 70°C Curing Temperature
Test Temperature
23°C
-30°C
Stress (MPa)
Free-End Slip (mm)
0
5
10
15
20
25
0
1
2
3
4
5
6
7
8
9

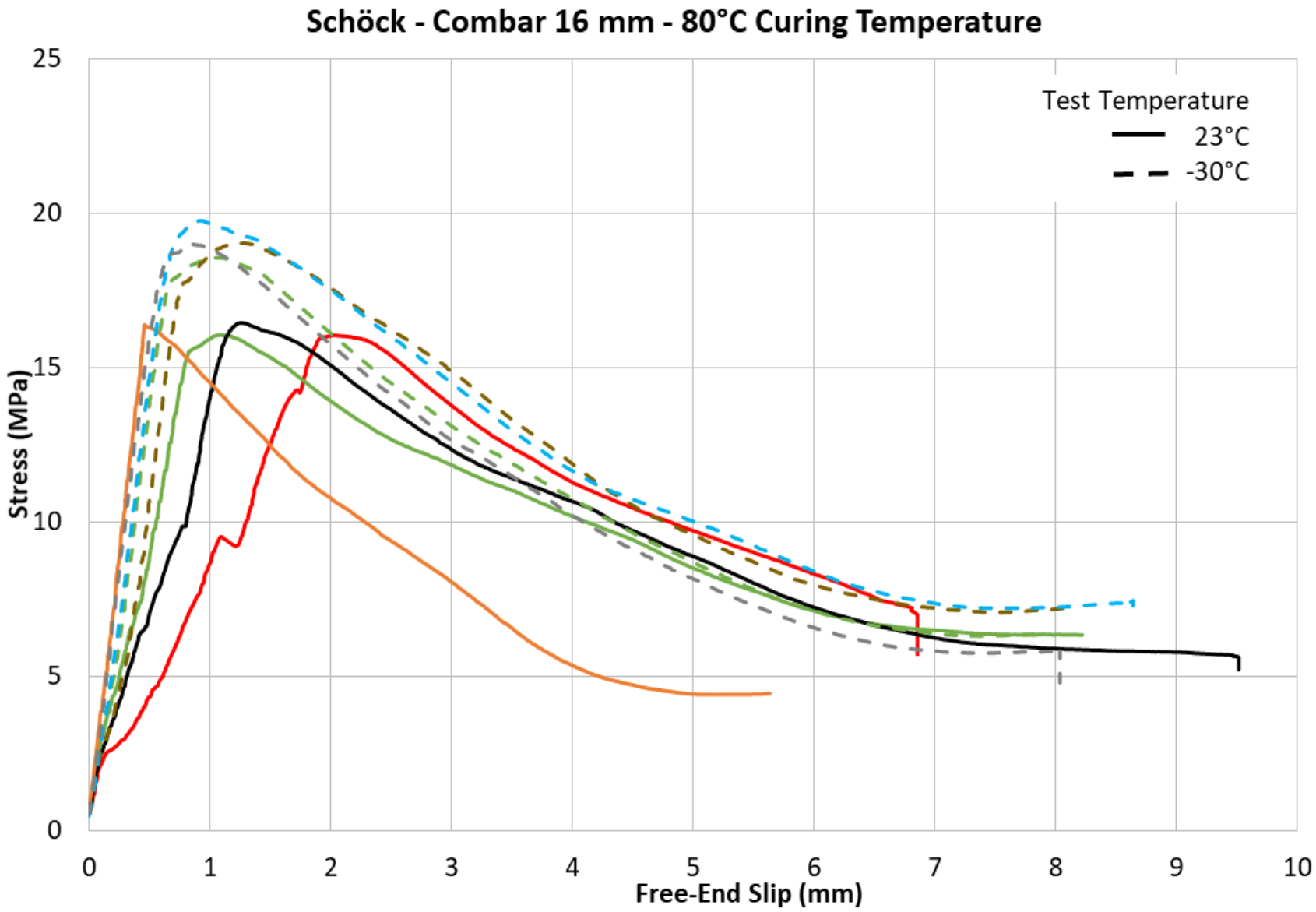
Schöck - Combar 16 mm - 80°C Curing Temperature
Test Temperature
23°C
-30°C
Stress (MPa)
Free-End Slip (mm)
0
5
10
15
20
25
0
1
2
3
4
5
6
7
8
9
10

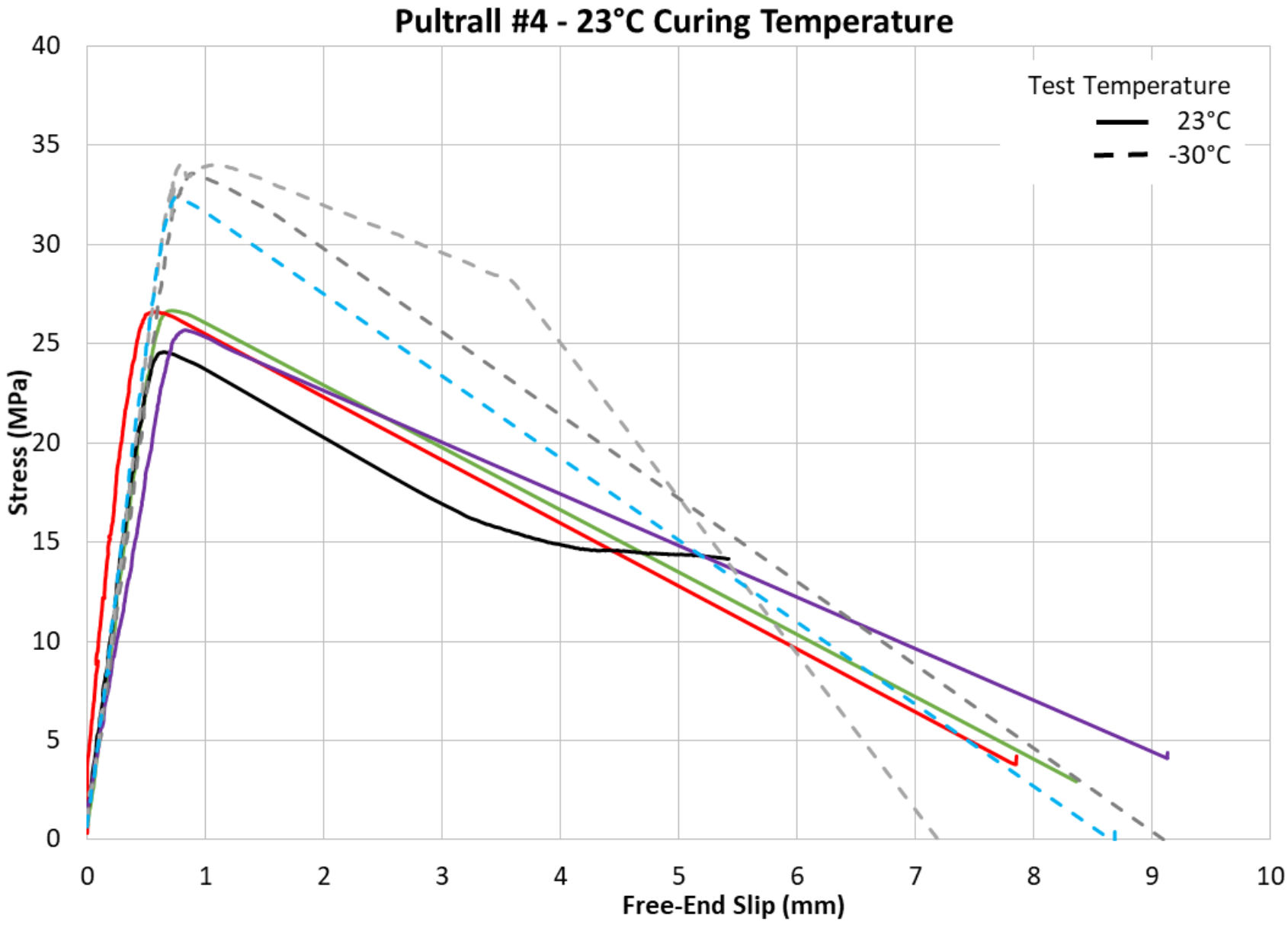
Pultrall #4 - 23°C Curing Temperature
Test Temperature
23°C
-30°C
Stress (MPa)
Free-End Slip (mm)
0
5
10
15
20
25
30
35
40
0
1
2
3
4
5
6
7
8
9
10

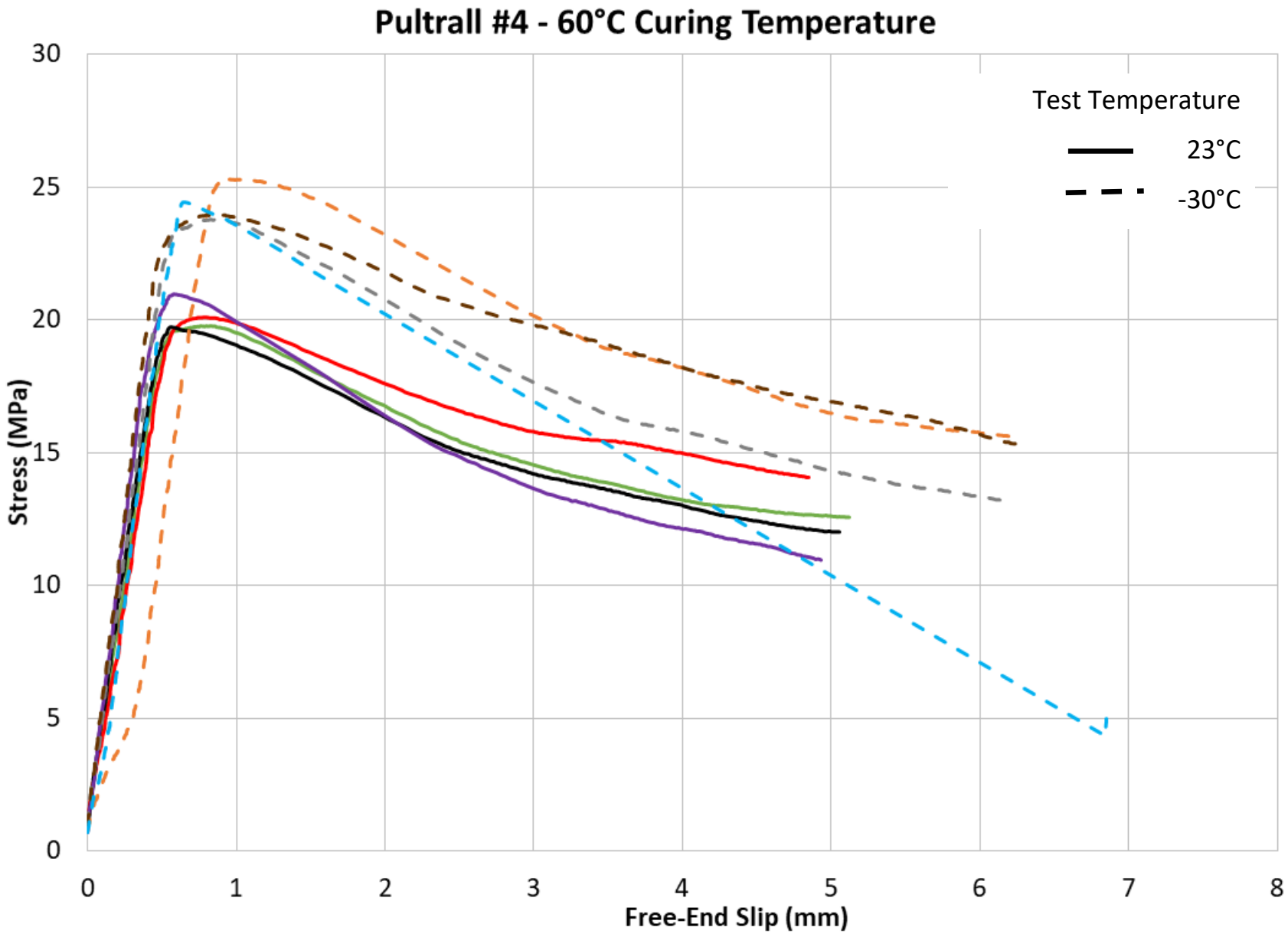
Pultrall #4 - 60°C Curing Temperature
Test Temperature
23°C
-30°C
Stress (MPa)
Free-End Slip (mm)
0
5
10
15
20
25
30
0
1
2
3
4
5
6
7
8

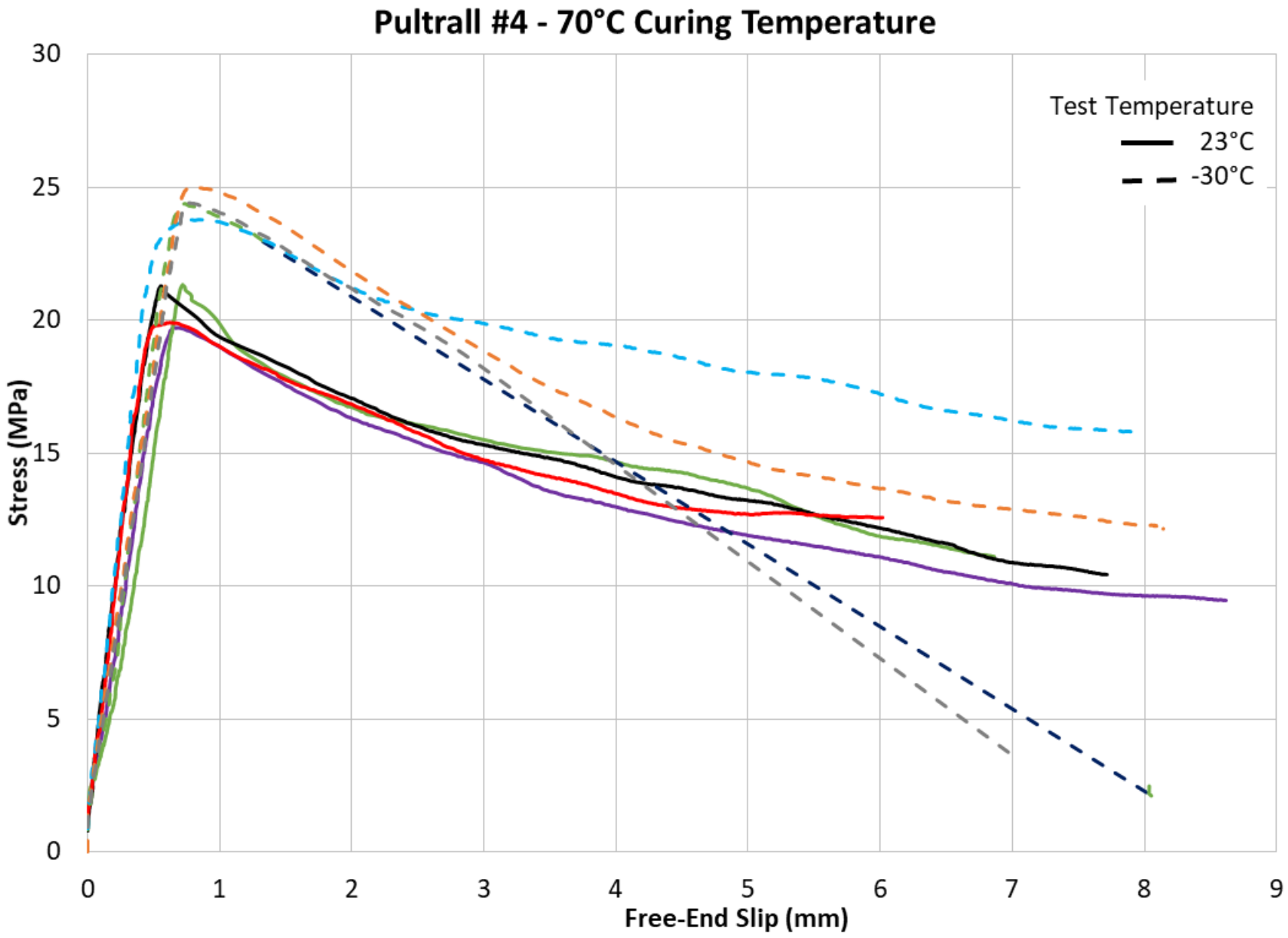
Pultrall #4 - 70°C Curing Temperature
Test Temperature
23°C
-30°C
Stress (MPa)
Free-End Slip (mm)
0
5
10
15
20
25
30
0
1
2
3
4
5
6
7
8
9

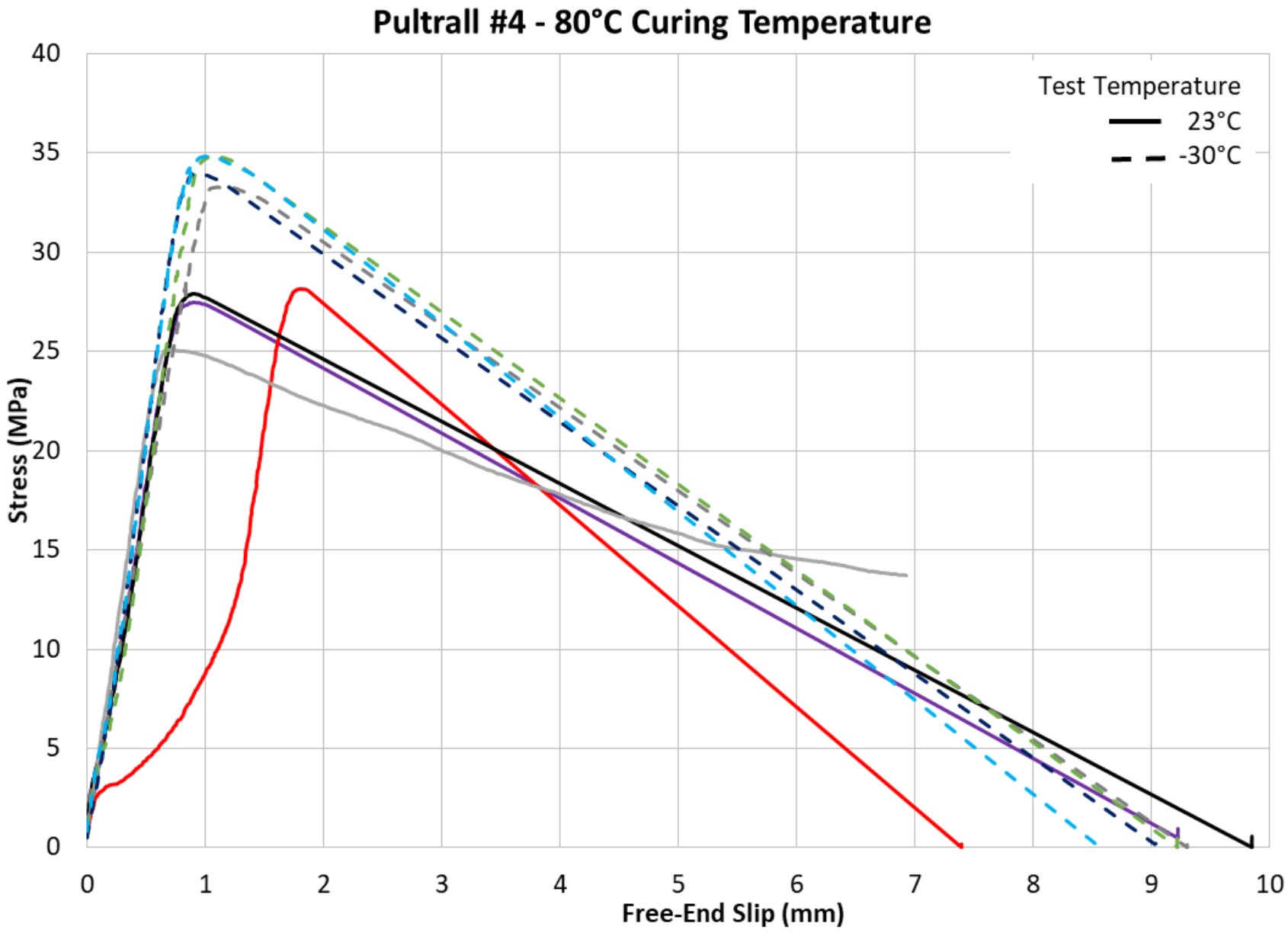
Pultrall #4 - 80°C Curing Temperature
Test Temperature
23°C
-30°C
Stress (MPa)
Free-End Slip (mm)
0
5
10
15
20
25
30
35
40
0
1
2
3
4
5
6
7
8
9
10

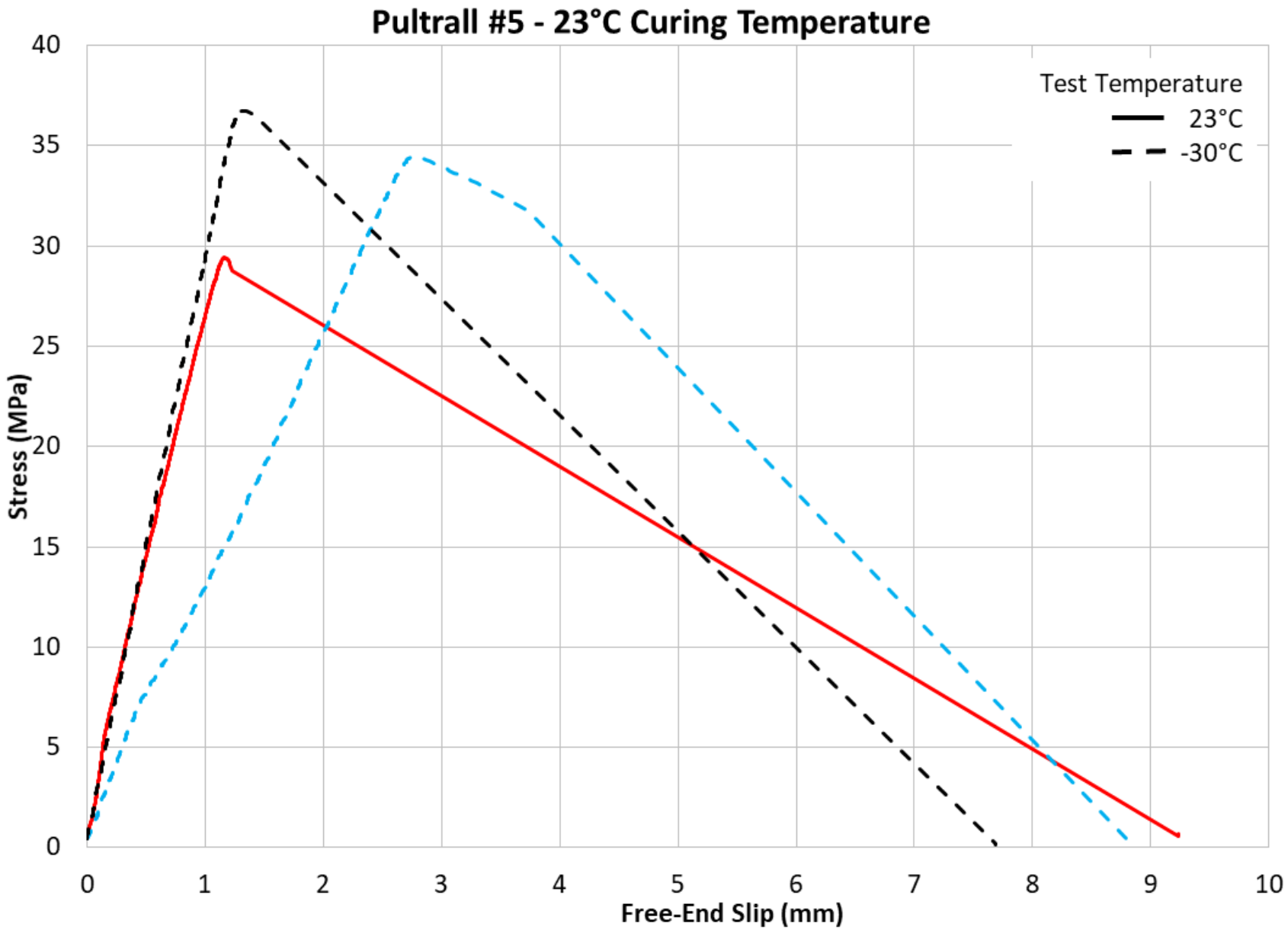
Pultrall #5 - 23°C Curing Temperature
Test Temperature
23°C
-30°C
Stress (MPa)
Free-End Slip (mm)
0
5
10
15
20
25
30
35
40
0
1
2
3
4
5
6
7
8
9
10

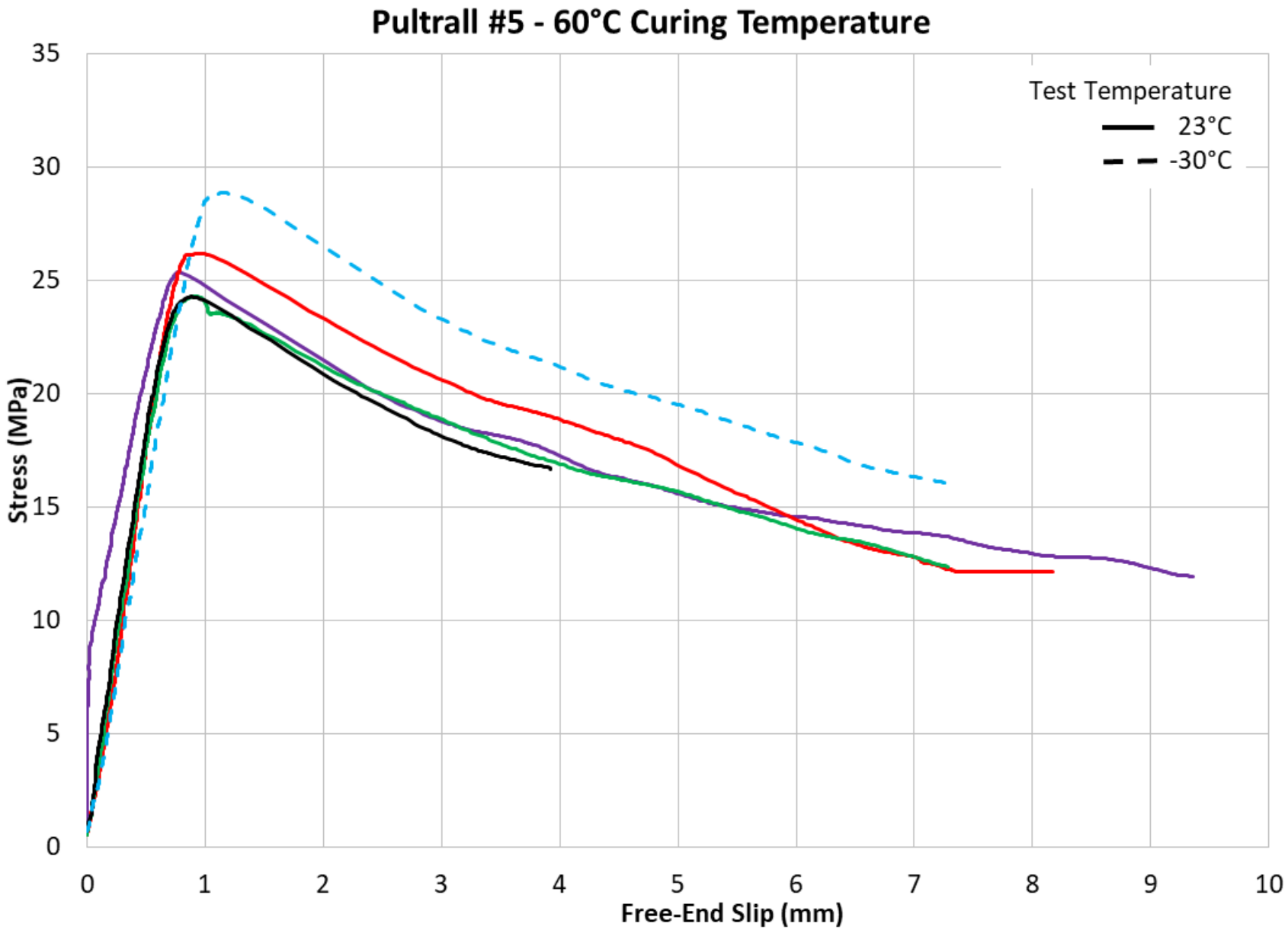
Pultrall #5 - 60°C Curing Temperature
Test Temperature
23°C
-30°C
Stress (MPa)
Free-End Slip (mm)
0
5
10
15
20
25
30
35
0
1
2
3
4
5
6
7
8
9
10

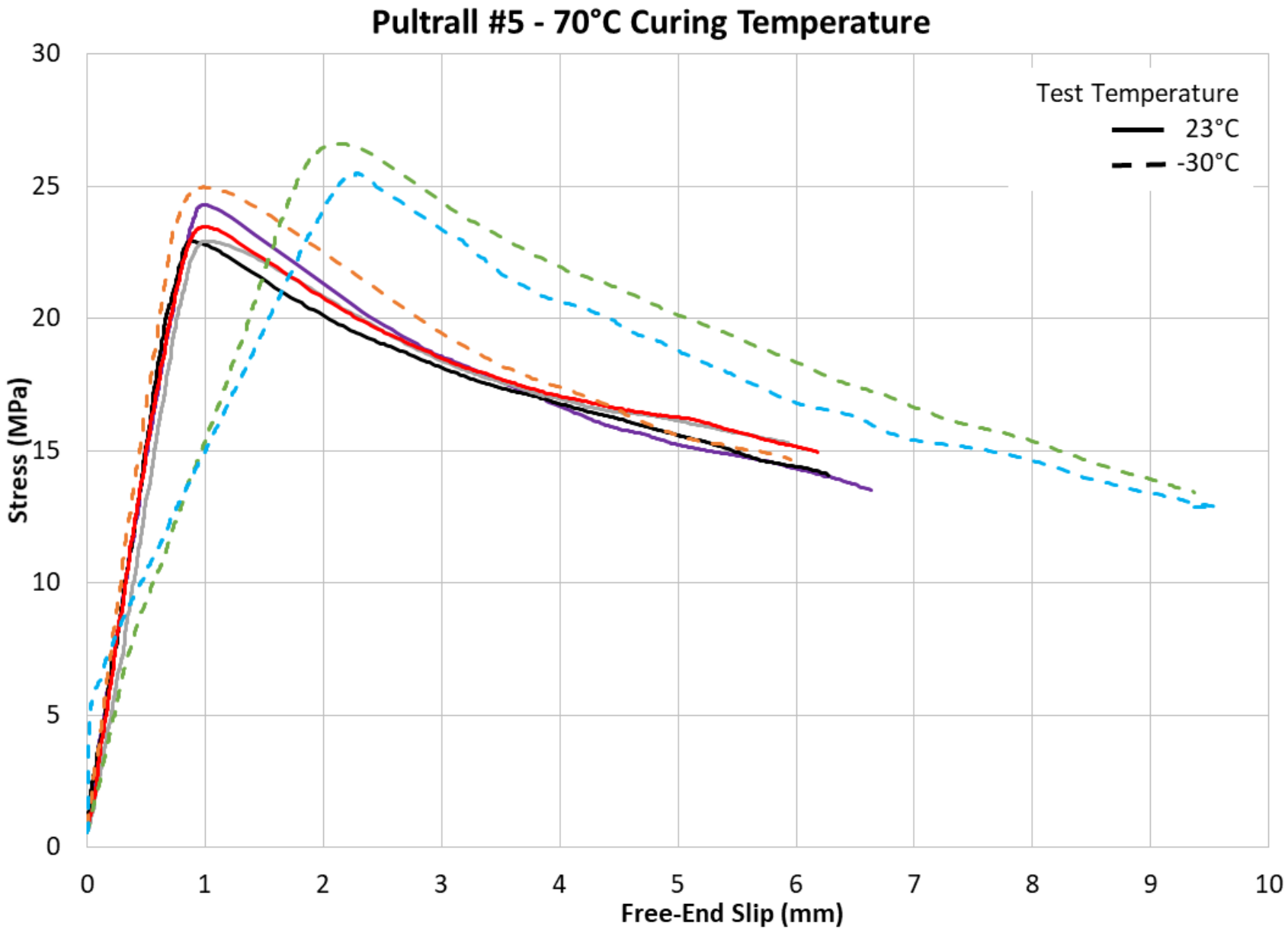
Pultrall #5 - 70°C Curing Temperature
Test Temperature
23°C
-30°C
Stress (MPa)
Free-End Slip (mm)
0
5
10
15
20
25
30
0
1
2
3
4
5
6
7
8
9
10

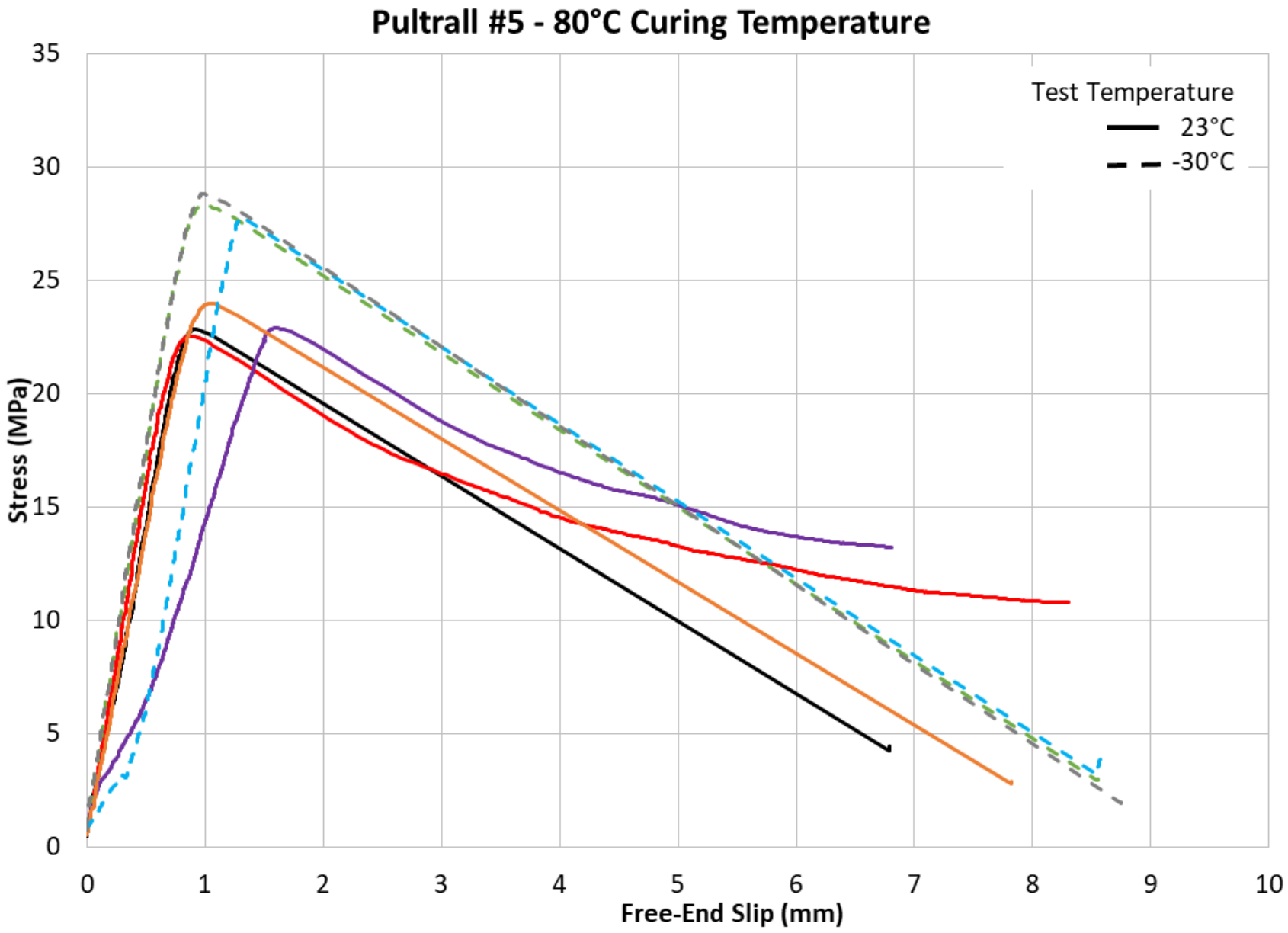
Pultrall #5 - 80°C Curing Temperature
Test Temperature
23°C
-30°C
Stress (MPa)
Free-End Slip (mm)
0
5
10
15
20
25
30
35
0
1
2
3
4
5
6
7
8
9
10

Appendix E – Statistical testing

In order to determine the statistical significance of the data collected throughout the experimental process two different statistical analyses were undertaken, the t-test and the ANOVA (anaylsis of Variance) test.

The t-test is used to prove a statistical difference between the mean of two sets of data, that cannot be accounted for by chance alone. The test utilizes a null hypothesis and an alternative hypothesis. The null hypothesis states that there is no difference between the mean of two groups of data, Equation 44. The alternative hypothesis states that the means are not equal, Equation 45. By accepting the null hypothesis, it is assumed that the mean of group A and B are equal and that statistically we cannot account for differences in the data. By rejecting the null hypothesis, it is assumed that there is a statistical difference between the mean of group A and B and that observed differences can statistically be defended.

$$H_o: \mu_1 = \mu_2 \qquad \text{Equation 44}$$

$$H_a: \mu_1 \neq \mu_2 \qquad \text{Equation 45}$$

The t-value is determined using Equation 46:

$$t = \frac{\mu_A - \mu_B}{\sqrt{\frac{S_A^2}{n_A} + \frac{S_B^2}{n_B}}} \qquad \text{Equation 46}$$

Where μ_A and μ_B are the means, S_A and S_B are the variances, and n_A and n_B are the sample size of data set A and B respectively. The t-value is then compared to a critical t-value based on the number of degrees of freedom and the required confidence interval (α), typically assumed to be 95%. A cumulative density function is then used to determine the probability that the samples came from the same population, presented as a p_{value}.

The ANOVA test works very similarly to the t-test and allows a statistical comparison between the two data sets. Additionally, the ANOVA test allows for a comparison of two independent variables allowing for two categories of the data. The ANOVA test relies on three hypotheses. First, that the mean of the observation of one group are the same. Second, that the means of the second group are the same. Third, that there is no interaction between the two factors. In terms of the data presented above, it determined the significant differences between means of curing conditions, test temperature and time on compressive strength by accepting or rejecting the null hypothesis.

The analysis was done using Microsoft excel and the F values compared to the critical over a confidence interval of 95%. A cumulative density function is then used to determine the probability that the samples came from the same population, presented as a p_{value}.